PSL★
UNIVERSITÉ PARIS

THÈSE DE DOCTORAT
DE L'UNIVERSITÉ PSL

Préparée à l'École Normale Supérieure

Fluctuations in turbulent flows

Soutenue par
Gaurav PRABHUDESAI
Le 17 février 2021

École doctorale n°564
Physique en Île-de-France

Spécialité
Physique

Composition du jury :

Alain PUMIR
École Normale Supérieure (Lyon)   *Président*

Nicolas MORDANT
Université Grenoble-Alpes   *Rapporteur*

Luminita DANAILA
Université de Rouen   *Rapporteur*

Michael LE BARS
IRPHÉ, Aix-Marseille Université   *Examinateur*

Bernard CASTAING
Université Grenoble-Alpes   *Examinateur*

François PÉTRÉLIS
École Normale Supérieure (Paris)   *Co-directeur de thèse*

Stephan FAUVE
École Normale Supérieure (Paris)   *Directeur de thèse*

ENS ÉCOLE NORMALE SUPÉRIEURE | PSL★ RESEARCH UNIVERSITY PARIS

Acknowledgements

After considering many possibilities on how to write this section, I came to the conclusion that there is no best way when it comes to expressing heartfelt emotions. I have found this part to be the most difficult to write in the manuscript and rightfully so! For I consider this work less of mine and more of the people who made it possible and I carry a certain responsibility in thanking each one of them.

First and foremost, I would like to thank Stephan Fauve and Francois Petrelis with whom I had utmost pleasure working over the course of almost four years. Their genuineness and ingenuity in approaching science is something I am proud to have learnt (atleast partially). It was indeed a pleasure to find in Stephan someone who loved dark humour as much as I did. I hope this humour does not get me in trouble in the future! And with Francois, I learnt to be a child at heart, equally curious and loving. Their support and belief in me was unwavering, having nudged me in the right direction when I needed it. I will always be indebted to them and I could not have asked for any other people to have as my supervisors. The freedom they gave me, though daunting at times, has made me immensely confident of my capabilities.

Next, I would like to thank Luminita Danaila and Nicolas Mordant for accepting to be my reporters and reading this long manuscript in the middle of holidays and the pandemic. I would like to extend my gratitude to Alain Pumir, Michael Le Bars and Bernard Castaing for agreeing to be a part of my jury. The pandemic has prevented us from meeting in person but I hope we are able to soon.

The acknowledgements section would be incomplete without thanking Stephane Perrard. He has been a brother, a friend and a mentor (in no particular order) for the last two years. It was with him, I learnt the pleasure of collaborative scientific endeavour. My only hope is that we don't smell of pastis for the rest of our lives. If only we got a euro everytime someone thought we were alcoholics, we would have been able to buy a sailing boat! Next, I would like to thank all the people with whom I shared the space of the group "physique non linéaire" and had countless coffees and lunches. Benoit and Kanna with whom I shared S11 when I first arrived and with whom I had very informative discussions on everything under the sun. If only I could be as organized as Benoit ... but pandemics seem more probable. I always admired the dedication of Alexis for marathons but somehow could not convince myself to run. I would like to thank Adrian van Kan whom I have asked the stupidest questions possible in physics and he was always nice enough to say that they were interesting! I thank Maxime for showing me what the limit is of loving clementine and being a good friend whenever I

> "*And when things start to happen,*
> *don't worry. Don't stew.*
> *Just go right along.*
> *You'll start happening too.*
>
> *With banner flip-flapping,*
> *once more you'll ride high!*
> *Ready for anything under the sky.*
> *Ready because you're that kind of a guy!*" [1]

— Dr. Seuss

Contents

Chapter 1

General Introduction

«*Fais quelque chose, crée quelque chose - n'importe quoi pour que cette affreuse solitude ne te détruise pas à petit feu...*»

"*Do something, create something - anything so that this dreadful loneliness does not slowly destroy you...*"[2]

Dimanche 26 octobre

The study of turbulence or turbulent flows forms an important part of the domain of fluid dynamics and is considered one of the longest unsolved problems of classical physics. The community of physics and engineering has devoted efforts for centuries to understand turbulence which is continued to this day. This is evidenced from a Google Scholar search which shows that roughly $44,000$ articles were published with the word turbulence in their titles in the year 2020 alone. Turbulent flows are characterized by an unpredictable behaviour of the flow across a range of *scales*[1] which calls for a probabilistic description of turbulence[3] and amounts to studying different statistical properties of the flow. As was shown by Reynolds [4], the transition of a laminar flow to a turbulent flow can be characterized by a dimensionless number (now called the *Reynolds number*) which is defined as,

$$Re = \frac{uL}{\nu}$$

where u and L are the typical velocity and length scales of the flow (for example the mean velocity across a cross section of a circular tube and the radius of the tube for the famous experiments performed by Reynolds). Reynolds found that for the values of this dimensionless number above a critical value, the flow became turbulent. As with any other dissipative system, turbulent flows dissipate energy and to sustain them, one needs to continuously inject energy in them. A physical picture of the process attributed to Richardson [5] is shown

---

[1]By scales we mean the length and time scales over which the fluid motion is observed to change.

in fig.I.1a. The mean energy per unit mass is injected in eddies of typical size of l_0[2] and whose rate per unit time is denoted by $\langle \epsilon \rangle$. This energy gets transferred to eddies of smaller sizes through non-linear interactions all the way down to eddies of typical size η which is also called as the Kolmogorov microscale where it gets dissipated into heat due to viscosity. In the stationary state, the mean rate of energy injected per unit mass would be equal to the mean rate of energy dissipated per unit mass, both of which we denote by $\langle \epsilon \rangle$. In quantitative terms, this can also be seen from the energy spectrum of the velocity fluctuations as a function of the wavenumber. If the velocity fluctuations are denoted by $\mathbf{u}$, then the wavenumber energy spectrum is defined as [6],

$$E(k) = \frac{1}{16\pi^3} \oint dS(k) \int d^3r \; \Gamma_u^{ii}(\mathbf{r}) \; e^{\iota \mathbf{k} \cdot \mathbf{r}} \tag{I.1}$$

where the integration over a surface of sphere with radius of 'k' is denoted by $\oint () dS(k)$. The two-point spatial correlation tensor of the velocity fluctuations $\overline{\overline{\Gamma}}_u$ is defined as,

$$\Gamma_u^{ij}(r) = \langle u_i(\mathbf{x}) u_j(\mathbf{x} + \mathbf{r}) \rangle$$

and angular brackets denote ensemble averaging. Fig.I.1b depicts the energy injected at the wavenumber $1/l_0$ which gets transferred to smaller scales eventually getting dissipated at the wavenumber $1/\eta$. The inertial scales are defined as the scales with $1/l_0 \ll k \ll 1/\eta$. As is evident from the description presented, a quantity of central interest when studying turbulent flows is velocity. A mathematical description on the statistical properties of turbulent velocity fluctuations was first given by Kolmogorov in the year 1941 which we refer to as the *K41* theory [7, 8]. Kolmogorov in his K41 theory hypothesized that the for very large Re, the inertial scales of velocity fluctuations would be homogeneous and isotropic; their statistical properties determined uniquely by $\langle \epsilon \rangle$. He showed that with the assumption of scale invariance, we obtain for the energy spectrum of the inertial scales,

$$E(k) = C_K \langle \epsilon \rangle^{2/3} k^{-5/3} \tag{I.2}$$

where C_K is called the Kolmogorov constant. The form of the energy spectrum as well as the universality of the Kolmogorov constant (eqn.(I.2)) have been validated through numerous experiments [9, 10]. The value of Kolmogorov constant is found to be $C_K \approx 0.53$. Later, in the year 1962 Kolmogorov refined his $K41$ theory to account for the spatial dependence of the rate of energy dissipation per unit mass (ϵ) and the effects of intermittency at small scales. The refined theory of Kolmogorov is referred to as *K62*. The quantity of fluctuations in energy dissipation rate per unit mass ($\epsilon' = \epsilon - \langle \epsilon \rangle$) too has drawn interest and a large body of experimental work [9] has evidenced its intermittent nature and deviation of its statistical properties from simple scale invariance arguments central to the K41 theory.

---

[2]Note that l_0 need not necessarily be the same as L as l_0 would be characteristic to the instability process that leads to the transition of a laminar flow to a turbulent one.

(a)

(b)
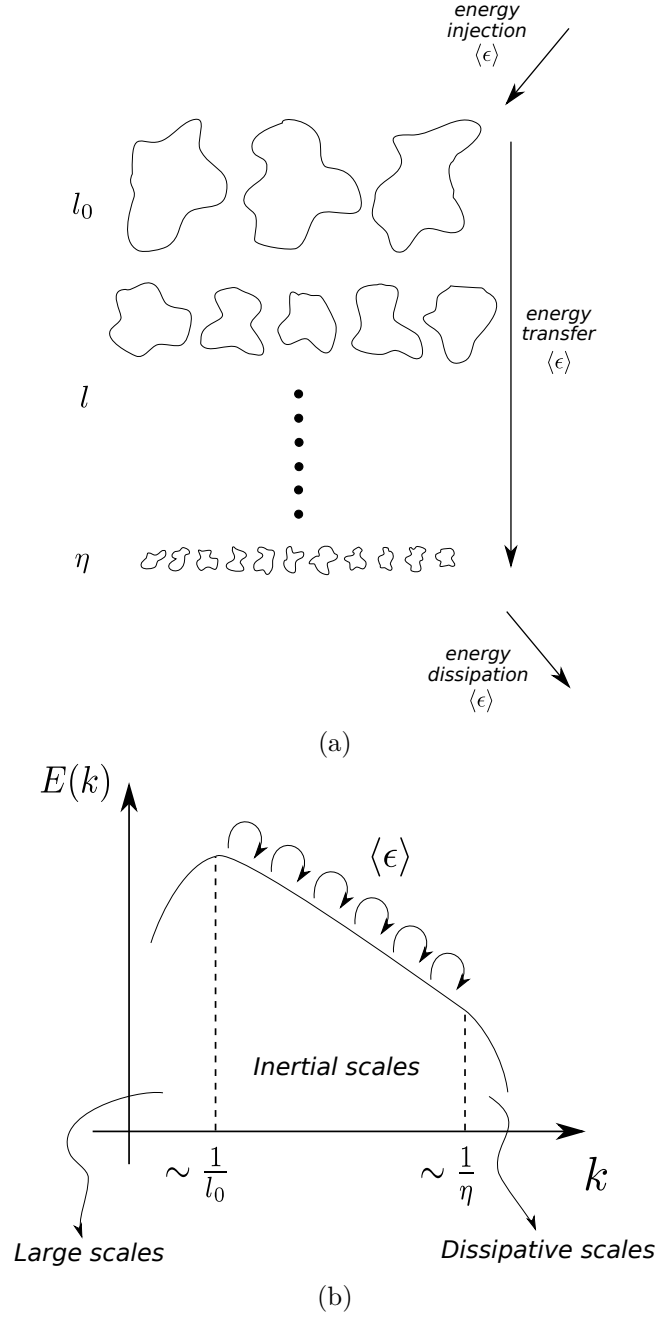
Fig. I.1 *(a) Figure shows the energy transferred between eddies of progressively smaller sizes as envisaged by Richardson [5] (b) A typical plot of the energy spectrum of velocity fluctuations $E(k)$ as a function of its wavenumber k. Energy is transferred between velocity fluctuations of adjacent wavenumbers. In the figures, l_0 denotes the size of the eddies at which energy is injected in the turbulent flow with a mean rate per unit mass of $\langle \epsilon \rangle$. The size of eddies at which energy is dissipated is denoted by η. The eddies of sizes intermediate to l_0 and η are denoted by l.*

In addition to fluctuations in velocity and dissipation rate, the statistical properties of pressure fluctuations too have been studied to characterize turbulent flows. The energy spectrum for pressure fluctuations predicted from dimensional analysis have been experimentally verified for isotropic turbulence and shear flows and have also been used to observe coherent structures in turbulent boundary layers [11, 12] and in the bulk of turbulent flows [13, 14].

All turbulent flows dissipate energy at small scales via viscous dissipation. As we noted earlier, the process of viscous dissipation has drawn considerable interest owing to its intermittent behaviour and departure from Kolmogorov's K41 theory. The heat generated in the process of viscous dissipation would be captured by the spontaneously generated temperature fluctuations. Studying such temperature fluctuations thus offers a way of characterizing the small scale structure of turbulence. Surprisingly, no experimental work exists in literature on the study of temperature fluctuations generated by viscous dissipation. The possible reason for this is that considerable efforts have been put to understand temperature fluctuations in turbulent flows in the general framework of passive scalars. Temperature fluctuations are externally injected in a turbulent flow and its statistical properties when undergoing turbulent advection and diffusion are studied [15]. In this scenario, the effects of viscous dissipation are neglected owing to its magnitude being smaller than the externally supplied temperature fluctuations. Nonetheless, spontaneously generated temperature fluctuations in turbulent flows are fundamental in characterizing the small scale structure of turbulence and as of yet their statistical properties remain unexplored.

Even for a quantity as well studied as velocity in turbulent flows, many questions about its statistical properties are yet to be understood. When studying turbulent velocity fluctuations in the Eulerian frame of reference, historically the focus has been on studying statistics either spatially or temporally. For example, studying the energy spectrum of velocity fluctuations in wavenumber $E(k)$ amounts to studying the two point velocity correlation (see eqn.(I.1)),

$$\Gamma_u^{ij}(r) = \langle u_i(\mathbf{x})u_j(\mathbf{x} + \mathbf{r}) \rangle$$

and studying the energy spectrum of velocity fluctuations in frequency $E(f)$ amounts to studying the one point temporal velocity correlation,

$$\Gamma_u^{ij}(\tau) = \langle u_i(t)u_j(t + \tau) \rangle$$

The lack in understanding the spatio-temporal characteristics of turbulence can be possibly linked to the limitations faced both experimentally and numerically in resolving turbulent flows across a wide range of scales in space and time simultaneously. With recent advances in computational power and comparatively newer experimental techniques like the particle image velocimetry (PIV), there has been a renewed interest in characterizing the spatio-temporal behaviour of turbulent flows. In their recent work, Leoni *et al.* [16] numerically studied the velocity spatio-temporal spectrum $E(k, f)$ for homogeneous, isotropic turbulence and reported observing the *sweeping effect* proposed by Tennekes [17]. Another spatio-temporal quantity which is relevant from an experimental point of view is *magnitude-squared coherence* or simply *coherence* $\mathcal{C}(r, f)$ [3] which is defined as,

---

[3]Since it is a quantity that can be measured by point measurement techniques like hot-wire anemometry

$$\mathcal{C}(r, f) = \frac{|E(r, f)|^2}{E(f)^2}$$

Studying the spatio-temporal spectrum $E(k, f)$ or coherence $\mathcal{C}(r, f)$ amounts to studying the two point temporal velocity correlation,

$$\Gamma_u^{ij}(r, \tau) = \langle u_i(\mathbf{x}, t) u_j(\mathbf{x} + \mathbf{r}, t + \tau) \rangle$$

Thus the quantity of coherence offers a way to experimentally characterize the spatio-teporal characteristics of turbulent flows.

Another physical problem closely related to turbulence is the scattering of electromagnetic or acoustic waves by disordered media. On one hand, with known statistical properties of the disordered medium, in our case turbulence, we can predict the statistical properties of the scattered wave. On the other hand, we can infer statistical quantities related to the turbulent flow from the scattered wave. One example is the visualization of the flow by the Schlieren technique wherein the incident light is scattered by density fluctuations in the flow. Similarly, studying the scattering of acoustic waves by turbulent flows, one can infer the statistics of turbulent velocity and temperature fluctuations in Fourier space [18] (sketch I.2a). The problem of acoustic scattering by turbulent flows can also be cast in a slighlt different way. Consider the scenario of an acoustic wave travelling through a turbulent flow. The fluctuations in velocity and temperature in the turbulent flow would result in fluctuations of the amplitude and phase of the acoustic wave (sketch I.2b). In principle, one can obtain statistical information about the turbulent velocity and temperature fluctuations by studying the fluctuations in amplitude and phase of the incident acoustic wave.

The presentation of this thesis is quite straightforward and is as follows,

- In chapter II, we study the temperature fluctuations generated due to viscous dissipation in a turbulent flow. We devise an experiment where the external effects of temperature are minimized. This is important since the magnitude of temperature fluctuations generated during the process of viscous dissipation is very small[4].

- In chapter III, we study the spatio-temporal statistics of velocity fluctuations, specifically its coherence in turbulent flows. Two experimental setups are developed to ensure the reproducibility and robustness of our results. Two different experimental techniques are used, one with better temporal resolution and the other with better spatial resolution. This ensures that the results are not technique dependent.

- In chapter IV, we study the problem of amplitude and phase fluctuations of an acoustic wave incident on a turbulent flow. Experimental results and the theory developed are shown to be in agreement with our understanding from chapters II and III.

---

or laser doppler anemometry (LDA). On the other hand evaluating the spatio-temporal spectrum requires measurement of the entire velocity field at every instant in time.

[4]Compared to the ambient fluctuations if turbulent flow is generated in air.
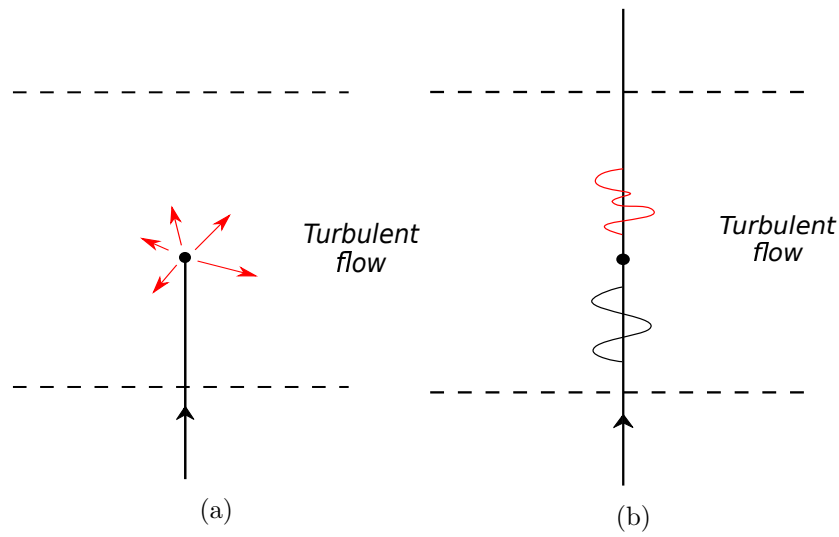
Fig. I.2   *(a) Sketch showing an incident acoustic wave being scattered by velocity and temperature inhomogeneities in the turbulent flow (b) Sketch showing the fluctuations in amplitude and phase of the incident acoustic wave due to velocity and temperature inhomogeneities in the turbulent flow.*

Chapter II

Temperature fluctuations in turbulent flows

«À quoi bon écrire? La vie est une cage de mots vides.»

"What is the use of writing? Life is a cage of empty words."[2]

<div align="right">Mercredi 3 septembre</div>

In many physical phenomena occurring in nature, the transport of scalar or vector fields by a turbulent flow plays an important role. The examples are ubiquitous ranging from concentration of chemical pollutants in the atmosphere (and the oceans)[19, 20] (fig. II.1a), the advection of thermodynamic quantities like temperature (humidity, etc.) (fig. II.1b) to the transport of magnetic fields in electrically conducting fluids and the generation of large scale magnetic fields in astrophysical bodies [21] (fig. II.1c).

These scalar (and vector) fields transported by the turbulent flow can have a significant effect on the turbulent flow itself and modify it, in which case they are called "*active*". An example of active scalar would be the magnetic field in 2D magnetohydrodynamic flows. If the presence of the scalar does not affect the flow and they are only transported by it, they are called "*passive*". For example, coloured dye in a turbulent flow would be a passive scalar.

Another scalar quantity of interest when studying turbulent flows is temperature, which can either be an active or a passive scalar depending on the problem being studied. Rayleigh-Bénard convection is a type of flow driven by buoyancy forces in a horizontal layer of fluid when the lower boundary of the fluid is maintained at a higher temperature than the upper boundary. The temperature field in Rayleigh-Bénard convection is an example of temperature as an active scalar. The study of temperature field in Rayleigh-Bénard convection has been a focus of research for decades. A review of Rayleigh-Bénard convection can be found in [22] which covers the developments on this topic till the late 1990s. The case of temperature field as a passive scalar in turbulent flows can be regarded as a particular example of transport and mixing of passive scalars in turbulent flows which has also been studied in detail

<div align="center">7</div>

over the years. The passive temperature field is either *forced* through bulk sources of heat or through a mean gradient of temperature in the bulk which then undergoes mixing due to the background turbulent flow. Recent advances in the field are summarized in the reviews by Warhaft [15], Sreenivasan [23], Shraiman [24] and Falkovich [25]. By using dimensional arguments, many different forms of the *energy spectrum*[1] of the fluctuations of temperature field have been proposed depending on the relative magnitudes of the kinematic viscosity of the fluid and the thermal diffusivity.

(a)

(b)

(c)
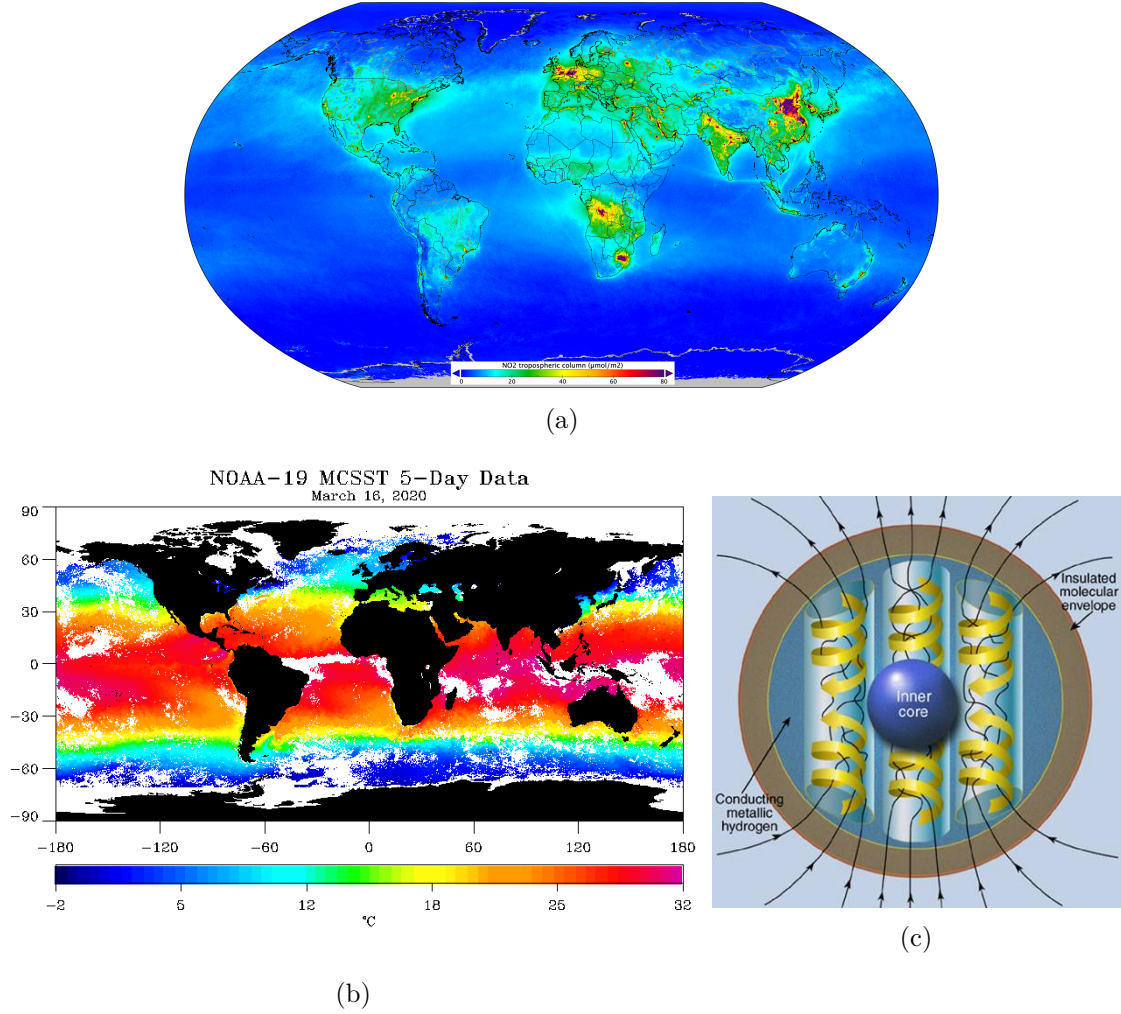
Fig. II.1   *(a) Concentration of nitrogen dioxide in the atmosphere. Data collected between April and September, 2018 by Copernicus Sentinel-5P mission, ESA [26]. (b) Sea surface temperature from satellite data obtained in March, 2020 [27]. (c) Illustration of the dipolar magnetic field of Jupiter [28].*

---

[1]We have to be careful when associating the words *energy spectrum* to temperature (or other scalar/vector quantities) fluctuations. Unlike energy spectra of velocity fluctuations, the area under the energy spectra of temperature fluctuations has the unit K^2 and thus does not correspond to energy in the conventional sense.

Most of the studies regarding passive scalars in turbulent flows have been performed on the basis that there exists a well defined length and time scale at which *energy* is injected in the passive scalar field. When studying temperature as a passive scalar, this may be reasonable when sources of heat or a temperature gradient is imposed in the bulk and maintained constant over time. However, this assumption might break down for temperature fluctuations produced by viscous dissipation in the turbulent flow itself. Surprisingly, the spontaneous temperature fluctuations arising from the inherent viscous dissipation of any turbulent flow have been overlooked over the years with only a few recent numerical investigations [29, 30, 31, 32, 33] leaving the problem far from being understood. The study of spontaneous temperature fluctuations is a theoretical and experimental challenge since the temperature fluctuations would be intertwined with the process of viscous dissipation. Theoretically, it is known that the viscous dissipation displays spatial and temporal intermittency [3, 34] affecting a wide range of spectral scales which breaks the scale invariance hypothesis at the base of simplest theories for turbulence. Experimentally, the fluctuations may take place at small scale and high frequency, requiring high sensitivity probes and careful signal analysis.

Can we measure, characterize and understand the temperature field generated by viscous dissipation with a laboratory experiment? Does the temperature field show behaviour possibly universal to all turbulent flows and can we obtain some predictions for it? This chapter is dedicated to answering these questions. The presentation of this chapter is as follows,

Sec. II.1: We present the theoretical background for studying temperature fluctuations produced by viscous dissipation in a turbulent flow. In subsections II.1.1 to II.1.4 we present the governing equations for the most general case, which is the compressible flow and therein obtain the governing equations under some limiting cases. In subsections II.1.5 and II.1.6 we study the behaviour of temperature due to viscous dissipation in an incompressible flow and obtain predictions for its energy spectrum and root-mean-square or RMS value from dimensional arguments.

Sec. II.2: Presents the experimental setup for studying temperature fluctuations due to viscous dissipation in an incompressible flow. In subsection II.2.3, we detail the basic properties of the flow.

Sec. II.3: Presents the measure of temperature fluctuations and their link to pressure fluctuations and small scale structures. We draw comparisons between the experimental observations and the behaviour as predicted from dimensional arguments. Some simple models are presented to explain these results.

Sec. II.4: Discussion of the results and their implications are presented.

II.1   Theoretical background

In this section, we will present the governing equations for three limiting cases of a weakly compressible flow which are the incompressible flow, acoustic waves and perfect fluid. We then proceed to focus on the limit of incompressible, homogeneous, isotropic turbulence and obtain predictions on the behaviour of root mean square (RMS) and energy spectrum of temperature fluctuations generated due to viscous dissipation. The presentation of this section loosely follows the article by Bayly *et al.* [35], lecture notes by Moffat [36] and books by Landau [37] and Yaglom [38, 9].

II.1.1   The governing equations

The set of governing equations for a viscous, compressible flows corresponding to conservation of mass, momentum, energy and an equation of state are,

$$
\begin{aligned}
&\frac{\partial \rho}{\partial t} + \nabla \cdot (\rho \mathbf{u}) = 0 \\
&\rho \left(\frac{\partial \mathbf{u}}{\partial t} + \mathbf{u} \cdot \nabla \mathbf{u} \right) = -\nabla p + \nabla \cdot \overline{\overline{\sigma}} = -\nabla p + \mu \nabla^2 \mathbf{u} + \left(\zeta + \frac{1}{3}\mu \right) \nabla(\nabla \cdot \mathbf{u}) + \mathbf{f} \\
&\frac{\partial}{\partial t}\left[\rho e + \frac{1}{2}\rho u^2 \right] = -\nabla \cdot \left[\left(\rho e + \frac{1}{2}\rho u^2 \right) \mathbf{u} + p\mathbf{u} - \overline{\overline{\sigma}} \cdot \mathbf{u} - \kappa \nabla T \right] \\
&\qquad\qquad\qquad p = p(\rho, T)
\end{aligned}
$$

where $T(\mathbf{x}, t)$ is the temperature field in the flow, $\mathbf{u}(\mathbf{x}, t)$ and $p(\mathbf{x}, t)$ are the turbulent velocity and pressure fields respectively, μ is the dynamic viscosity, ζ is the bulk viscosity, ρ is the density, e is the specific internal energy or internal energy per unit mass and κ is the thermal conductivity of the fluid. The body force per unit volume is denoted by $\mathbf{f}(\mathbf{x}, t)$, which in case of turbulent flows would be the forcing mechanism needed to sustain them. The stress tensor $\overline{\overline{\sigma}}$ is given by,

$$
\overline{\overline{\sigma}} = \mu \left(\overline{\overline{\nabla \mathbf{u}}} + \overline{\overline{\nabla \mathbf{u}}}^{\mathsf{T}} \right) + \left(\zeta - \frac{2\mu}{3} \right) \left(\nabla \cdot \mathbf{u} \right) \overline{\overline{I}}
$$

where the superscript 'T' implies transpose of the tensor and $\overline{\overline{I}}$ is the identity tensor. The term involving ζ and μ is often called the second viscosity λ_v with the definition,

$$
\lambda_v = \zeta - \frac{2\mu}{3}
$$

We can obtain the equation for specific entropy from the equation of energy by using the *Gibbs equation* and the definition of specific enthalpy,

$$Tds = de + pdv \Rightarrow de = Tds + \frac{p}{\rho^2}d\rho$$

$$e = h - pv \Rightarrow e = h - \frac{p}{\rho}$$

where s is the specific entropy, v is the specific volume (i.e. inverse of density ρ) and h is the specific enthalpy. On using the above identities to evaluate both sides of the energy equation and equating them, we obtain the equation for specific entropy [37],

$$\rho T \left(\frac{\partial s}{\partial t} + u_i \frac{\partial s}{\partial x_i} \right) = \frac{\partial}{\partial x_i} \left(\kappa \frac{\partial T}{\partial x_i} \right) + \frac{\mu}{2} \left(\frac{\partial u_i}{\partial x_j} + \frac{\partial u_j}{\partial x_i} - \frac{2}{3} \delta_{ij} \frac{\partial u_k}{\partial x_k} \right)^2 + \zeta \left(\frac{\partial u_k}{\partial x_k} \right)^2 \qquad \text{(II.1)}$$

where $\bar{\bar{\delta}}$ is the *Kronecker delta* tensor. The thermodynamic variables involved are the specific entropy s, pressure in the fluid p, the density of the fluid ρ and the temperature of the fluid T. Since, in a compressible flow, both the pressure and temperature result in variations in the density of the fluid, it cannot be regarded as constant. We can proceed then by evaluating the derivatives of the thermodynamic quantities with respect to pressure and temperature,

$$\frac{\partial s}{\partial t} = \left(\frac{\partial s}{\partial T} \right)_p \frac{\partial T}{\partial t} + \left(\frac{\partial s}{\partial p} \right)_T \frac{\partial p}{\partial t}$$

$$\frac{\partial s}{\partial x_i} = \left(\frac{\partial s}{\partial T} \right)_p \frac{\partial T}{\partial x_i} + \left(\frac{\partial s}{\partial p} \right)_T \frac{\partial p}{\partial x_i}$$

Substituting these in eqn.(II.1) and rearranging, we obtain [9],

$$\frac{\partial T}{\partial t} + u_i \frac{\partial T}{\partial x_i} = \alpha \frac{\partial^2 T}{\partial x_i^2} + \frac{\epsilon}{c_p} + \frac{\epsilon^c}{c_p} + \frac{\beta}{\rho c_p} \left[T \left(\frac{\partial p}{\partial t} + u_i \frac{\partial p}{\partial x_i} \right) \right] \qquad \text{(II.2)}$$

where c_p is the specific heat at constant pressure of the fluid, $\alpha = \kappa/\rho c_p$ is the thermal diffusivity of the fluid and is assumed to be constant. To obtain the above equation, we have used,

$$T \left(\frac{\partial s}{\partial T} \right)_p = c_p$$

$$\left(\frac{\partial s}{\partial p} \right)_T = -\frac{\beta}{\rho}$$

where β is the coefficient of thermal expansion of the fluid. To obtain the second relation above, we have used one of the Maxwell relations,

$$\left(\frac{\partial s}{\partial p}\right)_T = -\left(\frac{\partial v}{\partial T}\right)_p$$

In eqn.(II.2), ϵ/c_p is the source terms arising from viscous dissipation due the incompressible part of the flow and ϵ^c/c_p is the source term due to the fluid undergoing compression (or dilatation). Their definitions are,

$$\frac{\epsilon}{c_p} = \frac{\nu}{2c_p}\left(\frac{\partial u_i}{\partial x_j} + \frac{\partial u_j}{\partial x_i}\right)^2 = \frac{\nu}{c_p}\left(\frac{\partial u_i}{\partial x_j}\frac{\partial u_i}{\partial x_j} + \frac{\partial u_i}{\partial x_j}\frac{\partial u_j}{\partial x_i}\right)$$
$$\frac{\epsilon^c}{c_p} = \frac{\lambda_v}{\rho c_p}\left(\nabla \cdot \mathbf{u}\right)^2 = \frac{\lambda_v}{\rho c_p}\left(\frac{\partial u_i}{\partial x_i}\frac{\partial u_j}{\partial x_j}\right)$$

where $\nu = \mu/\rho$ is the kinematic viscosity of the fluid and ϵ is the rate of kinetic energy dissipation per unit mass. Thus, from their definitions, ϵ and ϵ^c are non-negative quantities and only transform kinetic energy into heat via viscous dissipation and compressible effects respectively and not the other way around. Any additional bulk heat sources are accounted for by adding another term S on the right hand side of eqn.(II.2). The final form of the governing equation for temperature reads,

$$\frac{DT}{Dt} = \alpha\nabla^2 T + \frac{\epsilon}{c_p} + \frac{\epsilon^c}{c_p} + \left(\frac{\beta T}{\rho c_p}\right)\frac{Dp}{Dt} + S \tag{II.3}$$

where $\frac{D}{Dt} = \frac{\partial}{\partial t} + u_i\frac{\partial}{\partial x_i}$ is the material derivative. Thus eqn.(II.3) is the most general form of the temperature equation for a closed system and accounts for compressibility effects (involving pressure), dissipative effects (viscous and compressible) and presence of additional heat sources/sinks in the bulk. Eqn.(II.3) along with the set of equations (II.4) form the set of governing equations for a compressible flow.

$$\frac{D\rho}{Dt} + \rho(\nabla \cdot \mathbf{u}) = 0$$
$$\rho\frac{D\mathbf{u}}{Dt} = -\nabla p + \mu\nabla^2\mathbf{u} + (\lambda_v + \mu)\nabla(\nabla \cdot \mathbf{u}) + \mathbf{f} \tag{II.4}$$
$$p = p(\rho, T)$$

If we consider the fluid being air under atmospheric conditions, the ideal gas hypothesis is a good approximation and henceforth we consider this to be the case. The temperature equation can be further simplified for an ideal gas, in which case, apart from the equation of state for an ideal gas, we have the following two relations,

$$\beta = \frac{1}{T}$$

$$c_p = \frac{R}{M}\left(\frac{\gamma}{\gamma - 1}\right)$$

where γ is the ratio of specific heats at constant pressure and volume, M is the molar mass of the gas and $R \approx 8.314 \,\mathrm{J\,K^{-1}\,mol^{-1}}$ is the universal gas constant. Thus, for a compressible viscous ideal gas, we obtain,

$$
\boxed{
\begin{aligned}
&\frac{D\rho}{Dt} + \rho(\nabla \cdot \mathbf{u}) = 0 \\
&\rho\frac{D\mathbf{u}}{Dt} = -\nabla p + \mu\nabla^2\mathbf{u} + (\lambda_v + \mu)\nabla(\nabla \cdot \mathbf{u}) + \mathbf{f} \\
&\frac{DT}{Dt} = \alpha\nabla^2 T + \frac{\epsilon}{c_p} + \frac{\epsilon^c}{c_p} + \left(\frac{1}{\rho c_p}\right)\frac{Dp}{Dt} + S \\
&pM = \rho RT
\end{aligned}
}
\tag{II.5}
$$

Let us denote the ambient pressure, density and temperature when the fluid is at rest by p_0, ρ_0 and T_0 respectively. We decompose the pressure, density and temperature fields in a flow as a sum of the ambient values and perturbations which are denoted by p', ρ' and T' respectively,

$$p = p_0 + p'$$
$$\rho = \rho_0 + \rho'$$
$$T = T_0 + T'$$

We also assume the amplitudes of the perturbations to be small compared to their ambient values,

$$p' \ll p_0$$
$$\rho' \ll \rho_0$$
$$T' \ll T_0$$

On substituting the decomposition in the governing equations (II.5), we obtain for the first order in fluctuations (p', ρ' and T'),

$$\frac{\partial \rho'}{\partial t} + \nabla \cdot \rho' \mathbf{u} + \rho_0 \nabla \cdot \mathbf{u} = 0 \tag{II.6}$$

$$\left(1 + \frac{\rho'}{\rho_0}\right)\left(\frac{\partial \mathbf{u}}{\partial t} + \mathbf{u} \cdot \nabla \mathbf{u}\right) = -\frac{1}{\rho_0}\nabla p' + \nu\nabla^2\mathbf{u} + \left(\frac{\lambda_v + \mu}{\rho_0}\right)\nabla(\nabla \cdot \mathbf{u}) \tag{II.7}$$

$$\left(1 + \frac{\rho'}{\rho_0}\right)\left(\frac{\partial T'}{\partial t} + \mathbf{u} \cdot \nabla T'\right) = \alpha\nabla^2 T' + \frac{\epsilon}{c_p} + \frac{\epsilon^c}{c_p} + \left(\frac{1}{\rho_0 c_p}\right)\frac{Dp'}{Dt} + S \tag{II.8}$$

$$\frac{p'M}{R} = \rho' T_0 + \rho_0 T' \tag{II.9}$$

where for the ambient, $p_0 M = \rho_0 R T_0$. Equations (II.6) to (II.9) form the set of governing equations for a weakly compressible flow. Let L, T be the characteristic length scale and time scale of the perturbed flow. We define the characteristic velocity scale[2] as $U = {}^L\!/_T$. The order of magnitude of the perturbed velocity is denoted by u. The relative orders of magnitude of the terms in eqn.(II.6) with respect to the term $\rho_0 \nabla \cdot \mathbf{u}$ are,

$$\frac{\nabla \cdot \rho'\mathbf{u}}{\rho_0 \nabla \cdot \mathbf{u}} \sim \frac{\rho'}{\rho_0}$$

$$\frac{\partial\rho'/\partial t}{\rho_0 \nabla \cdot \mathbf{u}} \sim \frac{\rho'/T}{\rho_0 u/L} \equiv \frac{\rho'/\rho_0}{u/U}$$

Similarly, the relative orders of magnitude of the terms in eqn.(II.7) with respect to $\frac{\partial \mathbf{u}}{\partial t}$ are,

$$\frac{\mathbf{u} \cdot \nabla \mathbf{u}}{\partial \mathbf{u}/\partial t} \sim \frac{u}{L/T} \equiv \frac{u}{U}$$

$$\frac{(\frac{\rho'}{\rho_0})\partial\mathbf{u}/\partial t}{\partial \mathbf{u}/\partial t} \sim \frac{\rho'}{\rho_0}$$

$$\frac{(\frac{\rho'}{\rho_0})\mathbf{u} \cdot \nabla \mathbf{u}}{\partial \mathbf{u}/\partial t} \sim \left(\frac{\rho'}{\rho_0}\right)\left(\frac{u}{U}\right)$$

$$\frac{(\frac{1}{\rho_0})\nabla p'}{\partial \mathbf{u}/\partial t} \sim \frac{p'}{\rho_0 u U}$$

$$\frac{\nu\nabla^2\mathbf{u}}{\partial \mathbf{u}/\partial t} \sim \frac{\nu}{UL} \equiv \frac{1}{Re}\left(\frac{u}{U}\right)$$

$$\frac{(\lambda_v + \mu)\nabla(\nabla \cdot \mathbf{u})}{\rho_0 \partial\mathbf{u}/\partial t} \sim \frac{(\lambda_v + \mu)\nabla({}^1\!/_{\rho_0}\partial\rho'/\partial t)}{\rho_0 \partial\mathbf{u}/\partial t} \equiv \left(1 + \frac{\lambda_v}{\mu}\right)\left(\frac{\rho'}{\rho_0}\right)\frac{\nu}{uL} \equiv \frac{1}{Re}\left(1 + \frac{\lambda_v}{\mu}\right)\left(\frac{\rho'}{\rho_0}\right)$$

---

[2]The flow can have more than one velocity scale associated with it. As an example, for acoustic waves, we have the typical order of magnitude of the velocity fluctuations and the isentropic speed of sound.

For eqn.(II.8), the relative order of magnitudes of the terms with respect to $\frac{\partial T'}{\partial t}$ are,

$$\frac{\mathbf{u} \cdot \nabla T'}{\partial T'/\partial t} \sim \frac{u}{L/T} \equiv \frac{u}{U}$$

$$\frac{(\frac{\rho'}{\rho_0})\partial T'/\partial t}{\partial T'/\partial t} \sim \frac{\rho'}{\rho_0}$$

$$\frac{(\frac{\rho'}{\rho_0})\mathbf{u} \cdot \nabla T'}{\partial T'/\partial t} \sim \left(\frac{\rho'}{\rho_0}\right)\left(\frac{u}{U}\right)$$

$$\frac{\alpha \nabla^2 T'}{\partial T'/\partial t} \sim \frac{\alpha}{UL} \equiv \frac{1}{Pe}\left(\frac{u}{U}\right)$$

$$\frac{\epsilon/c_p}{\partial T'/\partial t} \sim \frac{1}{Re}\frac{1}{(T'/T_0)}\left(\frac{u}{c}\right)^2\left(\frac{u}{U}\right)$$

$$\frac{\epsilon^c/c_p}{\partial T'/\partial t} \sim \left(\frac{\lambda_v}{\mu}\right)\frac{1}{Re}\frac{1}{(T'/T_0)}\left(\frac{U}{c}\right)^2\left(\frac{\rho'}{\rho_0}\right)^2\left(\frac{u}{U}\right)$$

$$\frac{\frac{1}{\rho_0 c_p}\partial p'/\partial t}{\partial T'/\partial t} \sim \frac{1}{(T'/T_0)}\frac{p'}{\rho_0 c^2} \sim \frac{(p'/p_0)}{(T'/T_0)}$$

$$\frac{\frac{1}{\rho_0 c_p}\mathbf{u} \cdot \nabla p'}{\partial T'/\partial t} \sim \frac{1}{(T'/T_0)}\frac{p'}{\rho_0 c^2}\left(\frac{u}{U}\right) \sim \frac{p'/p_0}{(T'/T_0)}\left(\frac{u}{U}\right)$$

where c is the isentropic speed of sound and we have used the relations,

$$c_p = \left(\frac{1}{\gamma - 1}\right)\frac{c^2}{T_0}$$

$$c^2 = \frac{\gamma p_0}{\rho_0} = \frac{\gamma R T_0}{M}$$

where the dimensionless numbers defined using velocity and temperature fluctuations are the *Reynolds* number (Re) and *Péclet* number (Pe). We can also define the dimensionless Prandtl number Pr from Re and Pe. The definitions of these numbers and their physical meanings are as follows,

$$Re = \frac{u'L}{\nu} = \left(\frac{\text{momentum transfer from advection}}{\text{momentum transfer from viscous diffusion}} \right)$$

$$Pe = \frac{u'L}{\alpha} = \left(\frac{\text{heat transfer from advection}}{\text{heat transfer from thermal diffusion}} \right)$$

$$Pr = \frac{Pe}{Re} = \frac{\nu}{\alpha} = \left(\frac{\text{momentum diffusivity}}{\text{thermal diffusivity}} \right)$$

Similarly, for the relative order of magnitudes of the terms in the equation of state eqn.(II.9) with respect to the term $\rho' T_0$,

$$\frac{p' M / R}{\rho' T_0} \sim \frac{(p'/p_0)}{(\rho'/\rho_0)}$$

$$\frac{\rho_0 T'}{\rho' T_0} \sim \frac{(T'/T_0)}{(\rho'/\rho_0)}$$

Eqn.(II.5) (or eqn.(II.8)) shows that there are two pathways of generating temperature fluctuations in the absence of any bulk sources of heat, viz. viscous dissipation and compressibility effects. We consider below the three standard limiting cases, viz., incompressible flow, acoustic wave and a perfect fluid and discuss the behaviour of temperature in these limits.

II.1.2   Limit I: Incompressible flow

Let us assume that mass flux at any fluid element in the flow is solely due to advection and the effect of density changes on the mass flux is negligible. Thus from the relative order of magnitudes of the terms in the equation of conservation of mass, we obtain the conditions,

$$\frac{\rho'}{\rho_0} \ll \frac{u}{U}$$

Eqn.(II.6) then becomes,

$$\boxed{\nabla \cdot \mathbf{u} = 0} \tag{II.10}$$

Similarly, assuming the effect of density changes on the momentum flux to be negligible while retaining the remaining terms gives,

$$\frac{u}{U} \sim O(1)$$

$$p' \sim \rho_0 u U \sim \rho_0 U^2$$

Eqn.(II.7) then becomes,

$$\boxed{\left(\frac{\partial \mathbf{u}}{\partial t} + \mathbf{u} \cdot \nabla \mathbf{u}\right) = -\frac{1}{\rho_0}\nabla p' + \nu\nabla^2\mathbf{u}} \tag{II.11}$$

where we have not made any assumption on the order of *Re*. Equations (II.10) and (II.11) form the governing equations of the hydrodynamic part of the incompressible flow limit. These equations form a critically determined system for the three components of velocity and pressure. The pressure thus obtained is not a dynamical variable and does not result in density fluctuations. Now we proceed to find the equation for temperature and the equation of state. We assume that the pressure which is determined from the hydrodynamic part does not play a role in the thermodynamic part and that viscous dissipation is the sole source of entropy generation. Along with the behaviour of the perturbed quantities as obtained from the hydrodynamic part, we get,

$$\boxed{\frac{DT'}{Dt} = \alpha\nabla^2 T' + \frac{\epsilon}{c_p} + S} \tag{II.12}$$

$$\boxed{\rho'T_0 + \rho_0 T' = 0} \tag{II.13}$$

where we have not made any assumption on the order of magnitude of *Pe*. In obtaining the above equations, we have assumed that the order of magnitudes of the perturbations in pressure and temperature are such that,

$$\boxed{\frac{p'}{p_0} \ll \frac{\rho'}{\rho_0} \sim \frac{T'}{T_0} \sim O(\mathcal{M}a^2) \ll 1}$$

where the Mach number is,

$$\mathcal{M}a = \frac{u}{c}$$

Equations (II.12) and (II.13) form the set of governing equations for the thermodynamic part of the problem. The equations (II.10) to (II.13) thus form the complete set of governing equations for the limiting case of incompressible flow. For a detailed asymptotic analysis to obtain these equations, refer to the article by Bayly *et al.* [35].

The eqn.(II.12) for temperature can also be obtained as presented by Landau [37]. The argument of Landau is as follows; for the equation of entropy, pressure can be regarded as

constant since the density fluctuations would only be affected by temperature fluctuations at the leading order. Thus, we have,

$$\frac{\partial s}{\partial t} = \left(\frac{\partial s}{\partial T}\right)_p \frac{\partial T}{\partial t}$$

$$\frac{\partial s}{\partial x_i} = \left(\frac{\partial s}{\partial T}\right)_p \frac{\partial T}{\partial x_i}$$

Using the above two relations and substituting them in eqn.(II.1) for entropy, we obtain the temperature eqn.(II.12) without the bulk source of heat S. It is important to note that even when considering the spontaneous generation of temperature fluctuations from viscous dissipation for an incompressible flow, the term involving pressure is often put under the rug by saying that its effects are negligible (see [37, 38]). As we have shown, this is true only when,

$$\frac{p'}{p_0} \ll \frac{T'}{T_0}$$

the validity of which should be checked for eqn.(II.12) to hold.

II.1.3 Limit II: Acoustic wave

We simplify the governing equations of the hydrodynamic part for a weakly compressible flow by linearizing them in velocity u. To do so, while accounting for all the linear terms in the equation for conservation of mass implies,

$$\frac{\rho'}{\rho_0} \sim \frac{u}{U}$$

Using this condition, eqn.(II.6) is linearized, giving,

$$\boxed{\frac{\partial \rho'}{\partial t} + \rho_0 \nabla \cdot \mathbf{u} = 0} \tag{II.14}$$

On doing the same for the equation of momentum implies,

$$p' \sim \rho_0 u U$$

and eqn.(II.7) is linearized, giving,

$$\rho_0 \frac{\partial \mathbf{u}}{\partial t} = -\nabla p' + \mu \nabla^2 \mathbf{u} + (\lambda_v + \mu)\nabla(\nabla \cdot \mathbf{u})$$

The momentum equation is further simplified by assuming the thermodynamic process for this weakly compressible limit to be isentropic (adiabatic). This would be true when the flow is inviscid, i.e., $\mu = 0 = \lambda_v$. Thus the final form of the momentum equation reads,

$$\rho_0 \frac{\partial \mathbf{u}}{\partial t} = -\nabla p' \tag{II.15}$$

Taking time derivative of eqn.(II.14), divergence of eqn.(II.15) and combining the resulting two equations gives us,

$$\frac{\partial^2 \rho'}{\partial t^2} + \nabla^2 p' = 0$$

Recall the the isentropic speed of sound in the medium is $c = \sqrt{\left(\frac{\partial p'}{\partial \rho'}\right)_s}$ and replacing it in the above equation, we obtain,

$$\frac{\partial^2 \rho'}{\partial t^2} + c^2 \nabla^2 \rho' = 0$$

To obtain the characteristic scales involved, we use the condition $p' \sim c^2 \rho' \sim \rho_0 uU$. This gives $\frac{\rho'/\rho_0}{u/U} \sim \left(\frac{U}{c}\right)^2$. Since the left hand side is of $O(1)$, we obtain that the characteristic velocity scale involved is the isentropic speed of sound. Thus the characteristic length and time scales involved are the wavelength and the inverse of frequency of the acoustic wave respectively.

$$L \sim \lambda$$
$$T \sim {}^1\!/_f$$
$$U \sim c$$

where λ and f are the wavelength and the frequency of the acoustic wave respectively. This also gives us the limiting conditions for which the acoustic wave equation holds true in terms of the Mach number $\mathcal{M}a$. Since,

$$\frac{u}{U} \sim \frac{u}{c} = \mathcal{M}a$$

For the thermodynamic part, we obtain,

$$\frac{\partial T'}{\partial t} = \frac{1}{\rho_0 c_p} \frac{\partial p'}{\partial t}$$

$$\boxed{\frac{p'M}{R} = \rho'T_0 + \rho_0 T'}$$

(II.16)

and the order of magnitudes of the perturbed quantities are,

$$\boxed{\frac{p'}{p_0} \sim \frac{\rho'}{\rho_0} \sim \frac{T'}{T_0} \sim O(\mathcal{M}a) \ll 1}$$

The set of equations (II.14) to (II.16) are the set of governing equations for the limit of acoustic wave of the weakly compressible flow equations. There are a few points to be noted here. First, for obtaining the governing equations for acoustic wave limit, we assumed the process to be isentropic. For this to be the case, effects of momentum and thermal diffusion have to be negligible. The order of magnitude of the terms involving viscosity and thermal diffusivity respectively are,

$$\frac{\nu \nabla^2 \mathbf{u}}{\partial \mathbf{u}/\partial t} \sim \frac{1}{Re}\left(\frac{u}{U}\right) \sim O(\mathcal{M}a)$$

$$\frac{\alpha \nabla^2 T'}{\partial T'/\partial t} \sim \frac{1}{Pe}\left(\frac{u}{U}\right) \sim O(\mathcal{M}a)$$

Thus viscous and thermal attenuation of the acoustic wave would be an $O(\mathcal{M}a)$ effect. Secondly, we obtain wave equation not only for ρ', p' and T' but also for the velocity field $\mathbf{u}$ on the assumption that the flow is *irrotational* (i.e., $\mathbf{u} = \nabla \psi$ for some scalar potential ψ), in which case we get wave equation independently for the three components of the velocity field.

II.1.4 Limit III: Perfect fluid

The case of *perfect fluid* implies that the fluid is inviscid and non heat-conducting but can be compressible. This limit would hold when,

$$Re \gg 1$$
$$Pe \gg 1$$

in which case, the set of equations (II.6) to (II.9) for a weakly compressible flow would become,

$$
\boxed{
\begin{aligned}
&\frac{\partial \rho'}{\partial t} + \rho_0 \nabla \cdot \mathbf{u} = 0 \\
&\frac{\partial \mathbf{u}}{\partial t} + \mathbf{u} \cdot \nabla \mathbf{u} = -\frac{1}{\rho_0} \nabla p' \\
&\frac{DT'}{Dt} = \left(\frac{1}{\rho_0 c_p} \right) \frac{Dp'}{Dt} + S \\
&\frac{p' M}{R} = \rho' T_0 + \rho_0 T'
\end{aligned}
}
\tag{II.17}
$$

where we see that when $S = 0$ (no bulk sources of heat), the temperature fluctuations are proportional to pressure fluctuations. We note that the equation of temperature would be satisfied if the fluctuating quantities undergo an adiabatic process. This can be shown as follows. For a weakly compressible flow undergoing adiabatic process, we would have,

$$\frac{p'}{T'} = \left(\frac{\gamma}{\gamma - 1} \right) \left(\frac{p_0}{T_0} \right) = \rho_0 c_p$$

which would imply,

$$\frac{DT'}{Dt} = \left(\frac{1}{\rho_0 c_p} \right) \frac{Dp'}{Dt}$$

The above three limits show that temperature fluctuations can arise in a flow at the leading order from different effects, viz.,

- Viscous dissipation $\Rightarrow$ Incompressible flow limit

- Pressure fluctuations for a compressible fluid $\Rightarrow$ Acoustic wave limit and Perfect fluid limit

- From bulk sources

The equations and limits derived above are applicable to all flows, laminar and turbulent. The first two cases corresponding to viscous dissipation and pressure fluctuations are the two candidates for spontaneous generation of temperature fluctuations in turbulent flows. Their study could offer an interesting avenue for investigation into possible universal behaviour of temperature fluctuations in turbulent flows. A priori, in a turbulent flow, we have no reason to neglect either of the three effects (viscous dissipation, pressure fluctuations and bulk heat sources) and we have to keep in mind that all of them can manifest simultaneously in different parts of the flow domain and generate temperature fluctuations.

In typical laboratory experiments studying turbulent flows, the Mach numbers achievable are smaller than unity and thus one would expect compressible effects to be negligible. In such incompressible, turbulent flows and in the absence of any bulk sources of heat, viscous dissipation would play a central role in generating temperature fluctuations. In this spirit, we begin by analyzing temperature fluctuations in a model of turbulent flow which is incompressible, statistically homogeneous and statistically isotropic.

II.1.5 Temperature fluctuations in incompressible, homogeneous and isotropic turbulent flows: Theory

As is customary in studying turbulence, we can proceed to obtain equations for mean and fluctuating temperature fields in the case which allows further analytical treatment; incompressible turbulent flow which is statistically homogeneous and isotropic with perfectly adiabatic and closed boundaries and no bulk sources or temperature gradients. This would correspond to eqn.(II.12) for temperature with $S = 0$,

$$\frac{\partial T}{\partial t} + u_i \frac{\partial T}{\partial x_i} = \alpha \frac{\partial^2 T}{\partial x_i^2} + \frac{\epsilon}{c_p} \tag{II.18}$$

We proceed by using *Reynolds decomposition* for the temperature field, velocity field and kinetic energy injection rate per unit mass ϵ,

$$T = \langle T \rangle + T'$$
$$\epsilon = \langle \epsilon \rangle + \epsilon'$$
$$\mathbf{u} = \underbrace{\langle \mathbf{u} \rangle}_{= 0} + \ \mathbf{u}'$$
$$\text{(isotropy)}$$

where the operator $\langle \cdot \rangle$ stands for ensemble averaging. The decomposition is such that the ensemble average of the fluctuating fields $\langle T' \rangle = \langle \epsilon' \rangle = \langle \mathbf{u}' \rangle = 0$. The root mean square (RMS) of the velocity fluctuations is denoted by u'_{rms}. From isotropy we have $\sqrt{\langle u_i^2 \rangle} = u'_{rms}$ where u_i denotes the ith component of the fluctuating velocity field. Due to the assumption of isotropy, we also have $\langle \mathbf{u} \rangle = 0$. Substituting in eqn.(II.18) and using that $\frac{\partial \langle T \rangle}{\partial x_i} = 0$ due to homogeneity, we obtain,

$$\frac{\partial \langle T \rangle}{\partial t} + \frac{\partial T'}{\partial t} + u_i' \frac{\partial T'}{\partial x_i} = \alpha \frac{\partial^2 T'}{\partial x_i^2} + \frac{\langle \epsilon \rangle}{c_p} + \frac{\epsilon'}{c_p} \tag{II.19}$$

Averaging eqn.(II.18) and using incompressibility condition $\frac{\partial u_i}{\partial x_i} = 0$, we obtain,

$$\frac{\partial \langle T \rangle}{\partial t} + \underbrace{\frac{\partial \langle u_i' T' \rangle}{\partial x_i}}_{\substack{= 0 \\ \text{homogeneity}}} = \frac{\langle \epsilon \rangle}{c_p}$$

where the second term on the left hand side is zero on account of homogeneity giving us,

$$\frac{\partial \langle T \rangle}{\partial t} = \frac{\langle \epsilon \rangle}{c_p} \tag{II.20}$$

which describes the temporal evolution of the mean temperature field. Subtracting eqn.(II.20) from eqn.(II.19) gives us the equation for the fluctuating temperature field,

$$\boxed{\frac{\partial T'}{\partial t} + u_i' \frac{\partial T'}{\partial x_i} = \alpha \frac{\partial^2 T'}{\partial x_i^2} + \frac{\epsilon'}{c_p}} \tag{II.21}$$

where,

$$\frac{\epsilon'}{c_p} = \frac{\nu}{c_p} \left(\frac{\partial u_i'}{\partial x_j} \frac{\partial u_i'}{\partial x_j} + \frac{\partial u_i'}{\partial x_j} \frac{\partial u_j'}{\partial x_i} \right) - \frac{\nu}{c_p} \left\langle \frac{\partial u_i'}{\partial x_j} \frac{\partial u_i'}{\partial x_j} + \frac{\partial u_i'}{\partial x_j} \frac{\partial u_j'}{\partial x_i} \right\rangle$$

Analogous to the equation for mean kinetic energy, we can write an equation for mean variance of temperature fluctuations (loosely called "*energy*" of the fluctuating temperature field) as,

$$\frac{\partial \langle T'^2/2 \rangle}{\partial t} = -\alpha \left\langle \frac{\partial T'}{\partial x_i} \frac{\partial T'}{\partial x_i} \right\rangle + \underbrace{\frac{\langle T' \epsilon' \rangle}{c_p}}_{\langle \epsilon_T \rangle} \tag{II.22}$$

Eqn.(II.20) shows that $\langle \epsilon \rangle$, which is the mean rate per unit mass of kinetic energy injected in the turbulent flow, is transformed into heat due to viscous dissipation and results in the linear increase with time of the mean temperature. The fluctuating part, ϵ', on the other hand, results in generating temperature fluctuations in the flow which undergo turbulent mixing and finally are smoothed out by molecular diffusion as seen from equations (II.21)

and (II.22). Similar to the $\langle \epsilon \rangle$ and ϵ', we define $\langle \epsilon_T \rangle$ and ϵ'_T, which are the mean and fluctuating rate per unit mass of energy injected in the fluctuating temperature field as,

$$\langle \epsilon_T \rangle = \frac{\langle T'\epsilon' \rangle}{c_p}$$

$$\epsilon'_T = \frac{T'\epsilon' - \langle T'\epsilon' \rangle}{c_p}$$

This shows that behaviour of temperature fluctuations is inherently tied to the behaviour of ϵ'. Similar to two-point velocity correlation equation, we can write two-point temperature correlation equation. Proceeding with the usual analytical steps as done for velocity, we obtain,

$$\frac{1}{2}\frac{\partial \langle T'(\mathbf{x})T'(\mathbf{x}+\mathbf{r})\rangle}{\partial t} - \frac{1}{4}\frac{\partial \langle |\delta T'(\mathbf{r})|^2 \delta u_i(\mathbf{r})\rangle}{\partial r_i} = \alpha \frac{\partial^2 \langle T'(\mathbf{x})T'(\mathbf{x}+\mathbf{r})\rangle}{\partial r_i^2}$$
$$+ \frac{\langle T'(\mathbf{x})[\epsilon'(\mathbf{x}+\mathbf{r}) + \epsilon'(\mathbf{x}-\mathbf{r})]\rangle}{2c_p} \quad \text{(II.23)}$$

where $\delta T'$ and $\delta u'$ are the temperature and velocity increments along the vector $\mathbf{r}$ separating the two points in the flow respectively. Eqn.(II.23) is analogous to the *Karman-Howarth-Monin* relation for velocity correlation in incompressible, homogeneous turbulence[3][3]. At this point, we cannot proceed with further simplification without knowledge about the process of viscous dissipation.

To illustrate the difficulties in obtaining analytical results, let us consider a simpler case of bulk source with known statistical properties in the absence of viscous dissipation. In this case, $\epsilon' = 0$ and $S \neq 0$. This can be particularly challenging to achieve experimentally and we list here the ways in which people have managed to do so,

1. Sources of heat in the bulk

For grid turbulence, which generates turbulent flow in an *open* domain, either the grid which was generating the turbulent flow was supplied with a constant power or an additional mesh was mounted and supplied with constant power in the wind tunnel downstream of the grid which was generating turbulence. This can be found in the work of Warhaft *et al.* [39] and Zhou *et al.* [40]. Moisy *et al.* [41] achieved this for turbulent von Kármán swirling flow in a closed domain using heated grid and studying temperature fluctuations in its wake. The equations (II.21) and (II.22), would then be rewritten as,

---

[3]Isotropy of the turbulent field need not be assumed to obtain the Karman-Howarth-Monin relation or the analogous equation for temperature fluctuations. Only the assumptions of homogeneity and incompressibility are sufficient.

$$\frac{\partial T'}{\partial t} + u'_i \frac{\partial T'}{\partial x_i} = \alpha \frac{\partial^2 T'}{\partial x_i^2} + S$$

$$\frac{\partial \langle T'^2/2 \rangle}{\partial t} = -\alpha \left\langle \frac{\partial T'}{\partial x_i} \frac{\partial T'}{\partial x_i} \right\rangle + \underbrace{\langle T'S \rangle}_{\Lambda}$$

2. Mean gradient of temperature in the bulk

Corrsin [42] showed that for non-decaying, isotropic turbulence with a a mean flow along one direction (say x-axis), an applied linear gradient of a passive scalar in the cross-stream direction (y-axis) will be maintained and will remain independent of the downstream distance x. This was experimentally validated for grid turbulence experiments though they produce turbulence decaying in the downstream direction [43, 44]. This characteristic behaviour was used for studying behaviour of temperature in grid turbulence experiments by Sirivat and Warhaft [45] and Mydlarski and Warhaft [46] by either differentially heating mesh downstream or differentially heating ribbons upstream. This would result in an additional term in the Reynolds decomposition of temperature field,

$$T = \langle T \rangle_{ext} + T'$$

where unlike the case of homogeneous turbulence in the absence of mean gradient, $\frac{\partial \langle T \rangle_{ext}}{\partial y} \neq 0$. The equations (II.21) and (II.22), would then be rewritten as,

$$\frac{\partial T'}{\partial t} + u'_i \frac{\partial T'}{\partial x_i} = \alpha \frac{\partial^2 T'}{\partial x_i^2} \underbrace{-u'_y \frac{\partial \langle T \rangle_{ext}}{\partial y}}_{S}$$

$$\frac{\partial \langle T'^2/2 \rangle}{\partial t} = -\alpha \left\langle \frac{\partial T'}{\partial x_i} \frac{\partial T'}{\partial x_i} \right\rangle \underbrace{-\langle T'u'_y \rangle \frac{\partial \langle T \rangle_{ext}}{\partial y}}_{\Lambda} \tag{II.24}$$

where we have said that the external temperature gradient is linear and is along the cross stream direction (y-axis). In the first case, it is clear to see that the source term will have a well defined length scale. For the second case, this cannot be said though the gradient of temperature in the bulk does have a well defined length scale. This scenario is analogous to mean injection of kinetic energy in the velocity field. Unlike $\langle \epsilon_T \rangle$ which would likely act as a source across multitude of scales owing to the intermittent behaviour of ϵ', Λ would possibly act as a source only for a narrow range of scales. In short, the energy spectrum of Λ would be peaked about some wavenumber whereas it would be spread out for $\langle \epsilon_T \rangle$. Analogous to the '*inertial scales*' usually defined for kinetic energy in turbulent flows, we can have a range of scales, also called inertial scales, for this system where the effects of thermal diffusivity (and viscosity) and Λ (and ϵ) would be negligible.

Under the assumption of isotropy and for Reynolds number (Re) and Péclet number (Pe) going to infinity, Yaglom [47] obtained an exact relation analogous to the Kolmogorov's $\frac{4}{5}^{th}$ law for the inertial scales,

$$\langle |\delta T'|^2 \delta u' \rangle = -\frac{4}{3} \Lambda r \tag{II.25}$$

In order to predict the form of the temperature energy spectrum $E_T(k)$ where k denotes the wavenumber, eqn.(II.25) is not of much help as it also includes velocity increments and the only way forward is to rely on dimensional arguments. This highlights that the situation is more complicated when we deal with effects due to viscous dissipation. We proceed with obtaining analytical predictions on the energy spectra and RMS of temperature fluctuations using dimensional arguments for the two cases of an applied mean temperature gradient in the bulk and viscous dissipation.

II.1.6 Temperature fluctuations in incompressible, homogeneous and isotropic turbulent flows: Energy spectrum and RMS

As was mentioned in the previous section, to obtain predictions for the energy spectrum and the RMS value of the temperature fluctuations, we have to rely on dimensional analysis. First, let us consider the case when a mean gradient of temperature is applied in the bulk. Then from dimensional analysis, we obtain,

$$E_T(k) = C_{KOC} \langle \epsilon \rangle^{-1/3} \Lambda \; k^{-5/3} \tag{II.26}$$

where C_{KOC} is called the Kolmogorv-Obukhov-Corrsin constant and the definition of Λ is given in eqn.(II.24). The prediction given by eqn.(II.26) was first proposed for the energy spectrum of passive scalars mixing in a turbulent flow for the inertial-convective range [48, 49] (when effects of both viscosity and thermal diffusivity can be neglected) and has been experimentally and numerically verified for the case of bulk source in the absence of viscous dissipation [23]. On this basis and on the relative magnitudes of Re and Pe one can obtain other scalings with $E_T(k)$ proportional to either $k^{-17/3}$ (inertial-diffusive range) or k^{-1} (viscous-convective range; also called Batchelor spectrum)[50] for the case of direct cascade. Whereas, for the large scales, the spectrum can be shown to be proportional to k^2 as $k \to 0$ [49]. Similarly, using dimensional arguments, we also obtain the scaling for the RMS of temperature fluctuations as,

$$T_{rms}^{'2} \sim \langle \epsilon \rangle^{-1/3} \Lambda \; l_I^{2/3}$$

If we assume that in the case of a mean temperature gradient in the bulk, Λ scales as,

$$\Lambda = \langle T' u_y' \rangle \frac{\partial \langle T \rangle_{ext}}{\partial y} \sim T_{rms}' u_{rms}' \frac{\partial \langle T \rangle_{ext}}{\partial y}$$

we obtain,

$$T'_{rms} \sim \left(\langle \epsilon \rangle^{-1/3} l_I^{2/3} u'_{rms} \right) \frac{\partial \langle T \rangle_{ext}}{\partial y} \tag{II.27}$$

The linear scaling of the RMS of temperature fluctuations with the mean temperature gradient given by eqn.(II.27) has been experimentally validated [45, 46]. On using dimensional arguments for the energy spectrum of temperature fluctuations produced by viscous dissipation, we obtain,

$$E_T(k) = C_{KOC} \langle \epsilon \rangle^{-1/3} \langle \epsilon_T \rangle k^{-5/3} \tag{II.28}$$

The scaling for the RMS value of temperature fluctuations can be obtained either by integrating eqn.(II.28) from the inverse of integral scale to the inverse of Kolmogorov length scale or from dimensional analysis, both of which give the same behaviour. On integration eqn.(II.28), we obtain,

$$T'^2_{rms} = \int_{1/l_I}^{1/\eta} dk \; E_T(k) \approx C \langle \epsilon \rangle^{-1/3} \langle \epsilon_T \rangle l_I^{2/3}$$

where the last equality holds when $\eta \ll l_I$ and C is a constant prefactor. If we assume that,

$$\langle \epsilon_T \rangle \approx \frac{T'_{rms} \langle \epsilon \rangle}{c_p}$$

which is a positive quantity and thus captures the two effects; one that the temperature fluctuations would depend on viscous dissipation since the quantity is non-zero and second it is a positive quantity and thus balances the dissipation of the temperature fluctuations. Thus, we obtain,

$$T'_{rms} = C \frac{(\langle \epsilon \rangle l_I)^{2/3}}{c_p} \tag{II.29}$$

The important parameter to be understood is the source of temperature fluctuations $\langle \epsilon_T \rangle$ which as was mentioned before would likely be spread out in spectral space and plays an important role in the above equations (II.28) and (II.29). Do the temperature fluctuations due to viscous dissipation in turbulent flows display behaviour of energy spectra and the scaling of the RMS values as predicted by equations (II.28) and (II.29)? Since a lot of simplifications went into obtaining predictions for their behaviour and also that dimensional analysis is unable to capture the finer details of the underlying physical processes, it is far from evident that the predictions will really hold against experimental data. In this spirit, we develop an experiment to investigate the behaviour of spontaneous temperature fluctuations generated by viscous dissipation in a turbulent flow.

II.2 Temperature fluctuations due to viscous dissipation

For investigating the temperature fluctuations generated by viscous dissipation in turbulence, we consider the von Kármán swirling flow produced by two counter-rotating disks in a closed domain. This flow has been chosen for three reasons,

- We need the turbulent flow to be isolated from the ambient surroundings and to be able to attain a stationary state. These requirements are satisfied by *closed* box turbulent flows. In contrast, *open* turbulent flows (grid turbulence, turbulent jets) would decay in space.

- The von Kármán swirling flow has been widely used to study turbulent flows. This allows us to compare and characterize our flow prior to venturing into studying temperature fluctuations. Since temperature fluctuations due to viscous dissipation have not been experimentally studied yet, it is wiser to use a flow that has already been used to understand other aspects of turbulence.

II.2.1 The von Kármán swirling flow

The problem of flow generated by one rotating disk with infinite radius was first studied by von Kármán in 1921 [51]. He showed that it is possible to reduce the stationary problem to a set of non-linear ordinary differential equations in one parameter (angular velocity of the disk) by searching for self-similar solutions. Though he could not arrive at an analytical solution of the flow since the non-linear differential equations needed to be solved numerically, in the words of Batchelor, "*…but to have carried a solution of the Navier-Stokes equations even so far by exact analysis was (and still is) something of a novelty*". In his analysis, Kármán had assumed that far from the disk, the flow is normal to the disk with no radial or azimuthal components. Later, in 1951, Batchelor [52] showed that the simplicity of Kármán's solution could still be retained for two families of solutions; viz. (1) flow due to a disk with the fluid far from the disk having an angular velocity wherein the solutions depend on one parameter (ratio of angular velocity of disk and of fluid at infinity) and (2) flow between two parallel disks rotating about the same axis wherein the solutions depend on two parameters (ratio of angular velocities and Reynolds number based on the distance between the disks). Batchelor did not obtain explicit analytical solutions and relied on physical arguments and properties of ordinary differential equations to obtain general characteristics and qualitative understanding of the flow. Particularly, in the case of counter-rotating disks, he proposed a solution where the flow is divided into two self contained regions of opposite solid body rotation with boundary layers close to the disks and a transition region of strong shear and where the azimuthal component of the flow becomes zero. This was shown experimentally to not be the case by Stewartson in 1953 [53] for large *Re*. His experiments, though qualitative, showed that in the case of exact counter-rotation, the bulk of the fluid has no angular velocity and has a small magnitude of radial velocity directed towards the axes of the disks. He reasoned this to be the case since the boundary layers would not have effect on the motion of the fluid in the bulk. Thus this would also result in the absence of a transition region with strong shear.

The disagreement of the Batchelor-Stewartson solutions gave rise to a range of studies, both experimental and numerical. A review of this by Zandbergen and Dijkstra [54] was published

in 1987. To this day the flow remains an important case of study, being one of the rare cases where an exact solution to the Navier-Stokes equations can be obtained.

For the study of properties of turbulence at small scales, the flow between two coaxial counter-rotating disks in a closed cylindrical container is a good candidate as the energy is injected at large scales comparable to the size of the experiment. Apart from being feasible for table-top experiments, it can attain high values of Re of the order $10^5 - 10^6$. This has resulted in its popularity to this day for many studies on turbulence. In addition to experiments on the characterization of the properties of the turbulent flow, it was also used in the first experimental evidence of existence of vorticity filaments in turbulence [55] and of generation of a large scale magnetic field by a turbulent flow [56, 57].

Over time, many modifications were proposed for the geometry of the disks to attain more efficient ways of generating turbulence. Disks with protruding rims were first used by Douady *et al.* [55]. Abry *et al.* [58] used disks with radial blades perpendicular to the disks and noted a five-fold increase in the RMS of velocity fluctuations compared to smooth disks. Cadot *et al.* [14] used radially curved blades and reported a sharp increase in the efficiency of turbulence generation. The absence of a strong mean flow (and thus mean advection) in the midplane between the two counter-rotating disks coupled with strong shear (and thus high intensity of turbulence) makes the flow particularly appealing for studying turbulent flows.

II.2.2 Experimental setup

The sketch of the experiment is shown in fig.II.2. The flow is generated in a closed domain bounded by a cylinder made out of copper of 2 mm thickness. Copper has been chosen for its high thermal conductivity to minimize temperature gradients along the boundaries of the experiment. The top and the bottom faces of the cylinder are closed with circular copper plates of the same thickness. Since we want to study the behaviour of temperature fluctuations generated due to viscous dissipation, it is important to remove the drift in mean temperature (as seen from eqn.(II.20)). To achieve this, the cylindrical part of the container has a copper tubing of outer diameter 10 mm welded around it. The inlet and the outlet of the copper tubing is connected to a *LAUDA Proline RP 1845* circulating water bath with thermostat control which maintains the temperature of the container at a given fixed value. It has a cooling capacity of 1.6 kW which is well above the range of turbulent power dissipation in our experiment (few watts) and has a temperature stability of ± 0.01 K. The working fluid in our experiment is air.

We use two brushless DC motors from *MDP-MAXON* (model *ECMAX*) with the angular velocity Ω ranging from of $0 - 2000$ rpm fit with Hall sensors (for position of the axes) and optical encoders (for the rotation rates of the axes) along with feedback loop controller (model *ESCON 50/5*) with access to both instantaneous rotation rates and torques on the motors. The motors have access to the experimental setup from holes drilled on the top and bottom faces. The diameter of the holes have been adjusted to the diameter of the motors' axes to minimize any flow to and from the experiment. Each of the motor is attached to a curved bladed disk to generate a strong flow inside the cylindrical cavity. The geometry of the disk can be seen in fig.II.4. The thickness of the disks and the height of the blades is 7.5 mm. Holes drilled on the surface of the cylinder provide access to the probes; one cold-

wire temperature probe ($DANTEC\ 55P31$)[4] and one acceleration compensated piezoelectric pressure probe ($PCB\ 103B02$) which are placed in the midplane with the pressure probe flushed to the wall. One 1D hot-wire velocity probe ($DANTEC\ 55P16$)[5] is placed close to one disk, roughly about 1 cm from the blades. The arrangement of the probes has been shown in top-view sketch, fig.II.3. Unless stated, the temperature of the circulating water bath has been maintained at 21°C. The properties of air at $21°C$ and 1 atm pressure are given in tab.II.1.
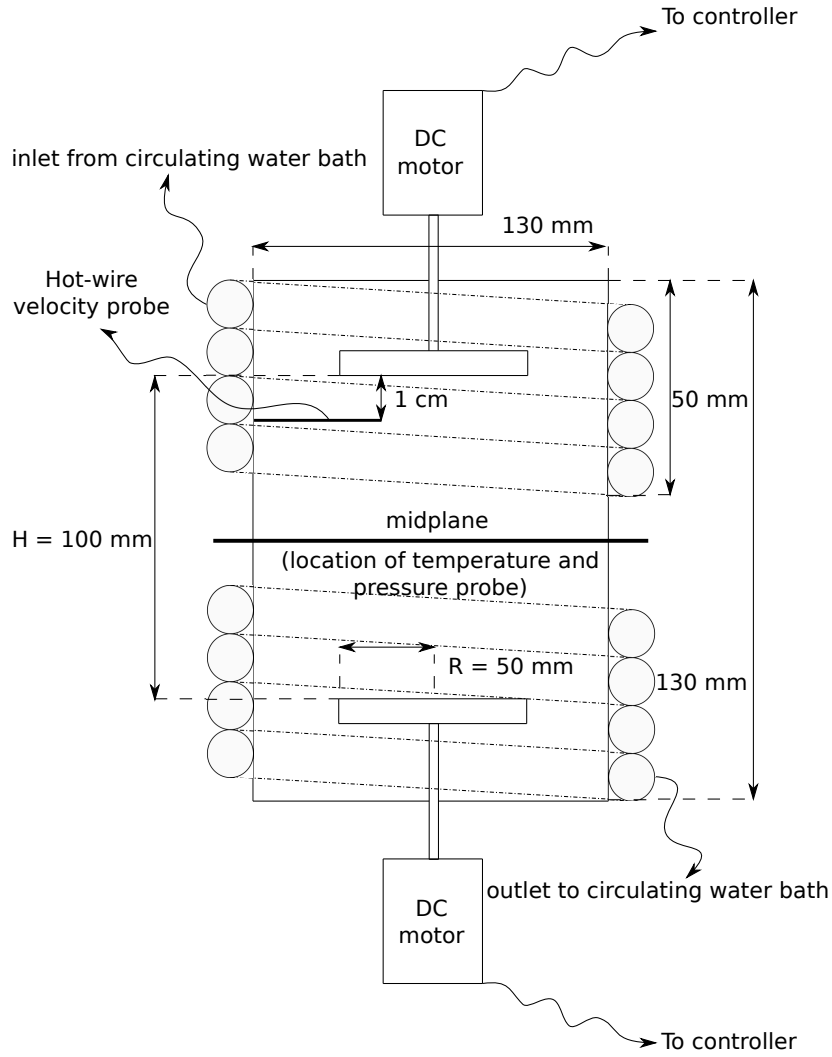
Fig. II.2 *Sketch of the experimental setup.*

---

[4](1) Platinum filament diameter ≈ 1 µm (2) Resistance $R\ (20°C) \approx 50\ \Omega$ (3) $\frac{\delta R}{\delta T}(20°C) \approx 1.7 \times 10^{-1}\ \Omega/\text{K}$
(4) Response time $\tau_{res} \approx O(0.1)$ ms [59]
[5](1) Tungsten filament diameter ≈ 5 µm (2) Resistance $R\ (20°C) \approx 3.5\ \Omega$ (3) $\frac{\delta R}{\delta T}(20°C) \approx 1.2 \times 10^{-2}\ \Omega/\text{K}$
(4) Minimum measurable velocity ≈ 0.05 m/s

cold-wire temperature
probe

outer cylinder: $R_c = 65$ mm

40 mm

pressure
probe

40 mm

disk: $R = 50$ mm

hot-wire velocity
probe
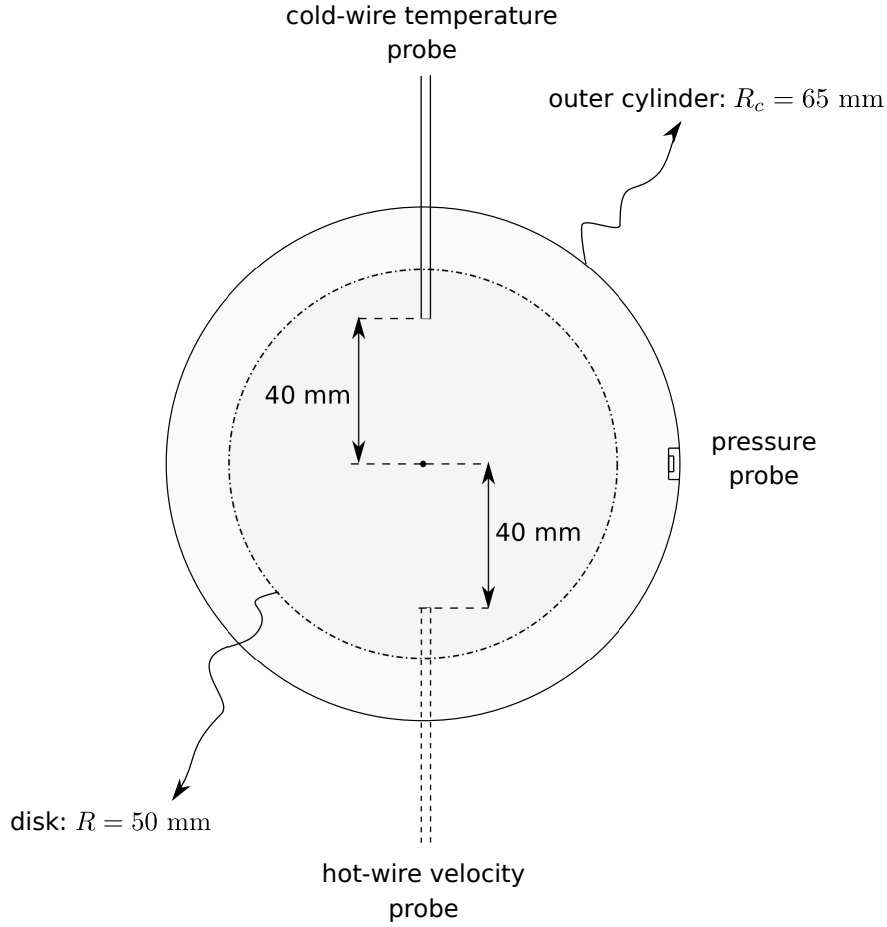
Fig. II.3   *Top view sketch of the midplane and the location of the different probes.*

The pressure probe is connected to a signal conditioner (*PCB 480E09*) whose output is connected to a data acquisition system. The temperature and velocity probes are connected to *DANTEC StreamWare Pro* system which provides a constant current of 2 mA to the temperature probes operated in CCA (Constant Current Anemometry) mode and simultaneously performs CTA (Constant Temperature Anemometry) measurement on the velocity probe. The output of the DANTEC *StreamWare Pro* system is connected to the data acquisition system. The acquisition system consists of NI BNC-2110 connector box connected to NI data acquisition card.
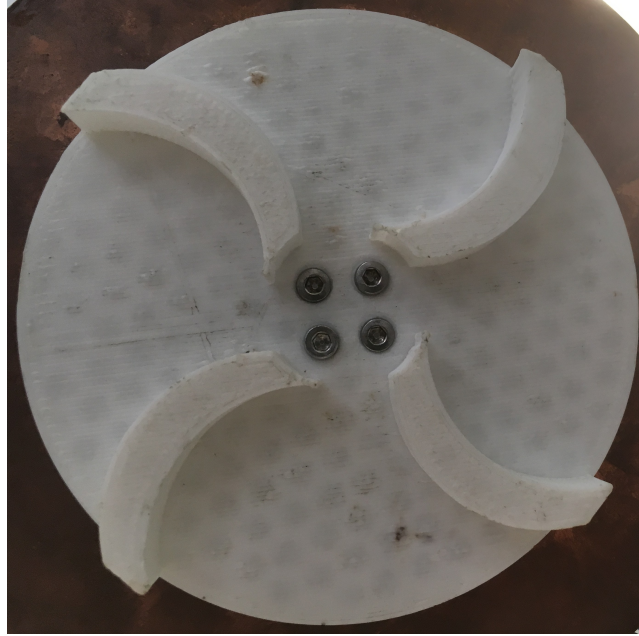
Fig. II.4   *Photograph showing the geometry of the curved bladed disks used in the experiment.*

ρ	$1.204 \;\; \mathrm{kg/m^3}$
c_p	$1007 \;\; \mathrm{J/kg\,K}$
η	$1.825 \times 10^{-5} \;\; \mathrm{kg/m\,s}$
ν	$1.516 \times 10^{-5} \;\; \mathrm{m^2/s}$
κ	$0.02514 \;\; \mathrm{W/m\,K}$
α	$2.074 \times 10^{-5} \;\; \mathrm{m^2/s}$

Table II.1: Properties of air at $21°C$ and $1 \; atm$ pressure

II.2.3 Characterization of the flow

The control parameter in our experiment is the rotation rate of the disks (or motors), denoted by Ω. For physical understanding, we keep the unit of the rotation rate in rotations per minute or ' rpm'. We only consider the case of counter-rotation of the disks which will leads to a strong shear and hence turbulence intensity in the mid-plane. In the context of the von Kármán swirling flow, we define the Reynolds number Re as,

$$Re = \frac{\pi R^2 \Omega}{30\nu}$$

where the constant $\pi/30$ appears from dimensional considerations since we decide to keep the unit of Ω in rotations per minute. We attain a maximum value of $Re = 3.5 \times 10^4$ in our experiment for $\Omega = 2000$ rpm. To present the basic properties of the flow, we start with the velocity field characterization.

Fig.II.5a shows the time series of the velocity signal close to one of the disk, at a rotation rate $\Omega = 2000$ rpm. Even though the hot-wire probe is placed close to the disk, the mean flow is not strong enough to capture the direction of the velocity fluctuations completely as seen from the asymmetry in the positive and negative fluctuations of the velocity signal. To estimate properly the mean and the RMS of the velocity fluctuations, we developed a statistical analysis based on the assumption of Gaussian distribution of velocity fluctuations, which is a well verified assumption for velocity fluctuations at high Re (appendix II.A). This gives us the RMS of velocity fluctuations generated in the flow to be of the order 1 m/s.

Fig.II.5b shows the dependence of RMS of velocity fluctuations, u'_{rms}, on the rotation rate Ω. It is observed to scale linearly with the rotation rate for rotation rates $\Omega \gtrsim 700$ rpm. The *large scale scaling*[6] of RMS of velocity fluctuations with the rotation rate Ω can be obtained using dimensional analysis which gives,

$$u'_{rms} = R\Omega \ f\left(Re, \frac{R}{H}\right) \xrightarrow[Re \to \infty]{} \propto \Omega$$

where f is some unknown function of the dimensionless numbers associated with the system. As $Re \to \infty$, we expect the scaling to become independent of the Reynolds number, in which case u'_{rms} will scale linearly with the rotation rate as observed in fig.II.5b. The departure from the predicted scaling at low rotation rates likely comes the flow not being fully developed turbulence at low rotation rates.

---

[6]By large scale scaling we mean the scaling for which the statistical quantity is independent of the small scale structure of turbulence and thus of kinematic viscosity ν.
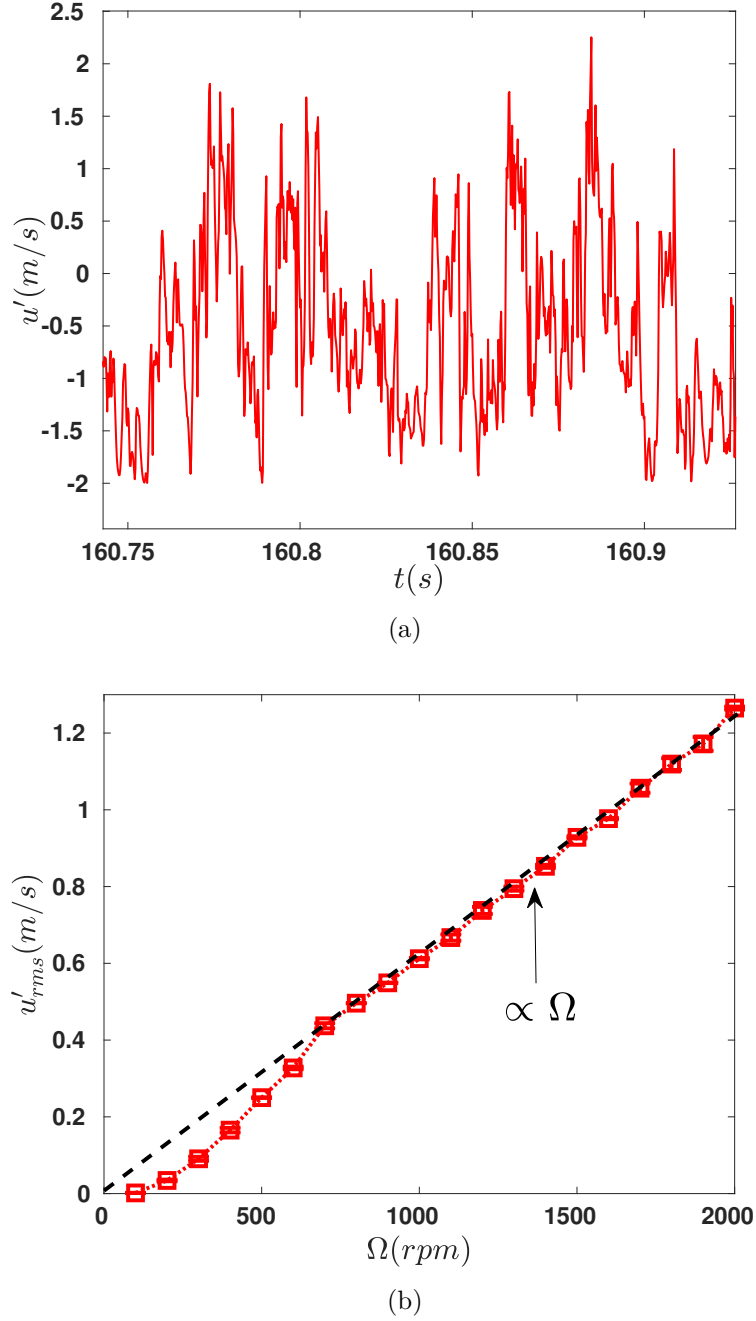
(a)

(b)

Fig. II.5   *(a) Time series of velocity signal as obtained from 1D hot-wire probe for a rotation rate of $\Omega = 2000$ rpm. (b) Scaling of u'_{rms} with the rotation rate Ω. Dashed line shows the linear scaling predicted from dimensional analysis.*

Fig.II.6a shows the energy spectrum of velocity fluctuations for a rotation rate $\Omega = 2000$ rpm. A peak is clearly seen in the energy spectrum at the frequency $f = \Omega/15 \approx 133$ Hz since,

$$f_{forcing} = \underbrace{\left(4 \times \frac{\Omega}{60} \right)}_{\text{due to four blades on the disks}} \text{Hz} \overset{2000 \text{ rpm}}{\approx} 133 \text{ Hz}$$

which corresponds to the forcing due to four blades present on the disks. At low frequency, it is interesting to note that the energy spectrum displays a power law behaviour with $E_u \propto f^{-0.6 \pm 0.02}$. This behaviour is reminiscent of the low frequency behaviour in the energy spectrum of pressure fluctuations in a turbulent flow as demonstrated by Abry *et al.* [13]. In the article of Abry *et al.* [13], the authors reported observing a low frequency power law behaviour for the energy spectrum of pressure fluctuations with $E_p \propto f^{-0.6}$ and showed that this behaviour is a result of the intermittent vorticity filaments being advected through the pressure probe. Such intermittent vorticity filaments would likely be captured by the velocity probe as well and result in our observation of $E_u \propto f^{-0.6}$ for low frequencies. The Kolmogorov spectrum is also seen for frequencies $f > f_{forcing}$ with $E_u \propto f^{-5/3}$. However, the two power law regions do not juxtapose. The wide transition region in frequency space between the two scaling can be attributed to the weakness of the mean flow, which breaks the Taylor's hypothesis invalidating the correspondence between the spatial and temporal spectrum.

We can also define the cross-over frequency (denoted by f_{cross}) as the frequency below which we observe the scaling of $E_u \propto f^{-0.6}$ in the energy spectrum. Since the low frequency $E_u \propto f^{-0.6}$ behaviour likely comes from vorticity filaments, their absence would result in the energy spectrum being flat at low frequencies. This was demonstrated by Abry *et al.* [13] for the case of pressure fluctuations. Thus, f_{cross} should be a good estimate of the integral frequency f_I. We evaluate f_{cross} as follows,

- For frequency f^*, we fit the energy spectrum of velocity fluctuations with $Cf^{-0.6}$ for frequencies $f < f^*$ and evaluate the RMSE. Here, C is a constant determined by the fit.

- We sweep f^* over a decade of values and obtain the RMSE of the fit for each f^*.

- We define the cross-over frequency f_{cross} as the frequency f^* for which we obtain the minimum RMSE.

For the energy spectrum shown in fig.II.6a for a rotation rate of $\Omega = 2000$ rpm, we obtain $f_{cross} \approx 16$ Hz. The large scale scaling of the cross-over frequency with the rotation rate Ω can also be obtained using dimensional analysis, which gives,

$$f_{cross} = \Omega \, g\left(Re, \frac{R}{H} \right) \xrightarrow[Re \to \infty]{} \propto \Omega$$

where g is an unknown function of the dimensionless numbers. As seen from fig.II.6b, f_{cross} scales linearly with the rotation rate as predicted from dimensional analysis.

(a)

(b)
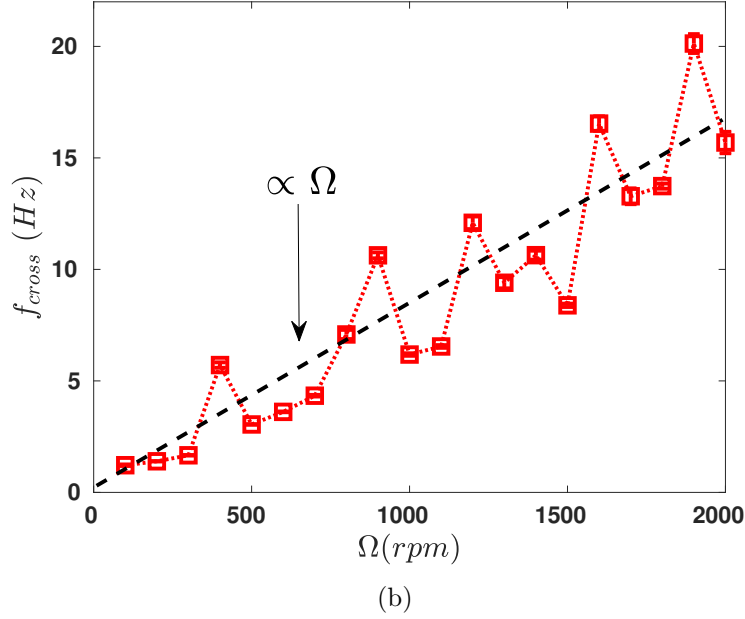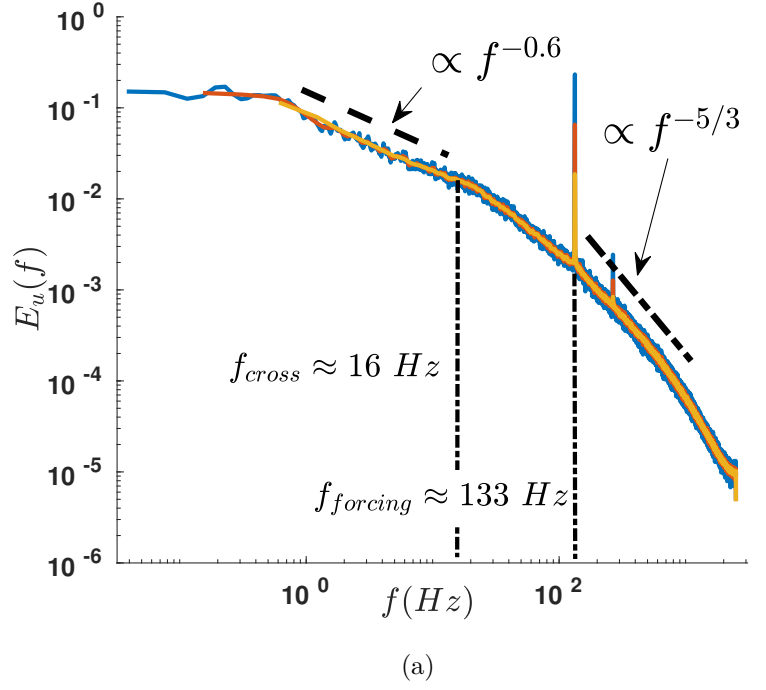
Fig. II.6 *(a) Energy spectrum of velocity signal as obtained from 1D hot-wire probe for $\Omega = 2000$ rpm. The cross-over frequency associated with deviation from $f^{-0.6}$ behaviour is denoted by f_{cross}. The forcing frequency is denoted by $f_{forcing}$. The different coloured curves correspond to different windowing lengths for evaluating the averaged spectrum. Dashed line: corresponds to $\propto f^{-0.6}$. Dash-dotted line: corresponds to $\propto f^{-5/3}$. (b) Scaling of cross-over frequency f_{cross} with the rotation rate Ω. Dashed line shows the large scale scaling as predicted from dimensional analysis.*

The large scale scaling of the mean power injected (or mean energy injection rate) per unit mass, $\langle \epsilon_I \rangle$ with the rotation rate as obtained from dimensional analysis is,

$$\langle \epsilon_I \rangle = R^2 \Omega^3 \, h\left(Re, \frac{R}{H}\right) \xrightarrow[Re\to\infty]{} \propto \Omega^3$$

where h is an unknown function of the dimensionless numbers. For evaluating $\langle \epsilon_I \rangle$, we perform two sets of measurements,

(1) Evaluation of the mean power required by the motors to run the experiment with load (disks) attached to the motor axes.
(2) Evaluation of the mean power required by the motors to run the experiment without load attached to the motor axes.

Since we have access to instantaneous torques and rotation rates, mean injected power is evaluated as $\langle \mathcal{P} \rangle = \langle \mathcal{T}\Omega \rangle$ in the two sets of experiments mentioned above where $\mathcal{P}$ and $\mathcal{T}$ denote injected power and torque respectively. Dividing by M_a gives us mean injected power per unit mass. The difference between the mean power injected per unit mass with and without the disks attached removes the contribution due to mechanical friction. This gives us the mean power injected in the turbulent flow. This method is most convenient since our working fluid is air and thus the fluctuations in torque (and power) imparted by the turbulent flow are smaller than those imparted by mechanical friction. From dimensional analysis, we expect torque fluctuations to be of the order of $p_{rms}R^3$ whereas the measured torque from one motor is greater by roughly an order of magnitude. Figures II.7a and II.7b show that indeed $\langle \epsilon_I \rangle \propto \Omega^3$ when evaluated this way. We assume that no other losses take place and thus the power dissipated per unit mass[7] $\langle \epsilon_D \rangle = \langle \epsilon_I \rangle = \langle \epsilon \rangle$.

Since, for homogeneous, isotropic turbulence, the Kolmogorov microscale $\eta = \left(\nu^3/\langle \epsilon \rangle\right)^{1/4}$ and the Taylor microscale $\lambda = \left(15\nu \frac{u'^2_{rms}}{\langle \epsilon \rangle}\right)^{1/2}$, we can obtain an order of magnitude estimates for their values[8]. This gives us,

$$\eta = \left(\nu^3/\langle \epsilon \rangle\right)^{1/4} \sim O(10^2)\ \mu\text{m}$$

$$\lambda = \left(15\nu \frac{u'^2_{rms}}{\langle \epsilon \rangle}\right)^{1/2} \sim O(1)\ \text{mm}$$

$$l_I \approx u'_{rms}/f_{cross} \sim O(10)\ \text{cm}$$

$$Re_\lambda = \frac{u'_{rms}\lambda}{\nu} \sim O(10^2)$$

where Re_λ is the Taylor microscale based Reynolds number. The integral length scale in our experiment has been evaluated as $l_I = u'_{rms}/f_{cross} \approx 10$ cm which is the same order as the

---

[7]Since the power injected by the motors is a global quantity, what we are measuring is the average power injected over the volume of the flow.

[8]The turbulent flow in the experiment would not be entirely homogeneous or isotropic even in the midplane. We only use the relations to obtain order of magnitude estimates.

diameter of the disks and the size of the experimental setup (diameter of the cylinder) and remains constant with the rotation rate of the motors.
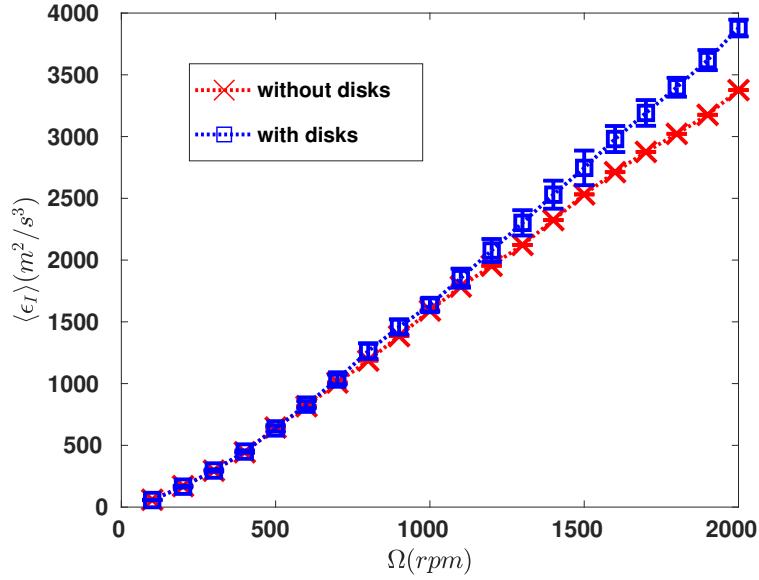
(a)
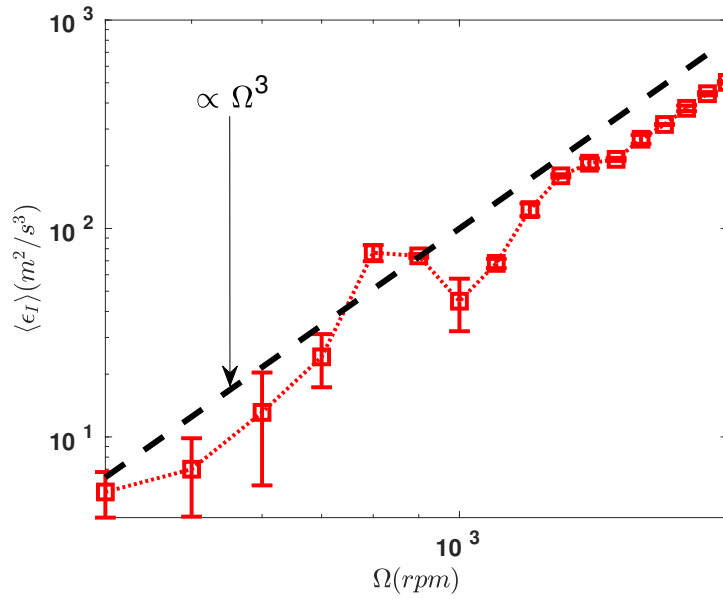
(b)

Fig. II.7   *(a) Mean injected power per unit mass with load (blue) and without load (red) evaluated from the power required by the motors. (b) Mean injected power per unit mass in the turbulent flow $\langle \epsilon_I \rangle$ evaluated from the power required by the motors with and without load. Dashed line shows the scaling as predicted from dimensional analysis.*

To summarize for the von Kármán swirling flow that we are studying, Re_λ is moderate, but the flow exhibits an inertial range. The dissipative length scales would be of the order of the Kolmogorov microscale $\eta \sim O(10^2)$ μm and are significantly larger than the dimension of the filament of the temperature probe (1 μm). The viscous time scale ($\tau_\eta \sim \langle \epsilon \rangle^{-1/3} \eta^{2/3} \sim O(1)$ ms) is larger than the response time of the temperature probe which is of $O(0.1)$ ms. Thus, in such a flow, we should be able to properly access the temperature fluctuations, even if they originate from the smallest scales involved.

II.3 Experimental Results

II.3.1 Statistics of temperature fluctuations

For brevity, we will drop the prime notation and denote the fluctuating part of temperature and pressure by T and p. The scaling for the RMS of temperature fluctuations, T_{rms}, as obtained in eqn.(II.29) can be written for the von Kármán swirling flow in terms of the control parameter, i.e., the rotation rate of the disks Ω. As was seen in the previous section, the integral length scale l_I remains constant with the rotation rate and the mean energy injection rate per unit mass scales as $\langle \epsilon \rangle \propto \Omega^3$, eqn.(II.29) tells us that,

$$T_{rms} \propto \Omega^2$$

The same can also be obtained directly from dimensional analysis similar to how the scaling for RMS of velocity fluctuations was obtained,

$$T_{rms} = \frac{R^2 \Omega^2}{c_p} \; k\left(Re, Pe, \frac{R}{H}\right) \xrightarrow[Re \to \infty]{} \propto \Omega^2 \qquad \text{(II.30)}$$

which corresponds to the large scale scaling of the RMS of temperature fluctuations and thus independent of the kinematic viscosity and thermal diffusivity. Here, k is an unknown function of the dimensionless numbers associated with the system. An assumption that goes into obtaining the above scaling is that,

$$\lim_{Re \to \infty} k\left(Re, Pe, \frac{R}{H}\right) = \text{constant}$$

Figures II.8a and II.8b show the time series of temperature fluctuations obtained for a rotation rate of $\Omega = 2000$ rpm and the RMS values as a function of the rotation rate of the motors Ω. Two important observations can be made,

- Sharp negative peaks or bursts are observed in the temperature signal, one of which has been shown in the inset of fig.II.8a.

- In contrast to u'_{rms}, the RMS of temperature fluctuations T_{rms} does not follow a large scale scaling with the rotation rate Ω. Thus the effect of kinematic viscosity and

thermal diffusivity cannot be discarded. We observe that the RMS of temperature fluctuations scales as $T_{rms} \propto \log(\Omega)$ shown in fig.II.8b.
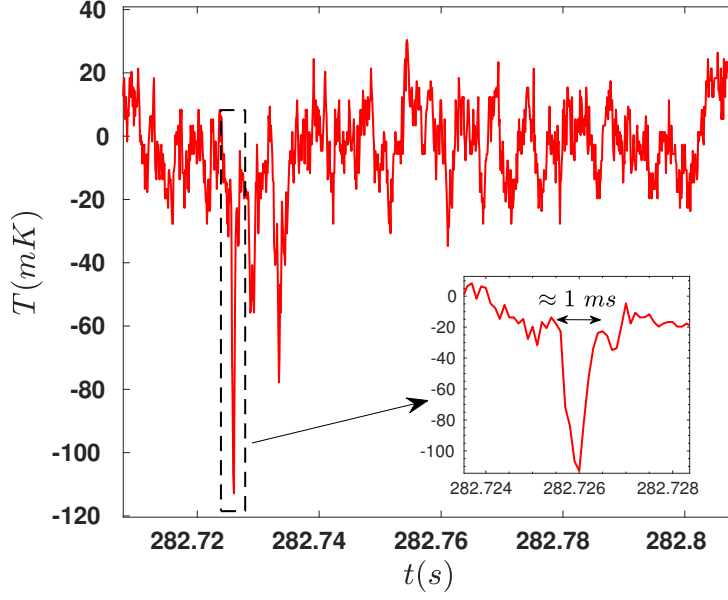
(a)
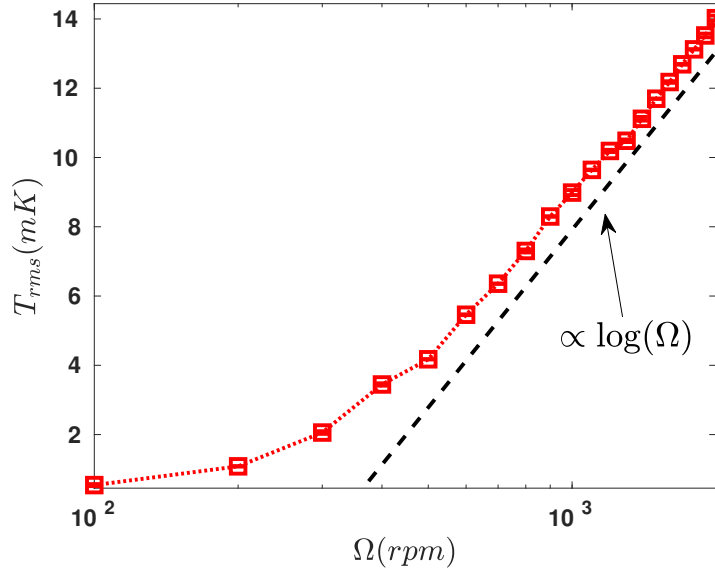
(b)

Fig. II.8   *(a) Time series of temperature signal as obtained from cold-wire probe placed in the midplane (fig.II.3) for $\Omega = 2000$ rpm. Inset: Zoomed-in time series of a negative peak observed in the signal. (b) Scaling of T_{rms} with the rotation rate Ω. Dashed line corresponds to $T_{rms} \propto \log(\Omega)$.*

The second observation implies that experimentally observed values of T'_{rms} grow slower with the rotation rate than the predicted behaviour from large scale scaling. Another interesting feature is observed if we measure the mean temperature difference between the bulk and the wall (which are maintained at a constant temperature) $\Delta\langle T \rangle$ which is defined as,

$$\Delta\langle T \rangle = \langle T \rangle - T_{wall}$$

where $\langle T \rangle$ is the mean temperature measured by the cold-wire probe located in the bulk and T_{wall} is the temperature of the wall and is constant. Fig.II.9 shows the scaling of $\Delta\langle T \rangle$ with the rotation rate Ω. We observe that it follows the large scale scaling with,

$$\Delta\langle T \rangle \propto \Omega^2$$
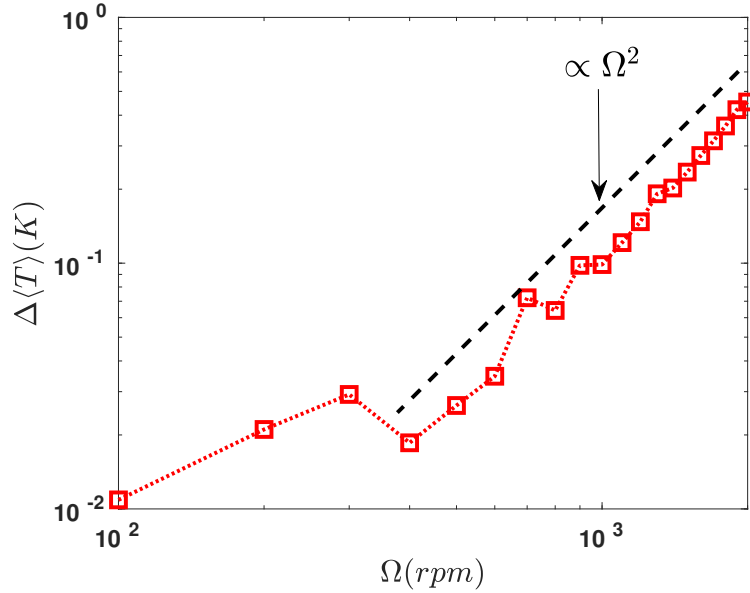
Fig. II.9   *Scaling of $\Delta\langle T \rangle$ with the rotation rate Ω. Dashed line corresponds to $\Delta\langle T \rangle \propto \Omega^2$.*

This can be understood from the sketch II.10 which shows the temperature being roughly constant in the bulk due to turbulent mixing. A gradient of $\Delta\langle T \rangle$ would exist close to the boundaries in a region of length scale δ.

In the region with the length scale δ where the mean temperature gradient would exist and dissipation would be negligible, we would have in steady state,

$$\frac{\langle \epsilon \rangle}{c_p} \sim \alpha \frac{\langle \Delta T \rangle}{R\delta} \tag{II.31}$$
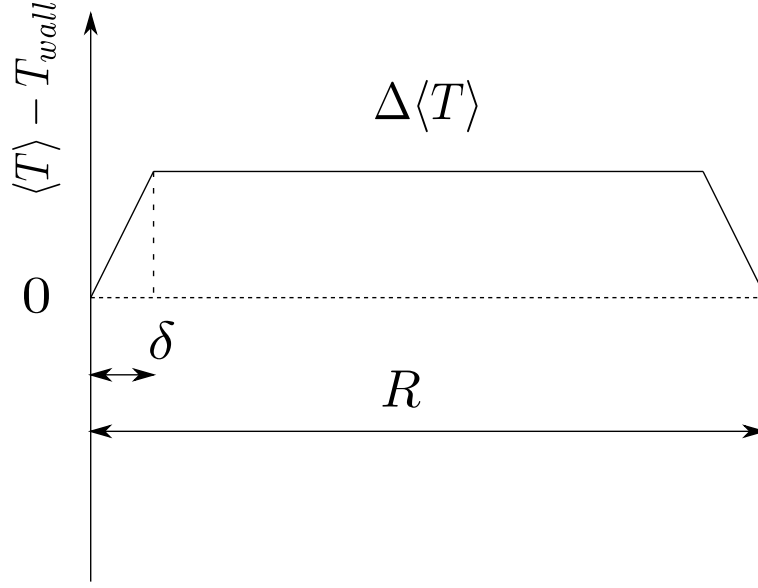
Fig. II.10 *Sketch showing heat being ejected at the boundaries. The length scale close to the coundary of the experiment at which a mean temperature gradient would exist is denoted by δ.*

where R is the radius of the cylinder. The equation eqn.(II.31) implies that in steady state, the energy injected in the mean temperature field in the form of heat by the mean dissipation rate would undergo diffusion and then ejected at the boundaries. The flow in the region of length scale δ would be turbulent and we can assume that the thermal diffusivity is a result of turbulent advection and hence,

$$\alpha \sim u'_{rms} l_I$$

Substituting in eqn.(II.31) and assuming that the length scale δ remains constant, we obtain,

$$\langle \Delta T \rangle = \frac{R\delta}{c_p l_I} \frac{\langle \epsilon \rangle}{u'_{rms}} \propto \Omega^2$$

To investigate further the statistics of temperature fluctuations, we plot the probability distribution function (PDF) of the temperature fluctuations on normalizing with their respective RMS values, $\Pi(T/T_{rms})$, seen in fig.II.11a. We observe large exponential tails for negative fluctuations which can be interpreted as a signature of the negative peaks observed from the temporal signal in fig.II.8a. Also, we notice that the PDFs $\Pi(T/T_{rms})$ coincide for all rotation rates except for the part of the negative exponential tails. Fig.II.11b shows the PDFs of temperature fluctuations on normalizing with the large scale scaling $\Pi(T/\Omega^2)$. We observe that the low amplitude fluctuations in temperature deviate from the large scaling scaling given by eqn.(II.30).

(a)

(b)
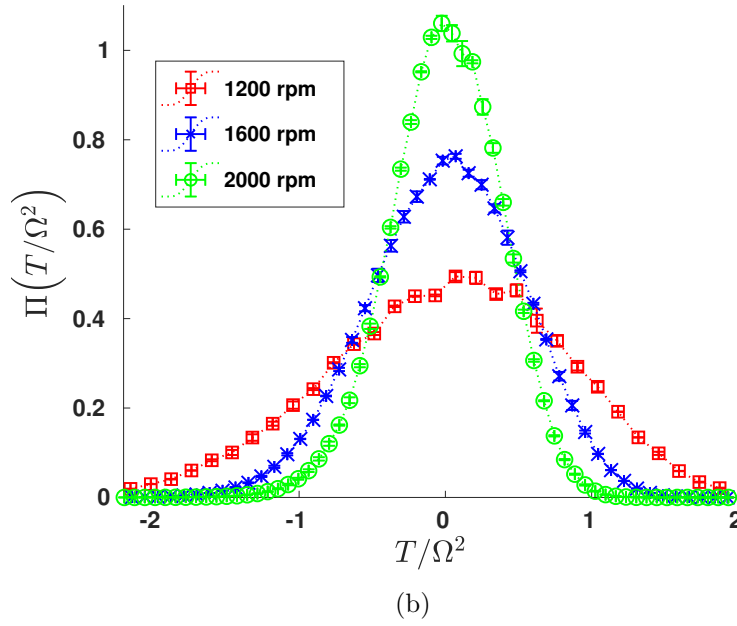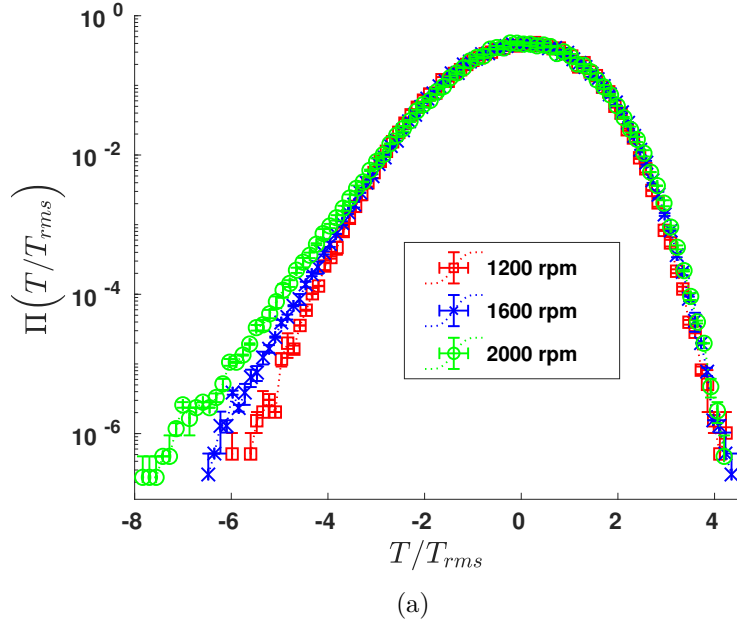
Fig. II.11 *(a) PDF of temperature fluctuations normalized by T_{rms}. Exponential tails in PDF for negative fluctuations are observed. The negative exponential tails do not coincide on normalization. (b) PDF of temperature fluctuations normalized by large scale scaling Ω^2. Red squares: 1200 rpm; Blue crosses: 1600 rpm; Green circles: 2000 rpm.*

To summarize,

- The negative exponential tails in PDFs $\Pi(T/T_{rms})$ do not coincide indicating that the negative peaks observed in the time signal of temperature does not affect the logarithmic scaling experimentally observed in T_{rms}.

- The PDFs on normalizing with large scale scaling of temperature fluctuations $\Pi(T/\Omega^2)$ do not coincide. The probability of observing low-amplitude temperature fluctuations does not obey the large scale scaling and increases with increasing rotation rate Ω. This indicates that the low amplitude temperature fluctuations result in the deviation of T_{rms} from the large scale scaling given by eqn.(II.30).

- These observations suggest that the energy in the temperature fluctuations and the negative peaks are a result of different physical structures in the temperature field.

These results call for two noteworthy questions,

Q1A: What is the origin of the negative peaks observed in the time signal of temperature fluctuations?

Q2A: If T_{rms} does not obey the prediction from dimensional analysis, does the energy spectrum follow the KOC spectrum (eqn.(II.28)) across some range of scales?

II.3.2 Pressure fluctuations and their similarity to temperature fluctuations

The velocity involved in the flow being more than two order of magnitude smaller the speed of sound, the incompressible limit may not be questioned. However, the presence of negative peaks in the temperature signal remind us of the pressure fluctuations in turbulent flows, which also exhibit sharp negative peaks [13]. We measure the temporal evolution of pressure fluctuations obtained from the pressure probe flushed to the wall, a typical time signal of which is shown in fig.II.12a. What is immediately noticeable is that pressure fluctuations also display negative peaks similar to what was seen for the temperature fluctuations. A zoom in of one of these peaks is shown in the inset figure of the time series. For the large scale scaling of the RMS of pressure fluctuations, we again turn to dimensional analysis which tells us,

$$ p_{rms} = \rho R^2 \Omega^2 \; j\left(Re, \frac{R}{H}\right) \xrightarrow[Re\to\infty]{} \propto \Omega^2 $$

where the function j depending on the dimensionless numbers is an unknown function. Similar to what was done in the case of T_{rms} and other dimensional scalings that we obtained, we have hypothesized that,

$$ \lim_{Re\to\infty} j\left(Re, Pe, \frac{R}{H}\right) = \text{constant} $$

The above scaling for p_{rms} is experimentally observed as seen from fig.II.12b. Similar to temperature fluctuations, the existence of negative peaks in the time signal of pressure fluctuations is evidenced by the exponential negative tails observed in their PDFs (fig.II.13). However, there are two noteworthy differences between the statistics of temperature and pressure fluctuations,

- The RMS of temperature fluctuations deviate from the large scale scaling whereas the RMS of pressure fluctuations, like velocity, follow the large scale scaling.

- The exponential tails observed in the PDFs of temperature fluctuations normalized by their RMS values do not coincide. The PDFs for pressure fluctuations, though, coincide on normalization with their RMS values. Thus the energy in the pressure fluctuations and the negative peaks are a result of physical structures which are of comparable magnitude and size, which is not the case for temperature fluctuations.

The negative peaks or depressions in pressure fluctuations in a turbulent flow and their statistics have been fairly well-studied and so is the physical phenomenon associated with it. These have been attributed to vortex filaments [55],[58],[14],[60], [61] and were shown to result in the low frequency power spectrum of pressure [13]. All except one from the references mentioned are experimental studies and were performed on von Kármán swirling flow similar to ours albeit with some geometrical changes.

(a)

(b)
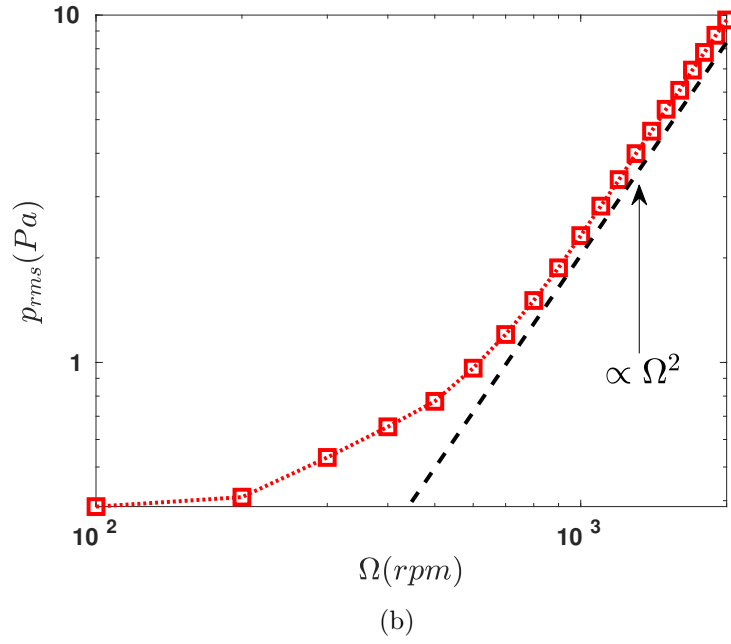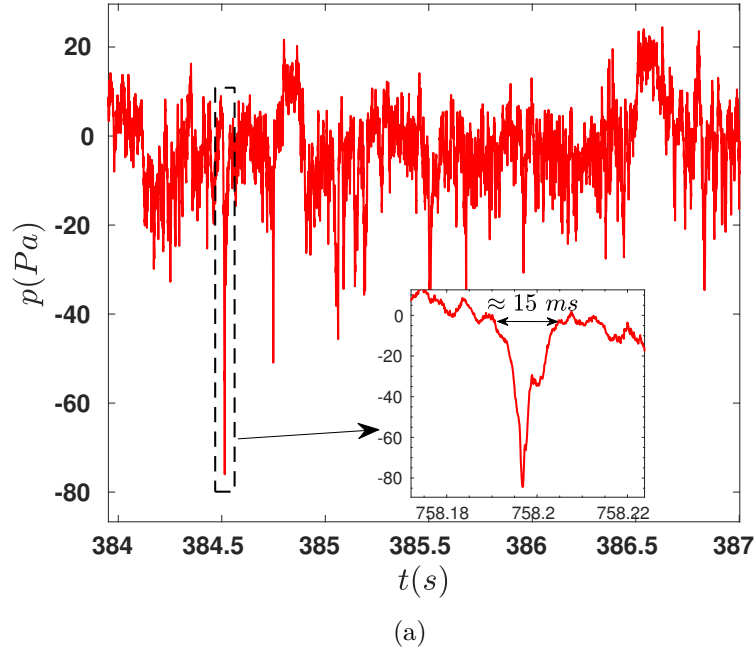
Fig. II.12   (a) Time series of pressure signal as obtained from pressure probe flushed to the wall in the midplane (fig.II.3) for $\Omega = 2000$ rpm. Inset: Zoomed-in time series of a negative peak observed in the signal. (b) Scaling of p_{rms} with the rotation rate Ω. Dashed line shows the scaling as predicted from dimensional analysis.

On the other hand, the characteristics of the vorticity filaments have been a source of debate for decades. The characteristics that have been reported in literature by both numerical and experimental studies can be summarized as follows ([62] and the the references cited therein),

- The radial size of these filaments is between the Kolmogorov length scale η and the Taylor microscale λ.

- The length of these filaments is of the same order of magnitude as the integral scale of the turbulent flow.

- The velocity increment encountered along the radial direction of these filaments is of the order of the RMS value of the velocity fluctuations.

- The lifetime of these vorticity filaments is of the same order as the integral time scale.

In the light of these observations Q1A can be rephrased as follows,

Q1B: Are the negative peaks in temperature and pressure fluctuations correlated? If so, what implications does it have on the physical picture of vorticity filaments?
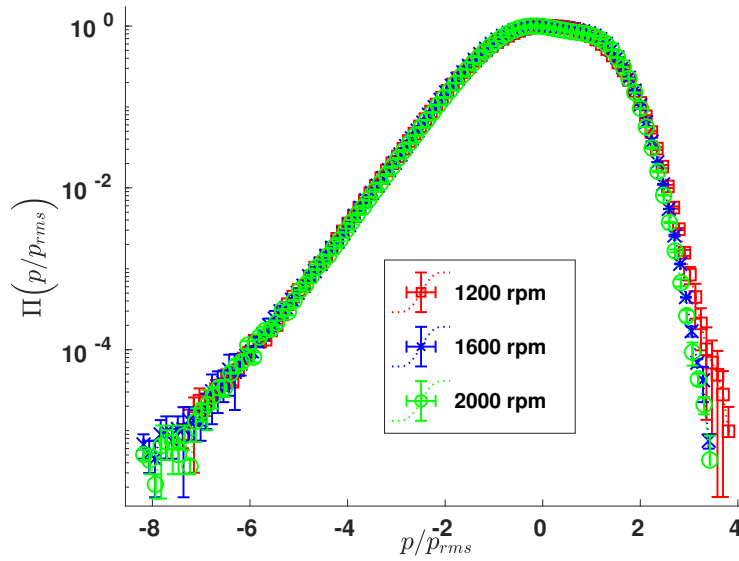
Fig. II.13   *PDF of pressure fluctuations normalized by p_{rms}. All the PDFs coincide on normalization. Exponential tails in PDF for negative fluctuations are observed. Red squares: 1200 rpm; Blue crosses: 1600 rpm; Green circles: 2000 rpm.*

II.3.3 Joint PDFs of pressure and temperature fluctuations

As was seen in the previous section, both the pressure and temperature signals are observed to have negative peaks. One immediate question that arises is whether they are correlated and thus a result of the same physical structures in the turbulent flow. To understand this, we evaluate the joint PDFs between pressure and temperature signals. To do so, we placed one temperature probe as close as possible to the pressure probe ($d \approx 3$ mm) which was still flushed to the wall. The sensing filament of the temperature probe was oriented along the midplane to capture the vorticity filaments being advected by the flow.

The joint PDF between pressure and temperature is defined as,

$$\Pi(p_0, T_0, \Delta t) = \text{probability}\Big(p(t) = p_0, T(t + \Delta t) = T_0\Big)$$

for any time lag Δt between the pressure and temperature signals. The introduction of a time lag Δt is required to account for the mean time required for any fluctuation to advect from one probe to another. The correlation between pressure and temperature shows a maximum for a non zero time lag Δt_{max}, corresponding to a mean advection speed of

$$\frac{d}{\Delta t_{max}} \sim O(1) \text{ m/s} \sim u'_{rms}$$

which is comparable to u'_{rms}. Fig.II.14 shows the joint PDFs $\Pi(p_0, T_0, \Delta t = \Delta t_{max})$ obtained for a rotation rate of $\Omega = 1000$ rpm and 1400 rpm respectively. We observe that the joint PDFs are skewed towards simultaneous negative values of both pressure and temperature. The joint PDFs are also observed to become increasingly skewed with increasing rotation rate Ω. In summary, following conclusions can be drawn,

- The fluctuations of temperature and pressure are correlated as seen from the joint PDFs.

- The joint PDFs are skewed towards a line of positive slope which by visual inspection is roughly (p_{rms}/T_{rms}) Pa/mK. The skewness of the PDFs towards this line increases with increasing rotation rate Ω.

- The skewness of the PDFs towards the line is not symmetric for positive and negative fluctuations. As seen from the isocontours, negative fluctuations in pressure and temperature that are correlated have a higher probability than positive fluctuations.

This implies that the negative peaks in pressure and temperature fluctuations are correlated and caused by the same physical structures present in the turbulent flow. This would mean that these peaks are a result of vorticity filaments occurring in turbulent flows. This partially answers Q1B which can be rephrased as follows,

Q1C: Since the negative peaks in temperature and pressure fluctuations are a direct observation of vorticity filaments, what can we say about the structure of these filaments?

Note that the joint PDFs of temperature and pressure fluctuations do not probe the structure of the filaments themselves but only tell us that there is a correlation between the fluctuations.
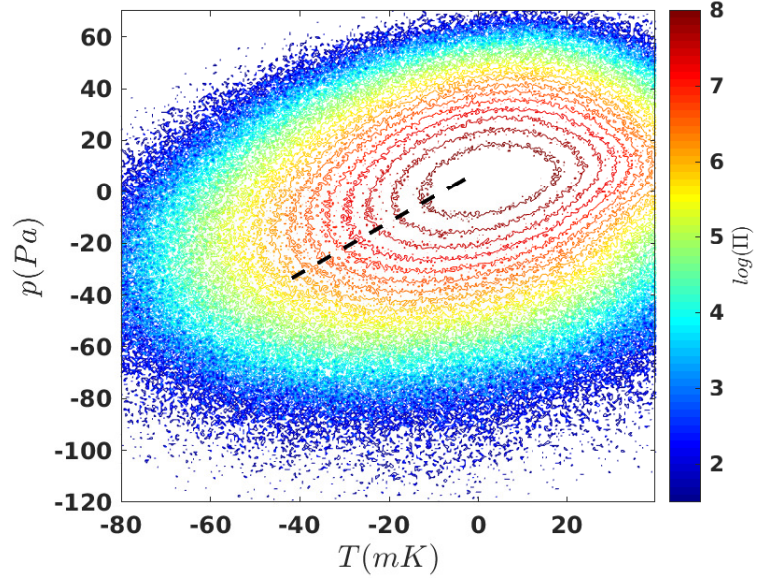
(a)
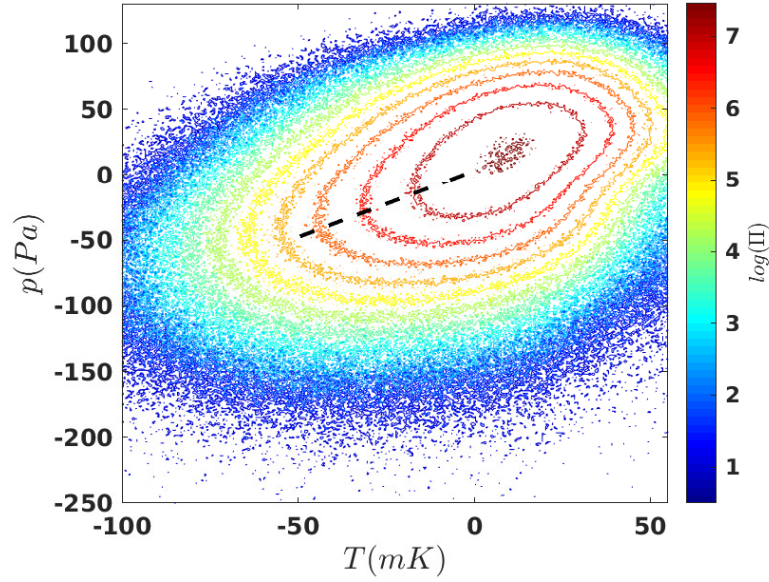
(b)

Fig. II.14 *Isocontours of the joint PDFs* $\Pi(p_0, T_0, \Delta t = \Delta t_{max})$ *(a)* $\Omega = 1000$ rpm *(b)* $\Omega = 1400$ rpm. *The colours are in logarithmic scale of the magnitude of PDFs. The isocontours are skewed towards simultaneous negative values of pressure and temperature. Dashed line shows a line of slope* (p_{rms}/T_{rms}) Pa/mK.

II.3.4 Structure of negative peaks in pressure and temperature fluctuations

As we concluded in the last section, vorticity filaments result in the negative peaks or bursts observed in the time signals of pressure and temperature fluctuations. In this section, we obtain the *average* internal structure of these filaments. In succeeding to do so, we can obtain the order of magnitudes of their width and the temperature (and pressure) drops between their cores and the surrounding turbulent flow.

To obtain the average structure of the vorticity filaments, we use the method of *coherent averaging* and its definition as used by Labbé *et al.* [63]. In their article, Labbé *et al.* demonstrated the technique and used it to extract a periodic structure from a signal with noise (velocity, temperature). In the above mentioned study, the structures were periodic but in our case the structures (negative peaks) are not. Since the method is not constrained to structures that are periodic, we can apply it to our case with some modifications. The details of the technique are presented in appendix II.B. Applying this method to the temperature and pressure signals in our case allows us to obtain the average temporal (and spatial) structure of the peaks.

Figures II.15a and II.15b show the result of coherent averaging when applied to peaks in temperature and pressure respectively for a rotation rate of $\Omega = 2000$ rpm. We observe that the actual amplitude of the averaged structure for both pressure and temperature is roughly three times smaller than the amplitudes of the peaks seen from the actual time signal. This would mean that the turbulent flow over which the vorticity filaments are superimposed affect the magnitude of the peaks but the overall structure of the peaks remains unaffected. If we measure the difference in temperature and pressure between the core of the structure and its edge (ΔT and Δp), we observe that,

$$\frac{\Delta p}{\Delta T} \approx \frac{p_{rms}}{T_{rms}} \approx 1 \text{ Pa/mK}$$

which we also observe from the slope of the line along which the joint PDFs are skewed in fig.II.14b. We comment on a statement made in the previous section as reported by other studies,

"*The velocity increment encountered along the radial direction of these filaments is of the order of the RMS value of the velocity fluctuations.*"

This statement would imply that the difference in pressure between the core and the edge of the structure we observe (Δp) would be,

$$\Delta p \sim \rho_\infty u_{rms}'^2 \overset{2000 \text{ rpm}}{\approx} O(1) \text{ Pa}$$

which is smaller than our observation from fig.II.15b. To summarize, vorticity filaments in a turbulent flow are observed as sharp negative peaks in the time signals of both temperature and pressure fluctuations. The results presented in this section imply that even though the turbulent flow is incompressible to the leading order in $\mathcal{M}a$, the vorticity filaments display an effect of compressibility owing to their direct measurement in both temperature and pressure fluctuations.

To understand the effect of compressibility, we turn to eqn.(II.8) which is the governing equation for temperature in the limit of a weakly compressible flow. We notice that pressure fluctuations would affect temperature fluctuations only when,

$$\frac{Dp'/Dt}{DT'/Dt} \sim \left(\frac{\gamma - 1}{\gamma}\right)\left(\frac{p'/p_0}{T'/T_0}\right) \sim O(1)$$

which would be the case when the thermodynamic process involved is adiabatic. For the structure of the vorticity filaments obtained via the method of coherent averaging (figures II.15a and II.15b), we indeed observe that,

$$\left(\frac{\gamma - 1}{\gamma}\right)\left(\frac{\Delta p/p_0}{\Delta T/T_0}\right) \sim O(1)$$

Though, we notice that the widths of the structures for the pressure and temperature profiles are different. The probes used for measuring pressure and temperature have different physical characteristics and as such would affect the quantities they measure differently. As for vorticity filaments, the characteristics of the probe would affect its width. The effect of the pressure transducer size on the measured width of the vorticity filaments was demonstrated by Abry *et al.* [13]. From our observation of the pressure-temperature joint PDFs being skewed (fig.II.14), we can confidently say that the vorticity filaments are compressible structures. Additionally, we also observe that the drops in pressure (Δp) and temperature (ΔT) as obtained from coherent averaging also follow the behaviour predicted for an adiabatic process. These observations encourage us to study the structure of the vorticity filaments and we can then ask,

Q1D: Can we create a simple model to understand the geometrical structure of vorticity filaments as obtained from the method of coherent averaging?
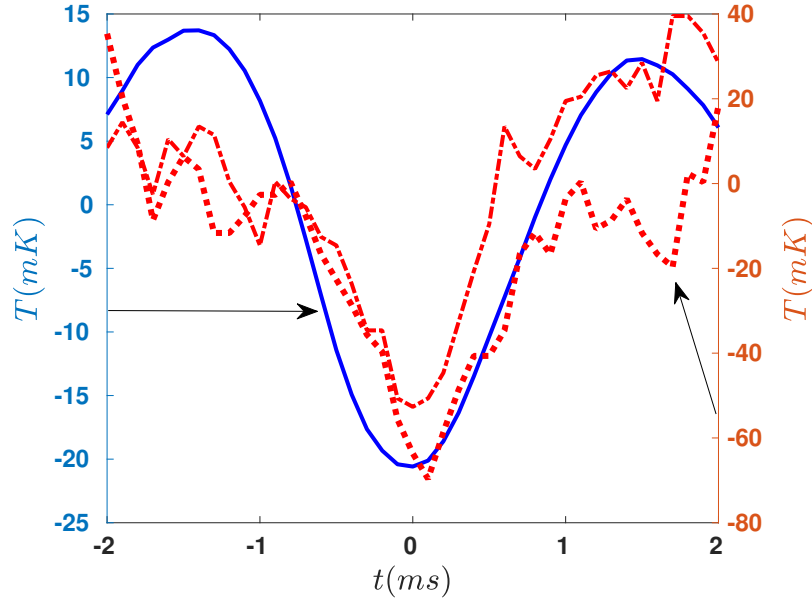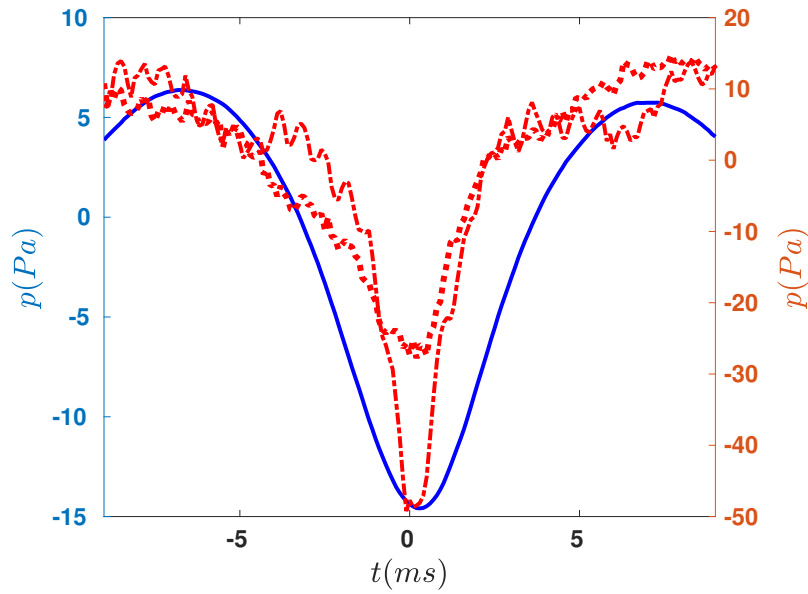
Fig. II.15   *Structure of negative peaks as obtained from the method of coherent averaging for $\Omega = 2000$ rpm. Examples of two peaks observed in the time signal (Red) and the structure as obtained from the method of coherent averaging (Blue) (a) For temperature signal (b) For pressure signal.*

II.3.5 A steady solution for single weakly compressible adiabatic vortex

One striking feature of turbulence is the existence of coherent elongated structures in the flow along which vorticity is concentrated called *vorticity filaments*. Since their discovery [64], they have been observed both numerically and experimentally [65, 62, 55] and are also proposed to be inherent to the physical picture of Kolmogorov's cascade of energy to small scales [66]. As a consequence of its definition, vorticity in a turbulent flow is a solenoidal (or divergence-free) field and thus vorticity filaments would form closed loops in a turbulent flow far from the boundaries that bound the turbulent flow. In the close vicinity of these vorticity filaments, we can thus consider them as cylindrical, tubular structures with a certain radius within which vorticity is concentrated. This physical picture forms the basis of our current model of a single steady vortex.

As a result of the physical picture given above, we proceed by writing the governing equations for compressible, viscous flow in cylindrical co-ordinates with the radial, azimuthal and axial components of the velocity denoted by u_r, u_θ and u_z respectively,

$$\frac{\partial \rho}{\partial t} + \frac{1}{r}\frac{\partial(\rho r u_r)}{\partial r} + \frac{1}{r}\frac{\partial(\rho u_\theta)}{\partial \theta} + \frac{\partial(\rho u_z)}{\partial z} = 0$$

$$\rho\Big(\frac{\partial u_r}{\partial t} + u_r\frac{\partial u_r}{\partial r} + \frac{u_\theta}{r}\frac{\partial u_r}{\partial \theta} + u_z\frac{\partial u_r}{\partial z} - \frac{u_\theta^2}{r}\Big) = -\frac{\partial p}{\partial r} + \mu\Big(\nabla^2 u_r - \frac{u_r}{r^2} - \frac{2}{r^2}\frac{\partial u_\theta}{\partial \theta}\Big)$$
$$+ \Big(\zeta + \frac{1}{3}\mu\Big)\Big(\frac{\partial^2 u_r}{\partial r^2} - \frac{u_r}{r^2} + \frac{1}{r}\frac{\partial u_r}{\partial r} - \frac{1}{r^2}\frac{\partial u_\theta}{\partial \theta} + \frac{1}{r}\frac{\partial^2 u_\theta}{\partial r \partial \theta} + \frac{\partial^2 u_z}{\partial r \partial z}\Big)$$

$$\rho\Big(\frac{\partial u_\theta}{\partial t} + u_r\frac{\partial u_\theta}{\partial r} + \frac{u_\theta}{r}\frac{\partial u_\theta}{\partial \theta} + u_z\frac{\partial u_\theta}{\partial z} + \frac{u_r u_\theta}{r}\Big) = -\frac{1}{r}\frac{\partial p}{\partial \theta} + \mu\Big(\nabla^2 u_\theta - \frac{u_\theta}{r^2} + \frac{2}{r^2}\frac{\partial u_r}{\partial \theta}\Big)$$
$$+ \Big(\zeta + \frac{1}{3}\mu\Big)\Big(\frac{1}{r}\frac{\partial^2 u_r}{\partial r \partial \theta} + \frac{1}{r^2}\frac{\partial u_r}{\partial \theta} + \frac{1}{r^2}\frac{\partial^2 u_\theta}{\partial \theta^2} + \frac{1}{r}\frac{\partial^2 u_z}{\partial \theta \partial z}\Big)$$

$$\rho\Big(\frac{\partial u_z}{\partial t} + u_r\frac{\partial u_z}{\partial r} + \frac{u_\theta}{r}\frac{\partial u_z}{\partial \theta} + u_z\frac{\partial u_z}{\partial z}\Big) = -\frac{\partial p}{\partial z} + \mu\nabla^2 u_z$$
$$+ \Big(\zeta + \frac{1}{3}\mu\Big)\Big(\frac{\partial^2 u_r}{\partial r \partial z} + \frac{1}{r}\frac{\partial u_r}{\partial z} + \frac{1}{r}\frac{\partial^2 u_\theta}{\partial \theta \partial z} + \frac{\partial^2 u_z}{\partial z^2}\Big)$$

$$\frac{\partial T}{\partial t} + u_r\frac{\partial T}{\partial r} + \frac{u_\theta}{r}\frac{\partial T}{\partial \theta} + u_z\frac{\partial T}{\partial z} = \alpha\nabla^2 T + \epsilon_T + \epsilon_T^c + \frac{\beta}{\rho c_p}\Big[T\Big(\frac{\partial p}{\partial t} + u_r\frac{\partial p}{\partial r} + \frac{u_\theta}{r}\frac{\partial p}{\partial \theta} + u_z\frac{\partial p}{\partial z}\Big)\Big]$$

$$p = p(\rho, T)$$

where we have neglected any interaction with the ambient surroundings. The six equations correspond to conservation of mass, conservation of the three momenta, conservation of energy and equation of state respectively. In cylindrical co-ordinates,

$$
\epsilon_T = \frac{2\nu}{c_p}\Big[\Big(\frac{\partial u_r}{\partial r}\Big)^2 + \Big(\frac{1}{r}\frac{\partial u_\theta}{\partial \theta} + \frac{u_r}{r}\Big)^2 + \Big(\frac{\partial u_z}{\partial z}\Big)^2\Big]
$$
$$
+ \frac{\nu}{c_p}\Big[\Big(\frac{1}{r}\frac{\partial u_r}{\partial \theta} + \frac{\partial u_\theta}{\partial r} - \frac{u_\theta}{r}\Big)^2 + \Big(\frac{\partial u_\theta}{\partial z} + \frac{1}{r}\frac{\partial u_z}{\partial \theta}\Big)^2 + \Big(\frac{\partial u_z}{\partial r} + \frac{\partial u_r}{\partial z}\Big)^2\Big]
$$
$$
\epsilon_T^c = \frac{\lambda_v}{\rho c_p}\Big(\zeta - \frac{2\mu}{3}\Big)\Big(\frac{\partial u_r}{\partial r} + \frac{u_r}{r} + \frac{1}{r}\frac{\partial u_\theta}{\partial \theta} + \frac{\partial u_z}{\partial z}\Big)^2
$$

and the Laplacian operator in cylindrical co-ordinates is,

$$
\nabla^2 = \frac{\partial^2}{\partial r^2} + \frac{1}{r}\frac{\partial}{\partial r} + \frac{1}{r^2}\frac{\partial^2}{\partial \theta^2} + \frac{\partial^2}{\partial z^2}
$$

For a single vortex, we can assume the flow to be axisymmetric. To make possible the mathematical analysis of obtaining vortex solutions, we assume the axial velocity u_z to be function of r, t and z and that it varies linearly in z. On the other hand, u_r and u_θ are assumed to be functions of r and t. We also assume that the vortex we are trying to model is a *strong vortex* which implies that the azimuthal component of the velocity is much larger than the other two components in order of magnitude. This means that the compressible effect would be a result of the azimuthal component which we have assumed to only depend on r and t. Thus to the leading order, ρ and T are functions of only the radial distance r and time t. These assumptions reduce the governing equations into partial differential equations of only two independent variables (r and t) while being as less restrictive as possible. Thus,

$$
\mathbf{u} = u_r(t,r)\hat{r} + u_\theta(t,r)\hat{\theta} + zw(t,r)\hat{z}
$$
$$
\rho = \rho(t,r)
$$
$$
p = p(t,r,z)
$$
$$
T = T(t,r)
$$
$$
|u_\theta| \gg |u_r|
$$
$$
|u_\theta| \gg |u_z|
$$

Assuming the fluid to be an *ideal gas*, the steady state equations we obtain to the leading order are,

$$\frac{1}{r}\frac{d(\rho r u_r)}{dr} + \rho w = 0$$

$$\frac{\partial p}{\partial r} = \frac{\rho u_\theta^2}{r}$$

$$\rho\left(\frac{u_r}{r}\frac{d(r u_\theta)}{dr}\right) = \mu\frac{d}{dr}\left(\frac{1}{r}\frac{d(r u_\theta)}{dr}\right)$$

$$\frac{\partial p}{\partial z} = 0 \tag{II.33a}$$

$$c_p(\rho u_r)\frac{dT}{dr} = \frac{\kappa}{r}\frac{d}{dr}\left(r\frac{dT}{dr}\right) + \mu r^2\left[\frac{d}{dr}\left(\frac{u_\theta}{r}\right)\right]^2 + u_r\frac{\partial p}{\partial r}$$

$$pM = \rho RT$$

where the equation for conservation of momentum along the z-direction (eqn.(II.33a)) implies that the pressure is independent of z at the leading order. A detailed asymptotic analysis for deriving the above set of equations can be found in the article by Vatistas *et al.* [67]. Now, let us consider the case of a weakly compressible steady vortex, for which we obtain the governing equations,

$$\frac{1}{r}\frac{d(r u_r)}{dr} + w = 0 \tag{II.34a}$$

$$\frac{dp'}{dr} = \frac{\rho_\infty u_\theta^2}{r} \tag{II.34b}$$

$$\left(\frac{u_r}{r}\frac{d(r u_\theta)}{dr}\right) = \nu\frac{d}{dr}\left(\frac{1}{r}\frac{d(r u_\theta)}{dr}\right) \tag{II.34c}$$

$$u_r\frac{dT'}{dr} = \frac{\alpha}{r}\frac{d}{dr}\left(r\frac{dT'}{dr}\right) + \frac{\nu r^2}{c_p}\left[\frac{d}{dr}\left(\frac{u_\theta}{r}\right)\right]^2 + \frac{u_r}{\rho_\infty c_p}\frac{dp'}{dr} \tag{II.34d}$$

$$\frac{p'M}{R} = \rho' T_\infty + T'\rho_\infty \tag{II.34e}$$

where $p = p(r,t)$ owing to the eqn.(II.33a). To find the appropriate boundary conditions, we consider a physical picture of a vortex as shown in fig.II.16. The vorticity is assumed to be concentrated in a finite circular region with radius r_c at all times and aligned along the z-direction. From our preliminary understanding of vorticity [68], we assume the close to the center ($r = 0$), the vortex undergoes solid-body rotation Thus, the boundary conditions are,

$$\text{For } r = 0 : \begin{cases} u_\theta = 0 \text{ (solid body rotation)} \\ \frac{dT'}{dr} = 0 \text{ (solid body rotation hence no heat source)} \\ u_r = 0 \text{ (from continuity equation)} \\ \frac{dw}{dr} = 0 \text{ (avoid discontinuity in the profile of w)} \end{cases}$$

$$\text{For } r = \infty : \begin{cases} u_\theta = \frac{\Gamma_\infty}{2\pi r} \text{ (strong vortex with finite circulation)} \\ T' = 0 \\ p' = 0 \\ \rho' = 0 \end{cases}$$
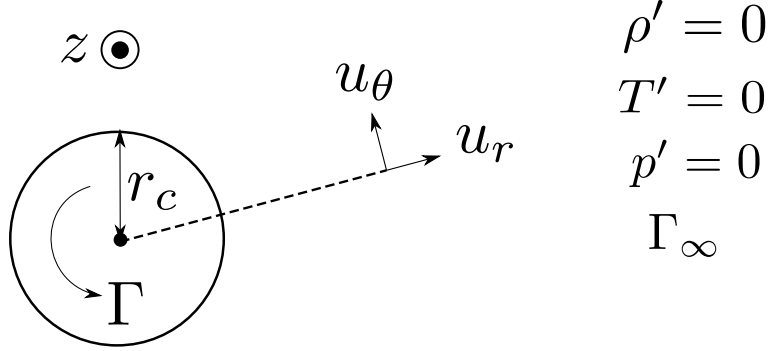
Fig. II.16 *Sketch of a strong vortex with vorticity aligned along z-axis.*

It is worthwhile to mention that the set of equations (II.34) are underdetermined (six variables and five equations) and would thus have infinite number of solutions. This is the reason for the variety of vortex solutions proposed in the literature depending on how the system of equations is closed. If we consider the case of an incompressible, viscous, strong vortex the hydrodynamic part of the governing equations which are equations (II.34a), (II.34b) and (II.34c) are,

$$\frac{1}{r}\frac{d(ru_r)}{dr} + w = 0$$
$$\frac{dp'}{dr} = \frac{\rho_\infty u_\theta^2}{r}$$
$$\frac{u_r}{r}\frac{d(ru_\theta)}{dr} = \mu\frac{d}{dr}\Big(\frac{1}{r}\frac{d(ru_\theta)}{dr}\Big) \tag{II.35}$$

and the thermodynamic part of the governing equations (equations (II.34d) and (II.34e)) is reduced to,

$$u_r\frac{dT'}{dr} = \frac{\alpha}{r}\frac{d}{dr}\Big(r\frac{dT'}{dr}\Big) + \frac{\nu r^2}{c_p}\Big[\frac{d}{dr}\Big(\frac{u_\theta}{r}\Big)\Big]^2$$
$$\rho'T_\infty + T'\rho_\infty = 0 \tag{II.36}$$

The set of governing equations for the hydrodynamic part (II.35) and the thermodynamic part (II.36) form an underdetermined system of equations and thus have an infinite number

of steady vortex solutions. This system can be closed with some assumption on the form of the velocity field. The simplest assumption of w being a constant in equations (II.33) gives us the Burgers vortex [69]. Another vortex solution by Sullivan called Sullivan vortex incorporates a radial dependence of w [70]. In both the vortex solutions, once we assume some form of the velocity field, solving the hydrodynamic part gives us the pressure field and the velocity field. On solving the thermodynamic part, we obtain the temperature and density fields. Note that in this case, pressure fluctuations do not result in either temperature or density fluctuations.

If we consider an incompressible, viscous vortex with only the azimuthal velocity component u_θ being non-zero, the governing equations form a closed set of equations but with no steady state solutions being possible. This can be seen from momentum equation in the azimuthal direction eqn.(II.35), the left hand side of which would be identically zero, whereas the right hand side would be non-zero in some part of the domain if the boundary conditions on u_θ are to be met. Such vortices undergo viscous spreading over time. Some well-known vortex solutions like the Rankine vortex [71], Scully vortex [72, 73] and the Lamb-Oseen vortex [74, 75] fall into this category.

The case of a steady, compressible, viscous vortex is governed by the set of equations (II.33). Such a vortex generated by a solid rotating cylinder in the core was studied by Mack *et al.* [76]. They considered only the azimuthal component of the velocity field and found analytical expression for the temperature field by using temperature-dependent viscosity. This was extended by Bellamy-Knights [77] with a radial inward flow in addition to a temperature-dependent viscosity. Since the core was considered to be a solid rotating cylinder, the temperature and pressure profiles obtained by both were for the irrotational part of the flow which would be outside the vortex core. Unsteady, compressible and viscous vortices were studied by Merzkirch [78], Mandella [79] and Colonius *et al.* [80].

We proceed to obtain a steady solution for weakly compressible vortex given by equations (II.34). Since the governing equations form an undetermined system, to obtain a solution we assume that w is constant. This enables us to solve the hydrodynamic part of the problem which gives us Burgers vortex. On solving equations (II.34a) and (II.34c), we obtain the velocity field whose azimuthal component is given by,

$$u_\theta = \frac{\Gamma_\infty}{2\pi r}\left(1 - \exp\left(\frac{-r^2}{r_c^2}\right)\right)$$

To obtain the pressure field, we integrate eqn.(II.34b),

$$\int_p^0 dp' = \frac{\rho_\infty \Gamma_\infty^2}{4\pi^2}\int_r^\infty dx \left[\frac{1 - \exp(-x^2/r_c^2)}{x^{3/2}}\right]^2$$

After proceeding with change of variables and then using integration by parts, we obtain,

$$p(r) = -\left[\frac{\rho_\infty \Gamma_\infty^2}{8\pi^2 r_c^2}\left(\frac{(1-\exp(-r^2/r_c^2))^2}{r^2/r_c^2} + 2\mathbf{Ei}\left(\frac{r^2}{r_c^2}\right) - 2\mathbf{Ei}\left(\frac{2r^2}{r_c^2}\right)\right)\right] \qquad \text{(II.37)}$$

where $\mathbf{Ei}(x)$ denotes 'exponential integral' with the definition,

$$\mathbf{Ei}(x) = \int_x^\infty dx\ \frac{\exp(-x)}{x}$$

which can be computed numerically. As noticed by Rott [81], the term involving the exponential is related to the dynamic pressure whereas the remaining terms are related to the change in stagnation pressure due to viscosity (where r_c depends on viscosity) in the case of a viscous Burgers vortex. Now, we concentrate on eqn.(II.34d) of the thermodynamic part of the problem. We non-dimensionalize eqn.(II.34d) such that,

$$r^* = r/r_c,\ u_r^* = u_r/\widetilde{u}_r,\ T^* = T'/\widetilde{T},\ u_\theta^* = u_\theta/u'_{rms}\ p^* = p'/\widetilde{p}$$

We recall that from our assumption of a strong vortex we would have,

$$u_\theta \sim u'_{rms} \gg u_r$$

Non-dimensionalized form of eqn.(II.34d) is then given by,

$$u_r^* \frac{dT^*}{dr^*} = \left[\frac{1}{Pe}\left(\frac{u'_{rms}}{\widetilde{u}_r}\right)\right]\left[\frac{1}{r^*}\frac{d}{dr^*}\left(r^*\frac{dT^*}{dr^*}\right)\right] + \left[(\gamma-1)\left(\frac{\mathcal{M}a^2}{\widetilde{T}/T_0}\right)\frac{1}{Re}\left(\frac{u'_{rms}}{\widetilde{u}_r}\right)\right]\left[r^{*2}\left[\frac{d}{dr^*}\left(\frac{u_\theta^*}{r^*}\right)\right]^2\right]$$
$$+ \left[\left(\frac{\gamma-1}{\gamma}\right)\frac{\widetilde{p}/p_0}{\widetilde{T}/T_0}\right]\left[u_r^*\left(\frac{dp^*}{dr^*}\right)\right]$$

where the Reynolds number Re, Peclet number Pe and Mach number $\mathcal{M}a$ are defined as,

$$Re = \frac{u_\theta r_c}{\nu} \sim \frac{u'_{rms} r_c}{\nu}$$
$$Pe = \frac{u_\theta r_c}{\alpha} \sim \frac{u'_{rms} r_c}{\alpha}$$
$$\mathcal{M}a = \frac{u_\theta}{c} \sim \frac{u'_{rms}}{c}$$

For *Re* and *Pe* tending to infinity, we would obtain the equation,

$$\frac{dT^*}{dr^*} = \frac{dp^*}{dr^*} \tag{II.38}$$

only when,

$$\left(\frac{\gamma - 1}{\gamma}\right)\frac{\widetilde{p}/p_0}{\widetilde{T}/T_0} \sim O(1)$$

which corresponds to the filament undergoing adiabatic process. Eqn.(II.38) can be solved since we already know the pressure field given by eqn.(II.37). This gives us the temperature field,

$$T(r) = -\left[\frac{\Gamma_\infty^2}{8\pi^2 r_c^2 c_p}\left(\frac{(1 - \exp(-r^2/r_c^2))^2}{r^2/r_c^2} + 2\mathbf{Ei}\left(\frac{r^2}{r_c^2}\right) - 2\mathbf{Ei}\left(\frac{2r^2}{r_c^2}\right)\right)\right] \tag{II.39}$$

Using the equation for state eqn.(II.34e), we also obtain the density field. We call this solution the weakly compressible adiabatic Burgers vortex. Figures II.17b and II.17a show the profile of pressure and temperature as obtained from the method of coherent averaging and compare it with the profiles as predicted by the model of weakly compressible adiabatic Burgers vortex (equations (II.37) and (II.39))[9]. We observe that this simple model is able to capture the structure of vorticity filaments. Note that we have transformed the time co-ordinate to space co-ordinate by using the relation $r = u'_{rms}t$.

For large values of r, the model deviates from the experimentally observed structure, as seen for $r > 1.5$ mm for the temperature structure and for $r > 8$ mm for the pressure structure. This possibly arises from the interaction of the vortex filament with the surrounding turbulent flow as well as other vorticity filaments. The weakly compressible adiabatic Burgers vortex models a single steady vortex with the fluid being at rest far from the vortex. The effects at the edges of the vorticity filaments would not be captured by the model and would lead to deviations from the experimentally observed structure far from the core of the vorticity filament.

---

[9]The fitting procedure involves three free parameters; the radius of the vortex r_c (which governs the width of the filament), the constant prefactor (which governs the height of the filament) and the values of the fields far from the filament (p_∞, T_∞). The first two would be affected by the characteristics of the probe.
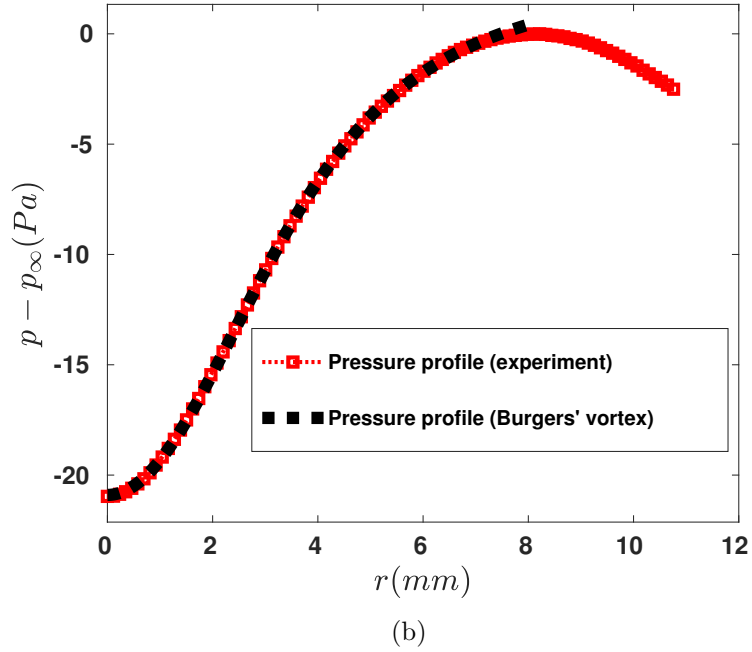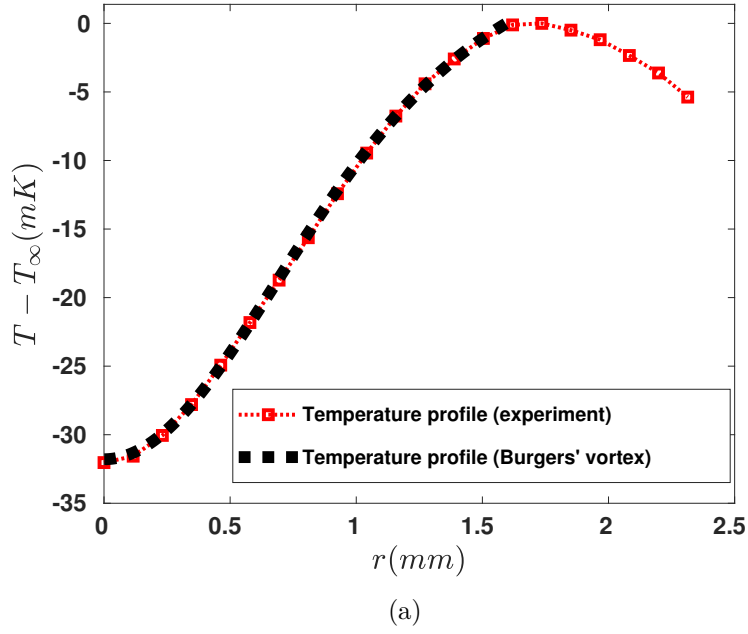
Fig. II.17   *(a) Temperature profile obtained from coherent averaging (red) and a fit for the pressure profile of weakly compressible adiabatic Burgers vortex solution (dashed line) (eqn.(II.39)). (b) Pressure profile obtained from coherent averaging (red) and a fit for the pressure profile of weakly compressible adiabatic Burgers vortex solution (dashed line) (eqn.(II.37)). We have used $r = u'_{rms}t$ to transform time to space co-ordinate. The rotation rate is $\Omega = 2000$ rpm.*

Since the physical dimensions of the measuring element of the temperature probe is smaller than that of the pressure probe, the temperature profile of the structure would be more accurate at estimating its width. From the fit of the temperature profile with the weakly compressible Burgers vortex, we obtain,

$$O(r_c) \approx 1 \text{ mm} \sim \lambda$$

In conclusion to questions posed Q1A-Q1D, we find experimentally that,

- Vortex filaments in a turbulent flow result in sharp negative peaks in time signals of temperature and pressure fluctuations.

- The vortex filaments undergo adiabatic process as deduced from the pressure and temperature drops $(\Delta p, \Delta T)$ which obey the adiabatic relation $\left(\frac{\gamma-1}{\gamma}\right)\left(\frac{\Delta p}{\Delta T}\right) \sim \frac{p_0}{T_0}$

- They are compressible structures and can be modeled by weakly compressible adiabatic Burgers vortex. This is surprising since the turbulent flow is of low Mach number and essentially incompressible.

- The radial size of the vorticity filaments is roughly the same order as the Taylor microscale.

With the current understanding from our analysis, we can rephrase Q2A,

Q2B: If T_{rms} does not obey the prediction from dimensional analysis, does the energy spectrum follow the KOC spectrum (eqn.(II.28)) across some range of scales? Do the vorticity filaments contribute significantly to the energy spectrum at some scales?

II.3.6 The energy spectra of temperature fluctuations

Fig.II.18 shows the energy spectrum of temperature fluctuation, E_T, when the rotation rate is $\Omega = 2000$ rpm. We observe two regimes in frequency where the energy spectrum displays a power law. At low frequencies, $E_T(f) \propto f^{-0.41\pm0.01}$ and an inertial regime with $E_T(f) \propto f^{-1.27\pm0.05}$. We recall that the KOC spectrum predicts that the energy spectrum of temperature fluctuations in the inertial range should scales as $E_T(f) \propto f^{-5/3}$ (eqn.(II.28)). Thus, across all scales in frequency, deviation from the KOC spectrum is observed.
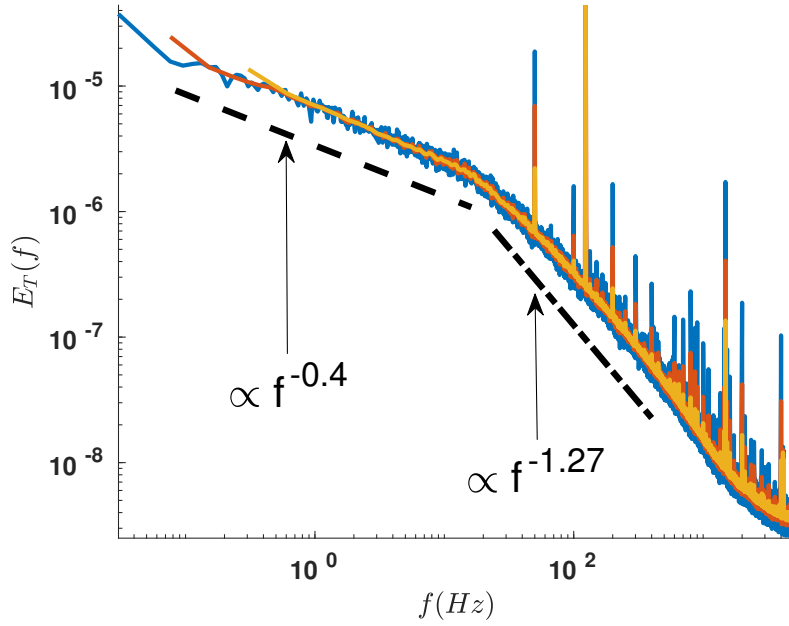
Fig. II.18   *Energy spectrum of temperature signal as obtained from cold-wire probe for $\Omega = 2000$ rpm. The different coloured curves correspond to different windowing lengths for evaluating the averaged spectrum. Dashed line: corresponds to $\propto f^{-0.4}$. Dash-dotted line: corresponds to $\propto f^{-1.27}$.*

Can we obtain a model to explain the behaviour of the energy spectrum of temperature fluctuations and the exponents observed? Where does the low frequency behaviour of the energy spectrum come from? To be able to model the behaviour of the observed energy spectrum of temperature fluctuations, we first need to understand the behaviour of the fluctuations in the rate of kinetic energy dissipation per unit mass or ϵ' and the mean rate of energy injected per unit mass in the field of temperature fluctuations or ϵ'_T (see eqn.(II.22)).

The behaviour of the fluctuations in the rate of dissipation (ϵ') have drawn interest as early as 1960s, largely owing to the observations that they did not obey the large scale scaling from dimensional analysis as is usually done in the Kolmogorov theory. The approach of dimensional analysis yields the energy spectrum of the form,

$$E_\epsilon(k) = C\nu^2 \langle\epsilon\rangle^{4/3} k^{5/3}$$

where C is a dimensionless constant, suggests that the energy spectrum would be an increasing function of the wavenumber. For the energy spectrum, it was experimentally observed that it was rather a decreasing function of wavenumber in contrast to the large scale scaling from dimensional analysis. Using the available experimental data, Yaglom [9] proposed a model which accounted for intermittency in the dissipation process (via the parameter μ called the intermittency exponent). He proposed the energy spectrum of the form,

$$E_\epsilon(k) = C\langle\epsilon\rangle^2 l_I (kl_I)^{-1+\mu} \tag{II.40}$$

where l_I is the *integral scale* of the turbulent flow. Similar to Kolmogorov theory, self-similarity across scales is assumed to obtain the above form of energy spectrum and thus is valid for $l_0^{-1} \ll k \ll \eta^{-1}$. Since then, a number of studies have concentrated on evaluating the intermittency exponent μ. For a review till 1975, refer to [9] and for a later review, refer to [82]. The values of the intermittency exponent reported in literature [9, 83] are in the range $0.25 < \mu < 0.5$. Later, it was also observed that the dissipation occurs on the surface of sheet like structures (long in two directions and short in the third) [34, 84] unlike structures of strong vorticity which are filamentary (long in one direction and short in the other two). With the aid of the energy spectrum for fluctuations in dissipation rate as predicted by Yaglom (eqn.(II.40)), we proceed to model the behaviour of $\langle\epsilon_T\rangle$. We recall that,

$$\langle\epsilon_T\rangle = \frac{\langle T'\epsilon'\rangle}{c_p}$$

which is the correlation between temperature and rate of viscous dissipation of kinetic energy per unit mass. To approximate it, we consider the eqn.(II.21) for the temperature fluctuations. Now, if we assume the diffusion of temperature fluctuations to be negligible for inertial scales, then eqn.(II.21) shows that a volume of fluid would undergo heating (and cooling as ϵ' can be negative) as it moves in a Lagrangian trajectory in the flow. Thus,

$$\langle\epsilon_T\rangle = \frac{\langle T'\epsilon'\rangle}{c_p} = \frac{1}{c_p^2}\int_0^t ds \left\langle\epsilon'\big(\mathbf{y}(s),s\big)\epsilon'\big(\mathbf{y}(t),t\big)\right\rangle ~\sim \tau_L \frac{\langle\epsilon'^2\rangle}{c_p^2} ~\sim \tau_I \frac{\langle\epsilon'^2\rangle}{c_p^2} = \langle\epsilon\rangle^{-1/3} l_I^{2/3} \frac{\langle\epsilon'^2\rangle}{c_p^2}$$

where $\mathbf{y}(s)$ is the Lagrangian trajectory of the fluid particle and τ_L is the Lagrangian correlation time. Though, it could have a more complicated form, for the ease of further analysis we assume it to be the integral timescale $\tau_L ~\sim \tau_I = \langle\epsilon\rangle^{-1/3} l_I^{2/3}$.

At this point, we note that $\langle\epsilon'^2\rangle$ corresponds to the total energy in the dissipation rate fluctuations and that this energy is spread across scales as seen from eqn.(II.40), including the inertial range. Thus, the appropriate form would then be,

$$\langle\epsilon_T\rangle = \frac{\langle\epsilon\rangle^{-1/3} l_I^{2/3}}{c_p^2} \int_{1/l_I}^k dk ~E_\epsilon(k) \tag{II.41}$$

Now that we have a relation for the behaviour of $\langle \epsilon_T \rangle$, we proceed by saying that though the KOC scaling does not match experimental observations, a better prediction on the behaviour of energy spectrum of temperature fluctuations would be the one resulting from the modification of the KOC spectrum. This modification results from a more accurate behaviour of $\langle \epsilon_T \rangle$ given by eqn.(II.41) than it being just a constant independent of the wavenumber. On combining equations (II.40), (II.28) and (II.41), we obtain,

$$E_T(k) = C(Re, Pr)\frac{\langle \epsilon \rangle^{4/3} l_0^{2/3} k^{-5/3}\left[(kl_I)^\mu - 1\right]}{c_p^2}$$

which for the inertial range ($kl_I \gg 1$) becomes,

$$E_T(k) = C(Re, Pr)\frac{\langle \epsilon \rangle^{4/3} l_I^{2/3+\mu} k^{-5/3+\mu}}{c_p^2} \tag{II.42}$$

Note that we have retained the dependence of the constant on the Reynolds and Prandtl numbers. Similar form of the energy spectrum (II.42) was also obtained by Bos *et al.* [31] though a slightly different method. Integrating the above equation, we obtain,

$$T_{rms}^2 = \int_{1/l_I}^{1/\eta} dk\ E_T(k) = C(Re, Pr)\frac{(\langle \epsilon \rangle l_I)^{4/3}}{(2/3 - \mu)c_p^2}$$

where the last equality holds when $\eta \ll l_I$. This is equivalent to,

$$T_{rms} = \sqrt{C(Re, Pr)}\frac{(\langle \epsilon \rangle l_I)^{2/3}}{(\sqrt{2/3 - \mu})c_p} \tag{II.43}$$

Our prediction (eqn.(II.42)) suggests that the inertial scales will follow the cascade-like picture for temperature fluctuations (and thus the KOC spectrum eqn.(II.28)) alongwith a correction in the power-exponent of the wavenumber due to intermittent behaviour of dissipation (characterized by the intermittency exponent). Thus the correction to the KOC like spectrum in the inertial range for temperature fluctuations would be a manifestation of dissipative events which are small spatial and temporal scales and intermittent (most probably in both space and time). It shows that the energy spectrum should scale as $E_T \propto k^{-5/3+\mu}$. Fig.II.18 shows that the energy spectrum in the inertial range scales as $E_T \propto f^{-1.27}$. Assuming that we can transform the co-ordinates from wavenumber to frequency with the relation $u'_{rms}k = f$, it gives us the intermittency exponent, $\mu \approx 0.4$. This is in agreement with previously reported values of $0.25 < \mu < 0.5$.

For the RMS of temperature fluctuations, T_{rms}, the prediction obtained (eqn.(II.43)) is proportional to the large scale scaling predicted from dimensional analysis (eqn.(II.29)) with

a correction by a constant factor which involves the intermittency exponent. This suggests that our assumption that,

$$\langle \epsilon_T \rangle \sim \tau_L \frac{\langle \epsilon'^2 \rangle}{c_p^2} \not\propto \tau_I \frac{\langle \epsilon'^2 \rangle}{c_p^2}$$

is incorrect and that τ_L will not be equivalent to τ_I which will lead to large scale scaling. We note that this however does not change the scaling of the energy spectrum of temperature fluctuations E_T with the wavenumber. We can further understand the possible reason for the RMS of temperature fluctuations deviating from large scale scaling from eqn.(II.22). In steady state, we would have,

$$\alpha \left\langle \frac{\partial T'}{\partial x_i} \frac{\partial T'}{\partial x_i} \right\rangle = \langle \epsilon_T \rangle \tag{II.44}$$

Taylor microscale λ is defined as the length scale at which the velocity gradients are maximum. If we assume that the gradients in temperature are also maximum at the Taylor microscale, we have,

$$\alpha \left\langle \frac{\partial T'}{\partial x_i} \frac{\partial T'}{\partial x_i} \right\rangle \sim \frac{\alpha T_{rms}^2}{\lambda^2} \tag{II.45}$$

The mean square of the dissipation rate fluctuations can be estimated by integrating the energy spectrum of dissipation rate fluctuations given by eqn.(II.40) between the integral scale and the Kolmogorov microscale,

$$\langle \epsilon'^2 \rangle = \int_{1/l_I}^{1/\eta} dk \ E_\epsilon(k) \sim \frac{\langle \epsilon \rangle^{2+\mu/4} \ l_I^\mu}{\mu \nu^{3\mu/4}}$$

Thus,

$$\langle \epsilon_T \rangle \sim \tau_L \frac{\langle \epsilon'^2 \rangle}{c_p^2} \sim \frac{\tau_L \ \langle \epsilon \rangle^{2+\mu/4} \ l_I^\mu}{\mu c_p^2 \ \nu^{3\mu/4}} \tag{II.46}$$

Equations (II.44), (II.45) and (II.46) then imply that,

$$T_{rms} \sim \left(\frac{l_I^\mu \nu^{1-3\mu/4}}{\mu \alpha c_p^2} \right)^{1/2} \left[u'_{rms} \tau_L^{1/2} \langle \epsilon \rangle^{1/2+\mu/8} \right] \tag{II.47}$$

where we have used the relation $\lambda = \left(15\nu \frac{u_{rms}'^2}{\langle \epsilon \rangle}\right)^{1/2}$ for homogeneous and isotropic turbulence.

We notice from eqn.(II.47) that if we assume $\tau_L \sim \tau_I \sim \langle \epsilon \rangle^{-1/3} l_I^{2/3}$ and for $\mu \to 0$ (which implies $\langle \epsilon'^2 \rangle = \langle \epsilon \rangle^2$), we obtain the large scale scaling with $T_{rms} \propto \Omega^2$. Since the exponent $\mu/8 \ll 1/2$, eqn.(II.47) shows that the the deviation of the RMS of temperature fluctuations from the large scale scaling likely arises from the behaviour of the timescale τ_L.

One more question of interest that remains unanswered is regarding the low frequency behaviour observed in the energy spectrum of temperature fluctuations,

Q2C: Where does the low frequency behaviour of energy spectrum of temperature fluctuations with $E_T(f) \propto f^{-0.4}$ come from? Is it due to vorticity filaments?

To answer this question, we look at the energy spectrum of pressure fluctuations, shown in fig.II.19. The inertial range of the energy spectrum is proportional to $f^{-7/3}$ as is expected from Kolmogorov's *K41* theory. We also see that for a small range of low frequencies, $E_p \propto f^{-0.6}$ is observed. This is not as clearly seen in the energy spectrum of pressure fluctuations as the energy spectrum of velocity fluctuations E_u since unlike velocity fluctuations, pressure fluctuations are polluted at low frequencies by the fluctuations from ambient surroundings. In their experimental study, Abry *et al.* [13] showed that the vorticity filaments result in the energy spectrum of pressure fluctuations displaying a low-frequency power law behaviour with $E_p \propto f^{-0.6}$. This is observed in our experiment with an identical exponent (fig.II.19).

As these vorticity filaments get advected by the turbulent flow, they pass through the stationary probes placed in the flow. Thus we would expect similar behaviour in the energy spectrum of velocity and temperature fluctuations as well[10]. Whether this behaviour is indeed observed or not would depend on the relative energy in the fluctuations due to these filaments with the rest of the signal. Indeed the energy spectrum of velocity fluctuations also displays a power law behaviour with $E_u \propto f^{-0.6}$ in the same range of frequencies as seen for pressure fluctuations (fig.II.6a). The expectation that the energy spectrum for temperature fluctuations should also display $f^{-0.6}$ behaviour can also be seen from the governing eqn.(II.17) for perfect fluid.

To confirm that the energy spectrum of the negative peaks observed in pressure signal indeed results in a power law behaviour with an exponent close to the one observed for velocity signal, we define a bursting signal 'S_p' using the pressure signal such that,

$$S_p(t) = \begin{cases} -1 & \text{when } p \leq -2 \times p_{rms} \\ 0 & \text{otherwise} \end{cases}$$

We expect the energy spectra of these signals to capture the energy spectra that would be resulting from the vorticity filaments [85]. Figures II.20 and II.21 show the bursting signal and its energy spectrum for pressure fluctuations when the rotation rate is 2000 rpm. Indeed, we observe that the negative peaks in pressure fluctuations result in the energy

---

[10]As we showed the structure of the vorticity filaments can be approximated by adiabatic, compressible Burgers' vortex which obeys the governing equations. The fine scale structure and the spectra it would produce is not what we are probing in our energy spectrum but rather the intermittent signal produced by the advection of these structures as whole.

Fig. II.19   *Energy spectrum of pressure signal as obtained for $\Omega = 2000$ rpm. The different coloured curves correspond to different windowing lengths for evaluating the averaged spectrum. Dashed line: corresponds to $E_p \propto f^{-0.6}$. Dash-dotted line: corresponds to $E_p \propto f^{-7/3}$.*

spectrum having a power law behaviour with exponent roughly $E_{S_p} \propto f^{-0.6 \pm 0.01}$. The range of frequencies in which this behaviour is observed coincides with the one in which the energy spectrum of velocity fluctuations has similar behaviour. On applying the same technique to temperature fluctuations and obtaining the energy spectrum for the peaks, a flat spectrum is observed at low frequencies. This is likely due to the observation that the negative peaks are easier to distinguish from the rest of the signal for pressure fluctuations than temperature signals. This can seen from the PDFs for pressure and temperature (fig.II.13 and fig.II.11a). The exponential tails observed in the PDFs are sharper for pressure fluctuations than the ones in PDFs of temperature fluctuations.

The energy spectrum of temperature fluctuations (fig.II.18) shows a low-frequency power law behaviour with $E_T \propto f^{-0.4}$. The range of frequencies for which this behaviour is observed is much larger and at even lower frequencies than the one in which the power-law behaviour due to vorticity filaments in energy spectra of velocity and pressure fluctuations is observed. As to where the large temporal scales observed in temperature fluctuations come from is still an open question. It is highly likely that it is a manifestation of dissipative structures in the turbulent flow but this needs further investigation.
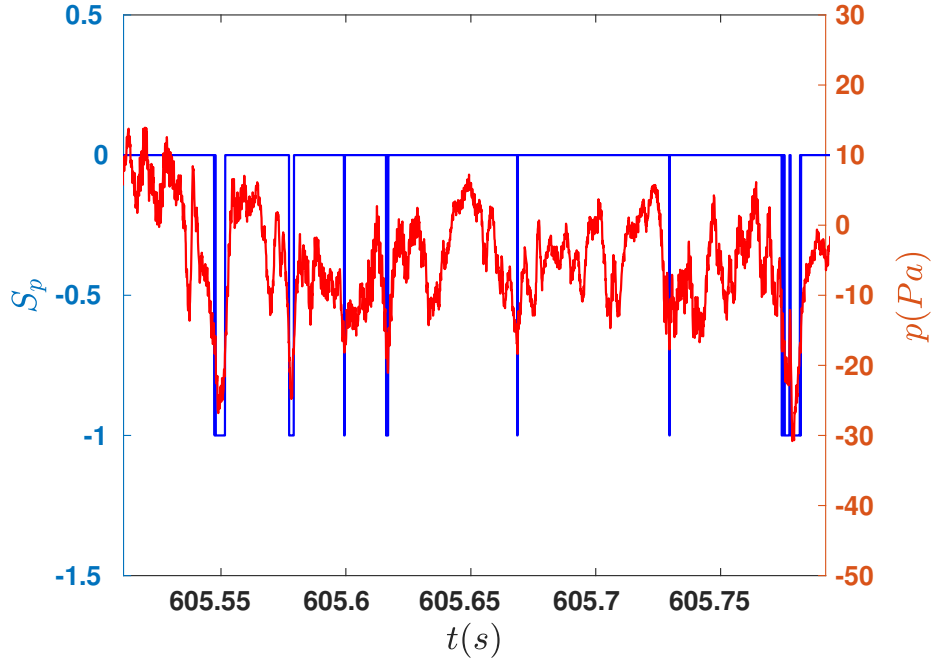
Fig. II.20   *Pressure signal and the bursting signal* (S_p) *defined from it. The threshold for defining the bursting signal is* $2 \times p_{rms}$. *For this figure, the rotation rate* $\Omega = 2000$ rpm.
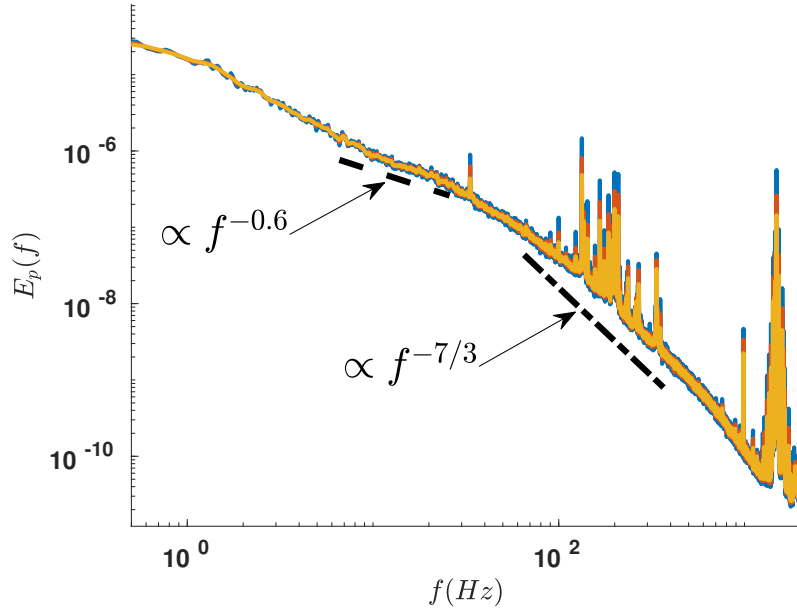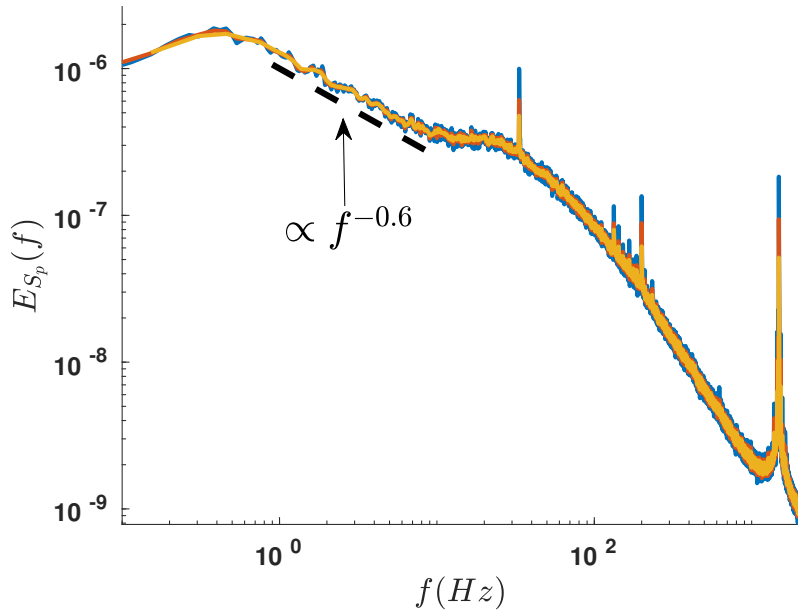

Fig. II.21   *Energy spectrum of the bursting signal* S_p *as obtained for* $\Omega = 2000$ rpm. *The different coloured curves correspond to different windowing lengths for evaluating the averaged spectrum. Dashed line: corresponds to* $E_p \propto f^{-0.6}$.

II.4 Conclusion

The two different type of intermittent structures observed in turbulent flow, vorticity filaments and viscous dissipative structures, result in many interesting features observed in measurements of velocity, pressure and temperature fluctuations in a turbulent flow. In the case of spontaneous temperature fluctuations in a turbulent flow, we observe experimentally that both the dissipation process and vorticity filaments play an important role.

The main features of the temperature fluctuations which are a consequence of the vorticity filaments can be summarized as follows,

- Vorticity filaments are characterized by a sharp decrease in temperature and pressure at their cores. This implies that though the turbulent flow is of low Mach number and incompressible to the leading order, the vorticity filaments are compressible.

- Their existence is evidenced by sharp negative peaks observed in the time signal of temperature fluctuations and exponential negative tails observed in the PDFs.

- Vorticity filaments can be accurately modeled by weakly compressible adiabatic Burgers vortex.

- Vorticity filaments do not contribute significantly to the total energy of the temperature fluctuations.

Whereas the features of the temperature fluctuations which are a consequence of dissipation can be summarized as follows,

- The energy at the inertial scales as seen from the energy spectra of temperature fluctuations is a direct consequence of the dissipation events in turbulent flows. The behaviour of energy spectra at the inertial scales gives us a direct measurement on the intermittency of the dissipation events. This is quantified with the intermittency exponent.

- The total energy in the temperature fluctuations which is quantified by the RMS of temperature fluctuations scales logarithmically with the Reynolds number. The RMS of temperature fluctuations is a result of the dissipation events which are experimentally observed to contribute the most energy to the fluctuating temperature field.

It is striking that from simple point measurement of temperature, we observe the signature of two long searched sources of intermittency in turbulence, vortex filaments and dissipative structures. One interesting feature that remains unanswered is the low-frequency behaviour of the energy spectrum of temperature fluctuations. Whether it results from the viscous dissipative events or not remains a question that requires further analysis.

As a concluding remark, it should be noted that even though most of our analysis is centred around the fluid being an ideal gas, the observations should be valid for liquids as well. As an example let us consider the case of air and water. For water, the coefficient of thermal expansion $\beta \approx 2 \times 10^{-4}$ K^{-1} and and is an order of magnitude smaller than for air at room temperature $\beta \approx 3 \times 10^{-3}$ K^{-1}.

For an incompressible flow, the temperature fluctuations generated by viscous dissipation

would be of $O(\mathcal{M}a^2)$ (see section II.1.2). Thus for compressible effects to be measurable, we would have the condition on the order of magnitude of pressure fluctuations,

$$Air \Rightarrow \; p' \sim \left(\frac{\gamma p_0}{\gamma - 1}\right)\mathcal{M}a^2 \; \approx \; O(1) \text{ Pa}$$

$$Water \Rightarrow \; p' \sim \left(\frac{\rho_0 c_p}{\beta}\right)\mathcal{M}a^2 \; \approx \; O(10^4) \text{ Pa}$$

where the order of magnitude on the pressure fluctuations is obtained considering $u'_{rms} \sim O(1)$m/s. For a turbulent flow in water pressure fluctuations of $O(10^4)$ Pa are easily achievable. This demonstration shows that spontaneously generated temperature fluctuations in water would also display effects of both viscous dissipation and vorticity filaments.

II.A Estimation of RMS of velocity fluctuations from 1D hot-wire probe

Hot-wire anemometry is one of the most widely used experimental technique for measuring velocity in turbulent flows. This is owing to its high accuracy, small response time[11] allowing to capture rapidly fluctuating velocity fields and high spatial resolution (about the diameter of the probe filament which is of order 1 µm). One of the main disadvantages of hot-wire anemometry technique is its intrusiveness. To minimize the errors owing to intrusiveness, we have used only 1D hot-wire probes in our experimental work. Though, using 1D hot-wire probes has one major disadvantage and that is the inability to obtain the direction of the flow. This results in the measurement of the norm of velocity or the speed rather than the velocity of the turbulent flow. One very important statistic in characterizing any turbulent flow is the RMS of the velocity fluctuations. Using 1D hot-wire probes results in the overestimation and thus an erroneous measurement of the RMS of velocity fluctuations. We present here a method to obtain a correct estimation of the RMS of velocity fluctuations from the signal measured by a 1D hot-wire probe.

We consider a signal which is a Gaussian white noise (denoted by u) with a standard deviation denoted by u'_{rms} and a mean value denoted by $\langle u \rangle$. This signal resembles velocity fluctuations in turbulent flows which are known to be close to Gaussian. We define the modulus of the signal and denote it by S. This signal is equivalent to the speed of the actual velocity fluctuations and resembles the measurement by a 1D hot-wire probe. The definition of the modulus signal S is,

$$S = |u|$$

From the modulus signal S, we consider two estimates of the actual RMS of velocity fluctuations (which is one according to our definition),

1. $S^1_{rms} = \sqrt{\langle S^2 \rangle}$
2. $S^2_{rms} = \sqrt{\langle (S - \langle S \rangle)^2 \rangle}$

With these definitions, we proceed to understand which of the two quantities S^1_{rms} and S^2_{rms} is a better estimate of the actual RMS of velocity fluctuations u'_{rms} as the mean of velocity fluctuations $\langle u \rangle$ is varied. Fig.II.22a shows the two estimates S^1_{rms} and S^2_{rms} normalized by the value of u'_{rms} as the ratio $u'_{rms}/\langle u \rangle$ is varied. We can draw two observations,

- When $u'_{rms}/\langle u \rangle \to \infty$, S^2_{rms} correctly estimates u'_{rms}. This agrees with the physical understanding that with strong mean flows, the hot-wire probe is able to capture correctly the fluctuations in the velocity.

- When $u'_{rms}/\langle u \rangle \to 0$, S^1_{rms} correctly estimates u'_{rms}. In this case, the absence of mean flow would result in $u'^2 = |u|$ and thus S^1_{rms} correctly estimating u'_{rms}.

---

[11] for example the hot-wire probe used in our experiments has a maximum acquisition frequency of 250 kHz.
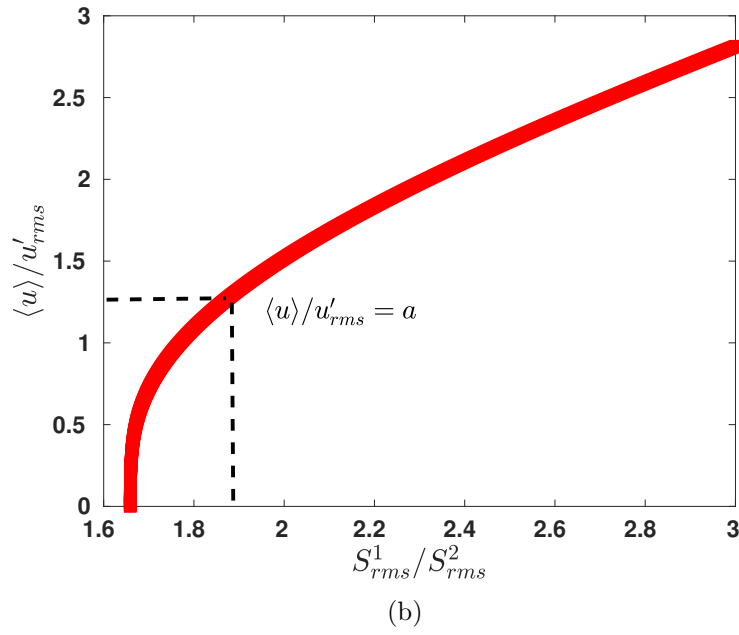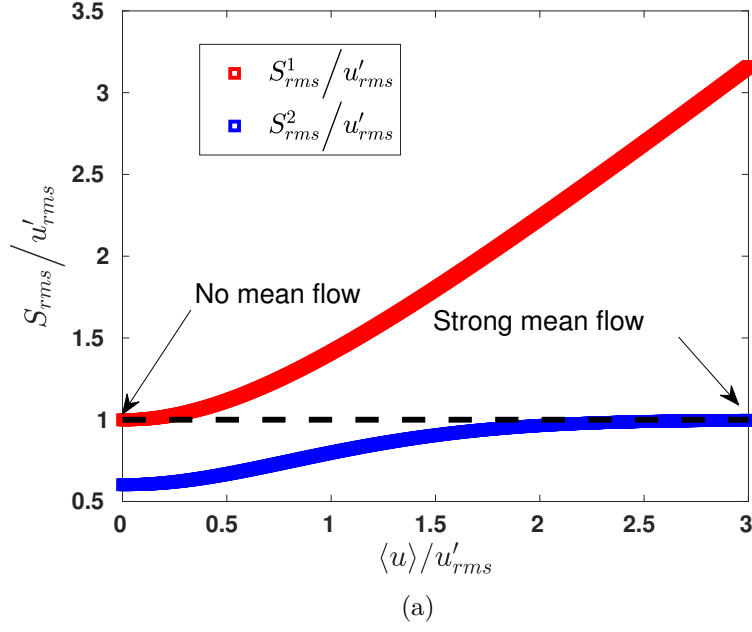
Fig. II.22   (a) The two estimates of the RMS of velocity fluctuations S^1_{rms} (red) and S^2_{rms} (blue) normalized by the value of u'_{rms} as the ratio $u'_{rms}/\langle u \rangle$ is varied. (b) $u'_{rms}/\langle u \rangle$ as a function of the ratio of the two estimates, S^1_{rms}/S^2_{rms}.

The procedure is as follows,

- We would have the modulus signal S, say the velocity measured by the 1D hot-wire probe.

- We obtain the values of the two estimates, S_{rms}^1 and S_{rms}^2. We would have no prior knowledge which of the two correctly estimates the actual RMS of the velocity fluctuations u_{rms}' and to what degree of error.

- We evaluate the ratio S_{rms}^1/S_{rms}^2. The ratio $u_{rms}'/\langle u \rangle$ is found to be a monotonic function of S_{rms}^1/S_{rms}^2 (fig.II.22b). Thus, we obtain the value of $u_{rms}'/\langle u \rangle$.

- From this we obtain the values of $R_1 = S_{rms}^1/u_{rms}'$ and $R_2 = S_{rms}^2/u_{rms}'$, shown in fig.II.23.

- We can then obtain u_{rms}' as $u_{rms}' = \frac{S_{rms}^1}{R_1} = \frac{S_{rms}^2}{R_2}$.

This procedure details the procedure of obtaining the correct value of the RMS of velocity fluctuations from 1D hot-wire probe measurement. Using this procedure we also obtain the correct mean velocity $\langle u \rangle$ once the other values S_{rms}^1, S_{rms}^2 and u_{rms}' are determined.
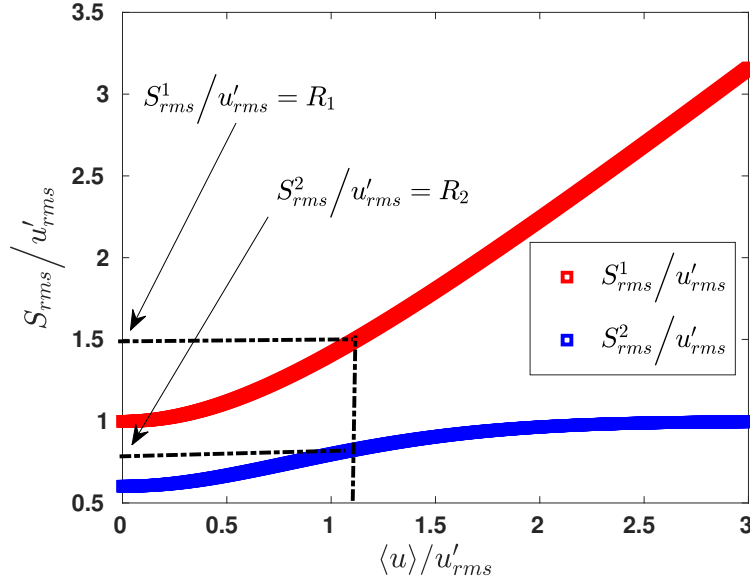
Fig. II.23

Fig. II.24 *PDFs of phase fluctuations normalized by its RMS value. Red squares: 1200 rpm; Blue crosses: 1600 rpm; Green circles: 2000 rpm. Dashed line: Gaussian*

II.B Method of *coherent averaging*

A signal obtained experimentally or numerically might contain a recurrent structure which would be observable, say, in its time signal for example. More often than not, the signal would not be comprised only of these structures but also noise which would pollute every individual structure and prevent us from studying the features of the structures. The method of coherent averaging described in this appendix enables us to remove the effect of noise and obtain an averaged structure. By averaged, we mean, all the structures appearing in the signal would be accounted for to obtain the averaged structure which can then be analysed to understand the properties of the structures in general.

Let us say, we have a signal $\zeta(t)$ with $0 < t < T_0$ and that we have identified a noisy structure in the signal for $t_1 < t < t_2$. We call this initial structure $\chi(\tau)$,

$$\chi(\tau) = \zeta(t_1 + \tau) \text{ where } 0 < \tau < t_2 - t_1$$

We can compute the correlation of this noisy structure with the signal,

$$C(T) = \frac{\int_0^{t_2 - t_1} d\tau \; \chi(\tau)\zeta(T + t_1 + \tau)}{\int_0^{t_2 - t_1} d\tau \; \left[\chi(\tau)\right]^2} \text{ where } -t_1 < T < T_0 - t_2$$

The procedure of coherent averaging is as follows,

- We start with $T = -t_1$ for the initial structure $\chi_1(\tau)$ and search for peaks in the correlation. Let us say we obtain the first peak in correlation for $T = T_1$.

- We average the structure at this value and obtain $\chi_2(\tau) = \left(\chi_1(\tau) + \zeta(T_1 + t_1 + \tau)\right)/2$.

- We proceed to find the peaks in correlation for $\chi_2(\tau)$ for $T > T_1$. Let us say we obtain a peak at $T = T_2$. Thus we obtain $\chi_3(\tau) = \left(2\chi_2(\tau) + \zeta(T_2 + t_1 + \tau)\right)/3$.

- Iterating over the process, we obtain for the kth iteration, $\chi_{k+1}(\tau) = \left((k)\chi_k(\tau) + \zeta(T_k + t_1 + \tau)\right)/k + 1$.

- We continue this process till no more peaks exist in correlation and we obtain the averaged structure.

Note: We have tweaked the process a bit as compared to what was described by Labbé *et al.* [63]. Before starting the iterative process, we treat the signal $\zeta(t)$ with a highpass moving average filter with a period $T_{filter} = t_2 - t_1$. This is done since we have low-frequency fluctuations and the correlation can be peaked because of large amplitude owing to these fluctuations.

II.B.1 Demonstration

Consider a signal S_N which is Gaussian white noise of both amplitude and standard deviation of unity. We generate a bursting signal S_B with the properties,

- The structure of the bursts is Gaussian.

- The standard deviation of the bursts is a random variable with uniform distribution with a mean value of σ_B. This is done to mimic the real scenario where for example the width in the peaks of temperature are distributed about some mean value.

- The location of the bursts is a random variable with uniform distribution.

We define the sum of the bursting signal and the noise as the noisy bursting signal S,

$$S = S_N + S_B$$

An example of this is shown in fig.II.25. We then choose a peak with the highest amplitude[12] and apply the method of coherent averaging.
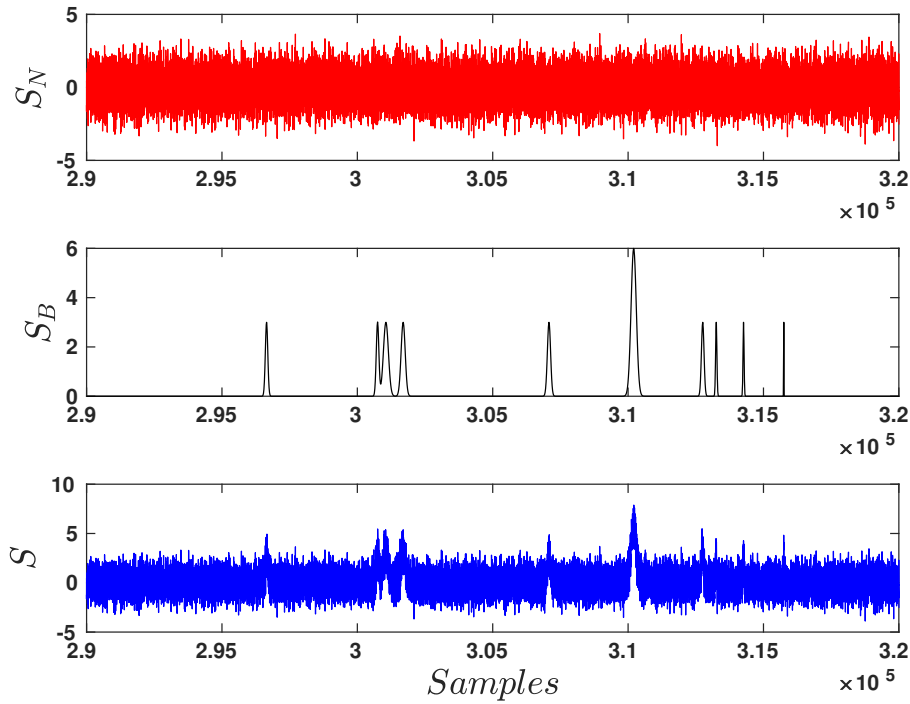
Fig. II.25   *An example of the Gaussian white noise S_N (red), signal with only bursts S_B (black) and the noisy bursting signal S (blue).*

---

[12]this improves the accuracy in finding peaks in the correlation when performing coherent averaging.

Fig.II.26 shows four bursts. The one in blue is the burst from the signal S that was chosen to initialize the process of coherent averaging. The one in magenta is the actual burst from S_B that corresponds to the chosen burst. The one in black is a Gaussian burst with the standard deviation being the mean value of σ_B. Finally, the one in red is the one obtained after coherent averaging. As this example demonstrates, the burst obtained from coherent averaging (red burst) closely resembles the mean behaviour of the bursts (black burst).
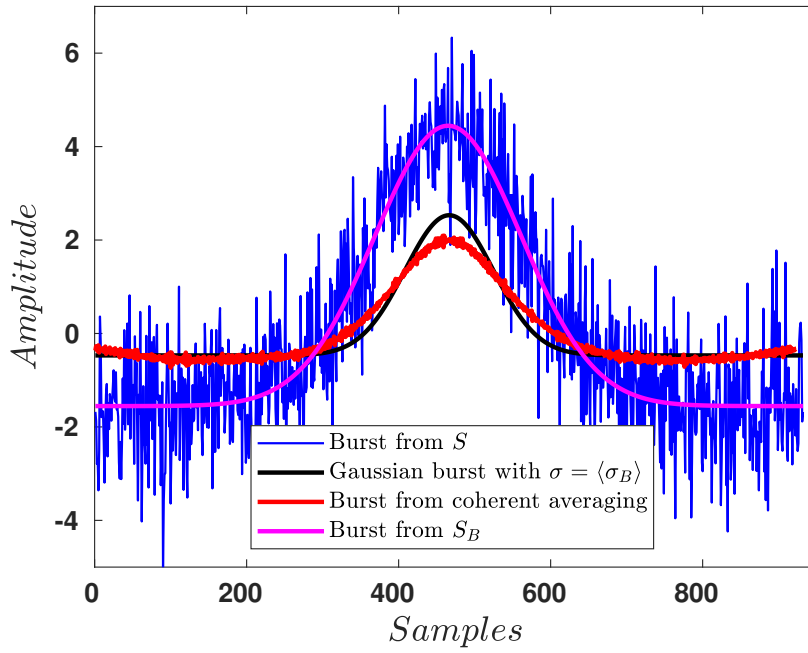
Fig. II.26   *Blue: The sample of the noisy bursting signal S with one burst that is chosen to initialize the process of coherent averaging. Black: A Gaussian burst with standard deviation of $\sigma = \sigma_B$. Red: The burst obtained after the method of coherent averaging. Magenta: The sample of the bursting signal S_B with one burst.*

Chapter III

Coherence of velocity fluctuations in turbulent flows

«Il faut que je combatte cette léthargie. Mon stylo pèse de plus en plus lourd.»

"I must fight this lethargy. My pen is getting heavier and heavier."[2]

Jeudi 11 septembre

The unpredictable nature of turbulent flows manifests on any flow related quantities, say, velocity, pressure or temperature to name a few. This inherent variability of turbulent flows calls for a probabilistic description of turbulence[3] which has remained the backbone of turbulence research to this day. This approach to turbulence amounts to studying different statistical properties of the flow, in the hope that their reproducibility and predictability[1] would enable us to formulate laws on the nature of turbulence.

An important example of exact result was obtained by Kolmogorov[2] [8] for the case of statistically homogeneous and isotropic turbulence in the limit of infinite Reynolds number which is often called the *Kolmogorv's four-fifths law*. The statement of the law, in the words of Frisch [3] is as follows,

"In the limit of infinite Reynolds number, the third order longitudinal structure function of homogeneous isotropic turbulence, evaluated for increments 'r' small compared to the integral length scale l_I, is given in terms of the mean energy dissipation rate per unit mass '$\langle \epsilon \rangle$' (assumed to remain finite and nonvanishing) by"

---

[1]As an example, the probability distribution function (PDF) of velocity fluctuations are reproducible across a range of experiments though the exact velocity field would vary from one experiment to another and even for different trials of the same experiment.

[2]Often called the *K41* theory named after the year in which Kolmogorov presented his celebrated work in a series of articles.

$$\langle (\delta u_{LL})^3 \rangle = -\frac{4}{5} \langle \epsilon \rangle r \tag{III.1}$$

where the subscript 'LL' stands for the longitudinal component of the turbulent velocity and the third order structure function is defined as,

$$\langle (\delta u_{LL})^3 \rangle = \langle (u_{LL}(\mathbf{x} + \mathbf{r}) - u_{LL}(\mathbf{x}))^3 \rangle$$

If the turbulent flow is assumed to be self-similar across scales we obtain the prediction for the scaling for the second order structure function,

$$\langle (\delta u_{LL})^2 \rangle \sim \langle \epsilon \rangle^{2/3} r^{2/3} \tag{III.2}$$

Eqn.(III.2) then implies that the energy spectrum at wavenumber 'k' is of the form,

$$E(k) \sim \langle \epsilon \rangle^{2/3} k^{-5/3} \tag{III.3}$$

where the energy spectrum in the case of isotropic turbulence is defined as,

$$E(k) = \int_0^\infty dr \; kr \Gamma_u^{ii}(r) \sin(kr)$$

and the two-point spatial correlation tensor of the velocity fluctuations $\overline{\overline{\Gamma}}_u$ is defined as,

$$\Gamma_u^{ij}(r) = \langle u_i(\mathbf{x}) u_j(\mathbf{x} + \mathbf{r}) \rangle$$

The behaviour of the third order structure function, second order structure function and the energy spectrum of the velocity fluctuations given by equations (III.1), (III.2) and (III.3) have been observed in a range of experiments and their validity has robust experimental evidence [6, 3, 9]. We note here that the second and third order structure functions and the Kolmogorov spectrum are functions of space and wavenumber and do not involve time. Historically, experiments measured these quantities in time and their spatial dependence was obtained via *Taylor's frozen hypothesis* [86].

For two point spatio-temporal characteristics of velocity fluctuations, there are only few known theoretical predictions and as a consequence, it has been overlooked numerically and experimentally. Leoni *et al.* [16] numerically studied the spatio-temporal spectra (spectra in both wavenumber and frequency) for homogeneous, isotropic turbulence and reported observing the *sweeping effect.* On the theoretical front Canet *et al.* [87] obtained the two-point velocity correlation function in wavenumber and time for homogeneous isotropic turbulence using techniques from field theory.

The sweeping effect deserves further elucidation and likely plays an important role on spatio-temporal statistics. Kolmogorov's K41 theory also obtains a prediction on the Lagrangian velocity energy spectrum, $E_{Lag}(f)$, in frequency [9] with,

$$E_{Lag}(f) \sim \langle \epsilon \rangle f^{-2}$$

in the inertial range. A naive assumption that the Lagrangian and Eulerian approach being similar would suggest the same scaling for the frequency energy spectrum for Eulerian velocity field, $E(f)$ (for example the velocity measured in homogeneous isotropic turbulence with no mean flow at a point using a point-measurement technique),

$$E(f) \sim \langle \epsilon \rangle f^{-2} \tag{III.4}$$

The controversy on the similarity of the Lagrangian and Eulerian approach was initiated by the experimental results by Favre *et al.* [88] and Comte-Bellot *et al.* [89] who reported discrepancy of a factor five between the Eulerian time microscale which was smaller than its Lagrangian counterpart. This discrepancy was analytically resolved by Tennekes [17, 90] by imploring *random sweeping hypothesis* and was shown to be a result of the advective sweeping of the inertial range eddies by the eddies containing the most energy (eddies with length scales close to the integral length scale). Tennekes' analysis predicted the Eulerian velocity frequency spectrum to be,

$$E(f) \sim \langle \epsilon \rangle^{2/3} u_{rms}^{2/3} \; f^{-5/3} \tag{III.5}$$

where scales containing the most energy are characterized by the total RMS of the velocity fluctuations u_{rms} which appears in the form of the energy spectrum $E(f)$. This was evidenced by the work of Nelkin *et al.* [91] and Sanada *et al.* [92]. The similarity in the scaling with wavenumber of $E(k)$ (eqn.(III.3)) and with frequency of $E(f)$ (eqn.(III.5)) comes from the interpretation that the inertial scales would be advected by the scales containing most energy implying the applicability of a slightly unconventional form Taylor's frozen hypothesis[3].

---

[3]Conventionally Taylor's frozen hypothesis means advection of all eddies due to and in the presence of a strong mean flow.

The aim of this experimental study and the results presented therein are twofold,

Q1A: What new insight on the nature of turbulence can we obtain by studying two-point statistics of velocity fluctuations in space and time?

Q1B: Can we observe the *sweeping effect* as hypothesized by Tennekes from two-point spatio-temporal statistics of velocity fluctuations?

As we mentioned earlier Q1A has been experimentally understudied whereas Q1B has been experimentally dealt with studying only one point statistics. To ensure the validity of our experimental observations,

- Experiments are performed on two different experimental setups with two different experimental techniques to ensure the robustness of the experimental results and its likely universality to turbulent flows.

- The chosen experimental techniques are such that one has higher resolution in space while the other has higher resolution in time. This ensures that our observations are not affected by the nature of the experimental technique.

The outline of this chapter is as follows,

Sec. III.1: Presents the theoretical background on the effect of sweeping and obtain the governing equations. We demonstrate the effect of sweeping as proposed by Tennekes for the energy spectrum of velocity fluctuations. We also study the behaviour of two point statistics, particularly the magnitude-squared coherence (for brevity we call it coherence) under the effect of sweeping.

Sec. III.2: Presents the first experiment for studying the coherence and the results obtained.

Sec. III.3: Presents a second novel experiment for studying coherence. A new technique is developed and presented for measuring turbulent flows using standard optical techniques.

Sec. III.4: Summarizes the results and the conclusions on the behaviour of coherence and how it is affected by the *sweeping effect*.

III.1 Theoretical background

The analysis presented in this section builds on the work by Tennekes [17] and Kraichnan *et al.* [90]. We explain the results obtained by the authors in the aforementioned articles in a simple manner by using their physical arguments. We then extend it to obtain results on the behaviour of coherence of velocity fluctuations under the effect of sweeping for homogeneous, isotropic turbulence.

We begin by considering a statistically homogeneous, isotropic and stationary turbulent flow of velocity $\mathbf{u}(\mathbf{x}, t)$ such that $\langle \mathbf{u} \rangle = 0$ (assumption of isotropy). For brevity, we denote the non-zero fluctuating velocity by $\mathbf{u}(\mathbf{x}, t)$. The fluctuating velocity field is such that $\sqrt{\langle u_i^2 \rangle} = u_{rms}$ for $i = 1, 2, 3$ (assumption of isotropy) with u_{rms} being independent of the spatial and temporal co-ordinates (assumption of homogeneity and stationarity). Additionally, we assume the turbulent flow to be incompressible. The governing equations for the hydrodynamic part of an incompressible flow are,

$$\frac{\partial u_i}{\partial x_i} = 0 \tag{III.6}$$

$$\frac{\partial u_i}{\partial t} + u_j \frac{\partial u_i}{\partial x_j} = -\frac{1}{\rho_0} \frac{\partial p}{\partial x_i} + \nu \frac{\partial^2 u_i}{\partial x_i^2} \tag{III.7}$$

where ρ_0 and ν are the density and the kinematic viscosity of the fluid at rest respectively. We decompose the flow into two parts, one due to the scales containing the most energy, i.e., close to the integral scales whose velocity and pressure are denoted by $\mathbf{u}_B$, p_B and the other due to the inertial scales whose velocity and pressure are denoted by $\mathbf{u}_I$, p_I. These two fields can also be thought of as band filtered fields after filtering about a wavenumber such that $k_B \ll k_{filter} \ll k_I$. Thus we have the decomposition,

$$\mathbf{u} = \mathbf{u}_B + \mathbf{u}_I$$
$$p = p_B + p_I$$

We also assume that $|\mathbf{u_B}| \sim u_{rms} \gg |\mathbf{u_I}|$ and $p_B \gg p_I$. For the asymptotic analysis that is to follow, this ensures that there is no back reaction of the inertial scales on the energy containing background scales and agrees with our physical understanding of energy being transferred from large to small scales. Substituting the decomposition in equations (III.6) and (III.7), we obtain for the zeroth order in perturbations in the flow of energy containing background scales,

<u>**O**(0)</u>

$$\frac{\partial u_{B,i}}{\partial x_i} = 0$$

$$\frac{\partial u_{B,i}}{\partial t} + u_{B,j}\frac{\partial u_{B,i}}{\partial x_j} = -\frac{1}{\rho_0}\frac{\partial p_B}{\partial x_i} + \nu\frac{\partial^2 u_{B,i}}{\partial x_i^2}$$

which are just the incompressible flow equations for the energy containing background scales. For the next order in the perturbations we obtain,

O(1)

$$\frac{\partial u_{I,i}}{\partial x_i} = 0$$

$$\frac{\partial u_{I,i}}{\partial t} + u_{B,j}\frac{\partial u_{I,i}}{\partial x_j} + u_{I,j}\frac{\partial u_{B,i}}{\partial x_j} = \nu\frac{\partial^2 u_{I,i}}{\partial x_i^2}$$

The term involving pressure is neglected since $p_I \sim \rho_0 u_I^2$. The relative order of magnitudes of the terms with respect to the term $\partial u_{I,i}/\partial t$ are,

$$\frac{u_{B,j}\partial u_{I,i}/\partial x_j}{\partial u_{I,i}/\partial t} \sim \frac{u_B}{\left(f_I/k_I\right)}$$

$$\frac{u_{I,j}\partial u_{B,i}/\partial x_j}{\partial u_{I,i}/\partial t} \sim \frac{u_B}{\left(f_I/k_I\right)}\left(\frac{k_B}{k_I}\right)$$

$$\frac{\nu\partial^2 u_{I,i}/\partial x_j^2}{\partial u_{I,i}/\partial t} \sim \left(\nu\frac{k_I^2}{f_I}\right) \sim \frac{1}{Re}$$

where f_B and f_I are the frequency scales associated with the energy containing background scales and the inertial scales respectively with $f_B \ll f_I$. The Reynolds number based on the inertial scales is defined as,

$$Re = \frac{f_I}{\nu k_I^2}$$

Since $k_B \ll k_I$, we obtain to the leading order (with $u_B \sim f_I/k_I$),

$$\boxed{\begin{array}{c} \nabla \cdot \mathbf{u}_I = 0 \\ \dfrac{\partial \mathbf{u}_I}{\partial t} + \mathbf{u}_B \cdot \nabla \mathbf{u}_I = \nu\nabla^2\mathbf{u}_I \end{array}} \tag{III.8}$$

The set of equations (III.8) essentially model the effect of the sweeping of the inertial scales ($\mathbf{u}_I$) by the scales containing the most energy which are close to the integral scales ($\mathbf{u}_B$).

We proceed to show that the physical arguments put forward by Tennekes [17] and Kraichnan [90] to obtain the energy spectrum of velocity fluctuations in the Eulerian framework accounting for the sweeping effect can be put in mathematical terms via equations (III.8).

III.1.1 The sweeping effect and the energy spectrum

We consider the case of Reynolds number tending to infinity whence the viscous effects will be negligible. In this case, the momentum equation of eqn.(III.8) becomes,

$$\frac{\partial \mathbf{u}_I}{\partial t} + \mathbf{u}_B \cdot \nabla \mathbf{u}_I = 0 \tag{III.9}$$

Since $k_B \ll k_I$, the background flow changes little over the distance $1/k_I$ and can essentially taken to be constant over the distances at which $\mathbf{u}_I$ varies. Similarly the background flow varies little over the timescale $1/f_I$ and can also be considered to be constant in time over which we study the evolution of the inertial scales. Thus, eqn.(III.9) becomes,

$$\frac{\partial \mathbf{u}_I(\mathbf{x}, t)}{\partial t} + \mathbf{u}_B \cdot \nabla \mathbf{u}_I(\mathbf{x}, t) = 0$$

On taking the Fourier transform in space and time, we obtain,

$$\iota\Big(\omega - \mathbf{u}_B \cdot \mathbf{k}_I\Big)\widetilde{\mathbf{u}}_I(\mathbf{k}_I, \omega) = 0 \tag{III.10}$$

where,

$$\widetilde{\mathbf{u}}_I(\mathbf{k}_I, \omega) = \int_{-\infty}^{\infty} d^3x \int_{-\infty}^{\infty} dt\ \mathbf{u}_I(\mathbf{x}, t) e^{\iota(\mathbf{k}_I \cdot \mathbf{x} - \omega t)}$$

We first observe from eqn.(III.10) that only the inertial scales whose wavevector is aligned with the velocity vector of the background flow will be affected by sweeping. Eqn.eqn.(III.10) also implies,

$$\omega = u_B k_I \tag{III.11}$$

There are two things to note here. First, $u_B = |\mathbf{u}_B|$ and thus is a non-negative quantity. Second u_B is a statistical quantity with a typical value of u_{rms} and would change over different realizations of the same flow. Since we are interested in the energy spectrum in

wavenumber and frequency, eqn.(III.11) implies that for a one realization of u_B, the energy spectrum in wavenumber and frequency will have the form,

$$E_{u_B}(k_I, \omega) = \delta\Big(\omega - u_B k_I\Big) E(k_I) \tag{III.12}$$

Thus the energy spectrum of the inertial scales in wavenumber and frequency would be the ensemble average of eqn.(III.12) over all realizations of u_B,

$$E(k_I, \omega) = \Big\langle \delta\Big(\omega - u_B k_I\Big) E(k_I) \Big\rangle_{u_B} = \int_0^\infty du_B \; \frac{1}{u_{rms}} P\left(\frac{u_B}{u_{rms}}\right) \delta\Big(\omega - u_B k_I\Big) E(k_I)$$

$$= \frac{1}{u_{rms} k_I} P\left(\frac{\omega}{u_{rms} k_I}\right) E(k_I) \tag{III.13}$$

where we have assumed that the energy containing scales and the inertial scales are statistically independent. The probability of obtaining a absolute value or speed of the background flow u_B is denoted by $\frac{1}{u_{rms}} P\left(\frac{u_B}{u_{rms}}\right)$. On substituting the form of Kolmogorov spectrum (eqn.(III.3)) in eqn.(III.13) and integrating in wavenumber we obtain the the frequency energy spectrum of the inertial scales in the Eulerian framework,

$$\boxed{E(f) \sim \langle \epsilon \rangle^{2/3} u_{rms}^{2/3} \; f^{-5/3}} \tag{III.14}$$

where we have assumed that the following integral converges,

$$\int_0^\infty dx \; P(x) x^{2/3}$$

It is important to note here the subtle difference between the sweeping effect due to a strong mean flow and the sweeping effect dueto the energy containing integral scales. In the presence of a strong mean flow (say $\mathbf{U}$), one obtains a similar expression with,

$$E(f) \sim \langle \epsilon \rangle^{2/3} U^{2/3} \; f^{-5/3}$$

which would hold true only for the wavevectors $\mathbf{k}_I$ aligned with the direction of the strong mean flow $\mathbf{U}$. This would be a result of the sweeping effect due to a unidirectional strong mean flow. Whereas, the eqn.(III.14) accounts for the sweeping effect due to the energy containing integral scales whose velocity would be randomly aligned in space. Thus, the expression (III.14) would be valid for all wavevectors belonging to the inertial scales. If one investigates the frequency energy spectrum of velocity fluctuations aligned with the strong mean flow[4], both the sweeping by the mean flow and the integral scales would result in the observation of $E(f) \propto f^{-5/3}$ for the inertial scales and it would not be possible to differentiate between the two effects.

---

[4]As is often done experimentally using Taylor's frozen hypothesis.

III.1.2 The sweeping effect and coherence

Consider eqn.(III.9) which models the sweeping of the inertial scales by the scales containing the most energy (which would be the scales close to the integral scale). Since $f_B \ll f_I$, $\mathbf{u}_B$ would essentially be stationary for timescales $1/f_I$ or smaller. Owing to $k_B \ll k_I$ we also treat $\mathbf{u}_B$ as being constant in space. For brevity, let us consider only the one dimensional case. We define the rectangular function $R_T(t)$ such that,

$$R_T(t) = \begin{cases} 0, & t \leq -T/2 \\ 1, & -T/2 < t < T/2 \\ 0, & t \geq T/2 \end{cases}$$

On multiplying $R_T(t)$ with eqn.(III.9) we obtain,

$$\frac{\partial \vartheta(x,t,T)}{\partial t} - u_I(x,t)\Big[\delta(t - T/2) + \delta(t + T/2)\Big] = -u_B \frac{\partial \vartheta(x,t,T)}{\partial x}$$

where $\vartheta(x,t,T) = u_I(x,t)R_T(t)$ and δ is the Dirac delta function. On taking the temporal Fourier transform of the equation, we obtain,

$$\iota\omega\widetilde{\vartheta}(x,\omega,T) - \Big[u_I(x,T/2)e^{-\iota\omega T/2} + u_I(x,-T/2)e^{\iota\omega T/2}\Big] = -u_B \frac{\partial \widetilde{\vartheta}(x,\omega,T)}{\partial x} \quad \text{(III.15)}$$

Similarly for a point x' located elsewhere in the turbulent flow, after taking the Fourier transform and its complex conjugate (denoted by superscripted asterix), we would have,

$$-\iota\omega\widetilde{\vartheta}^*(x',\omega,T) - \Big[u_I(x',T/2)e^{\iota\omega T/2} + u_I(x',-T/2)e^{-\iota\omega T/2}\Big] = -u_B \frac{\partial \widetilde{\vartheta}(x',\omega,T)}{\partial x'} \quad \text{(III.16)}$$

On multiplying eqn.(III.15) with eqn.(III.16), we obtain,

$$\omega^2\Big[\widetilde{\vartheta}(x,\omega,T)\widetilde{\vartheta}^*(x',\omega,T)\Big] = u_B^2 \frac{\partial^2\Big[\widetilde{\vartheta}(x,\omega,T)\widetilde{\vartheta}^*(x',\omega,T)\Big]}{\partial x \partial x'} + \{\text{cross terms}\}$$

where the cross terms would comprise of terms with order one or less in $\widetilde{\vartheta}$. Now if we average over T and take the limit of $T \to \infty$, we have,

$$\lim_{T\to\infty} \frac{1}{T}\, \omega^2\Big[\widetilde{\vartheta}(x,\omega,T)\widetilde{\vartheta}^*(x',\omega,T)\Big] = \lim_{T\to\infty} \frac{1}{T}\, u_B^2 \frac{\partial^2\Big[\widetilde{\vartheta}(x,\omega,T)\widetilde{\vartheta}^*(x',\omega,T)\Big]}{\partial x \partial x'}$$
$$+ \lim_{T\to\infty} \frac{1}{T}\{\text{cross terms}\} \quad \text{(III.17)}$$

If we assume the signal u_I and the Fourier transform $\widetilde{\vartheta}$ to be finite, the last term on the right hand side of eqn.(III.17) will go to zero. We obtain,

$$\omega^2 E_{u_B}(x, x', \omega) = u_B^2 \frac{\partial^2 E_{u_B}(x, x', \omega)}{\partial x \partial x'} \tag{III.18}$$

where,

$$E_{u_B}(x, x', \omega) = \lim_{T \to \infty} \frac{1}{T} \left[\widetilde{\vartheta}(x, \omega, T) \widetilde{\vartheta}^*(x', \omega, T) \right]$$

is the cross-spectrum of u_I in frequency and between two points in space located at x and x' for one realization of u_B.

We observe that the physically plausible solution to eqn.(III.19), would be of the form,

$$E_{u_B}(x, x', \omega) = A(\omega) \exp\left[\iota\omega \left(\frac{x' - x}{u_B} \right) \right] + B(\omega) \exp\left[-\iota\omega \left(\frac{x' - x}{u_B} \right) \right]$$

and $E_{u_B}(x, \omega) = E_{u_B}(x', \omega) = A(\omega) + B(\omega)$. Now, the coherence is defined as,

$$\mathcal{C}(r, \omega) = \left| \left\langle \frac{E_{u_B}(x, x', \omega)}{\sqrt{E_{u_B}(x, \omega)} \sqrt{E_{u_B}(x', \omega)}} \right\rangle_{u_B} \right|^2 = \left| \left\langle \exp\left[\iota\omega \left(\frac{x' - x}{u_B} \right) \right] \right\rangle_{u_B} \right|^2 \neq 1$$

where the ensemble averaging is evaluated over all the realizations of u_B. Note that the ensemble average is evaluated before taking the modulus. Thus, the coherence could have a value less than one. On evaluating the ensemble average over the realizations of u_B, we would have,

$$\mathcal{C}(r, \omega) = \left| \int_{-\infty}^{+\infty} du_B \ \frac{1}{u_{rms}} \Pi\left(\frac{u_B}{u_{rms}} \right) e^{\frac{\iota\omega r}{u_B}} \right|^2 = \left| \int_{-\infty}^{+\infty} du_B \ \frac{1}{u_{rms}} \Pi\left(\frac{u_B}{u_{rms}} \right) e^{\frac{\iota\omega r}{u_{rms}} \left(\frac{u_{rms}}{u_B} \right)} \right|^2$$

where the probability density function of the velocity fluctuations of the energy containing scales is given by $\frac{1}{u_{rms}} \Pi\left(\frac{u_B}{u_{rms}} \right)$ and the spatial distance between the two points x and x' is denoted by $x' - x = r$. We denote the quantity $k = \frac{\omega r}{u_{rms}}$ and change the variables to $v = \frac{u_{rms}}{u_B}$. This gives us,

$$\mathcal{C}(r, \omega) = \left| \int_{-\infty}^{+\infty} dv \ \frac{\Pi(1/v)}{v^2} e^{\iota k v} \right|^2 \tag{III.19}$$

Fig. III.1 *The magnitude of the Fourier transform from eqn.(III.19) evaluated numerically with $\Pi(u_B) = Ne^{-u_B^2/2u_{rms}^2}$. An exponential decay can be observed.*

which is just the absolute value of the Fourier transform of the quantity $\frac{\Pi(1/v)}{v^2}$. Let us consider that the PDF of velocity fluctuations is a Gaussian distribution,

$$\Pi(u_B) = Ne^{-u_B^2/2u_{rms}^2}$$

where N is a normalization constant. Then eqn.(III.19) reads,

$$\mathcal{C}(r,\omega) = N \left| \int_{-\infty}^{+\infty} dv \, \frac{1}{v^2} \exp\left[-\frac{1}{2v^2} \right] e^{\iota kv} \right|^2$$

Fig.III.1 shows the absolute value of the Fourier transform of the function $\frac{\Pi(1/v)}{v^2}$. An exponential decay in the variable k is observed implying,

$$\boxed{\mathcal{C}(r,\omega) = \exp\left[-\frac{crf}{u_{rms}} \right]} \tag{III.20}$$

where the constant $c \approx 1.5$. Eq.(III.20) shows that the coherence for the inertial scales decays exponentially both in frequency and separation length. We again note the subtle difference between the sweeping effect due to a strong mean flow and due to the energy containing integral scales. If we are given a strong unidirectional mean flow **U** and if we are measuring

the coherence between two points whose direction vector is aligned with the direction of $\mathbf{U}$, i.e., $\widehat{\mathbf{r}} = \widehat{\mathbf{U}}$ (overhat denotes the unit vector), we obtain,

$$\mathcal{C}(r,\omega) = \left| \int_{-\infty}^{+\infty} du \; \delta(u_B - U) e^{\frac{\iota \omega r}{u_B}} \right|^2 = 1$$

Thus the coherence due to sweeping by a stationary mean flow would be one. The behaviour of coherence given by eqn.(III.20) can be shown to remain unchanged even when $U \sim u_{rms}$. In this case, we would still have eqn.(III.19) with only the PDF of velocity fluctuations modified to,

$$\Pi(u_B) = N e^{-(u_B - U)^2 / 2u_{rms}^2}$$

Fig.III.2 shows the absolute value of the Fourier transform of the function $\frac{\Pi(1/v)}{v^2}$ with $\Pi(u_B) = N e^{-(u_B - U)^2/2u_{rms}^2}$ when $U = u_{rms}$. An exponential decay in observed implying that the eqn.(III.20) is still valid and coherence decays exponentially. Thus the quantity of coherence will be able to differentiate between the sweeping effect due to a mean flow and due to the energy containing integral scales. Any deviation of coherence from a value of one would be a result of the sweeping due to the energy containing integral scales.
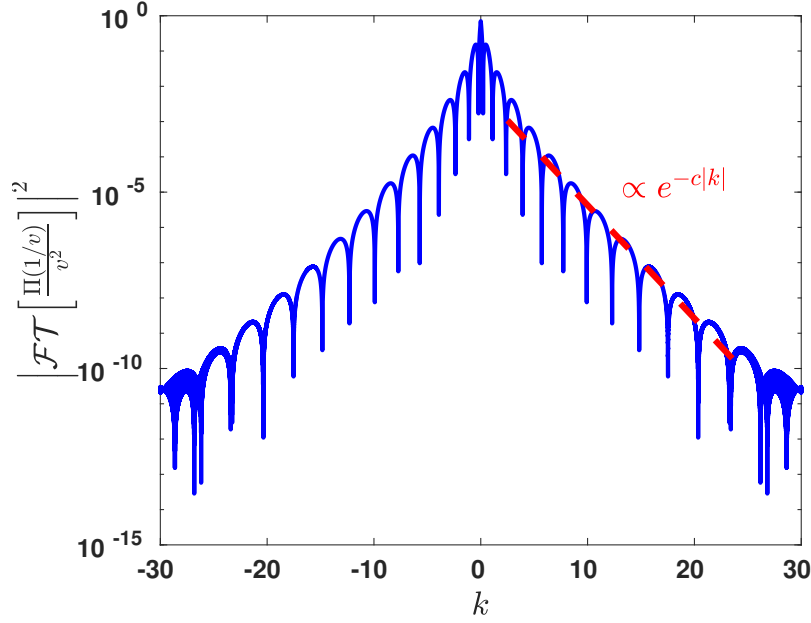

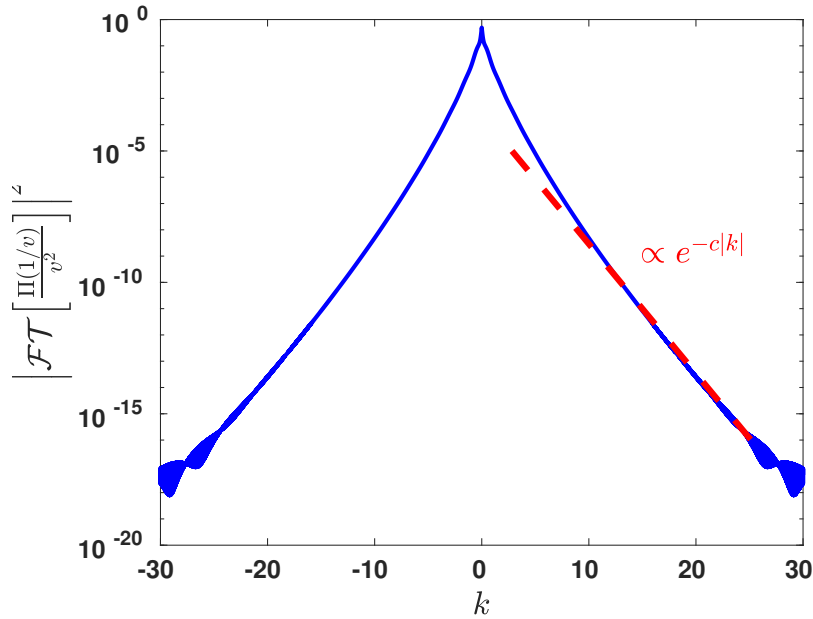
Fig. III.2   *The magnitude of the Fourier transform from eqn.(III.19) evaluated numerically with $\Pi(u_B) = N e^{-(u_B - U)^2/2u_{rms}^2}$ and $U = u_{rms}$. An exponential decay can be observed.*

We make two important remarks regarding the analytical work presented in this section and the functional form of coherence eqn.(III.20),

1. The governing equation for the sweeping effect eqn.(III.8) resembles the equation for the advection of a passive scalar by a turbulent flow. If our analytical results are true, they should also hold for the coherence of any passive scalar.

2. The quantity of coherence has not been studied for homogeneous isotropic turbulence. Though, in the community of wind-engineering, there has been focus on studying this quantity for its practical reasons on predicting the correlation of wind flows. One of the earliest was an experimental study in large open wind farms by Davenport *et al.* [93] where they studied the statistical properties of streamwise velocity fluctuations along the direction normal to the ground. Based on their experimental observations Davenport *et al.* suggested an empirical formula for the decay of coherence,

$$\mathcal{C}(r, f) = \exp\left[-\frac{crf}{U}\right]$$

where c is a constant, r is the distance between two points of measurement normal to the ground and U is the mean streamwise velocity. Further references can be found in the work by Marusic *et al.* [94, 95] and the articles cited therein. The empirical form suggested by Davenport *et al.* resembles the form that we just derived (eqn.(III.20)). Though we should not draw further comparisons as the flow that Davenport *et al.* studied was essentially that for a turbulent boundary layer whereas our analysis is for homogeneous isotropic turbulence.

In the light of these analytical results, we ask, does the behaviour of coherence derived analytically in eqn.(III.20) for velocity fluctuations hold against experimental observations for a turbulent flow? How does the spatial variation in the velocity of the energy containing scales affect the behaviour of coherence? To answer these questions, we develop two experiments to investigate the behaviour of coherence in a turbulent flow. When developing the experiments, we should choose flows such that they have the following property,

- Apart from checking the validity of eqn.(III.20), we also want to investigate how the spatial variation of the energy containing integral scales affects the coherence. Since the integral scales would vary spatially on a length scale which is the integral length scale, the spatial dimensions of our flow should be much larger than the associated integral length scale. This would enable us to measure the coherence at two points with separation length larger than the integral length scale.
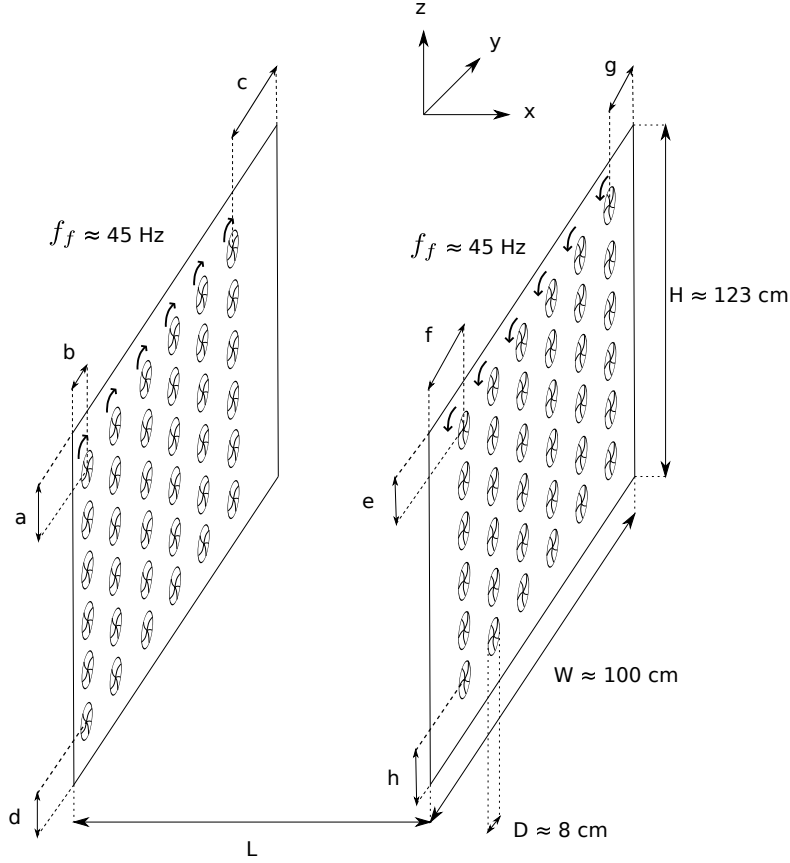
III.2 Experimental setup I

Fig. III.3   *Sketch of experimental setup along with dimensions.*

Fig.III.3 shows the sketch of the first experimental setup used for studying the coherence of velocity fluctuations in three dimensional turbulence. The experimental setup has been placed in air which is the working fluid for this setup. The experiment consists of two *plexiglass* plates of dimensions 100 cm (W) × 123 cm (H) fixed vertically using aluminium supports. The other dimensions that are denoted in the figure are; $a \approx$ 28cm, $b \approx 9$ cm, $c \approx 16$ cm, $d \approx 18$ cm, $e \approx 20$ cm, $f \approx 17$ cm, $g \approx 8$ cm and $h \approx 26$ cm. The distance between the two plates is denoted by 'L' and is our experimental control parameter which is varied to obtain different flow configurations. For the current setup, we have performed experiments for five values of the control parameter $L = 23$, 44, 55, 62 and 80 cm.

Each of the plates is fitted with 36 AC ball and sleeve bearing axial fans (*ebm-papst 8550 VW*). They have five helical blades and a radius of $R_{fan} = 4$ cm (fig.III.4). The circular housing for the motor at the center is of radius 2.5 cm. Each of the fans has a power rating of 12 W and they are connected to the main power supply in parallel configuration. They have asynchronous motors with a rotation rate of approximately $\Omega = 46$ Hz for AC power supply at 50 Hz. All the fans on the same plate rotate in the same direction, whereas, the fans on the two plates are in counter-rotation. Additionally, the fans on the two plates are geometrically staggered. Thus we obtain a staggered configuration of counter-rotating fans
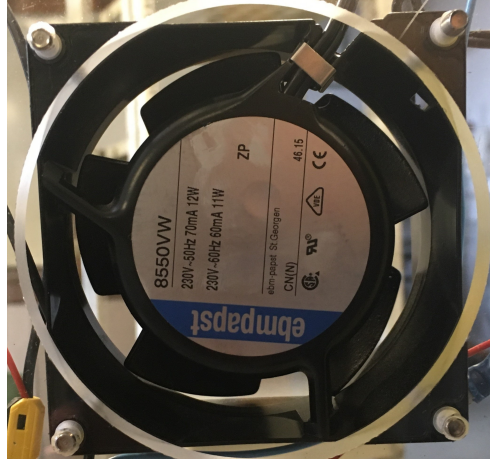
Fig. III.4   *Image of a fan used in the experiments.*

which can be imagined to create a Roberts-like flow [96] in the volume between the plates. A sketch of the Roberts flow is shown in fig.III.5. The 3D flow comprises of periodic array of counter-rotating vortices (whose axial velocities are denoted by the positive and negative symbols) and is invariant along the axial direction (x-axis). This is not entirely the case in our experiment since our flow is not invariant along the axial direction and the alternating vortical flow is imposed only at the boundaries and not in the bulk.
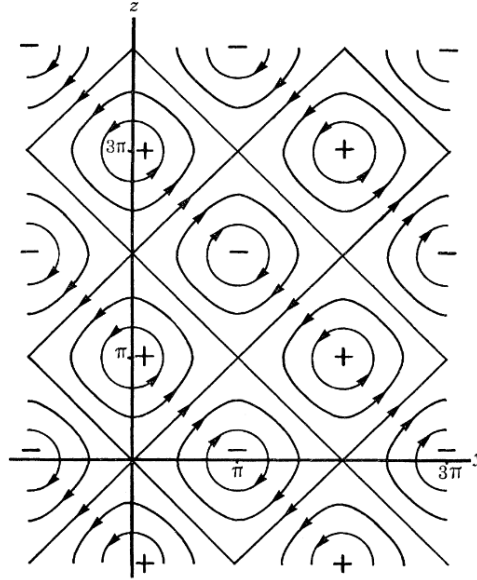
Fig. III.5   *Sketch of Roberts flow taken from the article by Roberts [96].   The positive and negative signs denote the direction of the axial flow.*

In our experiment, there is a mean inflow of air in the volume between the plates and as a result, a mean outward flow exists at the open faces. Nonetheless, a stagnation point with vanishing mean flow would be expected at the center of the experimental volume.

The velocity fluctuations in the flow are measured with *Constant Temperature Anemometry* (CTA) technique using two 1D hot-wire probes *DANTEC 55P16*. The velocity probes are connected to *DANTEC StreamWare Pro* system which performs the CTA measurement, the output of which is connected to *National Instruments* DAQ card. For spatial measurements, one of the velocity probes has been attached to *DANTEC* 2D traverse system for translation. The traverse system has the capability of moving the probe in the x-z plane with a minimum increment of 6.25 µm. This arrangement enables us to precisely obtain the spatial dependence of velocity as well as its two-point spatio-temporal statistics for a stationary flow.

One of the velocity probes is fixed at the center of the experimental volume close to the stagnation point of the flow. When measuring velocity signals at two points, the orientation of the filaments of the hot-wire probes is kept perpendicular to the direction vector joining the location of the two probes and whose magnitude is denoted by 'r'. This arrangement is shown in fig.III.6. In the experimental results presented henceforth, the second probe is moved vertically with the filaments of the hot-wire probes oriented horizontally. The probe can also be moved horizontally with both the probes being oriented vertically. It was experimentally verified that the results between these two cases remain unchanged.
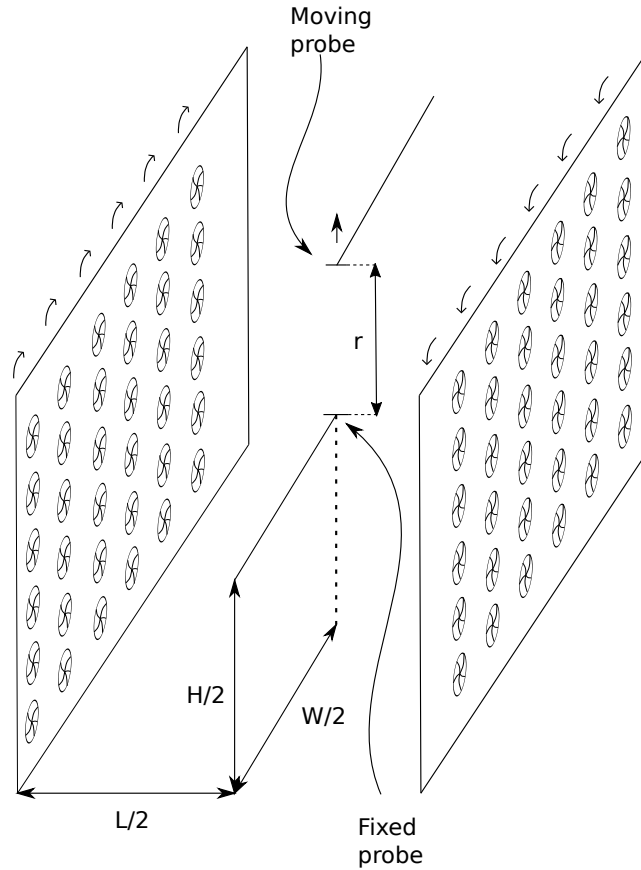

Fig. III.6   *Sketch of the location of the hot-wire probes and the orientation of their filaments when measuring velocities at two points in the flow simultaneously.*

Since we are using 1D hot-wire probes and which are placed in the part of the turbulent flow with weak to vanishing (for the fixed hot-wire probe) mean flow, it becomes important to note that we are measuring speed and information on the directionality of velocity is inaccessible. We will continue calling it velocity for the usage of notation but it must be kept in mind that it is indeed speed. The reason for choosing this flow is that we expect the integral length scale to be the same order of magnitude as the dimensions associated with the fan which is of $O(1)$ cm. Whereas, the size of the experiment is of $O(1)$ m. This large scale separation between the expected integral length scale and the experimental size would enable us to explore the behaviour of coherence for separation lengths between the two points of measurement larger than the integral length scale.

III.2.1 Characterization of the flow

We start with the characterization of the velocity field and define the Reynolds number for the experiment as,

$$Re = \frac{R_{fan}\Omega L}{\nu}$$

where the frequency of rotation of the fans is constant for the experiment with $\Omega \approx 46$ Hz and ν is the kinematic viscosity of air. For the experimental setup under consideration, we obtain the order of magnitude of the Reynolds number $Re \sim O(10^4)$.

Fig.III.7 shows the time series of the velocity fluctuations (after the removal of the temporal mean) obtained at the center of the experimental volume for $L = 44$ cm. We observe strong asymmetry in the positive and negative fluctuations of the velocity. This is indicative of the absence of a mean flow owing to the probe being located in the vicinity of the stagnation point. For determining the RMS (root mean square) of the velocity fluctuations, its value evaluated after the removal of temporal mean would be an underestimation of the actual value of the RMS of velocity fluctuations. Thus, a more accurate estimate of RMS of velocity fluctuations would be given by $u'_{rms} \sim \sqrt{\langle u^2 \rangle}$ where the velocity without the removal of its mean is denoted by u. For $L = 44$cm, we obtain $u'_{rms} \approx 0.24$ m/s. The accuracy of this estimate on the RMS of velocity fluctuations was double checked and was in agreement with the process described in appendix II.A.

Fig.III.8a shows the energy spectrum of the velocity fluctuations for $L = 44$ cm. We observe that for low frequencies the energy spectrum follows a power-law with $E_u(f) \propto f^{-0.6\pm0.02}$. This can also be seen from fig.III.8b where we observe that the quantity $f^{0.6}E_u(f)$ is roughly flat for low frequencies. The inertial range scaling of the energy spectrum of velocity fluctuations corresponding to Kolmogorov spectrum with $E_u(f) \propto f^{-5/3}$ is also observed for higher frequencies. The two power law regions corresponding to $E_u(f) \propto f^{-0.6}$ and $E_u(f) \propto f^{-5/3}$, however, do not juxtapose. Since the point of measurement has a vanishing mean flow, Taylor's hypothesis would not applicable. Also, as noted by Tennekes [17], the Kolmogorov spectrum is expected in frequency even in the absence of a mean flow (eqn.(III.5)) but we recall that in the absence of a mean flow, we measure speed using the 1D hot-wire probe and not velocity. It is possible that this modifies the behaviour of the energy spectrum resulting in the absence of a clear inertial range with Kolmogorov scaling of the energy spectrum.
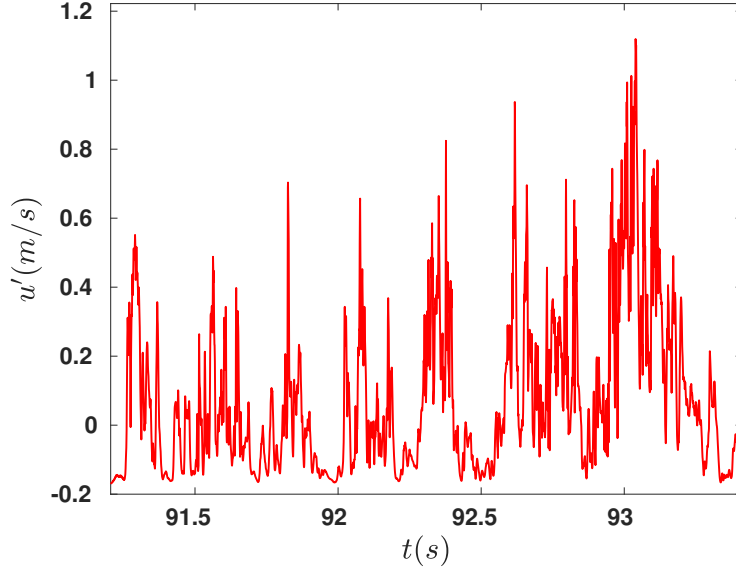
Fig. III.7   *Time series of velocity signal as obtained from the 1D hot-wire probe located at the center of the experimental volume close to the stagnation point for $L = 44$ cm. The temporal mean has been removed from the signal.*

The low-frequency power-law behaviour of the energy spectrum likely arises from vorticity filaments being swept through the probe[5]. We can define cross-over frequency 'f_{cross}' as the frequency at which the energy spectrum deviates from being $E_u \propto f^{-0.6}$. The cross-over frequency f_{cross} is evaluated by finding the frequency below which we obtain a fit of $E_u \propto f^{-0.6}$ with the least error. For the case of $L = 44$ cm whose velocity energy spectrum is shown in fig.III.8a, we obtain the cross-over frequency of $f_{cross} \approx 13$ Hz.

Next, we can proceed to characterize the flow using two point statistics of velocity fluctuations. Specifically, we can obtain the integral length scale of the turbulent flow from two-point correlation of velocity fluctuations. First, we note that owing to the filament of the hot-wire probes being perpendicular to the direction vector between their positions, what we measure from the hot-wire probes is the quantity,

$$u' = \sqrt{u_{LL}^2 + u_{NN}^2} - \left\langle \sqrt{u_{LL}^2 + u_{NN}^2} \right\rangle \tag{III.21}$$

---

[5]The low frequency behaviour of the energy spectrum of velocity fluctuations with $E_u(f) \propto f^{-0.6}$ was also observed for the von Kármán swirling flow. Refer to chapter II, figures II.6a, II.21 and the explanation provided therein.

(a)

(b)
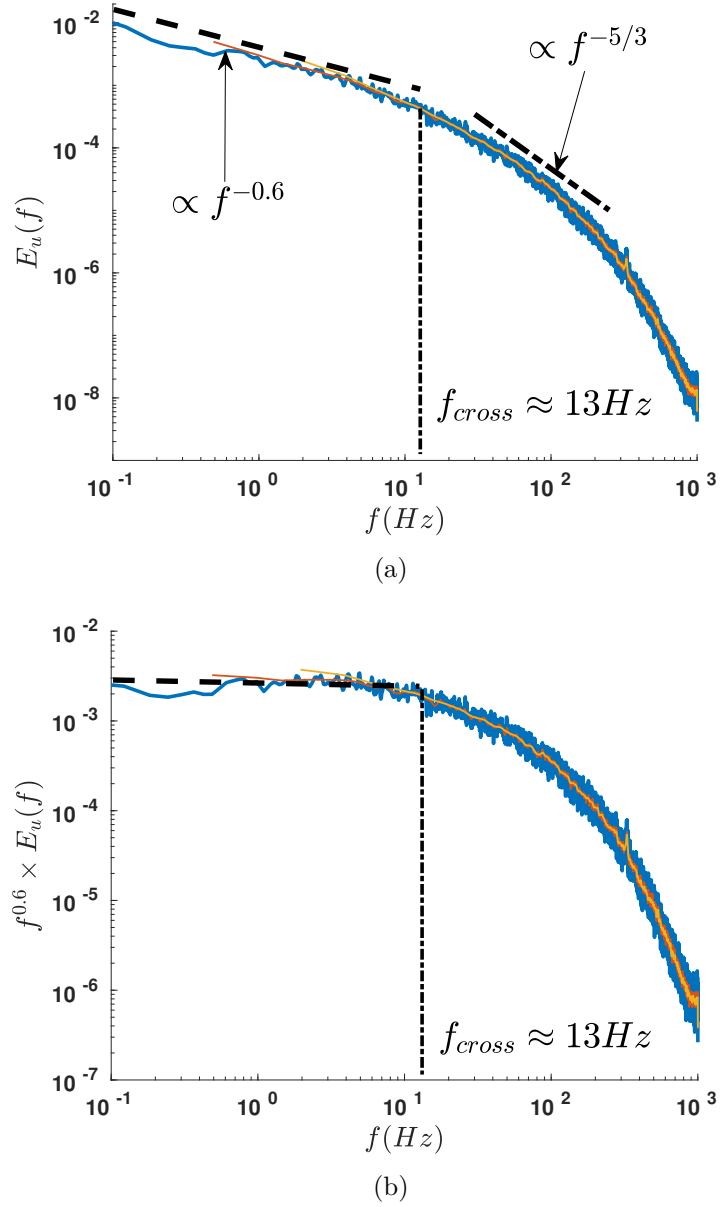
Fig. III.8 *(a) Energy spectrum of velocity signal as obtained from 1D hot-wire probe at the centre of the experimental volume for $L = 44$ cm. Dashed line: corresponds to $E_u \propto f^{-0.6}$. Dash-dotted line: corresponds to $E_u \propto f^{-5/3}$. (b) Energy spectrum of velocity signal from (a) normalized by $f^{-0.6}$. The cross-over frequency is denoted by f_{cross}. The different coloured curves correspond to different windowing lengths for evaluating the averaged spectrum.*

where the subscripts 'LL' and 'NN' correspond to the longitudinal and normal directions with respect to the direction vector as shown in the sketch III.9. We define the two-point velocity correlation as,

$$\Gamma_u(r) = \frac{\left\langle u'(z=0)u'(z=r)\right\rangle}{\sqrt{\left\langle u'(z=0)^2\right\rangle\left\langle u'(z=r)^2\right\rangle}}$$

and which, by definition, is unity for zero separation length $r = 0$. Fig.III.10 shows the two-point velocity correlation for $L = 44$ cm. An exponential decay is observed and from the corresponding exponential fit, we obtain the characteristic length scale of the decay or the integral length scale, which, in this case is $l_I \approx 2.11$ cm. We also note that velocity fluctuations are correlated for separation lengths much larger than the integral length scale as seen from fig.III.10.

Fig. III.9   *Sketch showing the longitudinal and the normal component of the velocity relative to the distance vector denoted by '$\mathbf{r}$' separating the two points of measurement in the flow.*
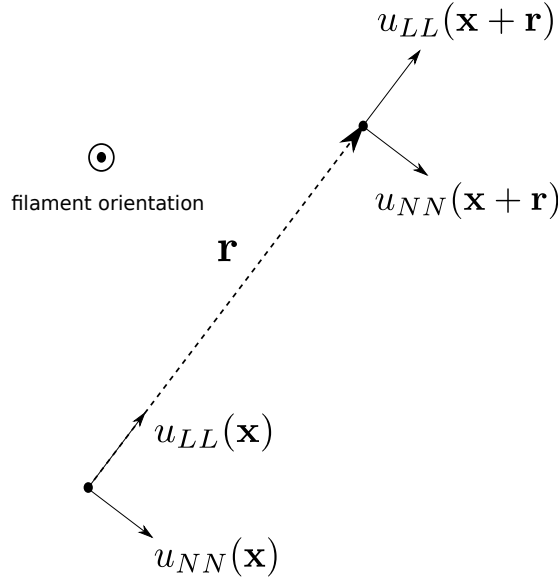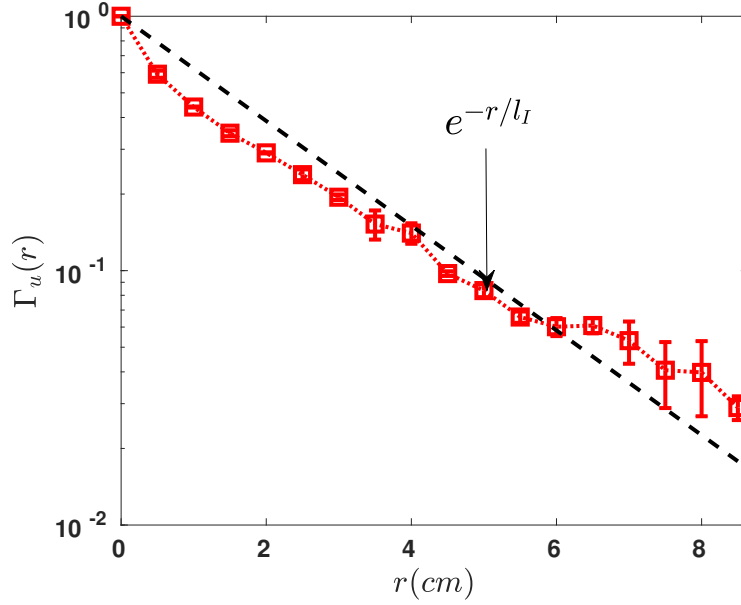
Fig. III.10 *Two-point correlation of velocity fluctuations,$\Gamma_u(r)$ for $L = 44$cm. The integral length scale is given by the characteristic length of the exponential decay and is $l_I \approx 2.11$cm.*

We can also evaluate the integral frequency defined as $f_I = u'_{rms}/l_I$ which for the case of $L = 44$ cm is $f_I \approx 11$ Hz and is roughly the same as the cross-over frequency f_{cross} evaluated earlier. To summarize, the values of the RMS of velocity fluctuations, the integral length scale, the integral frequency and cross-over frequency are given in tab.III.1 for different values of the distance between the walls, L (which is our control parameter). From the information experimentally obtained till this point, we also get the estimates on the order of magnitudes of the mean energy dissipation rate per unit mass $\langle \epsilon \rangle$, the Taylor microscale λ, the Kolmogorov microscale η and Taylor microscale based Reynolds number Re_λ,

$$\langle \epsilon \rangle \sim (u'_{rms})^3/l_I \sim O(1)\ m^2/s^3$$

$$\lambda = \left(15\nu \frac{u_{rms}^2}{\langle \epsilon \rangle} \right)^{1/2} \sim O(1)\ \text{mm}$$

$$\eta = \left(\nu^3/\langle \epsilon \rangle \right)^{1/4} \sim O(10^2)\ \text{µm}$$

$$Re_\lambda = \frac{u'_{rms}\lambda}{\nu} \sim O(10^2)$$

The integral length scales in our experiment are more than an order of magnitude smaller than the size of the experiment which is about $W \sim H \sim O(1)$ m. This reaffirms the choice of our flow and we should be able to investigate the behaviour of magnitude-squared coherence for separation lengths larger than the integral length scale.

	$L(cm)$				
	23	44	55	62	80
$u'_{rms}(m/s)$	0.46	0.23	0.15	0.16	0.16
$l_I(cm)$	1.42	2.11	2.19	3.73	3.62
$f_I(Hz)$	32.4	11.1	6.9	4.3	4.4
$f_{cross}(Hz)$	24.6	13.9	5.5	4.8	5.5

Table III.1: Values of the RMS of velocity fluctuations (u'_{rms}), the integral scales (l_I, f_I) and the cross-over frequency (f_{cross}) for different values of the distance between the walls, L.

III.3 Experimental results of setup I

The coherence for the velocity fluctuations is defined as,

$$
\mathcal{C}(r, f) = \frac{\left\| \int_{-\infty}^{\infty} \left\langle u'(0,t)u'(r,t+\tau) \right\rangle e^{-if\tau} d\tau \right\|^2}{\left[\int_{-\infty}^{\infty} \left\langle u'(0,t)u'(0,t+\tau) \right\rangle e^{-if\tau} d\tau \right] \left[\int_{-\infty}^{\infty} \left\langle u'(r,t)u'(r,t+\tau) \right\rangle e^{-if\tau} d\tau \right]}
$$

We recall that when we say velocity, we mean the norm of the longitudinal and the normal component of the velocity as defined by eqn.(III.21). The averaging in the above definition of coherence is performed over time t.

Fig.III.11 shows the coherence of velocity fluctuations for two different separation lengths (r) for the case of $L = 44$ cm. The following observations can be made,

1. The coherence decays exponentially for all separation lengths r for frequencies larger than the integral frequency, i.e., $f > f_I$. The coherence deviates from an exponential decay for frequencies smaller than the integral frequency f_I.

2. The frequency scale associated with the exponential decay which we denote by f_c depends on the separation length and decreases with increasing separation length. This is seen by the exponential decay of coherence becoming sharper with increasing separation length.

3. The value of coherence at zero frequency which we denote by C_0 is a function of the separation length and decreases with increasing separation length.

These three observations suggest that the coherence for the inertial scales can be written in the following functional form,

$$
\boxed{\mathcal{C}(r, f) = \mathcal{C}_0(r)e^{-f/f_c(r)}}
\tag{III.22}
$$

where $\mathcal{C}_0$ is the value of coherence at zero frequency and f_c is the frequency scale associated with the exponential decay and thus has the units of hertz. Both $\mathcal{C}_0$ and f_c are decaying functions of the separation length r. We proceed to investigate the behaviour of the two functions $\mathcal{C}_0$ and f_c.

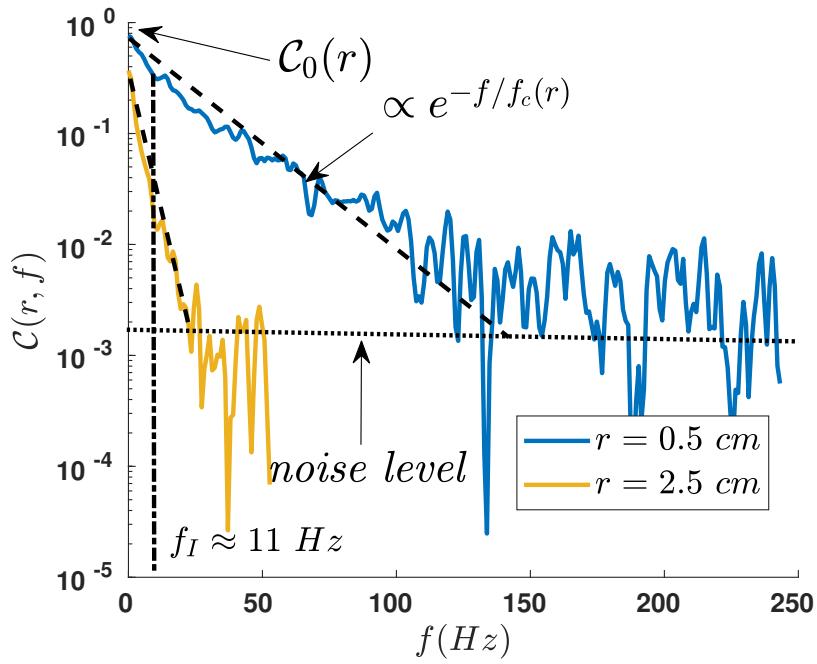Fig. III.11   *Coherence of velocity fluctuations for two different separation length between the points of measurement; $r = 0.5$ mm (blue) and $r = 2.5$ mm (yellow). The coherence at $f = 0$ is denoted by $\mathcal{C}_0$. Dashed line: corresponds to an exponential decay of coherence with a frequency scale denoted by f_c. The distance between the walls is $L = 44$ cm and the integral frequency is denoted by f_I.*

Fig.III.12 shows the dependence of value of coherence at zero frequency, $\mathcal{C}_0$, on the separation length, r, when the distance between the walls is $L = 44$ cm. As we observe, it decays exponentially with increasing separation length. The velocity fluctuations are also observed to be coherent at zero frequency and for separation lengths larger than the integral length scale as is evident from a non-zero value of $\mathcal{C}_0$ for $r > l_I \approx 2.1$ cm. Thus we infer that the functional form of the coherence at zero frequency would be,

$$\boxed{\mathcal{C}_0(r) = e^{-r/r^\dagger}} \tag{III.23}$$

where '$r^\dagger$' is the length scale associated with the decay of coherence at zero frequency.
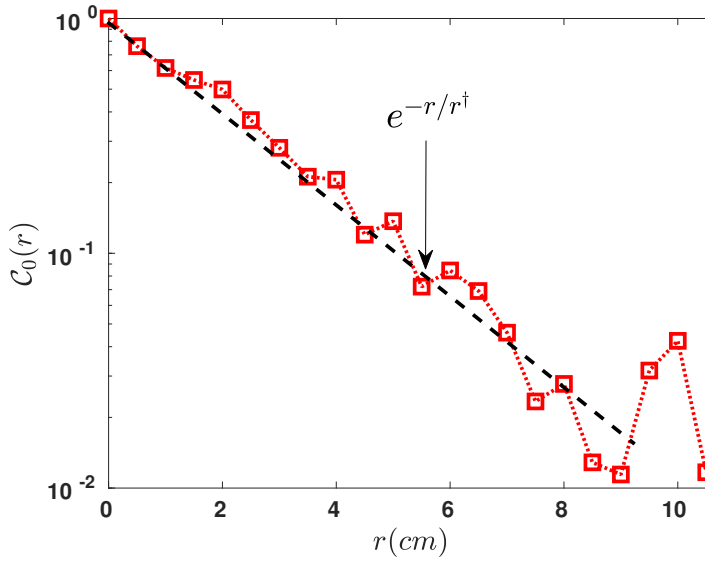
Fig. III.12 *The decay of the coherence at zero frequency ($\mathcal{C}_0$) with increasing separation length between the two points of measurement (r). Dashed line: corresponds to exponential decay with the length scale associated with the exponential decay being $r^\dagger \approx 2.26$ cm.*

Similarly, fig.III.13 shows the dependence of the frequency scale associated with the decay of coherence, f_c, on the separation length, r, when the distance between the walls is $L = 44$ cm. It displays a power-law decay with,

$$f_c(r) \propto r^{-1 \pm 0.1}$$

This allows us to infer the functional form of the frequency associated with the decay of coherence with,

$$\boxed{f_c(r) = u^\dagger/r} \tag{III.24}$$

where '$u^{\dagger}$' is the velocity scale associated with the decay of f_c.
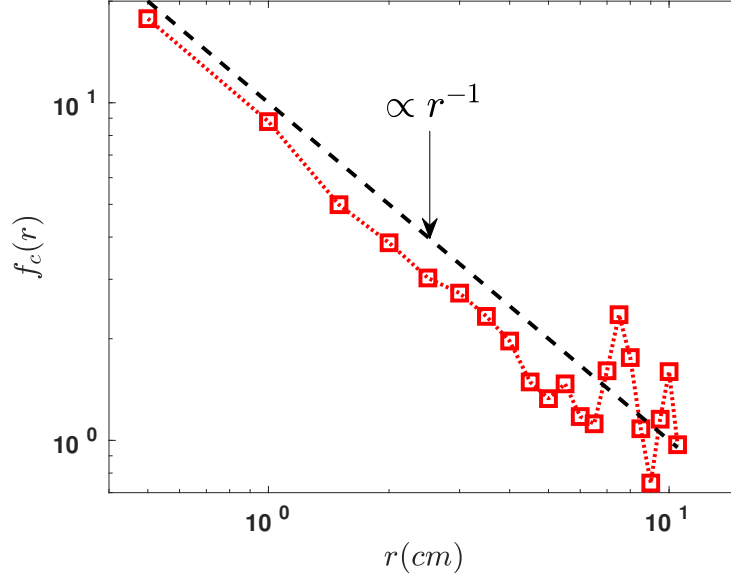
Fig. III.13   *The frequency scale f_c of the exponential decay of coherence versus the separation length between the two points of measurement (r). Dashed line: corresponds to $\propto r^{-1}$.*

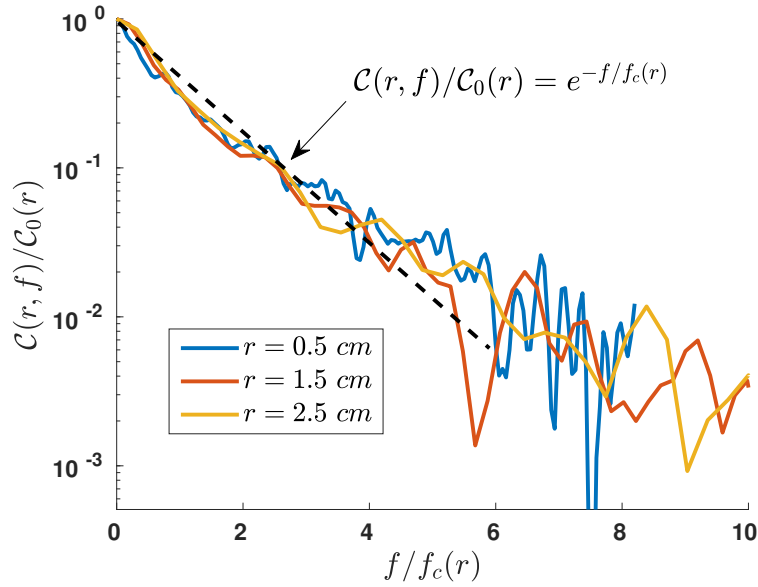
Fig. III.14   *Coherence normalized by its value at zero frequency, $\mathcal{C}/\mathcal{C}_0$, versus the frequency normalized by the frequency scale of decay f/f_c. Dashed line: corresponds to $\mathcal{C}/\mathcal{C}_0 = e^{-f/f_c}$.*

Fig.III.14 shows the coherence normalized by its value at zero frequency, $\mathcal{C}/\mathcal{C}_0$, versus the frequency normalized by the frequency scale of decay f/f_c. Indeed the plots coincide for all separation lengths between the two points of measurement. In summary, equations (III.22), (III.23) and (III.24) suggest that the coherence of velocity fluctuations of the inertial scales is of the form,

$$\mathcal{C}(r, f) = \exp\left[-\left(\frac{r}{r^\dagger} + \frac{rf}{u^\dagger} \right) \right]$$

which can be rearranged in the form,

$$\mathcal{C}(r, f) = \exp\left[-\left(\frac{r}{r^\dagger} \right)\left(1 + \frac{f}{f^\dagger} \right) \right] \tag{III.25}$$

where $f^\dagger = u^\dagger/r^\dagger$. The length and frequency scales of the decay of coherence $(r^\dagger, f^\dagger)$ would be characteristic of the turbulent flow. The next natural question that arises is,

Q3: How are the length scale $(r^\dagger)$ and the frequency scale $(f^\dagger)$ of the decay of coherence related to the length and frequency scales associated with the turbulent flow?

To obtain an estimate on the values of the length and frequency scales associated with the decay of coherence, figures III.15a and III.15b show the length scale $r^\dagger$ normalized by the integral length scale l_I and the frequency scale $f^\dagger$ normalized by the integral frequency f_I (as well as the cross-over frequency f_{cross}) respectively as the distance between the walls, L, is varied. We observe that the value of characteristic length scale $r^\dagger$ remains roughly the same as that of the integral length scale l_I. As for the frequency scale $f^\dagger$, we observe that its order of magnitude is comparable to the integral frequency f_I and the cross-over frequency f_{cross}, differing by a constant factor [6]. This suggests that the coherence for the inertial scales has the form,

$$\boxed{\mathcal{C}(r, f) = \exp\left[-\left(\frac{r}{l_I} \right)\left(1 + \frac{cf}{f_{cross}} \right) \right] = \exp\left[-\left(\frac{r}{l_I} \right)\left(1 + \frac{cf}{f_I} \right) \right]} \tag{III.26}$$

where for the current experiment, the mean value of the constant factor $c \approx 2.5$.

---

[6]For the flow generated by two walls of staggered counter-rotating fans, the integral frequency f_I and the cross-over frequency f_{cross} are found to be roughly equal. Thus the cross-over frequency is a good estimate of the integral frequency. The former can be obtained from one point measurement whereas the latter requires the integral length scale and thus is obtained from two-point measurement.
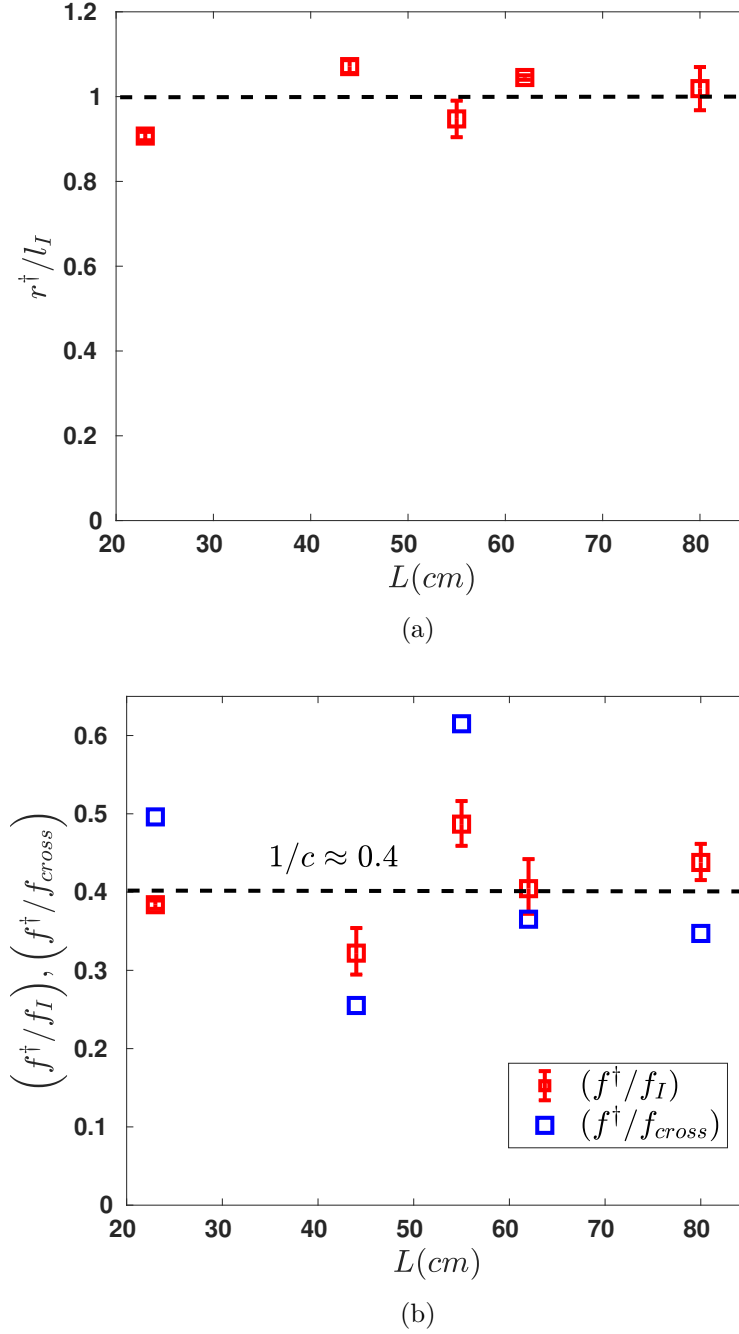
(a)

(b)

Fig. III.15   (a) Values of $r^\dagger$ normalized by the integral scale l_I. Dashed line corresponds to a value of unity. (b) Values of $f^\dagger$ normalized by the integral frequency $f_I = u'_{rms}/l_I$ (red) and by the cross-over frequency f_{cross} (blue). Dashed line corresponds to a value of $1/c \approx 0.4$.

There are numerous implications of the form described by eqn.(III.26) for the coherence of velocity fluctuations,

- The exponential decay in coherence is observed for the inertial scales, i.e. for frequencies greater than the integral frequency $f > f_I$.

- The characteristic scales of length and frequency associated with the decay of coherence of velocity fluctuations belonging to the inertial scales in turbulence are those of the scales containing most energy, i.e., integral scales. This strongly resembles the form derived analytically in eqn.(III.20) and shows that indeed the sweeping effect is observed when studying coherence. This needs further emphasis since the form obtained experimentally has an additional term with only spatial decay (e^{-r/l_I}). Eq.(III.26) when written in terms of the integral length scale and the RMS of the velocity fluctuations has the form,

$$\mathcal{C}(r,f) = \exp\left[\underbrace{-\left(\frac{r}{l_I}\right)}_{\text{integral scales}} \underbrace{-\left(\frac{crf}{u'_{rms}}\right)}_{\text{inertial scales}} \right]$$

In the theoretical analysis given at the beginning of this chapter where we modeled the coherence for the inertial scales due to the sweeping effect, the spatial dependence of the velocity fluctuations at the integral scales was neglected. This would be the case only when $r \ll l_I$ in which case we obtain the form of coherence that was derived analytically. The part of the decay from $\mathcal{C}_0 = \exp\left[-\left(\frac{r}{l_I}\right)\right]$ would likely come from the spatial dependence of the integral scales whose correlation would decay exponentially in space. If we consider only the sweeping of the inertial scales, it would be characterized by,

$$\frac{\mathcal{C}(r,f)}{\mathcal{C}_0(r)} = \exp\left[-\left(\frac{crf}{u'_{rms}}\right)\right]$$

- For frequencies smaller than the integral frequency $f < f_I$, we observe that the coherence deviates from decaying exponentially. This behaviour is not predicted by our analytical model. So, where does the low frequency behaviour of coherence come from? As we observed in the energy spectrum of velocity fluctuations in fig.III.8a, the low frequency behaviour with $E(f) \propto f^{-0.6}$ possibly comes from the vorticity filaments. This suggests that the behaviour of the coherence for frequencies smaller than the integral frequency $f < f_I$ likely arises from the sweeping of the vorticity filaments by the energy containing integral scales.

The experimentally obtained values of integral scales and those associated with the decay of coherence are given in table III.2.

	$L(cm)$				
	23	44	55	62	80
$u'_{rms}(m/s)$	0.46	0.23	0.15	0.16	0.16
$l_I(cm)$	1.42	2.11	2.19	3.73	3.62
$f_I(Hz)$	32.4	11.1	6.9	4.3	4.4
$f_{cross}(Hz)$	22.2	12.7	8	3.3	5.3
$r^\dagger(cm)$	1.29	2.26	2.07	3.9	3.68
$f^\dagger(Hz)$	11.2	3.8	3.2	1.8	1.9

Table III.2: Values of the u'_{rms}, the integral scales (l_I, f_I), the cross-over frequency (f_{cross}) and the scales corresponding to the decay of coherence $(r^\dagger, f^\dagger)$ for different values of flow configuration as the distance between the walls is changed (L).

III.4 Experimental setup II

The sketch of the second experimental setup is shown in fig.III.16. Turbulent flow is generated in a cubical volume of size 15 cm × 15 cm × 15 cm. The flow is forced using eight helices, four each of left and right chirality. The helices are attached to four axes, each having two helices of opposite chirality, and oriented along y-axis. Two adjacent axes are separated by a distance of 5 cm. Each of the axes is connected to a motor which rotates the helices in clockwise direction thus driving a flow in the cubical volume. For measurement of velocity, we use the technique of Particle Image Velocimetry (PIV) and seed the flow with reflective particles. A laser sheet in the x-y mid-plane is generated using an optical setup, the light of which is reflected by the particles seeded in the flow. The motion of the seeded particles is tracked using a high-speed camera oriented perpendicular to the laser sheet. Using this technique we obtain two components of the flow (u_x and u_y) in the plane of laser sheet (2D-2C) shown in fig.III.17a.
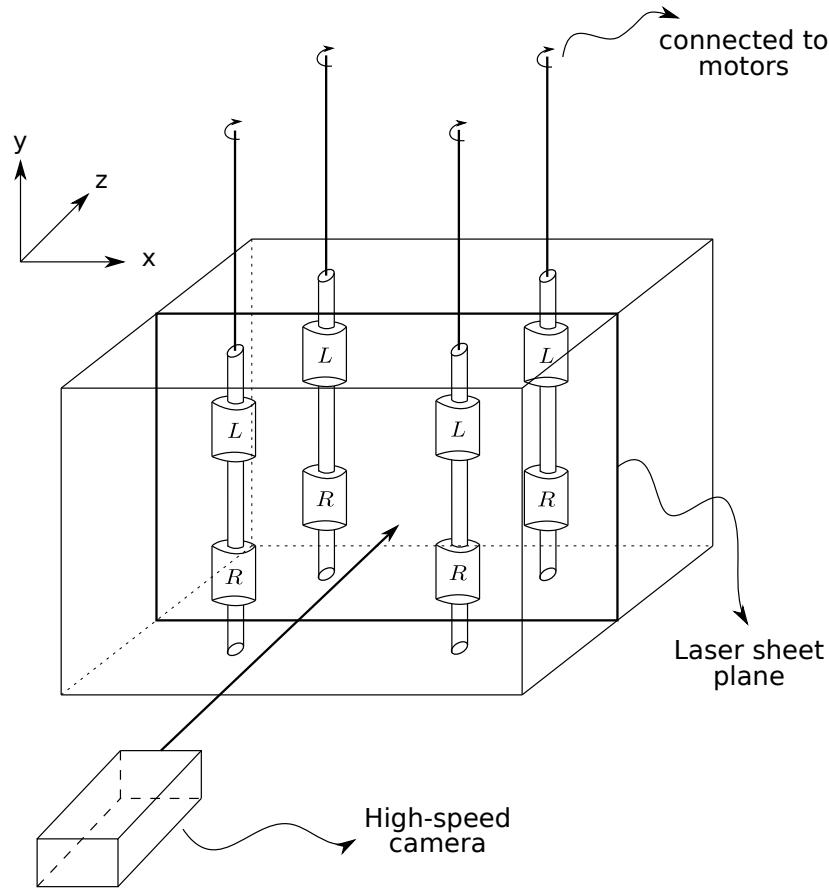
Fig. III.16 *Sketch of the experimental setup. The laser sheet is in the x-y plane and camera is oriented along the z-direction. L (for left) and R (for right) denote the chirality of the helices.*

(a)

(b)
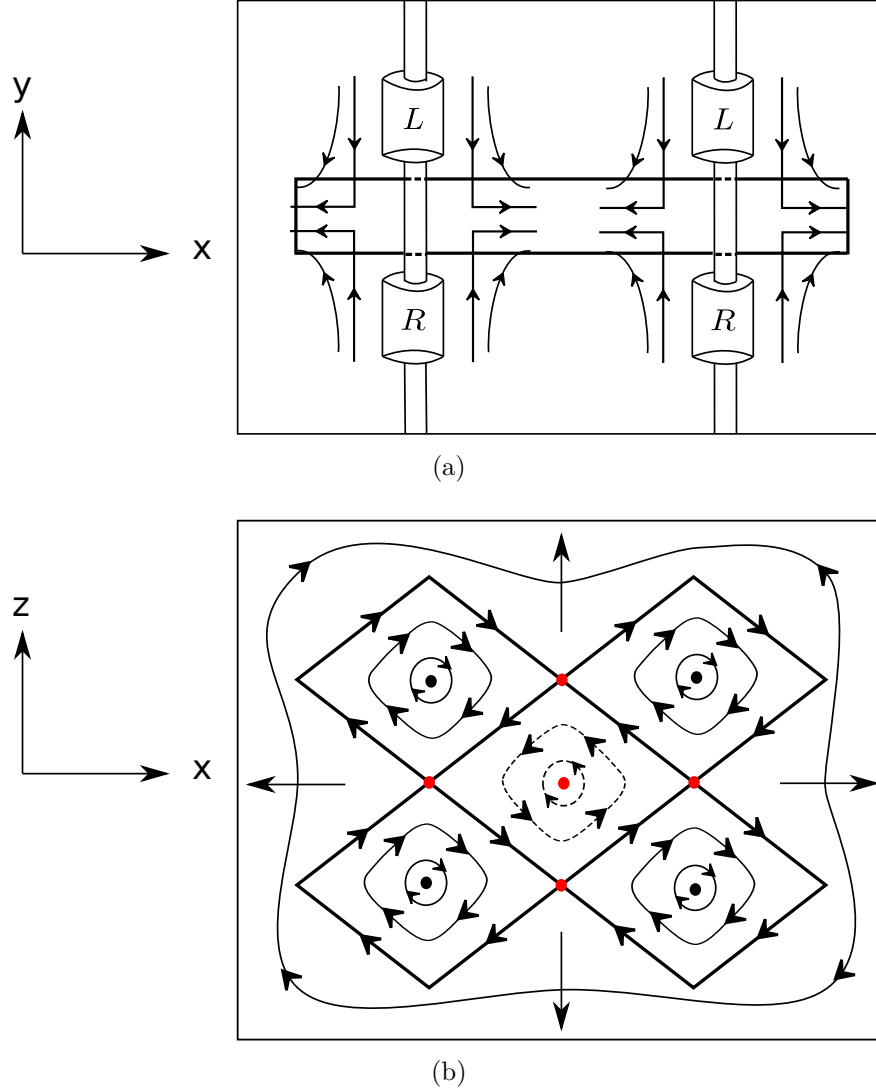
Fig. III.17   *(a) Front view sketch of the measurement plane. It lies in the midplane along z-direction and located in the region between the helices. (b) Top view sketch of the midplane along y-direction. Arrows indicate the geometry of the mean flow. The stagnation points have been marked in red.*

Figures III.17a and III.17b sketch the mean flow in the midplanes along z-axis and y-axis respectively. In fig.III.17b, the cells indicating mean flow around the helices will not be rectangular and have been exaggerated to show the stagnation points. We observe that the flow is similar to Roberts flow (fig.III.5) except for two differences. First, all the vortices are co-rotating and the midplane along y-axis has no axial flow but instead a radial flow. Second, this results in a flow having a mean circulation having the same sense as the rotation of the helices. The reason for choosing this flow is that we expect the integral length scale to be of the order of either the size of the helix or the distance between the axes of the helices

both of which are smaller than the size of the experimental volume. Similar to the previous experiment, this should allow us to investigate the behaviour of coherence at separation lengths larger than the integral length scale.

III.4.1 Forcing mechanism: Helices and motors

Fig.III.18 shows one of the four axes which are used for forcing the turbulent flow. Each of the axes is attached with two helices. The diameter of the helix is 25 mm, the length of the helix is 30 mm, the diameter of the axis is 7 mm and the maximum distance between the blades of the helix is 7 mm. Each helix has eight blades and the two helices have opposite chirality.

The helices and the axes are fabricated using UV polymerizing 3D printing technique in the 3D printing and fabrication facility of the department. The resin used was *Nano Clear* (Lumi Industries) which has a refractive index $RI \approx 1.52$.
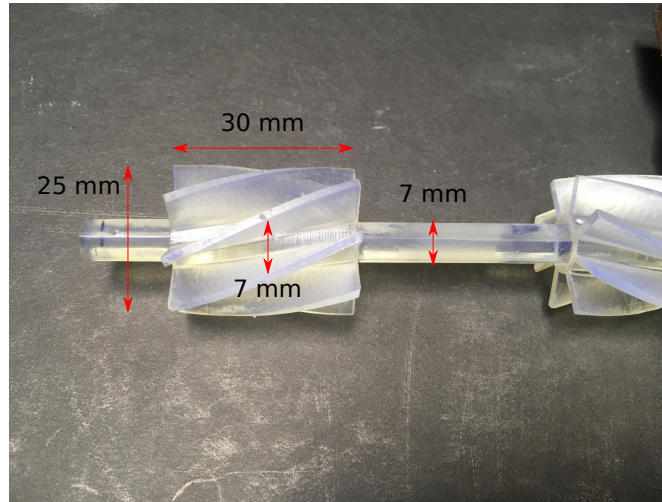
Fig. III.18   *Image shows one of the four axes each one of which is attached with two helices of opposing chirality.*

The axes are rotated using four brushless DC motors from *MDP-MAXON* (model *EC-i40HT*) with the rotation rate Ω ranging from of 0-3200 rpm. Each of the motors is fitted with Hall sensors (for position of the axes) and optical encoders (for the rotation rates of the axes) along with feedback loop controller (model *ESCON 70/10*) with access to both instantaneous rotation rates and torques on the motors.

III.4.2 Working fluid and its properties

The working fluid in our experiment is a mixture of anise oil and mineral oil (*Alfa Aesar Nujol light oil*). The purpose of this specific mixture is to match the refractive indices of the working fluid with that of the material of the forcing structure (helices and axes). Since the refractive index of the forcing structure material ($RI \approx 1.52$) lies in between that of mineral oil ($RI \approx 1.461$) and anise oil ($RI \approx 1.556$), it should be possible to match the refractive indices with a mixture of the two oils. The reason for working with a fluid where the refractive indices of the fluid and forcing structure are matched is that it allows us to obtain the velocity field in the flow using optical techniques in any region of the flow without having to worry about the obstruction to the optical technique from the forcing structure. Though numerous empirical relations exist in literature for estimating the refractive index of a binary mixture, we use the simplest of the empirical relations proposed by Arago and Biot [97] for a rough estimation of the refractive index of our mixture. Arago and Biot proposed an empirical relation where the refractive index of a mixture is the sum of the refractive indices of the components times their volume fraction. If we denote the volume fraction of the mineral oil by $\phi_{mineral}$ which is defined as

$$\phi_{mineral} = \left(\frac{\text{Volume of mineral oil}}{\text{Volume of mixture}} \right) \times 100$$

Then to obtain a mixture with refractive index $RI = 1.52$, we would need a mixture with $\phi_{mineral} \approx 38\%$ and $\phi_{anise} = 1 - \phi_{mineral} \approx 62\%$. Whether this empirical relation is correct and to what degree is not an issue since we match the refractive indices of the mixture and the forcing structure experimentally. The procedure for determining the volume fraction that matches the refractive indices of the mixture and the forcing structure is as follows,

- We pass a laser beam through the center of the axis of the helix and rotate the helix with some rotation rate Ω (the exact value of the rotation rate is irrelevant to the procedure).

- Owing to the hexagonal shape of the axis, when the refractive indices of the mixture and the axis are not matched the transmitted beam would be deflected by a maximum distance 'd' while remaining parallel to the incident laser beam.

- For two configurations while the helix rotates, the deflection would be zero; one when the beam is incident on any of the vertices of the hexagon and second when it is exactly perpendicular to the face of the hexagonal axis it is incident upon.

- The maximum distance of deflection 'd' would be a function of the difference in the refractive indices of the axis and that of mixture, i.e., the mismatch between the two refractive indices.

- We change the volume fraction of the two components of the mixture (anise oil and mineral oil) and obtain the exact volume fraction at which the distance of deflection is roughly zero.

(a)

(b)
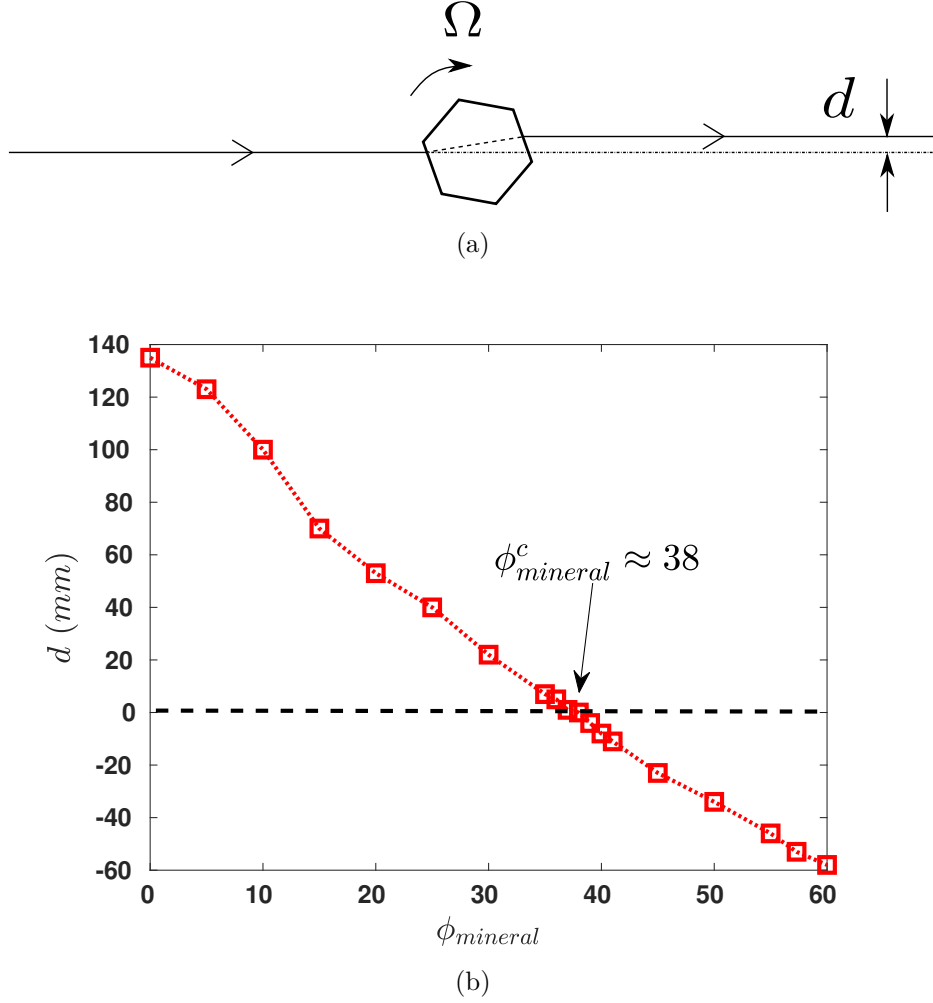
Fig. III.19   *(a) Sketch showing the incident beam being deflected by a distance 'd' by the rotating hexagonal axis. When the incident beam is perpendicular to the faces of the axis or when it falls on the vertices of the hexagonal axis, it is not deflected. (b) Plot showing the maximum distance of deflection 'd' of the incident laser beam versus the volume fraction of mineral oil $\phi_{mineral}$. The volume fraction of mineral oil at which we obtain matching of refractive indices is denoted by $\phi^c_{mineral}$.*

The above mentioned procedure is shown in the sketch III.19a. The maximum distance that the incident laser beam is deflected due to the mismatch between the refractive indices of the mixture and the axis is shown in fig.III.19b as a function of the volume fraction of mineral oil in the mixture. The exact volume fraction of the two fluids for matching the refractive indices is found to be a mixture of 62% anise oil and 38% mineral oil (as indicated by $\phi^c_{mineral}$ in fig.III.19b). The volume fractions of the mineral oil and anise oil evaluated experimentally for matching the refractive indices of the mixture and the forcing structure are close to the rough estimation made using the Arago-Biot empirical relation. Fig.III.20 shows images of the helix and the axis taken in air and in the mixture after matching the refractive indices of the mixture and the forcing structure. We observe that, except for the sharp edges of the helix and the region where the axis and helix is glued together, the forcing structure becomes essentially transparent to light[7]. The techniques of fabricating transparent plastics using 3D printing are quite recent [98] and its application to studying visualization of flows was demonstrated by Song *et al.* [99].

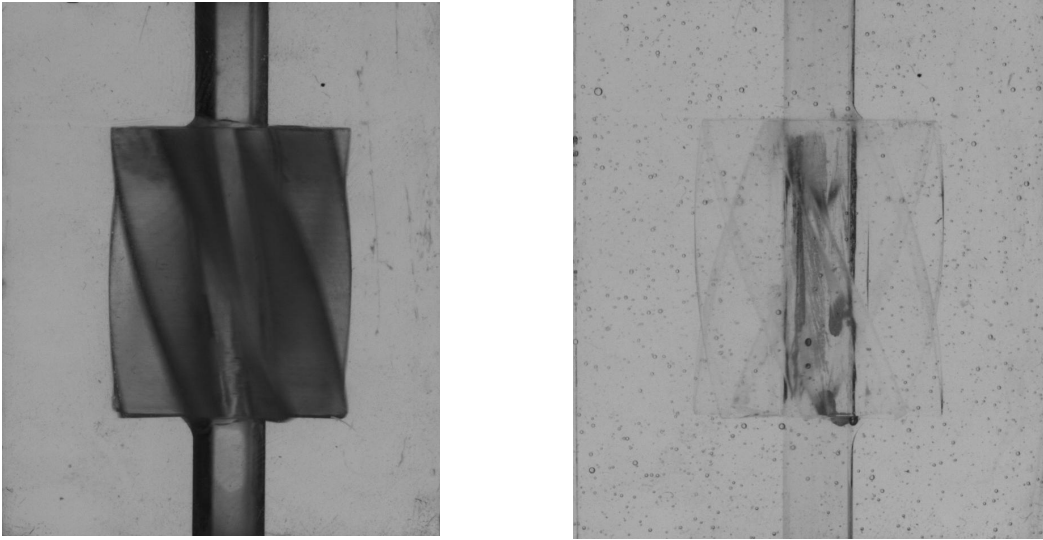Fig. III.20 *(a) Helix and the axis of the forcing structure as pictured in air. (b) Helix and the axis of the forcing structure as pictured in the mixture after matching the refractive indices. (The mixture contains 62% anise oil and 38% mineral oil by volume fraction.)*

---

[7]To be precise, this would depend on the wavelength of the light. But for all our experimental purposes, it was almost entirely transparent.

Concerning other physical properties of the mixture, the density can be evaluated easily since it would be a combination of the densities and volume fractions of the components of the mixture. The viscosity of the mixture, on the other hand, needs to be experimentally determined. We measure the viscosity of the mixture by using Ostwald's viscometer. For the mixture of 62% Anise oil + 38% Mineral oil, we obtain a kinematic viscosity of $\nu = 4.5 \times 10^{-6} \ m^2/s^3$. The physical properties of working fluid mixture and its component fluids, anise oil and mineral oil, are given in table III.3.

	Anise oil	Mineral oil	Mixture (62% Anise oil + 38% Mineral oil)
$\rho \ (kg/m^3)$	980	838	926
$\eta \ (kg/ms)$	2.4×10^{-3}	6.7×10^{-3}	4.2×10^{-3}
$\nu \ (m^2/s)$	2.5×10^{-6}	8×10^{-6}	4.5×10^{-6}
Refractive Index (RI)	1.556	1.461	1.52

Table III.3: Physical properties of anise oil, mineral oil and the mixture used as the working fluid in our experiment.

III.4.3 The setup of the PIV technique

We generate a laser sheet using an optical setup which is shown in fig.III.21. It consists of *CNI solid state green laser* (wavelength of 532 nm) with output power of 2.4 W, two convex lenses, two cylindrical lenses and three mirrors. The two convex lenses, denoted by Co_1 and Co_2 are in telescopic configuration and have focal lengths of $f_1^{co} = 15$ cm and $f_2^{co} = 4$ cm respectively. Similarly, the two cylindrical lenses, Cy_1 and Cy_2, have focal lengths $f_1^{cy} = 3$ cm and $f_2^{cy} = 1$ cm respectively. The lenses Co_2, Cy_1 and Cy_2 are attached to a translation stage. This allows us to vary the relative distances between the lenses and thus the magnification factor. The laser beam is first passed through the two convex lenses which gives us a circular beam of desired magnification. In the next step, we pass it through the two cylindrical lenses by which we obtain a laser sheet of desired width. The laser sheet thus generated is passed through the experimental volume.

The flow is seeded with *Goodfellow* polyamide-Nylon 12 particles which have a size of about 30 µm and a density of 1000 kg/m^3 which is close to the density of our mixture. This ensures that the particles remain suspended in the flow when in operation. They have a good chemical resistance to hydrocarbons and thus non-reactive to our working fluid mixture.

The light reflected by the particles in the flow is imaged by a *Phantom V1840* high speed camera. The camera is equipped with a 4 megapixels sensor and can capture images at a maximum rate of $233,380$ frames per second which is way above our requirement. The velocity field is obtained from the images by using the freely available time-resolved particle image velocimetry software *PIVlab* [100].

(a)
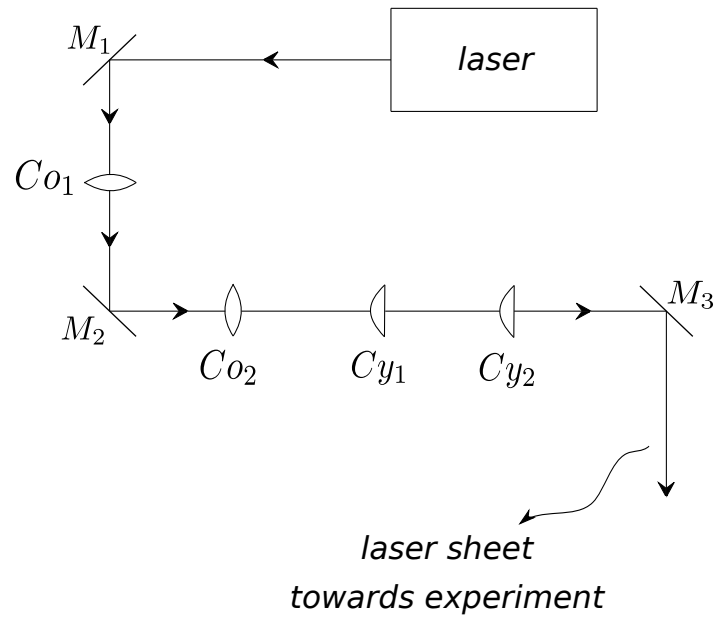
(b)

Fig. III.21   (a) Photo of the optical setup. (b) Sketch of the optical setup for generating a laser sheet.

III.4.4 Characterization of the flow

We begin characterizing the flow by first defining the Reynolds number as,

$$Re = \frac{\pi R^2 \Omega}{30\nu}$$

where R is the radius of the helix and Ω is the rotation rate of the forcing structure in rotations per minute (or rpm). The rotation rate is varied between $\Omega = 0 - 3200$ rpm. In the definition of the Reynolds number, the constant $\pi/30$ appears from dimensional considerations since we decide to keep the unit of Ω in rotations per minute. We attain a maximum value of $Re \sim 10^4$ in our experiment for a rotation rate of $\Omega = 3200$ rpm. Figure III.22a shows the velocity as obtained from the PIV technique at one instant in time for a rotation rate of $\Omega = 3200$ rpm. The figure also outlines in red the borders of the axes of the forcing structure. The axes are encountered by the light reflected off the particles before reaching the camera since we are measuring in the x-y plane midway along the z-axis. As can be seen from fig.III.22a, we are indeed able to observe the velocity field almost without any obstruction from the axes of the helices. This is more evident when we plot the percentage error in evaluating the velocity field which is shown in fig.III.22b for a rotation rate of $\Omega = 3200$ rpm. If the total samples in time for each point in space is denoted by N, the percentage error N_{error} is defined as,

$$N_{error} = \left(\frac{\delta_{u_x,NaN} + \delta_{u_y,NaN}}{2N} \right) \times 100$$

where $\delta_{k,NaN}$ stands for Kronecker delta and has a value of one when 'k' attains a non-numeric value. Even with the axes having relatively higher percentage error compared to the rest of the flow, the percentage error never exceeds 0.15 % thus quantifying the loss of data due to refraction by the axes. Apart from the axes, the percentage error is observed to be within 0.04 % for the rest of the flow.

We note that the error would likely increase if the light reflected off the seeding particles has to travel through the part of the forcing structure that has helices. The sharp edges of the helices would result in higher errors due to the stronger refraction of the light. But for the current experimental study, our plane of measurement is close to the center of the experimental volume and thus the light reflected off the seeding particles has to only travel through the axis of the forcing structure.
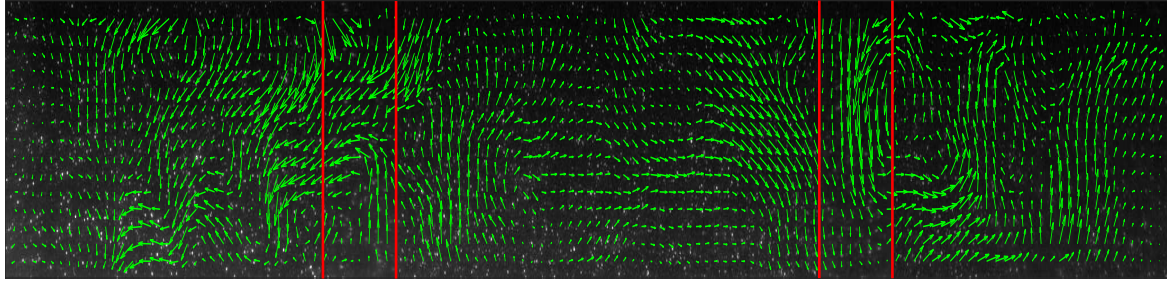
(a)
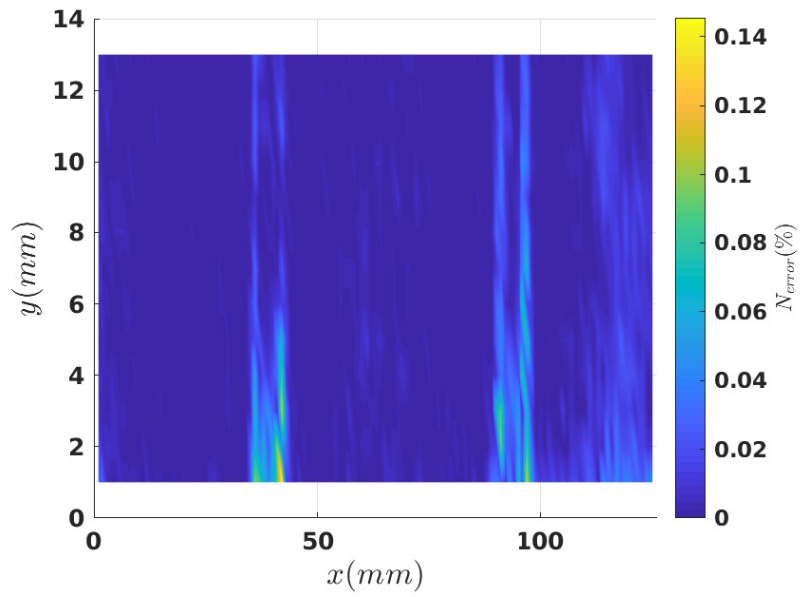
(b)

Fig. III.22   *(a) Velocity field at an instant in time for a rotation rate of $\Omega = 3200$ rpm. The outline of the axes of helices are outlined in red. (b) Percentage error in the velocity field when the rotation rate is $\Omega = 3200$ rpm. The outline of the axes is visible with relatively higher percentage error.*

Fig.III.23 shows the field of mean and RMS of the velocity components along x and y axes denoted by $\langle u_x \rangle$, $\langle u_y \rangle$, $u_x^{'rms}$ and $u_y^{'rms}$ respectively. For obtaining the mean and RMS of the velocity field, the averages are evaluated over time. The red lines in the figure mark the outlines of axes of the forcing structure and we observe that the axes do not interfere with the measurement of the mean and RMS of velocity. Notice that the measured mean flow resembles fig.III.17. The RMS of velocity fluctuations along the x-axis $u_x^{'rms}$ (and due to symmetry along z-axis as well) is observed to be homogeneous in the region between the axes with an error of $\pm 0.08\%$. The same cannot be said for the RMS of velocity fluctuations along y-axis, $u_y^{'rms}$, which varies by about $\pm 29\%$ in the region between the axes. Henceforth, the results presented are for the velocity fluctuations in the region between the axes marked with black dashed lines in fig.III.23. Obtaining statistical quantities in this region ensures their homogeneity along the two directions, x and z.
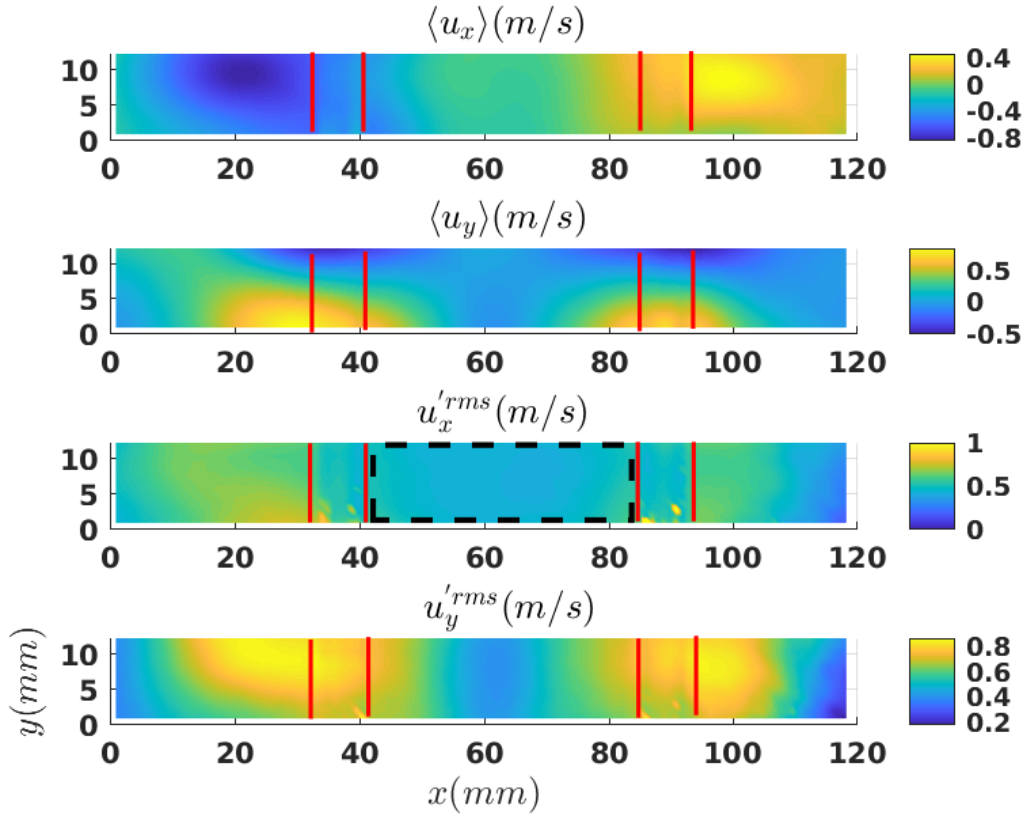

Fig. III.23 *Mean and RMS of velocity fluctuations for $\Omega = 3200$ rpm. From top to bottom: $\langle u_x \rangle$, $\langle u_y \rangle$, $u_x^{'rms}$ and $u_y^{'rms}$. Red lines mark the outlines of the axes. Black dashed box denotes the area in which homogeneity for $u_x^{'rms}$ is observed.*

We begin first by characterizing the flow using one point statistical quantities. We define the norm of the velocity as $u_{norm} = \sqrt{u_x^2 + u_y^2}$. Figure III.24 shows the RMS of the two velocity components $u_x^{'rms}$, $u_y^{'rms}$ and of the norm of velocity $u_{norm}^{'rms}$ versus the rotation rate of the motors Ω. The values are obtained after averaging the respective quantities in time and over the region of measurement. We observe that all the three RMS quantities, $u_x^{'rms}$, $u_y^{'rms}$ and $u_{norm}^{'rms}$ grow linearly with the rotation rate Ω but with different slopes. The magnitude of $u_y^{'rms}$ is higher than that of $u_x^{'rms}$ implying that the flow is more turbulent along the y-axis than the x-axis. This is also seen from fig.III.23 for a rotation rate of $\Omega = 3200$ rpm where we observe that the flow is highly turbulent along the y-axis in the immediate vicinity of the two axes of the forcing structure.
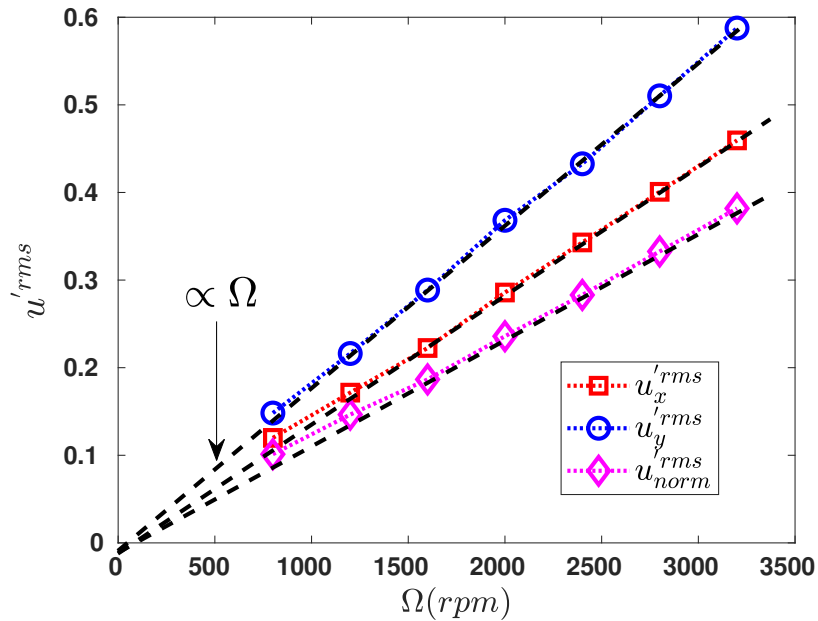
Fig. III.24   *The RMS of velocity along x, y axes denoted by $u_x^{'rms}$ (red squares), $u_y^{'rms}$ (blue circles) and the RMS of the norm of velocity $u_{norm}^{'rms}$ (magenta diamonds) versus the rotation rate of motors Ω. Black dashed line denote linear dependence.*

At this point, we note that we can obtain the large scale scaling of the RMS of velocity fluctuations by using dimensional analysis similar to the way we obtained scaling for different statistical quantities in the von Kármán swirling flow. Dimensionally speaking, the current flow that we are studying and the von Kármán swirling flow share a lot of similarities. For example, the only experimental parameter that involves time in both flows is the rotation rate; of the disks in the case of von Kármán swirling flow and that of the forcing structure in the current flow denoted by Ω. In both the von Kármán swirling flow and the current flow, the control parameter for the experiment is the rotation rate. Applying dimensional arguments for the RMS of velocity fluctuations, we would have for the large scale scaling,

$$u'_{rms} = R\Omega \ F\left(Re, \frac{R}{l_{helix}}, \frac{R}{l_{box}}, \frac{R}{l_{hh}}\right) \xrightarrow{Re\to\infty} \propto \Omega$$

where F is an unknown function of the dimensionless numbers. We have denoted the radius of the helix, the length of the helix, the size of the box and the distance between two adjacent helices by R, l_{helix}, l_{box} and l_{hh} respectively. We observe that as compared to the von Kármán swirling flow, the current flow has more parameters with the dimensions of length. The linear scaling for the RMS of velocity fluctuations with the rotation rate derived using dimensional arguments would be valid for the components as well as the norm of the velocity. As seen from fig.III.24, the RMS of the components and the norm of the velocity fluctuations scale linearly with the rotation rate Ω as predicted by dimensional analysis for large scale scaling.

Fig.III.25 shows the energy spectrum of the x-component of the velocity fluctuations denoted by $E_{ux}(f)$ for a rotation rate of $\Omega = 3200$ rpm. The energy spectrum has been averaged in space over all points in the region of measurement. At low frequencies a power-law behaviour close to $E_{ux}(f) \propto f^{-0.6}$ is observed albeit not as clearly as was observed for the experiments presented earlier (see fig.II.6a and fig.III.8a). We note that the low-frequency behaviour is not observed for the energy spectrum of the norm of velocity. As for the higher frequencies the behaviour is unclear as the exponent of the scaling lies somewhere between the one predicted for the Lagrangian velocity field (eqn.(III.4) with $E(f) \propto f^{-2}$) and the one predicted for Eulerian velocity field due to sweeping effect proposed by Tennekes [17] (eqn.(III.5) with $E(f) \propto f^{-5/3}$). Thus, from the energy spectrum, we cannot conclude either the presence or the absence of the sweeping effect.
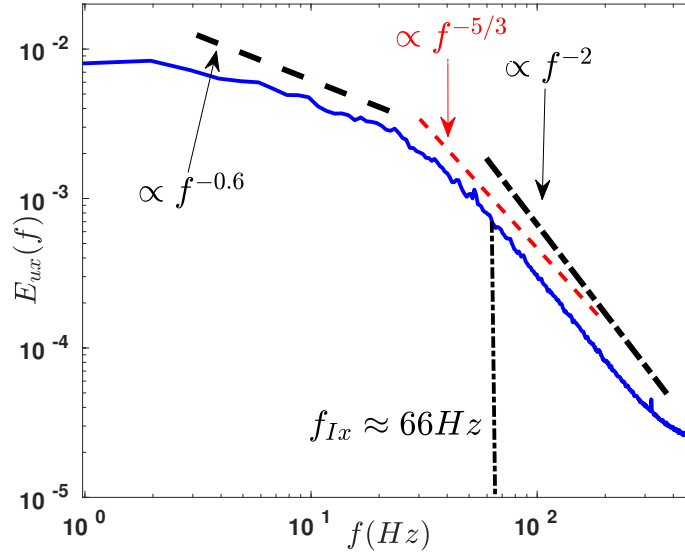
Fig. III.25   *The frequency energy spectrum of the x-component of velocity fluctuations $E_{ux}(f)$ for $\Omega = 3200$ rpm. Black dashed line denotes $E_{ux}(f) \propto f^{-0.6}$, black dotted dashed line denotes $E_{ux}(f) \propto f^{-2}$ and red dashed line denotes $E_{ux}(f) \propto f^{-5/3}$. The integral frequency is denoted by f_{Ix} and given by eqn.(III.28).*

As was done in the case of von Kármán swirling flow in chapter II, we measure the mean energy injection (and thus mean dissipation for a stationary flow) rate per unit mass $\langle \epsilon \rangle$ by measuring the power required by the motors in two sets of experiments, one with the fluid and the other without the fluid. The difference in the power required by the motors in these two sets of experiments gives the power injected in maintaining the turbulent flow. This directly gives us mean energy injection rate per unit mass $\langle \epsilon \rangle$ on dividing the power injected in maintaining the flow by the mass of the fluid in the experiment. Fig.III.26 shows the dependence of the mean energy injection rate per unit mass $\langle \epsilon \rangle$ on the rotation rate Ω. A power law behaviour with $\langle \epsilon \rangle \propto \Omega^3$ is clearly observed. A large scale scaling of the mean energy injection rate per unit mass with the rotation rate can be obtained from dimensional analysis with,

$$\langle \epsilon \rangle = R^2 \Omega^3 \; F_{eps}\left(Re, \frac{R}{l_{helix}}, \frac{R}{l_{box}}, \frac{R}{l_{hh}} \right) \xrightarrow{Re \to \infty} \propto \Omega^3$$

where F_{eps} is an unknown function of the dimensionless numbers. This prediction is in agreement with the scaling observed experimentally.
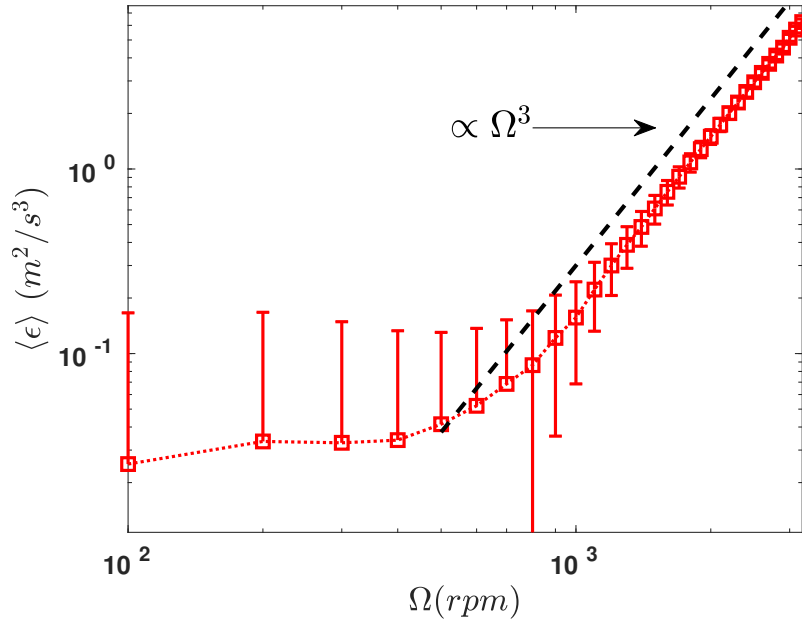
Fig. III.26   *The mean energy injection rate per unit mass $\langle \epsilon \rangle$ versus the rotation rate of the motors Ω. Black dashed line denotes $\langle \epsilon \rangle \propto \Omega^3$.*

Next, we characterize the flow using velocity correlations which are two point statistical quantities. We define the longitudinal two-point correlation functions for the two velocity components and the two-point correlation function for the norm of velocity as,

$$\Gamma_{ux}(r) = \frac{\left\langle u'_x(t,x,y)u'_x(t,x+r,y)\right\rangle}{\sqrt{\left\langle u'^2_x(t,x,y)\right\rangle\left\langle u'^2_x(t,x+r,y)\right\rangle}}$$

$$\Gamma_{uy}(r) = \frac{\left\langle u'_y(t,x,y)u'_y(t,x,y+r)\right\rangle}{\sqrt{\left\langle u'^2_y(t,x,y)\right\rangle\left\langle u'^2_y(t,x,y+r)\right\rangle}}$$

$$\Gamma_{norm}(r) = \frac{\left\langle u'_{norm}(t,x,y)u'_{norm}(t,x+r,y)\right\rangle}{\sqrt{\left\langle u'^2_{norm}(t,x,y)\right\rangle\left\langle u'^2_{norm}(t,x+r,y)\right\rangle}} \tag{III.27}$$

where the ensemble averaging is performed over the space variables x, y and time t. Fig.III.27 shows the longitudinal correlation functions along x and y axes and correlation function of the norm, denoted by Γ_{ux}, Γ_{uy} and Γ_{norm} respectively. We observe that all the three correlation functions decay exponentially with the separation length r. The characteristic length scale of the exponential decay gives us the integral scales along x and y axes which are denoted by l_{Ix} and l_{Iy} respectively and the integral scale of the norm denoted by l_{Inorm}.
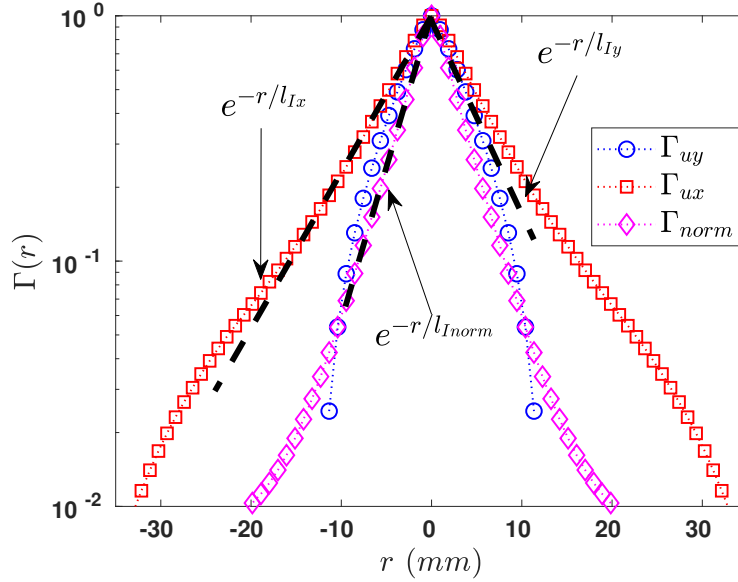
Fig. III.27 *The longitudinal two-point correlation function along the x and y axes and the two-point correlation function of the norm, denoted by Γ_{ux}, Γ_{uy} and Γ_{norm} respectively and defined by eqn.(III.27). The dashed lines denote exponential decay with characteristic length scales l_{Ix}, l_{Iy} and l_{Inorm}.*

Fig.III.28 shows the dependence of the three integral length scales l_{Ix}, l_{Iy} and l_{Inorm} on the rotation rate of the motors Ω. We observe that the integral scales are roughly constant with the rotation rate as was the case with von Kármán swirling flow. Similarly, we can define the integral frequency scales f_{Ix}, f_{Iy} and f_{Inorm} using the RMS of velocity fluctuations and the integral length scales as,

$$f_{Ix} = \frac{u_x^{'rms}}{l_{Ix}}$$
$$f_{Ix} = \frac{u_y^{'rms}}{l_{Iy}}$$
$$f_{Inorm} = \frac{u_{norm}^{'rms}}{l_{Inorm}} \tag{III.28}$$
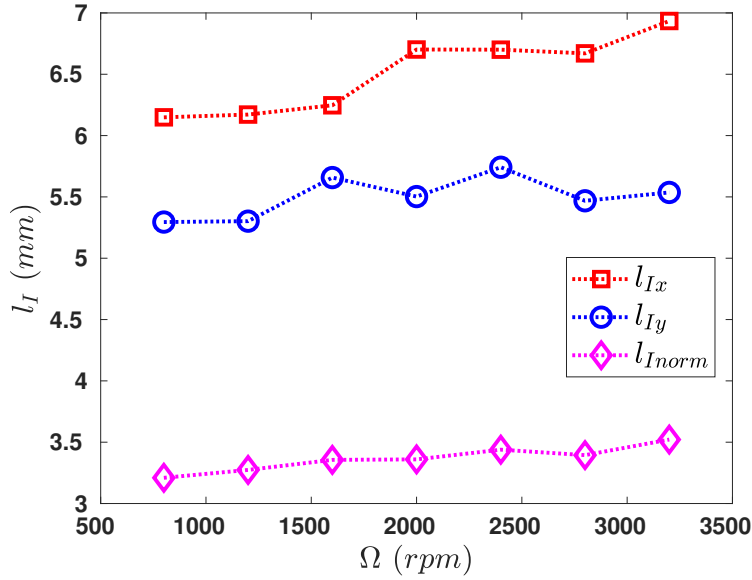
Fig. III.28 *The integral length scales along x, y axes denoted by l_{Ix}, l_{Iy} and the integral length scale of the norm of velocity denoted by l_{Inorm} versus the rotation rate of the motors.*

From fig.III.29, we observe that all the integral frequencies linearly depend on the rotation rate of the motors Ω as expected from the behaviour of $u^{'rms}$ and l_I. Dimensional analysis gives linear scaling for the integral frequency with the rotation rate Ω as was the case for the cross-over frequency which is in agreement with our observed scaling of the integral frequencies.
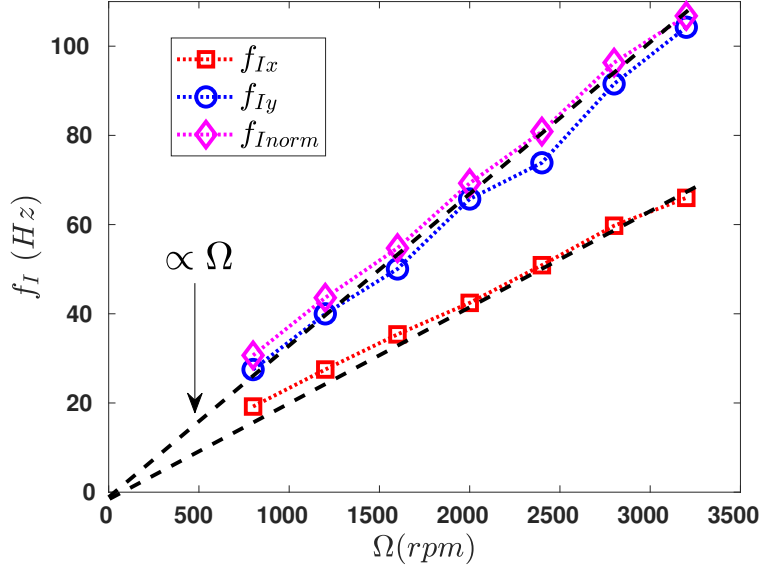
Fig. III.29 *The integral frequency scale denoted by f_I versus the rotation rate of the motors whose definition is given by equation* (III.28). *The dashed black line denotes a linear dependence.*

From all the experimentally obtained characterization of the flow till this point, we can obtain estimates on the order of magnitudes of the Taylor microscale λ, Kolmogorov microscale η and the Taylor microscale based Reynolds number Re_λ,

$$\lambda = \left(15\nu \frac{u_{rms}^2}{\langle \epsilon \rangle} \right)^{1/2} \sim O(1) \text{ mm}$$

$$\eta = \left(\nu^3 / \langle \epsilon \rangle \right)^{1/4} \sim O(10^2) \text{ µm}$$

$$Re_\lambda = \frac{u'_{rms}\lambda}{\nu} \sim O(10^2)$$

In summary, the characteristics and scaling of the different statistical quantities of the flow are similar to the von Kármán swirling flow. Finally, the choice of the flow suits our purpose for studying the coherence since we observe that the integral length scales are smaller than the size of the domain where we measure the flow by an order of magnitude. This should allow us to study the behaviour of coherence for separation lengths larger than the integral length scales.

III.5 Experimental results of setup II

Unlike measurements of velocity acquired using 1D hot-wire probes, we obtain two-components of the velocity with the PIV technique used in the current experiment (2D-2C). We can thus define two-point measurements for either the longitudinal (u_{LL}) or normal (u_{NN}) components of the velocity as well as for its norm (u_{norm} or speed). The longitudinal and normal components of velocity are defined according to the separation vector '**r**' separating the two points in the flow as shown in fig.III.9. The statistics obtained for the norm of velocity would be analogous to the statistics obtained by 1D hot wire probes. This enables us to compare the results for two point statistics between the current and the previous experiment in addition to investigating their behaviour for the velocity components.

We present the results obtained for coherence evaluated using either the longitudinal component or the norm of the velocity component, denoted by $\mathcal{C}^{LL}(r,f)$ and $\mathcal{C}^{norm}(r,f)$ respectively. We have checked experimentally and similar results are obtained for the normal component. The definitions of the coherence for the longitudinal component and the norm of velocity are,

$$\mathcal{C}^{LL}(r,f) = \frac{\left\| \int_{-\infty}^{\infty} \left\langle u'_x(x,t)u'_x(x+r,t+\tau) \right\rangle e^{-if\tau} d\tau \right\|^2}{\left[\int_{-\infty}^{\infty} \left\langle u'_x(x,t)u'_x(x+0,t+\tau) \right\rangle e^{-if\tau} d\tau \right] \left[\int_{-\infty}^{\infty} \left\langle u'_x(x+r,t)u'_x(x+r,t+\tau) \right\rangle e^{-if\tau} d\tau \right]}$$

$$\mathcal{C}^{norm}(r,f) = \frac{\left\| \int_{-\infty}^{\infty} \left\langle u'_{norm}(x,t)u'_{norm}(x+r,t+\tau) \right\rangle e^{-if\tau} d\tau \right\|^2}{\left[\int_{-\infty}^{\infty} \left\langle u'_{norm}(x,t)u'_{norm}(x,t+\tau) \right\rangle e^{-if\tau} d\tau \right] \left[\int_{-\infty}^{\infty} \left\langle u'_{norm}(x+r,t)u'_{norm}(x+r,t+\tau) \right\rangle e^{-if\tau} d\tau \right]}$$

where we have chosen the x-axis for the separation vector since we have better spatial resolution along x-axis than y-axis. The averages for evaluating the coherences are performed in space x, y and time t. Fig.III.30 shows the behaviour of the coherence for the longitudinal component and the norm of the velocity fluctuations when the rotation rate of the motors is $\Omega = 3200$ rpm. We observe that the coherence decays exponentially in the frequency range of inertial scales ($f > f_I$) and the behaviour is similar to that observed in the previous experiment. We observe two additional features on the behaviour of coherence,

- The coherence decays exponentially for both the longitudinal component and the norm of the velocity fluctuations.

- The coherence decays exponentially even for frequencies smaller than the integral frequency ($f < f_I$).
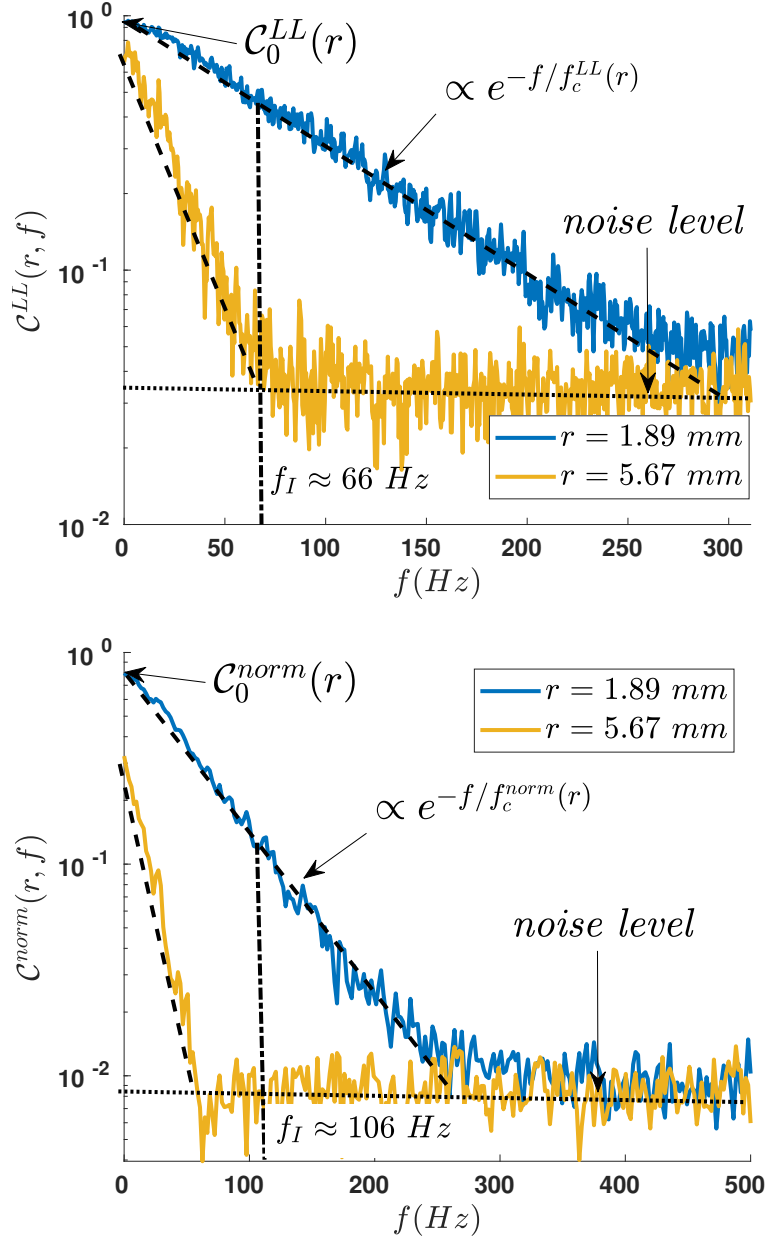
Fig. III.30   *Coherence of velocity fluctuations when the rotation rate of the motors is $\Omega = 3200$ rpm (a) For longitudinal component, denoted by $\mathcal{C}^{LL}$. (b) For the norm, denoted by $\mathcal{C}^{norm}$.*

The two observation imply that the functional form of the coherence for both the longitudinal component and the norm of velocity at all frequencies (inertial scales as well as low frequency) resembles eqn.(III.22) with,

$$\boxed{\mathcal{C}^{LL}(r,f) = \mathcal{C}_0^{LL}(r)e^{-f/f_c^{LL}(r)}}$$ (III.29)

$$\boxed{\mathcal{C}^{norm}(r,f) = \mathcal{C}_0^{norm}(r)e^{-f/f_c^{norm}(r)}}$$ (III.30)

In equations eqn.(III.29) and eqn.(III.30), f_c^{LL} and f_c^{norm} are the frequency scales associated with the decay of coherence of the longitudinal component and the norm of velocity respectively. The value at zero frequency of coherence of the longitudinal component and norm of velocity is denoted by $\mathcal{C}_0^{LL}$ and $\mathcal{C}_0^{norm}$ respectively. We recall here the conclusions drawn from the previous experiment that the decay of coherence at zero frequency, $\mathcal{C}_0^{LL}$ and $\mathcal{C}_0^{norm}$, would capture the spatial dependence of the integral scales. On the other hand, the frequency dependence, f_c^{LL} and f_c^{norm}, would capture the sweeping by the integral scales. All of the four quantities, f_c^{LL}, f_c^{norm}, $\mathcal{C}_0^{LL}$ and $\mathcal{C}_0^{norm}$ decay with the separation length r as seen from fig.III.30.

Fig.III.31 shows the decay of the coherence at zero frequency for the longitudinal component and the norm of the velocity (denoted by $\mathcal{C}_0^{LL}$ and $\mathcal{C}_0^{norm}$) with the separation length for $\Omega = 3200$ rpm. We observe an exponential decay with the separation length which suggests a functional form similar to eqn.(III.23), with,

$$\boxed{\mathcal{C}_0^{LL}(r) = e^{-r/r_{LL}^{\dagger}}}$$ (III.31)

$$\boxed{\mathcal{C}_0^{norm}(r) = e^{-r/r_{norm}^{\dagger}}}$$ (III.32)

Figure III.32 shows the dependence of frequency scale associated with the exponential decay (denoted by f_c^{LL} and f_c^{norm}) of coherence on the separation length for a rotation rate of the motors $\Omega = 3200$ rpm. It displays a power law decay with,

$$f_c^{LL}(r) \propto r^{-1.1\pm0.1}$$
$$f_c^{norm}(r) \propto r^{-1.2\pm0.1}$$
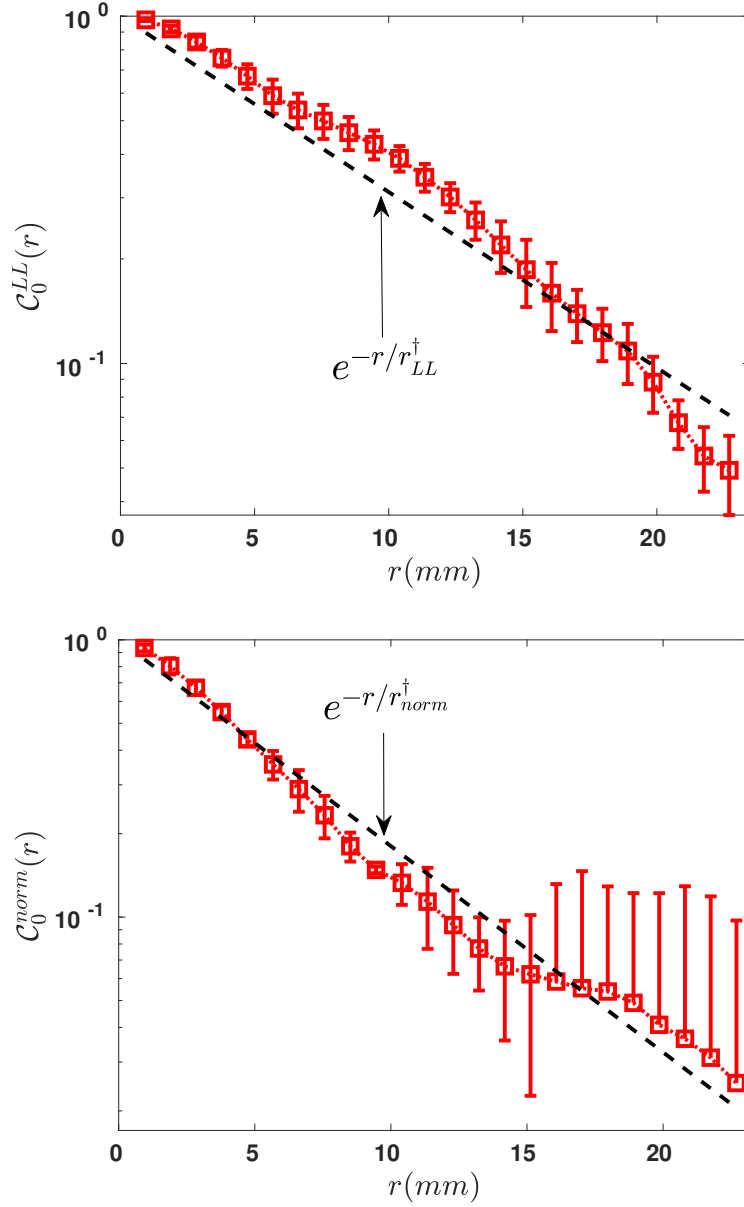
Fig. III.31   *The decay of the coherence of velocity at zero frequency* $(\mathcal{C}_0)$ *with increasing separation length between the two points of measurement* (r) *when the rotation rate of the motors is* $\Omega = 3200$ *rpm. Dashed line: corresponds to exponential decay with the length scale of the exponential decay being* $r^{\dagger}$*. (a) For longitudinal component. (b) For the norm.*
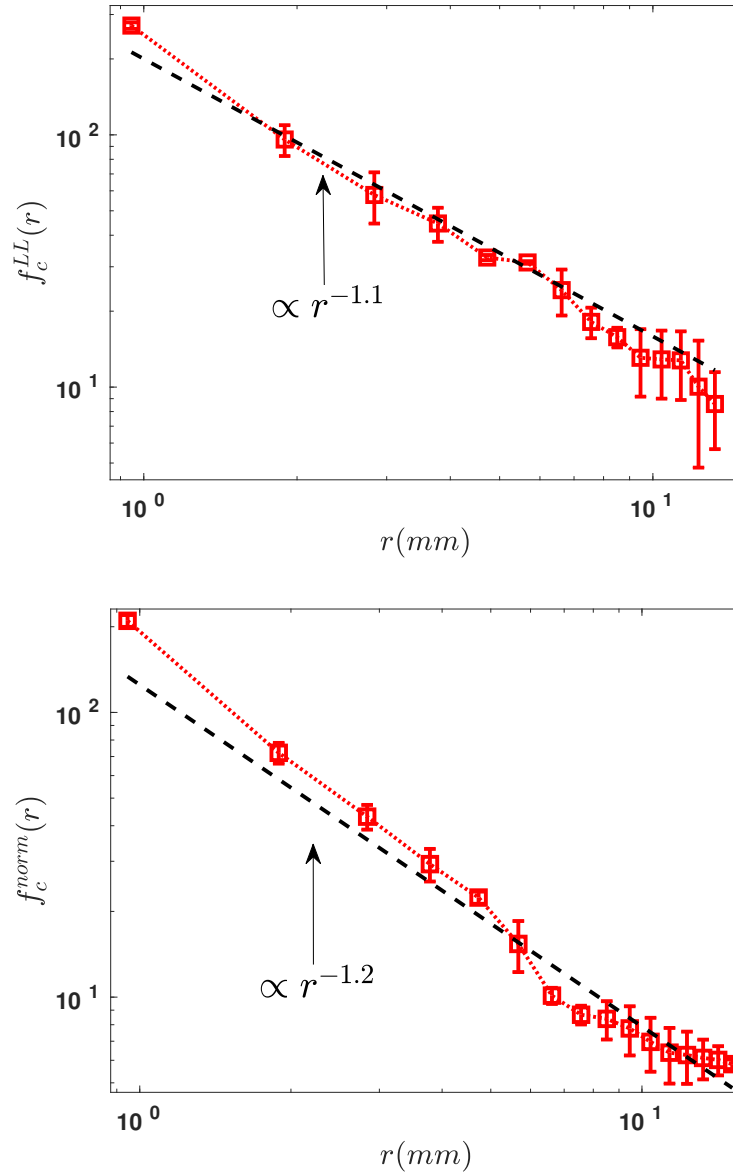
Fig. III.32   *The frequency scale of the exponential decay of coherence of velocity versus the separation length between the two points of measurement (r) for a rotation rate of the motors $\Omega = 3200$ rpm. Dashed line: corresponds to $f_c \propto r^{-1}$ (a) For longitudinal component. (b) For the norm.*

We can approximate the behaviour of f_c^{LL} and f_c^{norm} by a functional form similar to equation (III.24),

$$\boxed{f_c^{LL}(r) = u_{LL}^\dagger/r} \tag{III.33}$$

$$\boxed{f_c^{norm}(r) = u_{norm}^\dagger/r} \tag{III.34}$$

The quantities $r_{LL}^\dagger$, $r_{norm}^\dagger$ (equations (III.31) and (III.32)) are the length scales associated with the exponential decay of coherence at zero frequency. The quantities $u_{LL}^\dagger$, $u_{norm}^\dagger$ (equations (III.33) and (III.34)) are velocity scales associated with the decay of the coherence with frequency. All these four quantities would be characteristic of the turbulent flow. So, how are these quantities related to the length and velocity scales associated with the turbulent flow?

To answer this question, we note that equations (III.29) to (III.34) imply that an expression similar to equation (III.25) is obtained for the coherence of the longitudinal component and the norm of velocity fluctuations, with,

$$\mathcal{C}^{LL}(r, f) = \exp\left[-\left(\frac{r}{r_{LL}^\dagger}\right)\left(1 + \frac{f}{f_{LL}^\dagger}\right)\right]$$

$$\mathcal{C}^{norm}(r, f) = \exp\left[-\left(\frac{r}{r_{norm}^\dagger}\right)\left(1 + \frac{f}{f_{norm}^\dagger}\right)\right]$$

where $f_{LL}^\dagger = u_{LL}^\dagger/r_{LL}^\dagger$ and $f_{norm}^\dagger = u_{norm}^\dagger/r_{norm}^\dagger$ and would be frequencies characteristic of the turbulent flow. Fig.III.33a shows the length scale associated with the decay of coherence normalized by the integral length scale for the longitudinal component and the norm of velocity. We observe that the value of characteristic length scale $r^\dagger$ remains roughly the same as that of the integral length scale l_I up to a constant factor (denoted by c_1). Fig.III.33b shows the frequency scale associated with the decay of coherence normalized by the integral frequency for the longitudinal component and the norm of velocity. We observe that the orders of magnitude of f_c^{LL} and f_c^{norm} are comparable to the integral frequencies. Their values differ from the corresponding integral frequencies by a constant factor (denoted by c_2). The constants c_1 and c_2 are observed to be of similar orders of magnitude for the longitudinal component and the norm of velocity. This implies that the coherence for all frequencies can be cast in a simple functional form,

$$\mathcal{C}^{LL}(r, f) = \exp\left[- \left(\frac{c_1 r}{l_{Ix}} \right) \left(1 + \frac{c_2 f}{f_{Ix}} \right) \right] \tag{III.35}$$

$$\mathcal{C}^{norm}(r, f) = \exp\left[- \left(\frac{c_1 r}{l_{Inorm}} \right) \left(1 + \frac{c_2 f}{f_{Inorm}} \right) \right] \tag{III.36}$$

The mean values of the constant factors are found to be $c_1 \approx 0.7$ and $c_2 \approx 3.1$. To summarize our observations for the second experiment,

- The exponential decay in coherence is observed for all frequencies and thus the functional form obtained experimentally (equations (III.35) and (III.36)) is valid for inertial scales ($f > f_I$) as well as for low frequency behaviour of coherence ($f < f_I$). For frequencies $f > f_I$ it would indicate the effect of sweeping of the inertial scales by the energy containing integral scales.

- The behaviour of the coherence for frequencies smaller than the integral frequency $f < f_I$ likely arises from the sweeping of the vorticity filaments by the energy containing integral scales. Our experimental observations suggest that even the sweeping of vorticity filaments is captured by an exponential decay in coherence.

- The exponential decay in coherence is observed for the components as well as the norm of velocity.

- The sweeping of the inertial scales as well as that at low frequencies (possibly from the sweeping of vorticity filaments) would be captured by normalizing with the decay of coherence at zero frequency,

$$\frac{\mathcal{C}^{LL}(r, f)}{\mathcal{C}_0^{LL}(r)} = \exp\left[- \left(\frac{c_3 r f}{u_x'^{rms}} \right) \right]$$

$$\frac{\mathcal{C}^{norm}(r, f)}{\mathcal{C}_0^{norm}(r)} = \exp\left[- \left(\frac{c_3 r f}{u_{norm}'^{rms}} \right) \right]$$

and would decay both with the separation length and the frequency of the scales being considered. The constant factor $c_3 = c_1 c_2 \approx 2.3$. This resembles the behaviour of coherence that we derived analytically and given by eqn.(III.20).
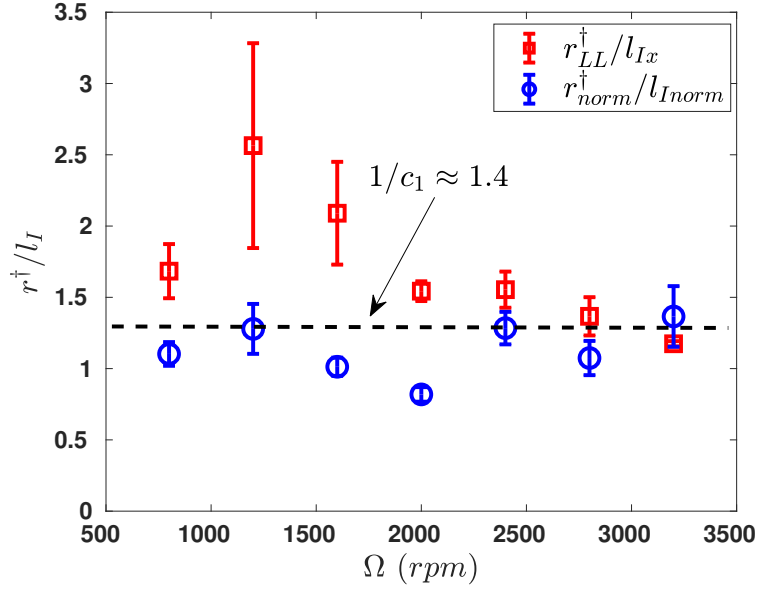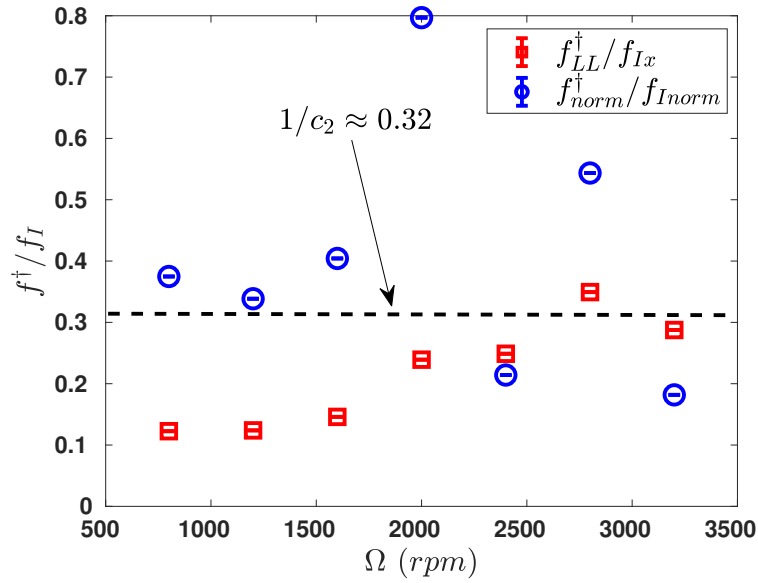
Fig. III.33 *(a) Values of $r^\dagger$ normalized by the integral scale l_I. Red squares: Longitudinal component of velocity fluctuations. Blue circles: Fluctuations of the norm of velocity. Dashed line corresponds to a value of $1/c_1 \approx 1.4$. (b) Values of $f^\dagger$ normalized by the integral frequency $f_I = u'_{rms}/l_I$. Red squares: Longitudinal component of velocity fluctuations. Blue circles: Fluctuations of the norm of velocity. Dashed line corresponds to a value of $1/c_2 \approx 0.32$.*

III.6 Conclusion

In this chapter we have studied the behaviour of coherence of velocity in a turbulent flow both analytically and experimentally. We can conclude our investigation into coherence as follows,

- Coherence is a quantity measured at two points in a turbulent flow and depending on both space and time. Our experiments show that it has a reproducible behaviour as evidenced for two different experiments. The results are observed to be independent of the experimental techniques where one experimental technique offered better temporal resolution while the other offered better spatial resolution.

- Single point as well as two-point spatio-temporal measurements in studying the dynamics of inertial scales would be affected by the effect of their sweeping by the larger, energetic integral scales.

- Energy spectrum in frequency evaluated at one point captures the effect of sweeping by the integral scales as well as a mean flow if present. The quantity of coherence captures only the effect of sweeping by the energy containing integral scales.

- For the inertial scales, $f > f_I$, magnitude squared coherence decays exponentially for both the components and the norm of velocity and has the functional form,

$$\mathcal{C}(r, f) = \exp\left[- \left(\frac{c_1 r}{l_I}\right) - \left(\frac{c_3 r f}{u'_{rms}}\right)\right]$$

  where the constants observed to be $c_1 \sim O(1)$ and $c_3 \sim O(1)$ for both the flows that we studied. The first part on the right hand side $\left(\exp[-c_1 r / l_I]\right)$ is owing to the spatial dependence of the velocity belonging to the integral scales and would be negligible for $r \ll l_I$. The second part on the right hand side $\left(\exp[-c_3 r f / u'_{rms}]\right)$ is due to the sweeping of smaller scales by the integral scales and is in agreement with the functional form derived analytically (eqn.(III.20)).

- The low frequency behaviour of coherence ($f < f_I$) possibly comes from the sweeping of the vorticity filaments by the integral scales. Its behaviour is inconclusive from our two experiments. In one experiment, the behaviour of coherence deviates from an exponential decay for low frequencies while in the other experiment it is observed to decay exponentially even at low frequencies.

Our theoretical and experimental work suggests that the characteristics of the sweeping of the inertial scales can be understood by studying the quantity of coherence normalized by its value at zero frequency. It has the form,

$$\frac{\mathcal{C}(r, f)}{\mathcal{C}_0(r)} = \exp\left[- c_3 \left(\frac{r f}{u'_{rms}}\right)\right]$$

where c is an experimental constant. We can also obtain this form of the behaviour of the

coherence for the inertial scales on qualitative arguments. If we are measuring the velocity fluctuations at two points in a turbulent flow separated by a distance r, the average time that a velocity fluctuation belonging to the inertial scales will take to get advected by a distance r would be given by,

$$\tau_{adv} \sim \frac{r}{u'_{rms}}$$

There would be a second timescale associated with the measurement of the coherence which would be the correlation between velocity fluctuations measured at points separated not only by a distance r but also temporally by,

$$\tau_{corr} \sim \frac{1}{f}$$

This simple qualitative analysis shows that,

$$\frac{\mathcal{C}(r,f)}{\mathcal{C}_0(r)} \sim F\left(\frac{\tau_{adv}}{\tau_{corr}}\right) \sim F\left(\frac{rf}{u'_{rms}}\right) \tag{III.37}$$

where F is some unknown function. Now, if the behaviour of the decay in $\mathcal{C}/\mathcal{C}_0$ is scale invariant which would be the case for inertial scales in homogeneous isotropic turbulence, the function F would have the property,

$$
\begin{aligned}
F^n(x) &= F(nx) \\
F(0) &= 1 \\
F(x) &\xrightarrow{x\to\infty} = 0
\end{aligned}
\tag{III.38}
$$

Equations (III.37) and (III.38) would then imply that,

$$\frac{\mathcal{C}(r,f)}{\mathcal{C}_0(r)} = \exp\left[-c_3\left(\frac{rf}{u'_{rms}}\right)\right]$$

which is exactly what we have observed experimentally. This resembles our observations without the dependence of the coherence at zero-frequency. As a concluding remark, in the experiments that were performed by Davenport *et al.* [93], the authors did not observe any decay in space corresponding to our experimental observation of coherence decaying exponentially at zero frequency. This is likely due to the fact that in the case of experiments performed in open wind farms the integral scale is associated with the atmospheric turbulent flow is very large compared to the distances between the points of measurement, in which case,

$$C_0(r) = e^{-\left(\frac{r}{l_I}\right)} \xrightarrow{l_I \to \infty} 1$$

Chapter IV

Acoustic scattering by turbulent flows

« J'écris, mais que sont les mots en définitive? Quelques éraflures sur une surface blanche et lisse. Je n'éprouve plus le besoin de garder une trace. »

"I write, but what are the final words? Some scratches on a smooth white surface. I no longer feel the need to keep track."[2]

Dimanche 19 octobre

Lighthill [101, 102] in his two seminal articles first studied the problem of sound generated aerodynamically (also called vortex sound) as intrinsic to an unsteady, inviscid incompressible flow (fig.IV.1a). This was different from the earlier studies on sound generated in flows which were attributed to fluctuating boundary conditions, body forces or mass sources [103]. This gave a mathematically rigorous basis to various physical phenomena like sound generated by storms in the atmosphere [104, 105], subsonic jets [106] and by the flight of an owl [107]. Lighthill showed that the incompressible flow acts as a field of quadrupole sources in generating sound unlike sound generated by moving boundaries which either act as monopoles or dipoles.

This phenomenon of unsteady flow generating sound can be further extended to probe turbulent flows using acoustic waves and their scattering by the flow. The earliest of studies on sound-flow interaction was presented by Rayleigh [108] who treated the problem of refraction of sound waves by flows. Subsequent work by Obukhov [109], Blokhintzev [110], Kraichnan [111] and others led to further development in this field and the study of sound scattering due to velocity gradients in the flow. Fabrikant *et al.* [112] and Lund *et al.* [113] related the scattered acoustic field with the vorticity field in the flow (instead of velocity gradients) and gave compact formulae in the far-field limit under the approximations of Born and low Mach number of the flow. Experimental studies and the verification of the theory was carried out consequently on laminar as well as turbulent flows and was also used in the study of vorticity filaments ([114, 63, 60, 115, 116, 117, 118, 119] and references cited therein). It was first noted by Chu *et al.* [120] that the governing equations can be decomposed into coupled equations for the three hydrodynamic modes of vorticity, sound and entropy. Under

135

the framework of asymptotic expansion, they obtained the equations of these three modes with the non-linear coupling deducible from the uncoupled equations. Accounting for the vorticity-sound interaction results in the scattering of sound due to vorticity inhomogeneities in the flow whereas accounting for the entropy-sound interaction results in the scattering of sound due to temperature inhomogeneities in the flow. The formulae for scattering of sound due to temperature inhomogeneities were given by Tatarskii [121] and Chernov [122]. Experimental studies performed on buoyancy driven flows [123, 124, 125, 126] and on weakly heated jet [127] validated the analytical results.

(a)
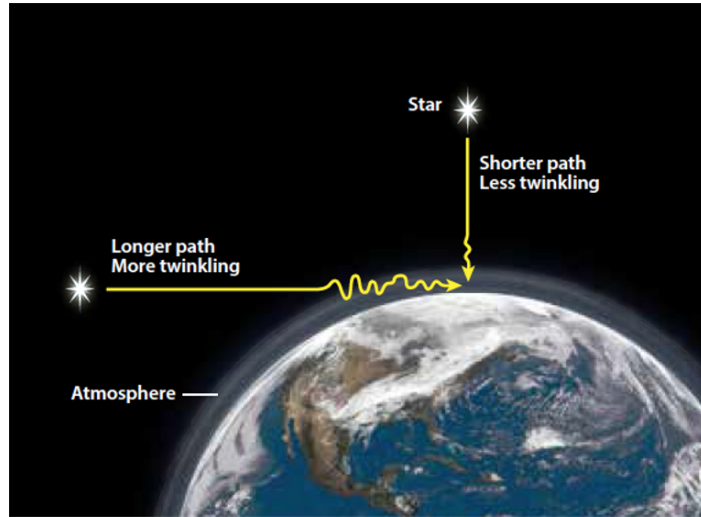
(b)

Fig. IV.1   *(a) Sequence of images shows the generation of tornado in Kansas in 2016. Tornadoes have strong vorticity concentrated in the unsteady flow at the core thus generating sound [128]. (b) Illustration showing star scintillation or twinkling which occurs due to scattering of light by turbulent atmosphere in LOS propagation [129].*

Apart from studying the scattered acoustic field due to vorticity and temperature inhomogeneities in the flow, there are two other effects which are equally if not more important due to their physical implications. As Tatarskii [121] notes, the scattering due to turbulent flow also results in fluctuations of the amplitude and phase of the incoming sound wave in the particular case of Line-Of-Sight (LOS) propagation, i.e., when the scattering angle is zero. This has practical use for example in underwater ultrasound transmission. This effect is not restricted to only acoustic waves but can also be extended to electromagnetic waves and is important, as an example, for optical ground based telescopes. The light reaching earth from the stars can be considered to be in LOS configuration. The fluctuations in its amplitude and phase due to atmospheric turbulence is the reason for the twinkling of stars (also known as star scintillation) seen by an observer on earth [130] (fig.IV.1b). Finally, as noted by Lund [18], the effect of multiple scattering of acoustic waves due to the inhomogeneities present in the flow result in coherent wave propagation and the change in speed of sound of the incident acoustic wave. In this chapter we experimentally study the scattering of acoustic waves in the LOS configureation. We ask the following two questions,

Q1A: What are the characteristics of the phase and amplitude fluctuations of the incident acoustic wave undergoing scattering? How are they related to the properties of the turbulent flow which scatters the incident acoustic wave? Inversely, can we comment on the properties of the turbulent flow from the behaviour of the fluctuations in the phase and amplitude of the incident acoustic wave?

Q1B: Can we experimentally observe the existence of a coherent wave propagating due to the effect of multiple scattering? Can we measure the resulting change in speed of sound which would be a direct indication of coherent wave propagation?

Two extensive references on the topics to be studied in this chapter are the books by Tatarskii [121] and by Ostachev [131]. The presentation of this chapter is as follows,

Sec.IV.1: presents the basic theoretical background of two effects, viz., the spontaneous generation of sound by an acoustic wave by an incompressible flow also called as *vortex sound* and the scattering of an incident acoustic wave by a turbulent flow. We derive the governing equation for the scattering of an acoustic wave by a turbulent flow in the limit of *geometrical acoustics.*

Sec.IV.2: is devoted to obtaining the governing equations and understanding the behaviour they predict for the two problems that will be experimentally studied. The two problems to be experimentally studied are the fluctuations in amplitude and phase of an acoustic wave by a turbulent flow and the change in the speed of sound due to the effect of multiple scattering in a turbulent flow.

Sec.IV.3 and IV.4: present the experimental setup and the results that are obtained for the two problems of interest to us. The relation between the parameter fluctuations of an acoustic wave and the *sweeping effect* is investigated and its validity is checked experimentally.

Sec.IV.5: We give a brief summary and conclusions of our analytical and experimental work of this chapter.

IV.1 Theoretical background

IV.1.1 Vortex sound

We have presented in chapter II the two limits of the weakly compressible flow at low Mach numbers; the limit of incompressible flow and the limit of acoustic waves with the following order of magnitudes of the perturbed quantities,

$$\frac{p'}{p_0} \ll \frac{\rho'}{\rho_0} \sim \frac{T'}{T_0} \sim O(\mathcal{M}a^2) \ll 1 \; \Rightarrow \text{incompressible flow}$$

$$\frac{p'}{p_0} \sim \frac{\rho'}{\rho_0} \sim \frac{T'}{T_0} \sim O(\mathcal{M}a) \ll 1 \; \Rightarrow \text{acoustic waves}$$

where p_0, ρ_0 and T_0 are the pressure, density and temperature of the fluid at rest. The perturbations in pressure, density and temperature of the weakly compressible flow are denoted by p', ρ' and T' respectively.

The interaction between the flows associated with the two limits results in the generation of acoustic waves by the incompressible flow which is called *vortex sound*. The qualitative understanding on the generation of vortex sound can be given as follows. Let us say we are given an unsteady, inviscid, incompressible flow of low Mach number such that the vorticity is bounded initially in some finite domain. Due to Kelvin's circulation theorem [68], the vorticity would remain bounded. Far from the bounded vorticity, the velocity would decay[1] as $|\mathbf{x}|^{-3}$ whereas the pressure, temperature and density fluctuations would decay[2] $|\mathbf{x}|^{-6}$. The velocity and pressure fields in this scenario would be entirely characterized by the vorticity field.

In the incompressible limit, the pressure fluctuations do not result in density fluctuations to the leading order. At higher order in the Mach number, the pressure fluctuations will result in density fluctuations, let us call them ρ''. Note that the density fluctuations ρ'' are different and of higher order in Mach number than the density fluctuations associated with the incompressible flow ρ'. If the density fluctuations ρ'' are at the same order as the pressure fluctuations, we would have,

$$\frac{p'}{p_0} \sim \frac{\rho''}{\rho_0} \ll \frac{\rho'}{\rho_0} \sim O(\mathcal{M}a^2)$$

To the leading order, the density fluctuations observed would still be the ones of $\rho'/\rho_0 \sim O(\mathcal{M}a^2)$ of the incompressible flow and which are independent of the pressure fluctuations.

---

[1]This can be shown by writing the equation for vector potential, which turns out to be a Poisson equation. If the vorticity is assumed to be bounded, the Green's function of this equation and thus the vector potential decays inversely with the distance and the velocity field as inverse of distance cubed far from the bounded vorticity.

[2]In the incompressible limit the source for temperature fluctuations is viscous dissipation which will decay as velocity squared or equivalently as $|\mathbf{x}|^{-6}$. Owing to the linear dependence of temperature and density fluctuations from the equation of state, density fluctuations will decay in the same manner as temperature fluctuations.

The density fluctuations ρ'' driven by the pressure fluctuations of the incompressible flow would be at orders higher than two in Mach number. These density fluctuations would result in acoustic waves and would decay slower in space than the density fluctuations of the incompressible flow[3]. Thus, in the far field limit, we would observe acoustic waves which would be a direct result of the pressure (and thus stress) fluctuations of the incompressible flow.

Since the background incompressible flow is completely characterized by vorticity at any given instant, we use the two terms '*incompressible flow*' and '*vortical flow*' interchangeably. The process of generation of vortex sound which has been described qualitatively in the previous paragraph is illustrated in sketch IV.2. The characteristic scales involved depend on the region of the flow considered. The length scales associated with the vorticity, the region of the domain bounding vorticity and the acoustic waves are l_0, l_B and the wavelength λ respectively. Since the acoustic waves are forced by the incompressible flow, the characteristic time-scales should be the same in both the regions. This gives us along with the condition $\mathcal{Ma} \ll 1$,

$$l_0 \leq l_B \ll \lambda$$

One point to note is that the acoustic waves observed far from the bounded vorticity is obviously a compressible effect and the relations between the thermodynamic quantities of pressure, density and temperature are given by the equation of state (say ideal gas law) and the equation for isentropic process which we have assumed to be the case. Whereas, an equation of state for incompressible flow does not involve pressure and the only role of pressure is to ensure that the incompressible flow remains divergence-less.
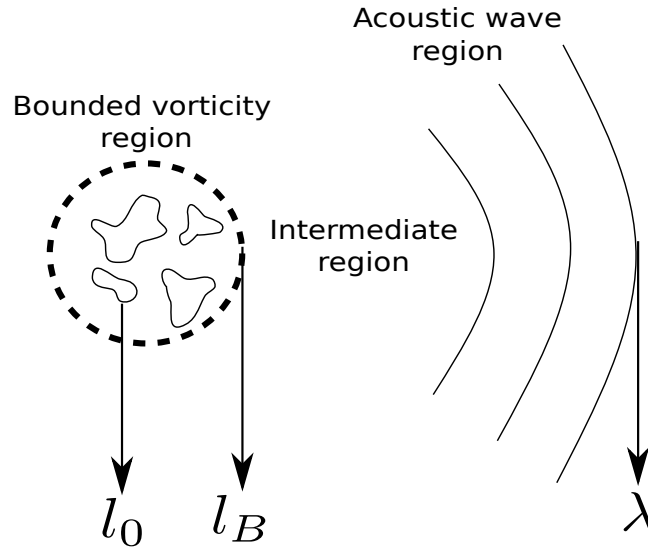

Fig. IV.2   *Sketch of weakly compressible flow with region of bounded vorticity, intermediate region and region with acoustic waves.*

---

[3]This can be seen from the Green's function for the wave equation. In 3D, the velocity, density and temperature field will decay as $|\mathbf{x}|^{-1}$ from the bounded vorticity in the far field limit.

The governing equation describing the effect of vortex sound is given by eqn.(IV.1) (for its derivation, see Appendix IV.A),

$$\frac{\partial^2 \rho}{\partial t^2} - c^2 \nabla^2 \rho = \rho_0 \frac{\partial^2 (u_{B,i} u_{B,j})}{\partial x_i \partial x_j} = \frac{\partial^2 T_{i,j}}{\partial x_i \partial x_j} \tag{IV.1}$$

where $\mathbf{u}_B$ is the velocity field associated with the incompressible background flow and the components of the tensor $\overline{\overline{T}}$ are,

$$T_{ij} = \rho_0 u_{B,i} u_{B,j}$$

This was the equation derived by Lighthill on physical grounds. Owing to the form of the source term on the right hand side, we infer that the acoustic field generated far from bounded vortical flow is a result of a field of quadrupoles. Ideally, a more mathematically rigorous analysis would involve decomposition of the velocity field into a solenoidal field (corresponding to the incompressible flow) and an irrotational field (corresponding to the acoustic waves) and using method of matched asymptotic expansions for the two regions. This was done by Crow [132]. After Lighthill's work, it was shown that the source could also be written as a field of monopoles [133] or dipoles [134, 135] involving vorticity and whose respective monopole and dipole strength vanish since they all describe the generation of the same acoustic field. It also showed that indeed the sound was generated by vorticity and the sources would vanish outside the region of bounded vorticity. Lighthill [101] showed that the density fluctuations in the vortex sound will be of $O(\mathcal{M}a^4)$ and thus are indeed much smaller than the density fluctuations in the incompressible background flow which are of $O(\mathcal{M}a^2)$.

IV.1.2 Acoustic scattering

In the previous section we briefly introduced the spontaneous generation of vortex sound by unsteady, inviscid vortical flow. If the bounded vortical flow has a characteristic timescale of evolution of $^1/f_0$, the vortex sound far from the bounded vortical flow would have a frequency of f_0.

Now, suppose, we send an acoustic wave incident on the region of bounded vorticity. Such an incident wave would be associated with an irrotational flow. In the absence of any non-linearities in the governing equations, the incident acoustic wave and the vortical flow would be decoupled and would evolve independently. Accounting for non-linearities in the governing equations would result in (1) generation of vortex sound as seen from the previous section and which would have characteristic timescale that of the vortical flow and (2) coupling between the incident acoustic wave and the bounded vortical flow which would result in the scattering of the incident wave by the vortical flow and advection of the vortical flow by the incident acoustic wave. The scattered wave would, thus, carry information about the vortical flow. Though, separating the contribution of the vortex sound from that of the scattered wave far from the bounded vorticity needs additional constraints on the properties of the incident wave. This can be achieved by ensuring that the incident wave evolves on a timescale much smaller than any timescale encountered in the vortical flow ($f_I \gg f_0$) and thus the vortex

sound and scattered wave would be observed in different range of frequencies. Additionally, if we assume the incident wave to be of low amplitude, the modifications to the vortical flow would be negligible. Thus, a low amplitude, high frequency incident wave would allow us to probe the vortical flow without being intrusive.

A physical interpretation of this process can be given as follows. A low-amplitude, high frequency incident wave would see the vortical flow as essentially frozen in time. This incident wave would generate high frequency fluctuations in the vorticity while keeping it undisturbed on timescales associated with the flow. The fluctuating, unsteady vorticity would generate acoustic waves[4]. A schematic diagram is shown in fig.IV.3. An equation for the scattered acoustic wave can be derived (Appendix IV.B) and is given by eqn.(IV.2). The frequency and wavevector of the incident wave are denoted by f_I and $\mathbf{k_I}$ respectively. The inverse of the time scale associated with the vortical flow is denoted by f_0 whereas the wavevector of the scattered wave and the scattering angle are denoted by $\mathbf{k_S}$ and θ respectively.
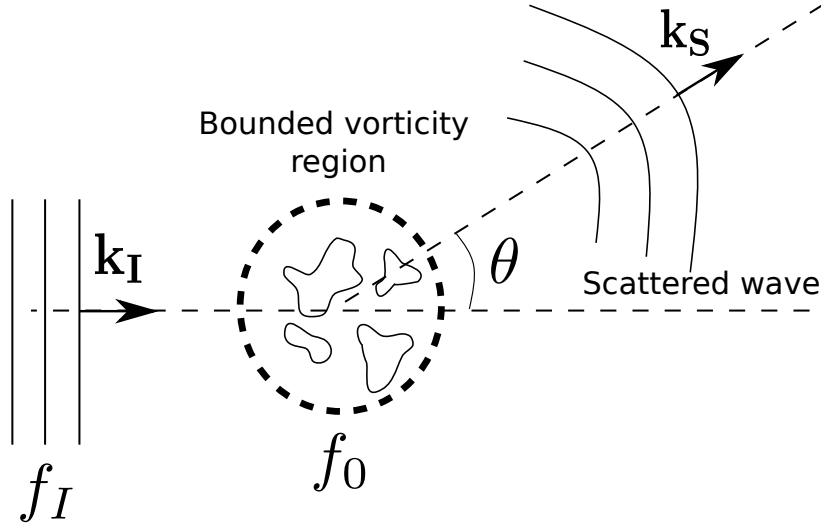
Fig. IV.3 *Sketch of plane wave incident on a region of bounded vorticity. The scattering angle is denoted by θ.*

We see that eqn.(IV.2) is a wave equation with the terms on the right hand side acting as sources. The first source term denotes the scattering due to interaction between the velocity field of the incident wave and the bounded vortical flow. The second source term denotes the interaction between the density field of the incident wave and the velocity field of the bounded vortical flow. The next two source terms are due to interaction between the density fluctuations in the weakly compressible vortical flow and the incident wave. If we account for temperature fluctuations in the vortical flow T_B (such that $\langle T_B \rangle = 0$) we obtain the last term with temperature fluctuations acting as source.

---

[4]This naive interpretation is not entirely correct as it neglects the interaction between the incident wave and the flow generated by the vorticity.

$$\frac{\partial^2 \rho_S}{\partial t^2} - c^2 \nabla^2 \rho_S = 2\rho_B \frac{\partial^2(u_{B,i}u_{S,j})}{\partial x_i \partial x_j} + \frac{\partial^2(\rho_S u_{B,i}u_{B,j})}{\partial x_i \partial x_j}$$
$$+ 2\left(\frac{\partial \rho_B}{\partial x_i}\right)\frac{\partial(u_{B,i}u_{S,j} + u_{B,j}u_{S,i})}{\partial x_j} + 2\left(\frac{\partial^2 \rho_B}{\partial x_i \partial x_j}\right)u_{B,i}u_{S,j} + c^2 \nabla \cdot \left(\left(\frac{T_B}{T}\right)\nabla \rho_S\right)$$

$$\text{(IV.2)}$$

where we have assumed that the incident and scattered waves have negligible temperature fluctuations associated with them owing to their small amplitudes. The speed of sound 'c' in the above equation is evaluated using the ambient values of pressure, density and temperature. For an ideal gas, it is given by,

$$c = \sqrt{\frac{\gamma p_0}{\rho_0}} = \sqrt{\frac{\gamma R T_0}{M}}$$

The relative order of magnitudes of the source terms in eqn.(IV.2) are as follows,

$$\rho_B \frac{\partial^2(u_{B,i}u_{S,j})}{\partial x_i \partial x_j} \Big/ c^2 \nabla^2 \rho_S \sim \frac{\rho_0 u_B u_S / \lambda^2 \left[1 + O(\mathcal{M}a^2) + O\left(\frac{\lambda}{l_0}\right) + ...\right]}{\rho_0 u_S c / \lambda^2} \sim O(\mathcal{M}a)$$

$$\frac{\partial^2(\rho_S u_{B,i}u_{B,j})}{\partial x_i \partial x_j} \Big/ c^2 \nabla^2 \rho_S \sim \frac{\rho_S u_B^2 / \lambda^2 \left[1 + O(\mathcal{M}a^2) + O\left(\frac{\lambda}{l_0}\right) + ...\right]}{\rho_0 u_S c / \lambda^2} \sim O(\mathcal{M}a^2)$$

$$\left(\frac{\partial \rho_B}{\partial x_i}\right)\frac{\partial(u_{B,i}u_{S,j} + u_{B,j}u_{S,i})}{\partial x_j} \Big/ c^2 \nabla^2 \rho_S \sim \frac{\rho_B u_B u_S / l_0 \lambda \left[1 + O(\mathcal{M}a^2) + O\left(\frac{\lambda}{l_0}\right) + ...\right]}{\rho_0 u_S c / \lambda^2} \sim O\left(\frac{\lambda}{l_0}\mathcal{M}a^3\right)$$

$$\left(\frac{\partial^2 \rho_B}{\partial x_i \partial x_j}\right)u_{B,i}u_{S,j} \Big/ c^2 \nabla^2 \rho_S \sim \frac{\rho_B u_B u_S / l_0^2 \left[1 + O(\mathcal{M}a^2) + ...\right]}{\rho_0 u_S c / \lambda^2} \sim O\left(\left(\frac{\lambda}{l_0}\right)^2 \mathcal{M}a^3\right)$$

$$c^2 \nabla \cdot \left(\left(\frac{T_B}{T}\right)\nabla \rho_S\right) \Big/ c^2 \nabla^2 \rho_S \sim \frac{\rho_0 u_S c / \lambda^2 \times (T_B/T) \times \left[1 + O\left(\frac{\lambda}{l_T}\right)\right]}{\rho_0 u_S c / \lambda^2} \sim O\left(\frac{T_B}{T}\right) \sim O(\mathcal{M}a^2)$$

where λ is the wavelength of the incident wave and l_0 and l_T are the characteristic length scales associated with the velocity and temperature fluctuations in the background vortical flow respectively. We have also used $O\left(\frac{\rho_S}{\rho_0}\right) \sim O\left(\frac{u_S}{c}\right)$ since for acoustic waves density fluctuations are of $O(\mathcal{M}a)$. Note that till this point we have not used the assumptions of $f_I \gg f_0$, amplitude of incident wave being much weaker than the background flow or the relative magnitudes of the wavelength of the incident wave and the typical length scale of the vortical flow.

IV.1.3 The geometrical acoustic limit

Let us first consider the case when the background flow is considered to be comprised of only the incompressible flow (i.e. neglecting any density fluctuations at $O(\mathcal{M}a^2)$ or from vortex sound). The continuity and momentum equations at next order (where the $O(1)$ equations would correspond to the background flow) without any assumptions can be written as,

$$\underbrace{\frac{\partial \rho_S}{\partial t}}_{O(1)} + \underbrace{(\mathbf{u}_B \cdot \nabla)\rho_S}_{O(\mathcal{M}a)} = -\underbrace{\rho_B \nabla \cdot \mathbf{u}_S}_{O(1)}$$

$$\underbrace{\frac{\partial \mathbf{u}_S}{\partial t}}_{O(1)} + \underbrace{(\mathbf{u}_B \cdot \nabla)\mathbf{u}_S}_{O(\mathcal{M}a)} + \underbrace{(\mathbf{u}_S \cdot \nabla)\mathbf{u}_B}_{O\left(\mathcal{M}a\left(\frac{\lambda}{l_0}\right)\right)} = -\underbrace{\frac{1}{\rho_B}\nabla p_S}_{O(1)} + \underbrace{\frac{\rho_S}{\rho_B^2}\nabla p_B}_{O\left(\mathcal{M}a^2\left(\frac{\lambda}{l_0}\right)\right)} \tag{IV.3a}$$

The geometrical acoustic limit is the case when,

$$\frac{\lambda}{l_0} \ll 1$$
$$\frac{\lambda}{l_T} \ll 1$$

On neglecting the terms of $O\left(\frac{\lambda}{l_0}\right)$, we obtain,

$$\frac{\partial \rho_S}{\partial t} + \mathbf{u}_B \cdot \nabla \rho_S \approx -\rho_B \nabla \cdot \mathbf{u}_S$$
$$\frac{\partial \mathbf{u}_S}{\partial t} + \frac{1}{\rho_B}\nabla p_S \approx -(\mathbf{u}_B \cdot \nabla)\mathbf{u}_S \tag{IV.4}$$

Combining the above two equations gives us,

$$\frac{\partial^2 \rho_S}{\partial t^2} - c^2 \nabla^2 \rho_S = \rho_B \nabla \cdot \left[(\mathbf{u}_B \cdot \nabla)\mathbf{u}_S\right] - \frac{\partial}{\partial t}\left[(\mathbf{u}_B \cdot \nabla)\rho_S\right]$$

$$\approx \rho_B(\mathbf{u}_B \cdot \nabla)(\nabla \cdot \mathbf{u}_S) - \frac{\partial}{\partial t}\left[(\mathbf{u}_B \cdot \nabla)\rho_S\right]$$

$$\approx -(\mathbf{u}_B \cdot \nabla)\left(\frac{\partial \rho_S}{\partial t} + \mathbf{u}_B \cdot \nabla \rho_S\right) - \frac{\partial}{\partial t}\left[(\mathbf{u}_B \cdot \nabla)\rho_S\right]$$

where we have used $\lambda/l_0 \ll 1$ for the second approximation and substituted the continuity equation again to obtain the last equation.

Rearranging the equation gives us,

$$\left(\frac{\partial}{\partial t} + \mathbf{u_B} \cdot \nabla\right)^2 \rho_S - c^2 \nabla^2 \rho_S = 0$$

Accounting also for fluctuations in temperature with $\lambda/l_T \ll 1$,

$$\left(\frac{\partial}{\partial t} + \mathbf{u}_B \cdot \nabla\right)^2 \rho_S - c^2 \nabla^2 \rho_S = c^2 \left(\frac{T_B}{T}\right) \nabla^2 \rho_S \qquad \text{(IV.5)}$$

The above equation can also be obtained from eqn.(IV.27) (Appendix IV.C) and as it illustrates, we have considered source terms upto $O(\mathcal{M}a^2)$ to arrive at the eqn.(IV.5) [5]. We involve scattering due to temperature fluctuations since the background flow is incompressible and thus $\left(\frac{T_B}{T}\right) \sim O(\mathcal{M}a^2)$. Tatarskii, in his monograph on waves in turbulent media [121], uses eqn.(IV.5) for studying scattering effects.

For the experimental study to be presented in this chapter, we are in the regime of geometrical acoustics. The results obtained therein and their theoretical understanding will be centered about this master equation.

---

[5]Till this point, we have not used the assumption of separation in temporal scales, $f_I \gg f_0$, which leads to further simplifications

IV.2 Acoustic scattering in Line Of Sight (LOS) propagation

IV.2.1 Parameter fluctuations of incident wave in LOS propagation

We consider the case of zero scattering angle (forward scattering or LOS propagation) with both the acoustic source and the receiver placed within the bounded flow region. The schematic of this arrangement is shown in figure IV.4. We disregard the flow lying before the source and after the receiver and thus consider only the region between the two.
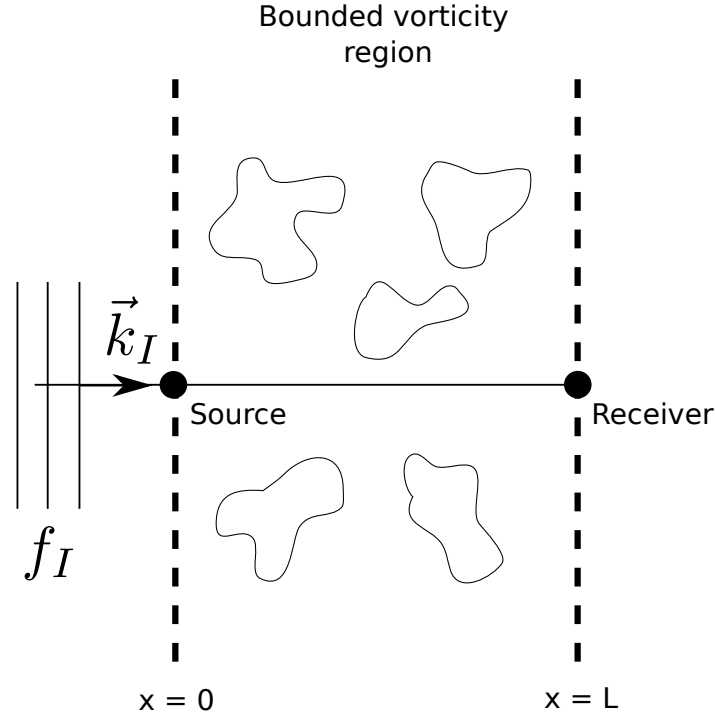
Fig. IV.4 *Sketch of line of sight propagation.*

The problem of scattering can be framed as either solving for the scattered wave (where the total acoustic field is the sum of the incident and the scattered acoustic field) or solving for the fluctuations in the parameters (namely amplitude and phase) of the incident wave. The second approach is practically more relevant for LOS propagation since the effects are intuitively easier to grasp. For example, scintillation of stars is due to fluctuations in amplitude and phase when light travels through turbulent atmosphere of the earth.

Since the scattering angle is zero, the problem can be reduced to one dimension, along the direction of the incident wavevector. For simplicity, assume this to be along x-axis ($\mathbf{k_I} = k_I \hat{x}$). In proceeding with our analysis we will use the method developed by Rytov [136, 137], where the complex scalar wave-field 'ζ' (whose real part could be components of velocity, pressure, density or temperature) is written as,

$$\zeta(x,t) = e^{\Psi(x,t)}$$

where $\Psi(x,t)$ is the complex phase.

For a plane wave traveling along x-direction, we have $\zeta(\mathbf{x}, t) = A e^{\iota(kx - ft)}$. Comparing it with the Rytov representation, we find,

$$\Re(\Psi) = \log(A) = \chi$$
$$\Im(\Psi) = kx - ft = \phi$$

Thus the real part of the complex phase corresponds to the log-amplitude of the wave-field (denoted by χ) and the imaginary part corresponds to the phase of the wave-field (denoted by ϕ). We start by rewriting our master equation, eqn.(IV.5) in terms of pressure, which reads,

$$\frac{1}{c^2}\left(\frac{\partial}{\partial t} + \mathbf{u}_B \cdot \nabla\right)^2 p_S - \nabla^2 p_S = \left(\frac{T_B}{T}\right)\nabla^2 p_S$$

On expanding and neglecting the term $(\mathbf{u}_B \cdot \nabla)(\mathbf{u}_B \cdot \nabla)p_S$ which is of $O(\mathcal{M}a^2)$, we obtain,

$$\frac{1}{c^2}\frac{\partial^2 p_S}{\partial t^2} - \nabla^2 p_S = -\underbrace{\frac{1}{c^2}\left(\frac{\partial \mathbf{u}_B}{\partial t}\cdot\nabla p_S\right)}_{O\left(\frac{f_0}{f_I}\right)} - \frac{2}{c^2}\left(\mathbf{u}_B\cdot\nabla\left(\frac{\partial p_S}{\partial t}\right)\right) + \left(\frac{T_B}{T}\right)\nabla^2 p_S$$

Further simplification is obtained if we assume the frequency of the incident wave to be much larger than the frequency of the background incompressible flow, i.e., $f_I \gg f_0$. The second term on the right hand side which is of $O\left(\frac{f_0}{f_I}\right)$ can then be neglected. Thus we obtain the equation,

$$\frac{1}{c^2}\frac{\partial^2 p_S}{\partial t^2} - \nabla^2 p_S = -\frac{2}{c^2}\left(\mathbf{u}_B\cdot\nabla\left(\frac{\partial p_S}{\partial t}\right)\right) + \underbrace{\left(\frac{T_B}{T}\right)\nabla^2 p_S}_{O(\mathcal{M}a^2)} \qquad (\text{IV.6})$$

where the first term on the right hand side is of $O(\mathcal{M}a)$. The last term on the right hand side involving temperature fluctuations would be negligible since $\left(\frac{T_B}{T}\right) \sim O(\mathcal{M}a^2)$ for an incompressible flow. Thus the final equation for the scattered wave is,

$$\frac{1}{c^2}\frac{\partial^2 p_S}{\partial t^2} - \nabla^2 p_S = -\frac{2}{c^2}\left(\mathbf{u}_B\cdot\nabla\left(\frac{\partial p_S}{\partial t}\right)\right) \qquad (\text{IV.7})$$

Eqn.(IV.7) can also be obtained from eqn.(IV.2) keeping source terms till $O(\mathcal{M}a)$ and using $\frac{\partial \rho_S}{\partial t} \approx -\rho_B \nabla \cdot \mathbf{u}_S$ from eqn.(IV.4) since, $\mathbf{u}_B \cdot \nabla \rho_S \big/ \rho_B \nabla \cdot \mathbf{u}_S \sim O(\mathcal{M}a)$. Substituting Rytov representation[6] and solving the equation at $O(\mathcal{M}a)$ (Appendix IV.D), we obtain,

$$\Phi_1(L, y, z, t) = k_I \int_0^L \ dx \ n'(x, y, z, t) \tag{IV.8}$$

$$\chi_1(L, y, z, t) = -\frac{1}{2} \int_0^L \ dx \ \int_0^x \ d\zeta \ \Big[\frac{\partial^2 n'(\zeta, y, z, t)}{\partial y^2} + \frac{\partial^2 n'(\zeta, y, z, t)}{\partial z^2} \Big] \tag{IV.9}$$

We reiterate that we have assumed the direction of propagation of the incident wave to be along the x-axis.. The fluctuations in the refractive index, denoted by $n'(\mathbf{x}, t)$ are given by,

$$n'(\mathbf{x}, t) = -\left(\frac{\hat{m} \cdot \mathbf{u}_B}{c} \right) \tag{IV.10}$$

The details of obtaining equations (IV.8)-(IV.10) are given in appendix IV.D. Equations (IV.8)-(IV.10) can also be found in Tatarskii's book [121] albeit with a slightly different method for obtaining them. Tatarskii [121] relates the spatial dependence of the fluctuations in phase and log-amplitude to that of the spatial structure of the turbulent flow. We, instead, will concentrate at the temporal characteristics of the phase and log-amplitude fluctuations.

IV.2.2 Statistical properties of phase fluctuations of the incident wave

We begin with assuming that the incompressible background flow is turbulent and statistically *homogeneous* and *isotropic*. Owing to isotropy, we have $\langle \mathbf{u}_B \rangle = 0$. We also have from definition $\langle T_B \rangle = 0$. Using equation (IV.8), we first notice that,

$$\Big\langle \Phi_1(t) \Big\rangle = k_I \int_0^L \ dx \ \Big\langle n'(x, t) \Big\rangle = 0$$

We can write the auto-correlation function for phase fluctuations,

$$\Big\langle \Phi_1(t) \Phi_1(t + \tau) \Big\rangle = k_I^2 \int_0^L \ dx \ \int_0^L \ dy \ \Big\langle n'(x, t) n'(y, t + \tau) \Big\rangle$$

Now,

$$\Big\langle n'(x, t) n'(y, t + \tau) \Big\rangle = \frac{\Big\langle u_{B,x}(x, t) u_{B,x}(y, t + \tau) \Big\rangle}{c^2}$$

---

[6]Note that the eqn.(IV.7) is linear in p_S and thus would hold for the complex wave-field.

Substituting it back in the equation of phase auto-correlation,

$$\left\langle \Phi_1(t)\Phi_1(t+\tau) \right\rangle = \frac{k_I^2}{c^2} \int_0^L dx \int_0^L dy \left\langle u_{B,x}(x,t)u_{B,x}(y,t+\tau) \right\rangle$$

Taking the temporal Fourier transform on both sides and using the Wiener-Khinchin theorem for a stationary process (we also assume the turbulent flow to be stationary),

$$\boxed{E_{\Phi_1}(f) = \frac{2k_I^2}{c^2} \int_0^L dz \int_{-z}^z dr \, \widetilde{E}_{u_{B,x}}(r,f)} \tag{IV.11}$$

where we have used the transformation $z = x+y$ and $r = y-x$. The temporal cross-spectrum of $u_{B,x}$ at two points separated by a distance r is denoted by $\widetilde{E}_{u_{B,x}}$ and has the definition,

$$\widetilde{E}_{u_{B,x}}(r,f) = \int_{-\infty}^{+\infty} d\tau \left\langle u_{B,x}(0,0)u_{B,x}(r,\tau) \right\rangle e^{-2\pi \iota f \tau}$$

Note that, the cross-spectra are, in general, complex quantities and thus carry phase information and the integrand on the right hand side of eqn.(IV.11) is a complex quantity, whereas the energy spectrum of phase fluctuations on the left hand side of the equation is a real quantity. The right hand hand side of eqn.(IV.11) would be real since,

$$\int_{-z}^z dr \, \widetilde{E}_{u_{B,x}}(r,f) = \int_0^z dr \left[\widetilde{E}_{u_{B,x}}(r,f) + \widetilde{E}_{u_{B,x}}(-r,f) \right]$$

$$= \int_0^z dr \left[\widetilde{E}_{u_{B,x}}(r,f) + \widetilde{E}^*_{u_{B,x}}(r,f) \right] \Rightarrow \text{Real}$$

where the asterisk denotes complex conjugate and $\widetilde{E}_{u_{B,x}}(-r,f) = \widetilde{E}^*_{u_{B,x}}(r,f)$ owing to the flow being statistically homogeneous and stationary. For the mean-square of the phase fluctuations, we get,

$$\left\langle \Phi_1^2 \right\rangle = \frac{4k_I^2 \left\langle u_{B,x}^2 \right\rangle}{c^2} \int_0^L dz \int_0^z dr \, \Gamma_u(r)$$

where the spatial two point correlation of velocity fluctuations is denoted by Γ_u and is defined as,

$$\Gamma_u(r) = \frac{\left\langle u_{B,x}(x)u_{B,x}(x+r) \right\rangle}{\left\langle u_{B,x}^2 \right\rangle}$$

If the spatial correlation has an exponential form [7],

$$\Gamma_u(r) = \exp(-|r|/l_0)$$

If we assume $l_0 \ll L$ and on subsequent substitution and solving, we obtain,

$$\boxed{\Phi_1^{rms} = \frac{2k_I u_B^{'rms}\sqrt{l_0 L}}{c}} \tag{IV.12}$$

where $u_B^{'rms}$ is the RMS of the velocity fluctuations in the turbulent flow. Note that eqn.(IV.12) gives an estimate on the magnitude of Φ_1^{rms} which can be experimentally validated.

IV.2.3 Statistical properties of log-amplitude fluctuations of the incident wave

The mean of the log-amplitude fluctuations would be given by,

$$\left\langle \chi_1(t) \right\rangle = -\frac{1}{2}\int_0^L \ dx \ \int_0^x \ d\zeta \ \left[\frac{\partial^2 \left\langle n'(\zeta,t) \right\rangle}{\partial y^2} + \frac{\partial^2 \left\langle n'(\zeta,t) \right\rangle}{\partial z^2} \right] = 0$$

where we have neglected any attenuation of the acoustic wave due to the turbulent flow. Similar to phase fluctuations, for the auto-correlation of log-amplitude fluctuations we obtain,

$$\left\langle \chi_1(t)\chi_1(t+\tau) \right\rangle = \frac{1}{4}\int_0^L \ dp \ \int_0^L \ dq \ \int_0^p \ d\alpha \ \int_0^q \ d\beta \ \left\langle \left(\frac{\partial^2 n'(\alpha,t)}{\partial x_i \partial x_i} \right)\left(\frac{\partial^2 n'(\beta,t+\tau)}{\partial x_i \partial x_i} \right) \right\rangle$$

$$= \frac{1}{4}\int_0^L \ dp \ \int_0^L \ dq \ \int_0^p \ d\alpha \ \int_{-\alpha}^{q-\alpha} \ dr \ \left\langle \left(\frac{\partial^2 n'(\alpha,t)}{\partial x_i \partial x_i} \right)\left(\frac{\partial^2 n'(\alpha+r,t+\tau)}{\partial x_i \partial x_i} \right) \right\rangle$$

We have used the index notation for brevity where $i = 2,3$ and $x_2 = y$ and $x_3 = z$. If the background turbulent flow is isotropic, homogeneous and stationary, we have,

$$\left\langle \frac{\partial^2 n'(\alpha,t)}{\partial y^2}\frac{\partial^2 n'(\alpha+r,t+\tau)}{\partial y^2} \right\rangle = \left\langle \frac{\partial^2 n'(\alpha,t)}{\partial z^2}\frac{\partial^2 n'(\alpha+r,t+\tau)}{\partial z^2} \right\rangle = \gamma_{yy}(r,\tau)$$

$$\left\langle \frac{\partial^2 n'(\alpha,t)}{\partial y^2}\frac{\partial^2 n'(\alpha+r,t+\tau)}{\partial z^2} \right\rangle = \left\langle \frac{\partial^2 n'(\alpha,t)}{\partial z^2}\frac{\partial^2 n'(\alpha+r,t+\tau)}{\partial y^2} \right\rangle = \gamma_{yz}(r,\tau)$$

---

[7]In chapter III, we experimentally observe this to be the case for two different flows and this behaviour is not far-fetched. See chapter III, figures III.10 and III.27

On substituting the form of fluctuations in refractive index (eqn.(IV.10)), we obtain,

$$\left\langle \chi_1(t)\chi_1(t+\tau) \right\rangle = \left(\frac{1}{2c^2}\right) \int_0^L dp \int_0^L dq \int_0^p d\alpha \int_{-\alpha}^{q-\alpha} dr \left[\gamma_{yy}^{u_{B,x}}(r,\tau) + \gamma_{yz}^{u_{B,x}}(r,\tau) \right]$$

On taking the temporal Fourier transform on both sides, we have,

$$\boxed{E_{\chi_1}(f) = \left(\frac{1}{2c^2}\right) \int_0^L dp \int_0^L dq \int_0^p d\alpha \int_{-\alpha}^{q-\alpha} dr \left[\widetilde{E}_{u_{B,x}}^{yy}(r,f) + \widetilde{E}_{u_{B,x}}^{yz}(r,f) \right]} \qquad \text{(IV.13)}$$

IV.2.4 Coherent wave propagation and change in speed of sound

In this section, we follow the analytical steps as laid out by Lund [18] and the details of calculations can be found therein. On neglecting the temperature fluctuations, eqn.(IV.5) along with eqn.(IV.3a) can be written in the form,

$$\left[\nabla^2 + k_I^2 - V(\mathbf{x})\right]p_S = 0 \tag{IV.14}$$

where $V(\mathbf{x}) = V^1(\mathbf{x}) + V^2(\mathbf{x})$ is a differential operator with $V^1(\mathbf{x})$ and $V^2(\mathbf{x})$ being the contributions from terms of $O(\mathcal{M}a)$ and $O(\mathcal{M}a^2)$ respectively. The scattered field of velocity, pressure and density is assumed to evolve with the incident frequency f_I and is greater than the frequency associated with the turbulent flow f_0. The time dependence is thus dropped in the ensuing analysis. The potential operator $V(\mathbf{x})$ has the form,

$$V^1\{p_S\} = \frac{2\iota}{f_I}\left(\frac{\partial p_S}{\partial x_j}\right)\left(\frac{\partial^2 u_{B,i}}{\partial x_j \partial x_i}\right)$$

$$V^2\{p_S\} = -\frac{1}{c^2}\left(u_{B,i}u_{B,j}\right)\frac{\partial^2 p_S}{\partial x_j \partial x_i} + \frac{2}{f_I^2}\frac{\partial^2}{\partial x_j \partial x_i}\left[u_{B,i}u_{B,l}\frac{\partial^2 p_S}{\partial x_l \partial x_j}\right] + k_I^2 \Delta c^2 p_S$$

where the speed of sound is a function of space denoted by $\tilde{c}(\mathbf{x})$ and has two contributions,

1. Owing to temperature fluctuations in the incompressible flow.

2. Owing pressure fluctuations in the incompressible flow driving density fluctuations.

The normalized change in speed of sound due to these two contributions is denoted by $\Delta c^2(\mathbf{x})$ and defined as,

$$\Delta c^2(\mathbf{x}) = \frac{\tilde{c}^2(\mathbf{x}) - c^2}{c^2}$$

Two observations can be made when studying eqn.(IV.14) as noted by Lund [18],

- The source operator $V(\mathbf{x})$ is a non-linear differential operator and is a function of the background flow and parameters of the incident wave.

- There will be two contributions to Δc^2, one from temperature fluctuations of the incompressible turbulent flow and second from the incompressible pressure fluctuations driving density fluctuations. The former can be shown to give a vanishing contribution to coherent wave propagation whereas the latter does not.

The Green's function for eqn.(IV.14) can be evaluated using perturbation method (which assumes that the interaction between the turbulent flow and incident wave to be weak). As outlined in [18], coherent wave propagation is indeed analytically seen to exist with the prediction for the change in speed of sound being,

$$\frac{\delta c}{c} = -\left(\frac{B_1}{2k_I^2} + \frac{\Re(B_2)}{2k_I^2} \right)$$

where δc is the change in the speed of sound of the medium owing to multiple scattering and,

$$B_1 = \frac{(\gamma - 4)k_I^2}{c^2 V} \int_V d^3x \, \langle (\hat{k}_I \cdot \mathbf{u}_B)^2 \rangle$$

$$B_2 = \frac{k_I^2}{2\pi^3 c^2 V} \int_V d^3x \, d^3q (\hat{k}_I \cdot \mathbf{q})^2 \widetilde{G}(\mathbf{q}) \Big\langle \Big(\hat{k}_I \cdot \tilde{\mathbf{u}}_B(\mathbf{q} - \mathbf{k}_I) \Big) \Big(\hat{k}_I \cdot \tilde{\mathbf{u}}_B(\mathbf{k}_I - \mathbf{q}) \Big) \Big\rangle$$

where the overhead tilde symbol in the above relations denote the spatial Fourier transforms. The Fourier transform of the Green's function of the Helmholtz operator is denoted by,

$$\widetilde{G}(\mathbf{k}) = \frac{1}{k^2 - k_I^2}$$

Evaluation of the integral will depend on the flow and would be a tedious task. Though, given a homogeneous and isotropic turbulent flow, the above equations show that,

$$\frac{\delta c}{c} \propto -\left(\frac{u_B'^{rms}}{c} \right)^2 \sim -O(\mathcal{M}a^2) \tag{IV.15}$$

IV.3 Experimental setup

The experimental setup is similar to the one described in chapter II with the von Kármán swirling flow. The main reasons for choosing this setup is as follows,

- We need a setup with good control on the temperature of the flow volume. In our setup of von Kármán swirling flow, this is achieved by using a cooling system which maintains a constant temperature at the boundaries (fig.II.2).

- For studying the regime of geometrical acoustics, the integral length scale (l_0) should be much larger than the wavelength of the incident wave (λ). In the von Kármán swirling flow, the integral scale is roughly the order of the size of the experimental setup.

- To avoid diffraction effects, the following condition needs to be met [121],

$$\sqrt{\lambda L} \ll l_0$$

where λ and L are the wavelength of the incident wave and the total distance travelled by the acoustic wave between the emitter and receiver respectively. Thus, a turbulent flow with a large integral length scale reduces errors that might arise due to diffraction of the acoustic wave.

The sketch of the setup is shown in fig.II.2 of chapter II. For the current set of experiments, we use two acoustic transducers *ITC-9073* (which act as both emitters and receivers) having a diameter of 12 mm and emit ultrasound at a frequency of 230 kHz (fig.IV.5). The transducers are flushed to the cylindrical wall facing each other as shown in fig.IV.6. The transducers are surrounded by sound absorbing foam to absorb any reflected acoustic waves not in LOS propagation.

The emitting transducer is supplied with a sine wave signal via *agilent 33220A* arbitrary waveform generator. The output of the receiving transducer is passed through an *EG&G 5185* wideband preamplifier. The amplified output is then is given to *SR844* lock-in amplifier whose output is recorded through *NI USB-6212* acquisition card. The lock-in amplifier directly measures the fluctuations in amplitude and phase of the incident wave after it travels through the bulk of the turbulent flow from the emitter to the receiver.

One cold wire temperature probe *DANTEC 55P31* measures the temperature of the flow and is connected to *DANTEC Streamware Pro* system. The working fluid in our experiment is air. For additional details of the setup, refer to chapter II.

Fig. IV.5   *Image of the ultrasound transducer used in the experiment. Diameter of the transducer is* 12 mm *and has emitting frequency of 230 kHz.*

The length scales and the frequency scales are as follows,

$$l_0 \sim O(10) \text{ cm}$$
$$\lambda \sim O(1) \text{ mm}$$
$$L \sim O(10) \text{ cm}$$
$$f_0 \sim O(10) \text{ Hz}$$
$$f_I = 230 \text{ kHz}$$

and the conditions for geometrical acoustics to be valid are satisfied with,

$$\frac{\lambda}{l_0} \approx O(10^{-2}) \ll 1$$
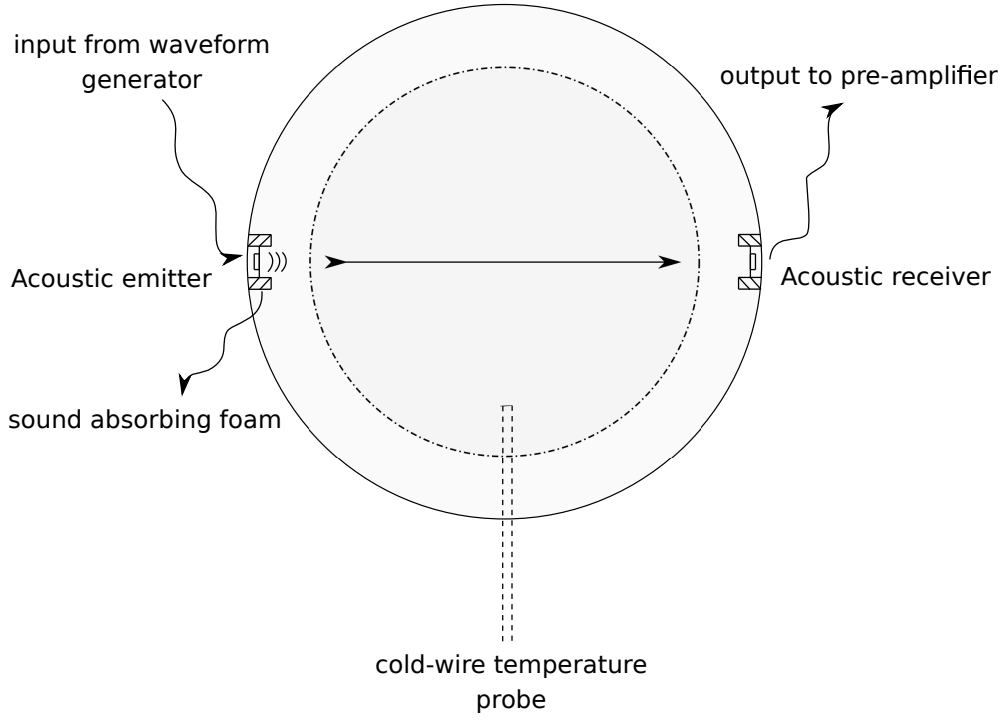$$\frac{\sqrt{\lambda L}}{l_0} \approx O(10^{-1}) \ll 1$$

Fig. IV.6 *Sketch of the experimental setup. Top view of the midplane of the cylindrical cavity.*

We use two different geometries of disks. The details and the reasons are as follows,

- For studying log-amplitude and phase fluctuations: We use disks with curved blades (fig.IV.7a). The curved blades result in higher turbulence intensity compared to disks with straight blades. However, we cannot use the symmetry $\Omega \to -\Omega$ with curved blades which will be used for the requirement of more accurate measurements.

- For studying the change in speed of sound: We use disks with straight blades (fig.IV.7b). The turbulence intensity in the flow is lower than the one generated by disks with curved blades. But on the other hand, we expect the flow to be symmetric when the rotation of the disks is reversed. Since, we aim to measure an effect which is very small and of $O(\mathcal{M}a^2)$, errors can be minimized by averaging the results over different symmetries of the flow and thus a disk with straight blades is preferable.

(a)
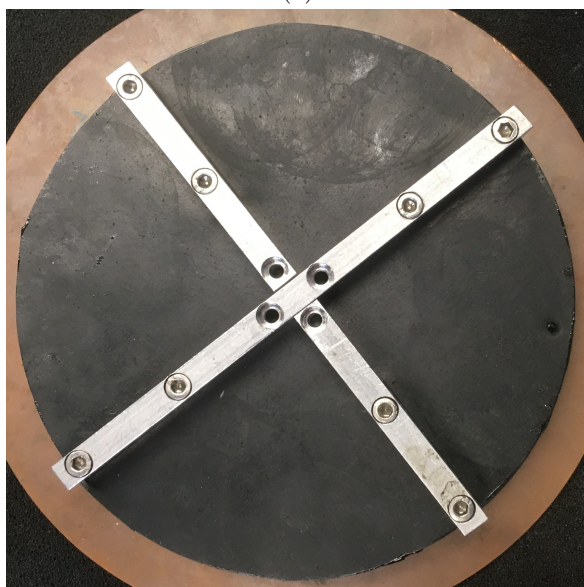
(b)

Fig. IV.7   *(a) Image of the disk with curved blades used for forcing the flow in experiments on studying log-amplitude and phase fluctuations. (b) Image of the disk with straight blades used for experiments on studying change in speed of sound.*

IV.4 Experimental results

IV.4.1 Parameter fluctuations of incident wave in LOS propagation

Fig.IV.8a shows the time series of the phase fluctuations (Φ_1) when the rotation rate of disks is 2000 rpm. Eqn.(IV.8) shows that the phase fluctuations depend linearly on the velocity fluctuations of the turbulent flow. As demonstrated by eqn.(IV.12) for the simple case of the velocity correlation function decaying exponentially in space, Φ_1^{rms} which characterizes the total energy in the phase fluctuations follows the behaviour,

$$\Phi_1^{rms} \propto u'_{rms}$$

Since for the von Kármán swirling flow, $u'_{rms} \propto \Omega$, we obtain,

$$\Phi_1^{rms} \propto \Omega$$

Fig.IV.8b shows the behaviour of Φ_1^{rms} with the rotation rate. We observe that it scales linearly with the rotation rate as predicted. We can also obtain the order of magnitude of Φ_1^{rms} from eqn.(IV.12). For $u'_{rms} \sim O(1)$ m/s, we find that $\Phi_1^{rms} \sim O(1)$. This corresponds to a rotation rate $\Omega = 2000$ rpm and from fig.IV.8b we observe that our prediction is in agreement with experimental observation. Fig.IV.9 shows the PDF of the phase fluctuations normalized by its RMS value for three different rotation rates. They all coincide are are observed to be roughly Gaussian.

Eqn.(IV.11) gives the prediction on the behaviour of the energy spectrum of the phase fluctuations and is seen to be related to the cross-spectrum of the velocity fluctuations. We can rewrite the formula obtained for the energy spectrum of phase fluctuations in terms of the *coherence* of velocity fluctuations instead of the cross-spectrum which gives,

$$E_{\Phi_1}(f) = \left(\frac{2k_I^2}{c^2}\right)\left(E_{u_{B,x}}(f)\right)\int_0^L \, dz \, \int_{-z}^{z} \, dr \, \sqrt{\mathcal{C}_{u_{B,x}}(r,f)}$$

where $\mathcal{C}_{u_{B,x}}$ is the coherence of $u_{B,x}$. When the turbulent flow is homogeneous, it has the definition

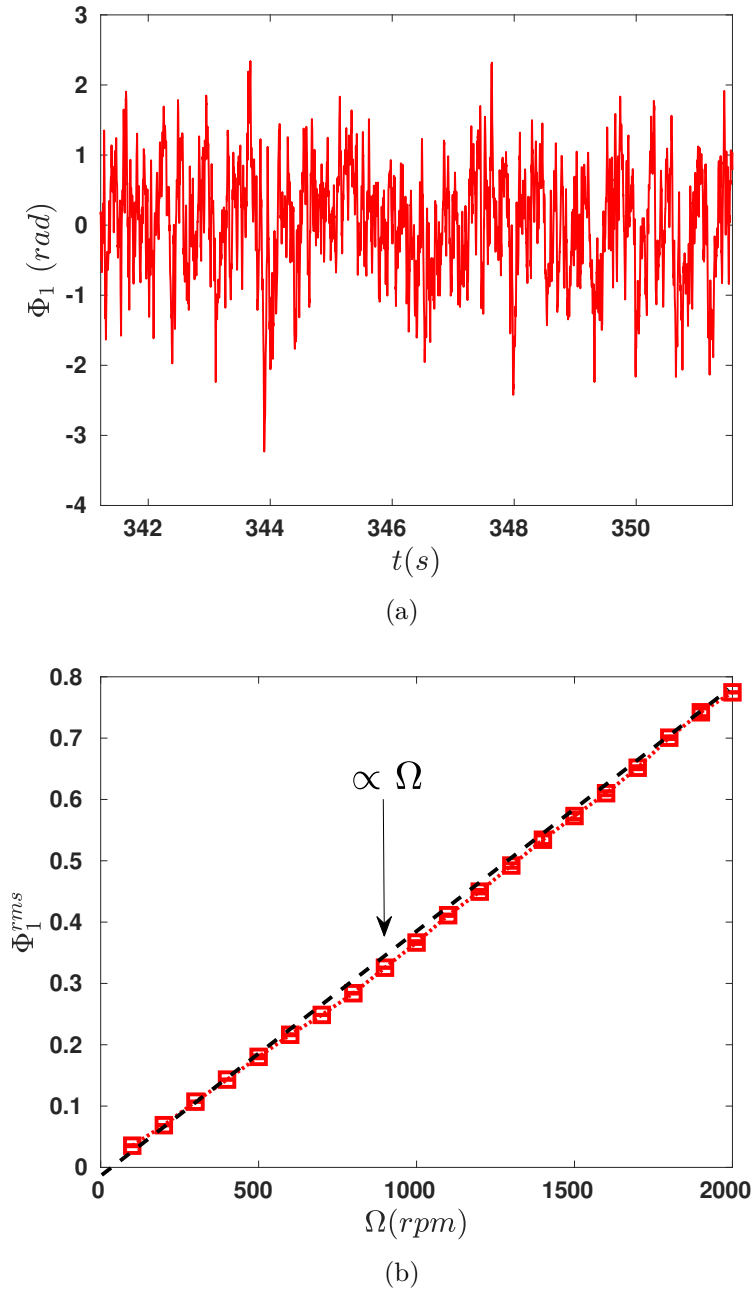$$\mathcal{C}_{u_{B,x}}(r,f) = \frac{\left|\widetilde{E}_{u_{B,x}}\right|^2}{\left(E_{u_{B,x}}\right)^2} \tag{IV.16}$$

Fig. IV.8   (a) Time series of phase fluctuations for $\Omega = 2000$rpm. (b) Scaling of RMS of phase fluctuations Φ_1^{rms} with the rotation rate Ω. Dashed line shows the predicted linear scaling.
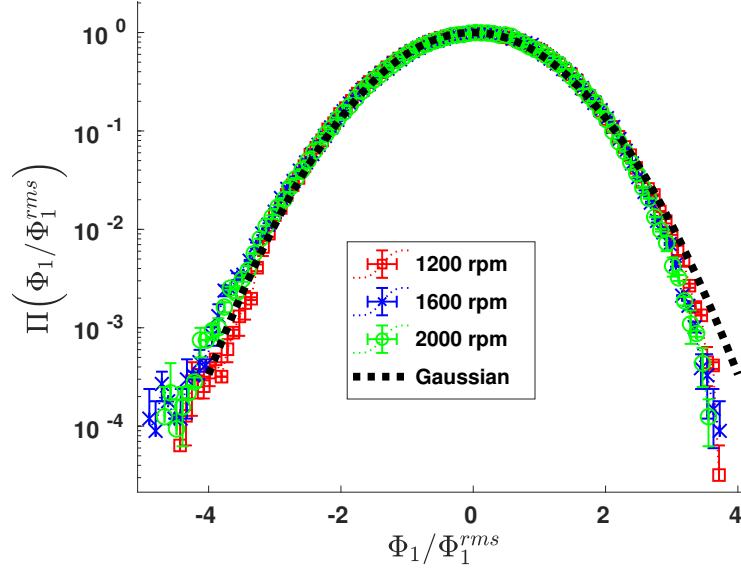
Fig. IV.9

Fig. IV.10   *PDFs of phase fluctuations normalized by its RMS value. Red squares:* 1200 rpm; *Blue crosses:* 1600 rpm; *Green circles:* 2000 rpm. *Dashed line: Gaussian*

If the coherence of velocity fluctuations has the form (see chapter II),

$$\mathcal{C}_{u_{B,x}}(r,f) = \exp\left[-\frac{r}{r^\dagger}\left(1 + \frac{f}{f^\dagger}\right)\right]$$

where $r^\dagger$ and $f^\dagger$ are the characteristic length and frequency scales of the decay of coherence and would be proportional to the integral length scale (l_0) and integral frequency scale (f_0) of the turbulent flow. On substituting this form of coherence in eqn.(IV.16), we obtain,

$$E_{\Phi_1}(f) = \left(\frac{8k_I^2 r^{\dagger 2}}{c^2}\right)\left(\frac{E_{u_{B,x}}(f)}{1 + f/f^\dagger}\right)\left[\left(\frac{L}{r^\dagger}\right) - \left(\frac{2}{1 + f/f^\dagger}\right)\left(1 - \exp\left(-\frac{L(1 + f/f^\dagger)}{2r^\dagger}\right)\right)\right]$$

(IV.17)

which can be written as,

$$E_{\Phi_1}(f) = \mathcal{A}(f/f^\dagger, r^\dagger/L, k_I r^\dagger) E_{u_{B,x}}(f)$$

(IV.18)

where $\mathcal{A}(f/f^\dagger, r^\dagger/L, k_I r^\dagger)$ is the frequency dependent prefactor which comes from the coherence of velocity fluctuations between two points in a turbulent flow. It would be associated with the effect of *sweeping* of the inertial scales by the integral scales. In chapter II, it was experimentally shown that the energy spectrum of velocity fluctuations has the behaviour,

$$E_{u_{B,x}}(f) \propto f^{-0.6} \text{ for } f < f_0$$

whereas, we would expect the inertial range scaling of the energy spectrum in the Eulerian framework [17],

$$E_{u_{B,x}}(f) \propto f^{-5/3} \text{ for } f > f_0$$

which accounts for the effect of sweeping of the inertial scales by the integral scales. This would give us for the energy spectra of phase fluctuations,

$$E_{\Phi_1}(f) \propto \begin{cases} \mathcal{A}(f/f^\dagger, r^\dagger/L, k_I r^\dagger) f^{-0.6} & \text{when } f < f_0 \\ \mathcal{A}(f/f^\dagger, r^\dagger/L, k_I r^\dagger) f^{-5/3} & \text{when } f > f_0 \end{cases}$$

It is important to comment that we observed in chapter III that the exponential decay in coherence is observed for the inertial scales ($f > f_0$). Its validity for the scales with $f < f_0$ was not conclusive with the coherence deviating from exponential behaviour for frequencies smaller than the integral frequency for one experiment while for the other experiment the decay remained exponential even for frequencies smaller than the integral frequency. Thus the form for the energy spectrum for $f < f_0$ might not be exactly valid.

We proceed with the assumption that the exponential decay in coherence is valid for all frequencies including those smaller than the integral frequency and show that this agrees with our experimental results on the energy spectrum of phase fluctuations. We recall that $r^\dagger$ and $f^\dagger$ are, as of yet, undetermined and whose values we expect to be proportional to the integral length scale and integral frequency scale of the turbulent flow. Since we are interested in the frequency dependence, the exact value of $r^\dagger$ does not radically affect the frequency behaviour of energy spectrum of phase fluctuations predicted by eqn.(IV.17). In chapter III we observed that $O(r^\dagger) \sim O(l_0)$ and hence we proceed to evaluate the value of $f^\dagger$ by fixing the value of $r^\dagger$ to that of the integral length scale l_0. The procedure for evaluating $f^\dagger$ is as follows,

- We define a range of frequencies $\hat{f}$ ranging over two decades of values centered logarithmically about the value of f_0.

- For one value of $\hat{f}$, we fit the spectrum with $\mathcal{A}(f/\hat{f}) f^{-0.6}$ for $f < f_0$ and with $\mathcal{A}(f/\hat{f}) f^{-5/3}$ for $f > f_0$ and evaluate the total root-mean-square error of the two fits (sum of the two errors). Here, the only free parameter in our fit is the constant prefactor.

- We sweep over the range of frequencies and find the frequency for which the total root-mean-square error is minimized. The frequency for which the total root-mean-square error is minimized is denoted by $f^\dagger$.

Fig.IV.11a shows the energy spectrum for phase fluctuations, $E_{\Phi_1}(f)$, when the rotation rate is $\Omega = 2000$ rpm. We observe that it has two power law behaviours, one for low frequencies with $E_{\Phi_1} \propto \mathcal{A}(f/f^\dagger)f^{-0.6}$ and the other for higher frequencies with $E_{\Phi_1} \propto \mathcal{A}(f/f^\dagger)f^{-5/3}$. Fig.IV.11b shows the values of $f^\dagger$ obtained from the fitting process mentioned above versus the integral frequency scale f_0 as the rotation rate of the motors is varied. As we observe, the dependence is linear with a slope close to a half. Our observations on the behaviour of the energy spectrum of phase fluctuations suggest that the coherence is of the form,

$$\mathcal{C}_{u_{B,x}}(r,f) = \exp\left[-\frac{r}{l_0}\left(1 + \frac{2f}{f_0}\right)\right]$$

and valid for all frequencies. The above functional form of coherence was also found for one of the experiments in chapter II (eqn.(III.26)). The form of the energy spectrum of the phase fluctuations given by eqn.(IV.18) can be understood by the two terms it comprises of,

$$E_{\Phi_1}(f) = \underbrace{\mathcal{A}(f/f^\dagger, r^\dagger/L, k_I r^\dagger)}_{I}\underbrace{E_{u_{B,x}}(f)}_{II}$$

where the prefactor $\mathcal{A}$ (term I) is evaluated from the coherence and thus encompasses the effect of sweeping on two-point statistics in a turbulent flow whereas the energy spectrum of the velocity fluctuations (term II) is the effect of sweeping on one-point statistics in a turbulent flow. If the inertial scales were being swept by a constant flow and not by the random velocity field of the integral scales, we would have the coherence being one everywhere in which case,

$$E_{\Phi_1}(f) = \left(\frac{2k_I^2 L^2}{c^2}\right) E_{u_{B,x}}(f)$$

and thus would be proportional to the energy spectrum of the velocity fluctuations. The deviation of the energy spectrum of phase fluctuations from that of the velocity fluctuations thus would be a direct result of the sweeping by the random velocity field of the integral scales. At this point, it is imperative to discuss the behaviour of the prefactor $\mathcal{A}$ in some limiting cases. From its form, we deduce that,

$$\mathcal{A}(f/f_0, l/L, k_I l) \rightarrow \begin{cases} C(k_I l_0)^2\left(\frac{L}{l_0}\right) & \text{when } f \ll f_0, l_0 \ll L \\ C(k_I l_0)^2\left[\left(\frac{L}{l_0}\right) - 2\left(1 - \exp\left(\frac{L}{2l_0}\right)\right)\right] & \text{when } f \ll f_0 \\ C(k_I l_0)^2\left(\frac{L}{l_0}\right)\left(\frac{1}{1+f/f_0}\right) & \text{when } l_0 \ll L \end{cases}$$

(a)

(b)
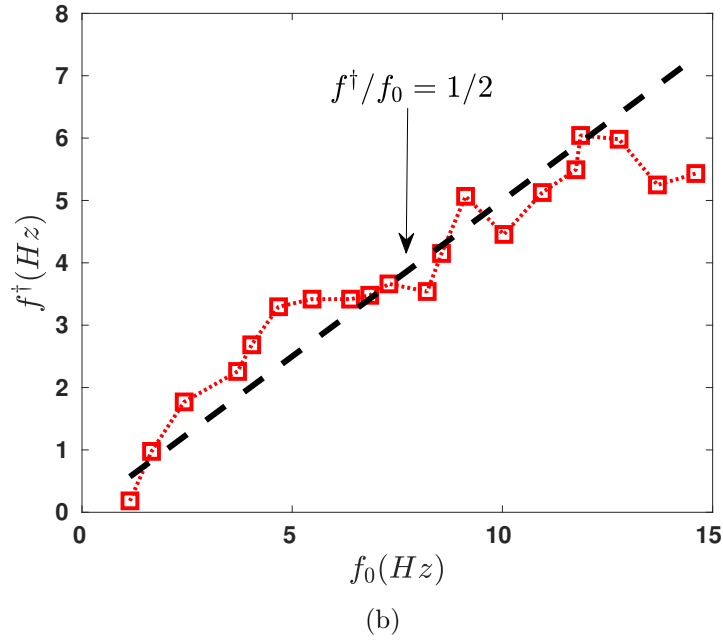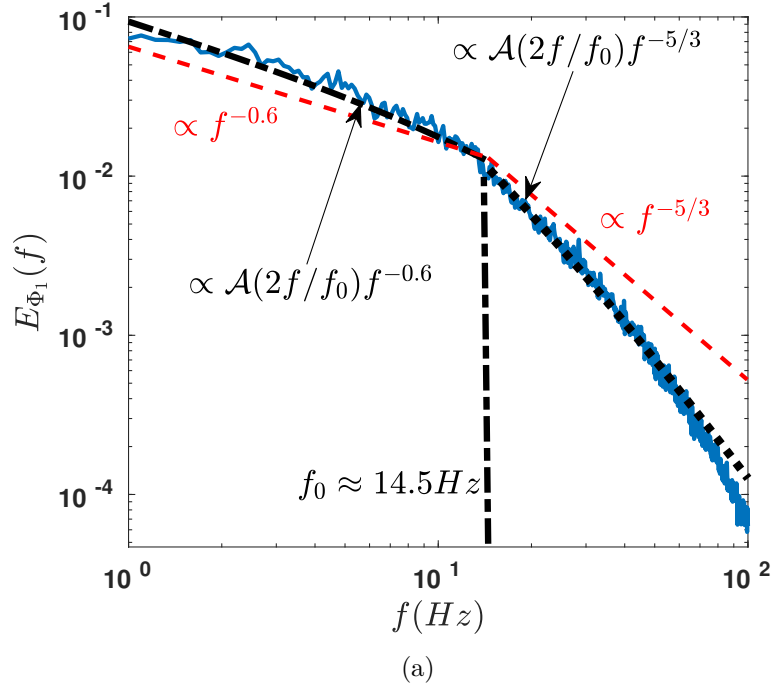
Fig. IV.11 (a) Energy spectrum of phase fluctuations for a rotation rate of $\Omega = 2000$ rpm. Dashed line: corresponds to $E_{\Phi_1}(f) \propto \mathcal{A}(2f/f_0)f^{-5/3}$. Dotted-dashed line: corresponds to $E_{\Phi_1}(f) \propto \mathcal{A}(2f/f_0)f^{-0.6}$. (b) The frequency scale $f^\dagger$ obtained from fitting versus the integral frequency f_0 as the rotation rate of the motors is varied. Dashed line denotes a slope of one half.

where the proportionality constant C depends only on the speed of sound. What we observe from the above limits is that the energy in the phase fluctuations is maximum when both the conditions $f \ll f_0, l \ll L$ are met. In this limit, the energy in phase fluctuations is directly proportional to the energy in the velocity fluctuations. This does make sense as the phase difference would be evaluated between two points in the turbulent flow much farther than the integral scale of the flow and at timescales much larger than the integral timescale. As such the phase measured at these two points would be statistically independent, resulting in the energy spectra of the phase difference being proportional to that of velocity fluctuations. However, the energy spectrum of the phase fluctuations would be proportional to the integral scales l_0 and thus carry information about the integral scales.

The interesting case arises when either of the above two conditions are not met. When the length travelled by the acoustic wave is much larger than the integral scale and if we consider the phase fluctuations at frequencies not necessarily smaller than the integral frequency, the energy in phase fluctuations is reduced by a factor of $1/(1+f/f_0)$ as compared to the previous case. Similarly when $f \ll f_0$ but the length travelled by acoustic wave and the integral scale are comparable, the energy in phase fluctuations is reduced as well.

The above discussion has two implications,

- Coherence between velocity at two points in a turbulent flow results in reduction of energy in phase fluctuations encountered by an acoustic wave travelling through it.

- The agreement of the experimentally observed energy spectrum of phase fluctuations with the analytical prediction suggests that the exponential decay in coherence is observed for all frequencies. The observed behaviour of the coherence and the energy spectrum of the phase fluctuations for frequencies smaller than the integral scale ($f < f_0$) is likely owing to the sweeping of the vorticity filaments by the integral scales. For frequencies larger than the integral scale ($f > f_0$) it is owing to the sweeping of the inertial scales by the integral scales.

Fig.IV.12a shows the time series of the log-amplitude fluctuations (χ_1) when the rotation rate of disks is 2000 rpm. What is immediately noticeable is that the log-amplitude fluctuations show sharp negative peaks similar to what has been observed for pressure and temperature fluctuations. As was the case for RMS of phase fluctuations, the RMS of log-amplitude fluctuations scale linearly with the rotation rate. This is seen in fig.IV.12b. The existence of negative peaks in log-amplitude fluctuations are clearly observed in its probability density function (figure IV.13) where the PDFs have exponential tails for negative fluctuations. On normalization with the RMS values the PDFs are observed to coincide.

In the case of phase fluctuations, we observed that the behaviour of phase fluctuations can be related to the behaviour of coherence of velocity fluctuations in the turbulent flow. This was evident from the agreement between the predicted and experimentally observed behaviour of the energy spectrum of phase fluctuations. The eqn.(IV.13) obtained for the behaviour of the energy spectrum of log-amplitude fluctuations shows that it is related to the cross-spectrum of the second derivatives of the velocity fluctuations. This equation cannot be further simplified without any prior knowledge about the nature of the second spatial derivatives of the turbulent velocity fluctuations.
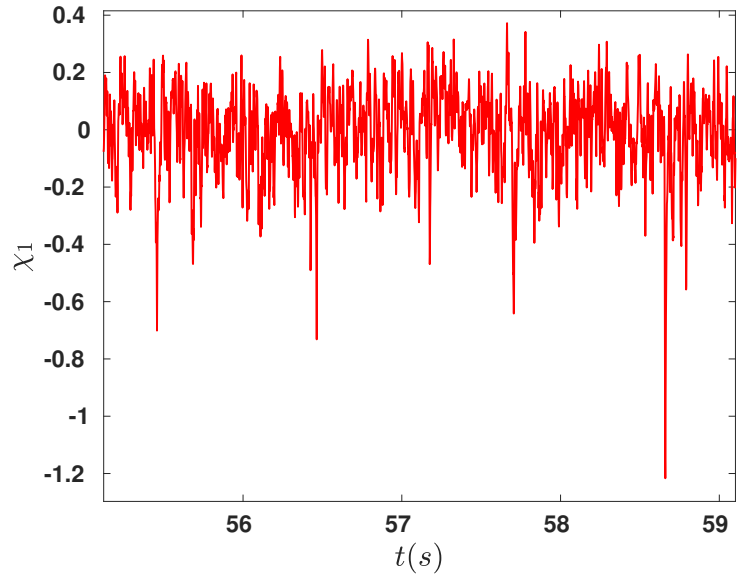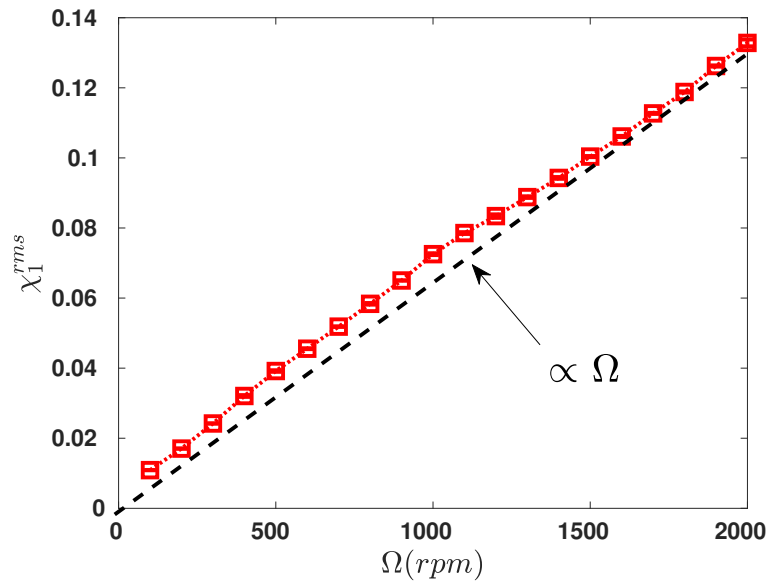
Fig. IV.12   (a) Time series of log-amplitude fluctuations for $\Omega = 2000$rpm. Note that the signal displays sharp negative peaks. (b) Scaling of RMS of log-amplitude fluctuations χ_1^{rms} with the rotation rate Ω. Dashed line shows the scaling as predicted from dimensional analysis.
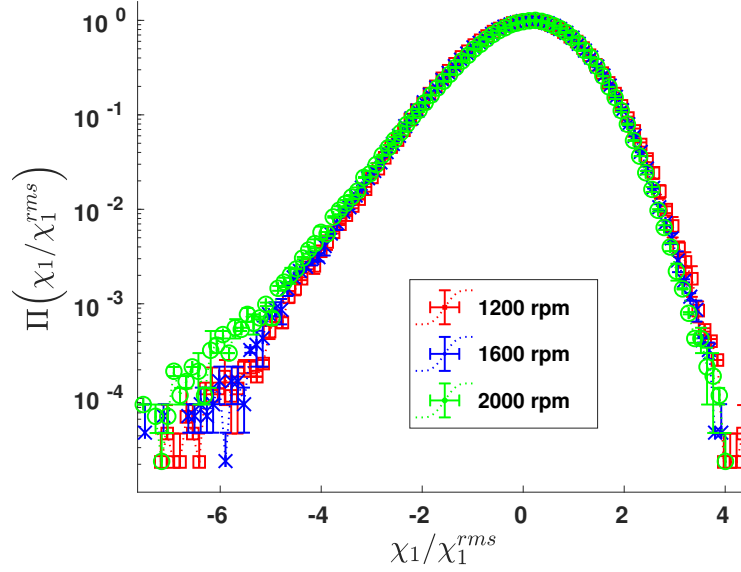
Fig. IV.13 *PDFs of log-amplitude fluctuations normalized by their RMS values. Red squares:* 1200 rpm*; Blue crosses:* 1600 rpm*; Green circles:* 2000 rpm.

The energy spectrum of log-amplitude fluctuations which is denoted by E_{χ_1} shows an exponential decay with frequency as seen in fig.IV.14. We also observe a peak at the forcing frequency which corresponds to the frequency of the disks. For the exponential behaviour of the energy spectrum, we can define a characteristic cut-off frequency f_c with the energy spectrum having the form,

$$E_{\chi_1}(f) = E_{\chi_1}^0 e^{-f/f_c}$$

Along with the behaviour of the energy spectrum of the log-amplitude fluctuations obtained analytically (eqn.(IV.13)), we deduce that the cross-spectrum of double velocity gradient would likely have the form[8],

$$\boxed{\widetilde{E}_{u_{B,x}}^{yy}(r,f) \sim \mathcal{B}(r/r_c)e^{-f/f_c}} \tag{IV.19}$$

---

[8]We assume that the the the cross-spectrum $\widetilde{E}_{u_{B,x}}^{yz}$ would decay faster in space than $\widetilde{E}_{u_{B,x}}^{yy}$. None the less, it would be the larger of the two that will contribute to the energy spectrum of log-amplitude fluctuations and will have the form given by eqn.(IV.19).
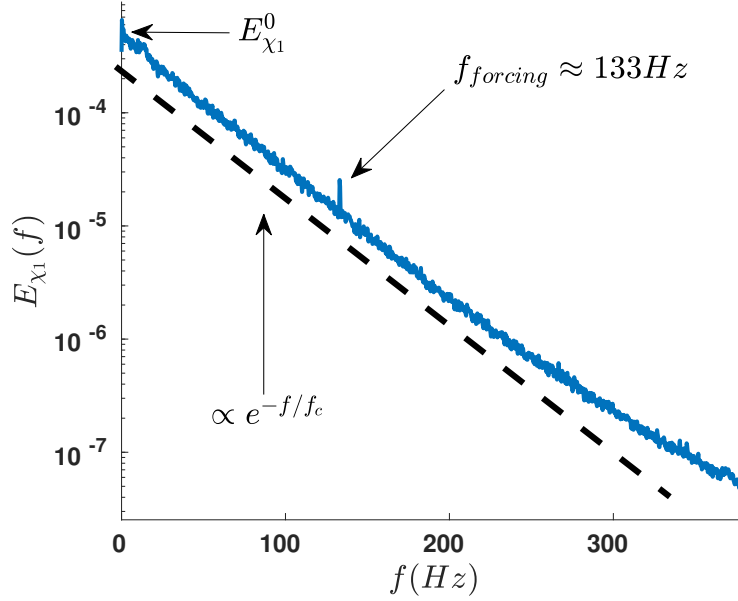
Fig. IV.14   *Energy spectrum of log-amplitude fluctuations for* $\Omega = 2000$rpm. *Dashed line: corresponds to* $E_{\chi_1} \propto e^{-f/f_c}$.

On taking the inverse temporal Fourier transform of eqn.(IV.19), we obtain,

$$\gamma_{yy}^{u_{B,x}}(r,\tau) \sim \mathcal{B}(r/r_c)\left(\frac{f_c}{(f_c\tau)^2 + 1}\right)$$

where the function inside brackets on the right hand size is a Lorentzian function. The length r_c corresponds to the characteristic length scale of the decay of the double velocity gradient $\gamma_{yy}^{u_{B,x}}$ and its temporal spectrum $\widetilde{E}_{u_{B,x}}^{yy}$. We recall that,

$$\gamma_{yy}^{u_{B,x}}(r,\tau) = \left\langle \frac{\partial^2 u_{B,x}(\alpha,t)}{\partial y^2} \frac{\partial^2 u_{B,x}(\alpha+r,t+\tau)}{\partial y^2} \right\rangle$$

The dependence of f_c with the rotation rate is plotted in figure IV.15a and shows a logarithmic dependence on the rotation rate. Its magnitude is comparable to that of the rotation rate of the disks which is $(\Omega/60)$ Hz. The dependence of r_c on the rotation rate cannot be deduced, though the dependence of $E_{\chi_1}^0$ can be deduced, where $E_{\chi_1}^0$ is given by,

$$E_{\chi_1}^0 = \left(\frac{1}{2c^2}\right) \int_0^L dp \int_0^L dq \int_0^p d\alpha \int_{-\alpha}^{q-\alpha} dr \, \mathcal{B}(r/r_c)$$

is shown in figure IV.15b and observed to scale with the rotation rate as $E_{\chi_1}^0 \propto \Omega^{1.2\pm0.1}$.
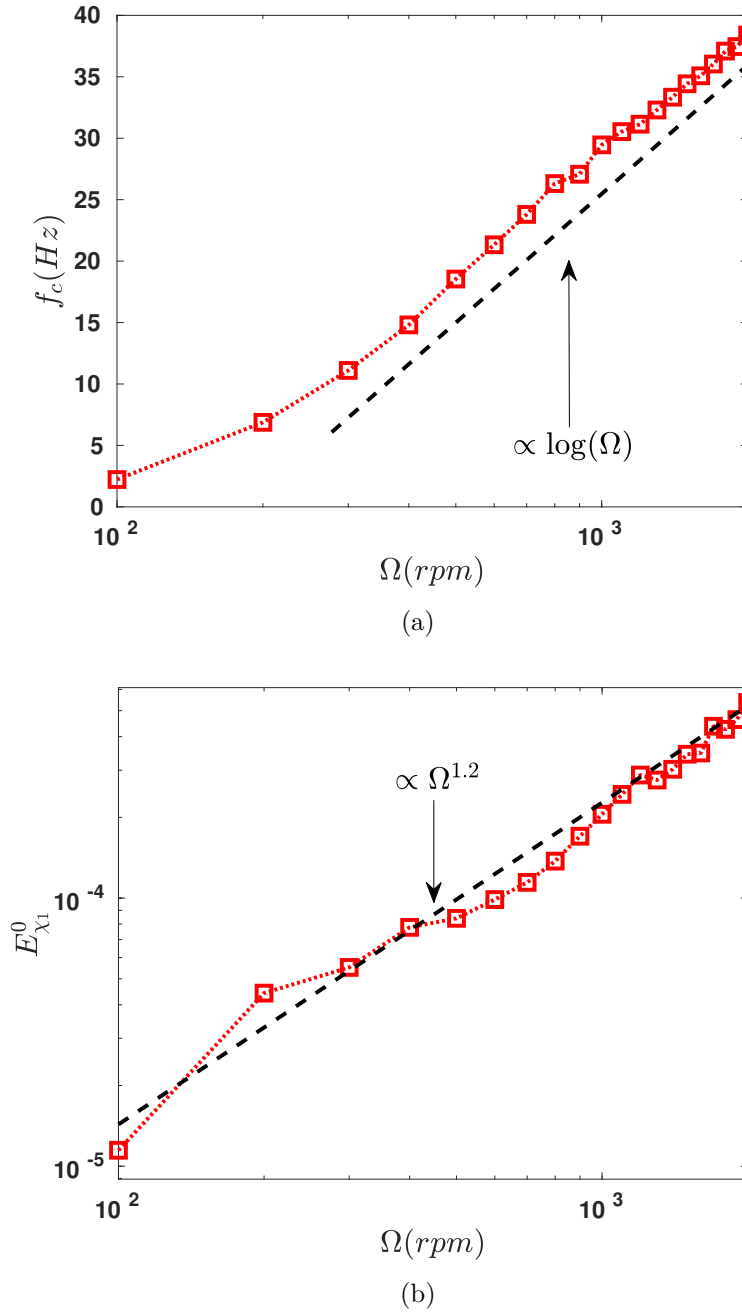
(a)

(b)

Fig. IV.15   (a) Cut-off frequency f_c corresponding to the energy spectrum of log-amplitude fluctuations as a function of the rotation rate Ω. (b) The energy spectrum of log-amplitude fluctuations at zero frequency denoted by $E_{\chi_1}^0$ as a function of the rotation rate Ω. Dashed line corresponds to $E_{\chi_1}^0 \propto \Omega^{1.2}$.

Another deduction that can be made is about the form of energy spectrum of the double-derivative of velocity fluctuations,

$$\boxed{E^{yy}_{u_{B,x}}(f) \sim e^{-f/f_c}}$$

since $E^{yy}_{u_{B,x}}(f) = \widetilde{E}^{yy}_{u_{B,x}}(r = 0, f)$ and we expect $\lim_{r \to 0} \mathcal{B}(r/r_c) = constant$. Thus the quantity $\left(\frac{\partial^2 u_{B,x}}{\partial y^2} \right)$ in a turbulent flow would likely display large temporal scales as is evident from the form of its spectra given above. This would result in the log-amplitude fluctuations also displaying large temporal scales.

To summarize,

- The phase fluctuations of an incident wave traveling through a turbulent flow is a direct result of the coherence of the velocity fluctuations of the turbulent flow. We show that if we know the behaviour of coherence of the turbulent velocity fluctuations, we can predict the behaviour of energy spectrum of the phase fluctuations.

- The energy spectrum of the log-amplitude fluctuations is observed to decay exponentially with frequency. This enables to predict some characteristics about the behaviour of double velocity gradients in a turbulent flow $\left(\frac{\partial^2 u_{B,x}}{\partial y^2} \right)$. This quantity, which is associated to the turbulent flow, likely displays an exponential behaviour in its frequency energy spectrum and cross-spectrum. The temporal correlation of this quantity, if measured, would likely display a behaviour described by a Lorentzian function. The time signal of log-amplitude fluctuations displays negative peaks. Further analysis is required to understand the source of these negative peaks.

IV.4.2 Change in speed of sound due to turbulent flow

Since the change in speed of sound resulting from the turbulent flow is an $O(\mathcal{M}a^2)$ effect, we need to be able to measure it with high level of precision. To wit, we measure it from the change in mean phase difference of the acoustic wave between the emitter and receiver ($\Delta\Phi_0$) in the two cases, viz., with and without turbulence. Since we are using a lock-in amplifier which measures the phase difference between the emitter and the receiver, we have,

$$\langle\Delta\Phi\rangle = \Delta\Phi_0 = \Phi_0(x = L) - \Phi_0(x = 0) = \frac{2\pi f L}{c}$$

Therefore,

$$\Delta\Phi_0^{\text{flow}} - \Delta\Phi_0^{\text{no flow}} = \delta\Phi_0 = \frac{2\pi f l}{c + \delta c} - \frac{2\pi f l}{c}$$

From which we have the relation,

$$\delta c = -\frac{c^2 \delta\Phi_0}{2\pi f L + c\delta\Phi_0}$$

Figure IV.16a shows the PDFs of $\Delta\Phi$ with and without the turbulent flow when the rotation rate is 2000rpm. From the point of minimizing any errors, we list two important sources of error and how we remove them from our measurements.

- When the background flow is turbulent, the mean temperature of air is increased as compared to when the flow is absent. This is due to viscous dissipation inherent to turbulent flow. This will result in change in speed of sound[9] $\delta c^T \approx 20.05(\sqrt{T + \Delta T} - \sqrt{T})$. We measure the temperature of the flow using cold-wire temperature probe and thus the change in speed of sound resulting from viscous dissipation. Figure IV.16b shows the contribution of viscous dissipation (δc^T) and the turbulent flow (δc^{turb}) to the measured change in speed of sound (δc) where $\delta c = \delta c^T + \delta c^{turb}$.

- Any asymmetry in the flow would result in erroneous measurement of the speed of sound due to net advection (in addition to the background turbulent flow) along the direction of propagation of the acoustic wave. To counter this effect, we measure and average the change in speed of sound,

  1. By reversing the rotation of the disks, i.e., $\frac{\delta c(\Omega) + \delta c(-\Omega)}{2}$. In figure IV.16b, we see that we do have asymmetry in the change of speed of sound for reversed rotation.

  2. By interchanging the emitter and the receiver, i.e., $\frac{\delta c(0 \to L) + \delta c(L \to 0)}{2}$. This is shown in figure IV.17a by the two paths for the acoustic wave, 1 and 2. As shown in figure IV.17b, indeed a small radial asymmetry in the flow leads to difference in the speed of sound measured along the two directions.

---

[9]For air under standard conditions, if we consider it as an ideal gas, $c = \sqrt{\gamma RT/M} \approx 20.05\sqrt{T}$.
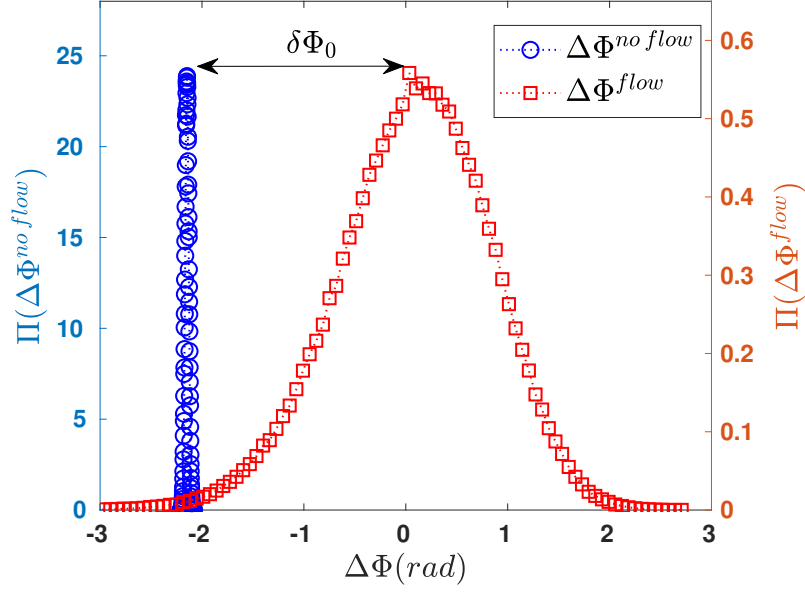
(a)
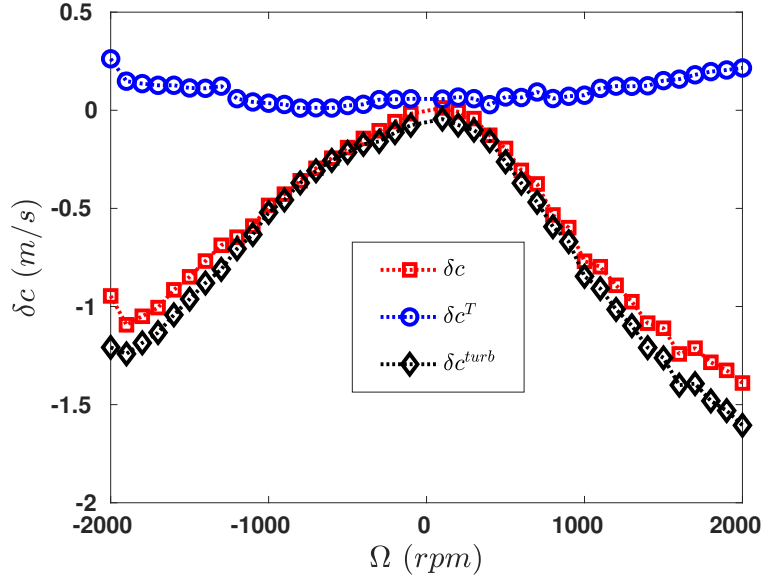
(b)

Fig. IV.16   (a) The PDFs of difference in phase at the receiver and emitter ($\Delta\Phi$) in the absence of turbulent flow with motors turned off (blue) and in the presence of turbulent flow with motors turned on (red). (b) Contribution of different effects to the observed change in speed of sound. Red squares (δc): as measured from the change in mean phase between the emitter and the receiver. Blue circles (δc^T): contribution from the change of mean temperature owing to turbulent viscous dissipation. Black squares (δc^{turb}): contribution from the turbulent flow.
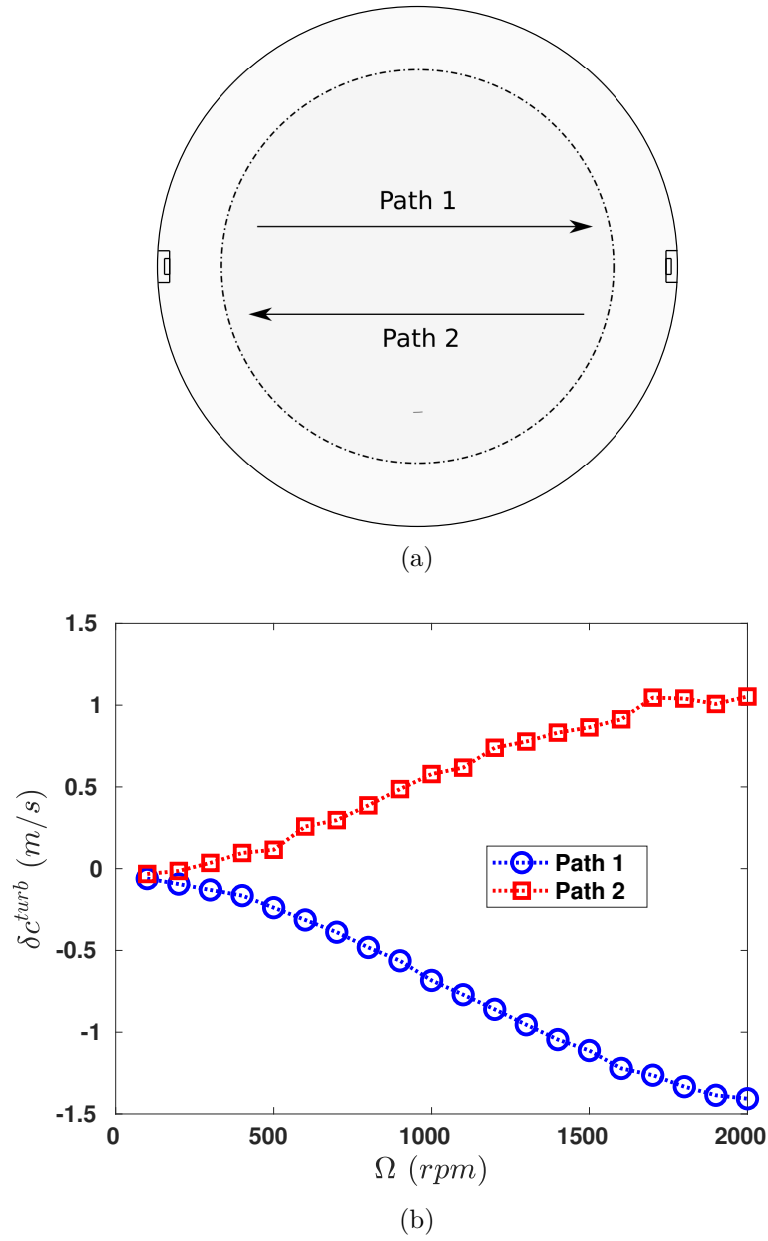
(a)

(b)

Fig. IV.17   (a) Sketch showing the two opposite paths for the direction of propagation of the incident wave. (b) The change in speed of sound obtained for the two opposite paths 1 and 2.

Equation (IV.15) when applied to the von Kármán flow suggests the scaling,

$$-\left(\frac{\delta c}{c}\right) \propto \Omega^2$$

Figure IV.18a shows the change in speed of sound as a function of the rotation rate Ω and the predicted scaling is indeed observed. In our experiments, we observe that the turbulent flow reduces the speed of sound and that it scales as the rotation rate squared. A maximum reduction in speed of sound of about 0.03% with respective to the speed of sound was obtained.

The results presented in this chapter on the change in speed of sound caused by a turbulent flow is the first reported experimental evidence and validates the theory developed by Lund [18]. This effect, arising due to multiple scattering by the turbulent velocity fluctuations acting as acoustic scatterers is, as expected, a very small effect. We note that in our experiment for $u'_{rms} \sim O(1)$ m/s, the speed of sound reduces by $\delta c_{turb} \sim O(10^{-1})$ m/s for the speed of sound in air being roughly 345 m/s.

Figure IV.18b shows that the actual magnitude of the normalized change in speed of sound as a function of $\mathcal{M}a^2$. Our observations suggest that,

$$-\left(\frac{\delta c}{c}\right) \approx -10\left(\frac{u'^{rms}_B}{c}\right)^2 = -10\left(\mathcal{M}a^2\right)$$
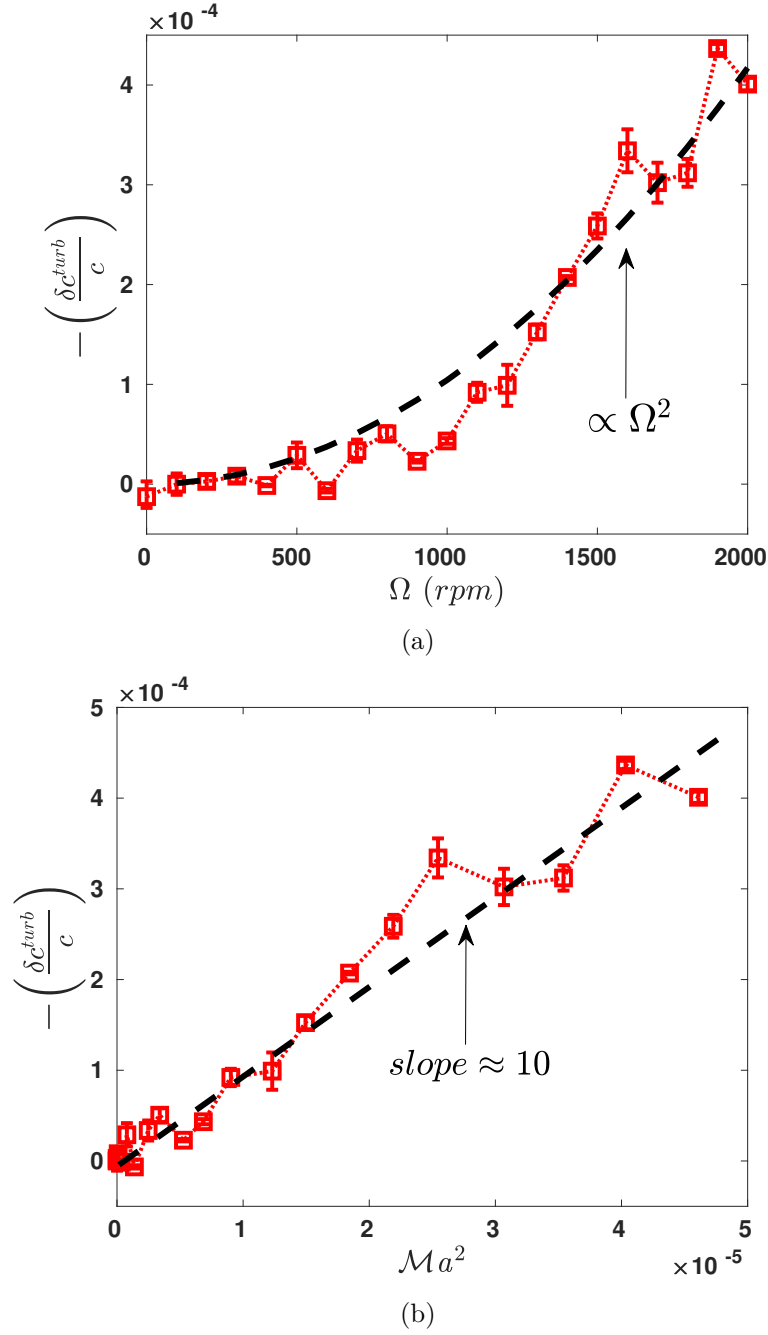
Fig. IV.18 (a) Normalized change in speed of sound due to turbulence $-\delta c^{turb}/c$ as a function of the rotation rate. Dashed line corresponds to $-\delta c^{turb}/c \propto \Omega^2$. Note that we plot the negative of the change in speed of sound, i.e., turbulence results in a reduction of speed of sound. (b) The non-dimensional change in speed of sound $-\delta c^{turb}/c$ versus the square of Mach number. Dashed line denotes a slope of ten.

We can also evaluate the *excess* inverse attenuation length 'α'. Consider an acoustic wave of amplitude A travelling from an emitter to receiver which are placed apart by a distance L. It will undergo attenuation in the presence as well as in the absence of a turbulent flow. In the absence of a turbulent flow, we can write,

$$\langle A \rangle_{no\ flow} = Ae^{-\alpha_{no\ flow}\frac{L}{2}} \tag{IV.20}$$

Similarly in the presence of turbulent flow,

$$\langle A \rangle_{flow} = Ae^{-\alpha_{flow}\frac{L}{2}} \tag{IV.21}$$

On taking the log of eqn.(IV.20) and subtracting log of eqn.(IV.21) from it, we obtain the excess inverse attenuation length,

$$\alpha = \alpha_{flow} - \alpha_{no\ flow} = \left(\frac{2}{L}\right)\left(\log\left(\langle A \rangle_{no\ flow}\right) - \log\left(\langle A \rangle_{flow}\right)\right) = \left(\frac{2}{L}\right)\left(\chi_0^{no\ flow} - \chi_0^{flow}\right)$$

Figure IV.19 shows the dependence of α on the rotation rate Ω. We observe that $\alpha \propto \Omega^{2.5\pm0.3}$.
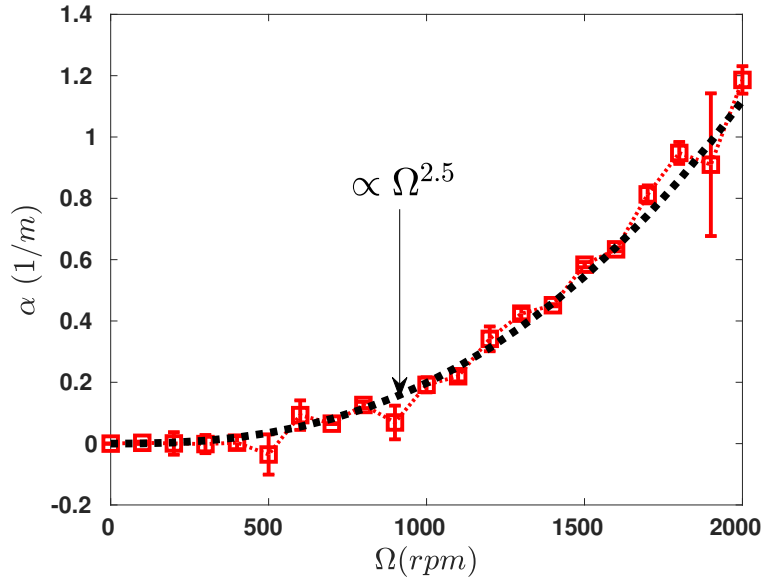

Fig. IV.19   *Excess inverse attenuation length α as a function of the rotation rate Ω. Dashed line corresponds to $\alpha \propto \Omega^{2.5}$.*

IV.5 Conclusion

The results presented in this chapter can be broadly categorized as studying the behaviour of an acoustic wave as it travels through a turbulent flow. First part dealt with the study of phase and log-amplitude fluctuations of the acoustic wave and the second with the change in the speed of sound of the acoustic wave.

For the fluctuations in phase and log-amplitude, we observe,

- Phase and log-amplitude fluctuations of an acoustic wave are a result of the scattering of the acoustic wave due to velocity fluctuations of the turbulent flow at $O(\mathcal{M}a)$.

- Phase fluctuations are directly related to the coherence of the turbulent velocity fluctuation and thus a result of the sweeping by the integral scales. For frequencies smaller than the integral frequency ($f < f_0$), they are likely a result of the sweeping of vorticity filaments and for frequencies higher than the integral frequency ($f > f_0$), they are a result of the sweeping of inertial scales.

- Log-amplitude fluctuations can be shown to be related to the second spatial derivatives of the velocity fluctuations of the turbulent flow. The second spatial derivatives of the velocity fluctuations is a difficult quantity to measure experimentally but we can comment on its possible behaviour by studying amplitude fluctuations of the acoustic wave travelling through the turbulent flow.

- The energy spectrum of log-amplitude fluctuations of the acoustic wave is observed to decay exponentially with frequency. This would imply that the energy spectrum of second spatial derivatives of the velocity fluctuations would likely decay exponentially with frequency.

The change in speed of sound was experimentally observed and can be summarized as follows,

- In our experiments, the turbulent flow results in a reduction of speed of sound. The reduction in speed of sound is observed to scale as $O(\mathcal{M}a^2)$.

- The plausible explanation for the reduction in speed of sound is the existence of a coherent wave due to multiple scattering as theoretically proposed by Lund [18].

- The process of multiple scattering alters the speed of sound in the turbulent medium which is a mean field property of the turbulent medium.

IV.A The governing equation of vortex sound

As shown in fig.IV.2, we note that the characteristic scales involved in the incompressible flow region (fig IV.2) are,

$$
\begin{aligned}
L &\sim l_0 \\
U &\sim u' \\
T &\sim l_0/u' \\
p &\sim \rho_0 u'^2
\end{aligned}
$$

and for the acoustic wave region,

$$
\begin{aligned}
L &\sim \lambda \\
U &\sim u_{ac} \\
T &\sim \lambda/c \sim l_0/u' \\
p &\sim \rho_0 u_{ac} c
\end{aligned}
$$

where u' stands for the solenoidal (or the incompressible) part of the velocity field and u_{ac} stands for the irrotational (or the acoustic) part of the velocity field. Since the acoustic waves are forced by the incompressible flow, the characteristic time-scales should be the same in both the regions. This gives us another definition of $\mathcal{M}a$,

$$
\mathcal{M}a = \frac{u'}{c} = \frac{l_0}{\lambda}
$$

implying that there is indeed a separation of the domain into the regions described above. We start with the equations for inviscid (isentropic), compressible flow,

$$
\begin{aligned}
\frac{\partial \rho}{\partial t} + \nabla \cdot (\rho \mathbf{u}) &= 0 \\
\frac{\partial \rho \mathbf{u}}{\partial t} + \nabla \cdot (\rho \mathbf{u}\mathbf{u}) &= -\nabla p \\
\frac{\partial p}{\partial \rho} &= c^2
\end{aligned}
$$

The equation of state would for a compressible flow under the assumption of isentropic process gives the last equation. Here, $\mathbf{u}$ involves both the solenoidal and irrotational part of the velocity field (u', u_{ac}). Taking the time derivative of the first equation, divergence of the second equation gives,

$$
\frac{\partial^2 \rho}{\partial t^2} - \nabla^2 p = \frac{\partial^2 (\rho u_i u_j)}{\partial x_i \partial x_j}
$$

Adding the term $c^2 \nabla^2 \rho$ on both sides of the equation and rearranging,

$$\frac{\partial^2 \rho}{\partial t^2} - c^2 \nabla^2 \rho = \frac{\partial^2 (\rho u_i u_j)}{\partial x_i \partial x_j} + \nabla^2 (p - c^2 \rho) \tag{IV.22}$$

Let us say that the mean temperature of the background flow is T and there exist fluctuations in temperature field $T'(\mathbf{x}, t)$. Then the speed of sound used above is the one at the mean temperature, i.e.,

$$c^2 = \frac{\gamma R T}{M}$$

Though accounting for the temperature fluctuations would give the speed of sound as a function of space and time, $\tilde{c}(\mathbf{x}, t)$. Thus,

$$\tilde{c}^2(\mathbf{x}, t) = \frac{\gamma R(T + T'(\mathbf{x}, t))}{M} = c^2 \left(1 + \frac{T'(\mathbf{x}, t)}{T}\right)$$

Thus the last term on the right hand side of equation (IV.22) would be,

$$\nabla^2(p - c^2 \rho) = \nabla \cdot (\nabla p - c^2 \nabla \rho) = \nabla \cdot ((\tilde{c}^2 - c^2)\nabla \rho) = \nabla \cdot \left(\left(\frac{T'}{T}\right) c^2 \nabla \rho\right)$$

Thus the relative order of magnitude of the last term would be,

$$\frac{\nabla^2(p - c^2 \rho)}{c^2 \nabla^2 \rho} \sim O\left(\frac{(T'/T)}{(l_0/\lambda)}\right) \sim O(\mathcal{M}a)$$

since the temperature fluctuations in the incompressible background flow will be of $O(\mathcal{M}a^2)$ and its effect on vortex sound would be negligible and we can assume the temperature to be constant everywhere. Thus we obtain,

$$\frac{\partial^2 \rho}{\partial t^2} - c^2 \nabla^2 \rho = \frac{\partial^2 (\rho u_i u_j)}{\partial x_i \partial x_j}$$

which on writing in terms of pressure gives,

$$\frac{1}{c^2} \frac{\partial^2 p}{\partial t^2} - \nabla^2 p = \frac{\partial^2 (\rho u_i u_j)}{\partial x_i \partial x_j}$$

Since we assume $\mathcal{M}a \ll 1$, to leading order we can rewrite the right hand side by neglecting terms of $O(\mathcal{M}a^2)$ due to density fluctuations in the incompressible background flow,

$$\frac{1}{c^2}\frac{\partial^2 p}{\partial t^2} - \nabla^2 p = \rho_0 \frac{\partial^2(u_i u_j)}{\partial x_i \partial x_j} \qquad\qquad (\text{IV.23})$$

Non-dimensionalizing the above equation with characteristic scales of the incompressible region gives to leading order,

$$\hat{\nabla}^2 \hat{p} = \rho_0 \frac{\partial^2(\hat{u}_i \hat{u}_j)}{\partial \hat{x}_i \partial \hat{x}_j}$$

which is the governing equation for pressure in an incompressible flow. Similarly, non-dimensionalizing with the characteristic scales of the acoustic wave region and that $u_{ac}/c \ll \mathcal{M}a$ gives us,

$$\frac{1}{c^2}\frac{\partial^2 \hat{p}}{\partial \hat{t}^2} - \hat{\nabla}^2 \hat{p} = 0$$

which is the governing equation for pressure in an acoustic field implying the existence of acoustic wave region far from the bounded vorticity. Since the flow in this region is irrotational, we would obtain wave equations for density, pressure and the three components of velocity fluctuations. We can write the equation (IV.23) in terms of density and to the leading order on right hand side we obtain the equation (IV.1).

IV.B The governing equation of acoustic scattering

We start with the compressible flow equations for an inviscid fluid and follow the procedure as outlined in [18],

$$\frac{\partial \rho}{\partial t} + \nabla \cdot (\rho \mathbf{u}) = 0$$
$$\frac{\partial \rho \mathbf{u}}{\partial t} + \nabla \cdot (\rho \mathbf{u}\mathbf{u}) = -\nabla p \qquad\qquad (\text{IV.24})$$
$$\frac{\partial p}{\partial \rho} = c^2$$

Let us denote the velocity and pressure fields of the low $\mathcal{M}a$ number, weakly compressible background flow with bounded vorticity by $\mathbf{u}_B$, p_B, ρ_B. The weakly compressible background flow is assumed to be incompressible at the leading order. They are governed by the compressible flow equations and the equation for temperature,

$$\frac{\partial \rho_B}{\partial t} + \nabla \cdot (\rho_B \mathbf{u}_B) = 0$$
$$\frac{\partial \rho_B \mathbf{u}_B}{\partial t} + \nabla \cdot (\rho_B \mathbf{u}_B \mathbf{u}_B) = -\nabla p_B \qquad\qquad (\text{IV.25})$$
$$\frac{\partial p_B}{\partial \rho_B} = c^2$$

Similarly the fields associated with the incident wave are $\mathbf{u}_I, p_I, \rho_I$ and the ones associated with the scattered wave are $\mathbf{u}_S, p_S, \rho_S$. Thus,

$$\mathbf{u}_I = \mathfrak{U}e^{\iota(\mathbf{k}_I \cdot \mathbf{x} - f_I t)}$$

$$p_I = \mathfrak{P}e^{\iota(\mathbf{k}_I \cdot \mathbf{x} - f_I t)} \sim \left(\rho_0 |\mathfrak{U}| c\right) e^{\iota(\mathbf{k}_I \cdot \mathbf{x} - f_I t)}$$

$$\rho_I = \mathfrak{R}e^{\iota(\mathbf{k}_I \cdot \mathbf{x} - f_I t)} \sim \left(\frac{\rho_0 |\mathfrak{U}|}{c}\right) e^{\iota(\mathbf{k}_I \cdot \mathbf{x} - f_I t)}$$

$$\mathbf{u}_I = \frac{1}{\iota \rho_0 f_I}\nabla p_I = \frac{c^2}{\iota \rho_0 f_I}\nabla \rho_I$$

where the last relation is obtained by using the momentum eqn.(II.15) for acoustic waves. From our assumption that the incident wave does not modify the background flow, we have,

$$|\mathbf{u}_I| \ll |\mathbf{u}_B| \ll c$$
$$p_I \ll p_B$$
$$\rho_I \ll \rho_B$$

From the equations (IV.24) and (IV.25), we obtain for the next order,

$$\frac{\partial^2 \rho_B}{\partial t^2} - \nabla^2 p_B = \frac{\partial^2 (\rho_B u_{B,i} u_{B,j})}{\partial x_i \partial x_j} \tag{IV.26a}$$

$$\frac{\partial^2 \rho}{\partial t^2} - \nabla^2 p = \frac{\partial^2 (\rho u_i u_j)}{\partial x_i \partial x_j} \tag{IV.26b}$$

where the first equation corresponds to the weakly compressible background flow for which we have $\rho_B = \rho_0 + \rho'_B$ with $\frac{\rho'_B}{\rho_0} \sim O(\mathcal{M}a^2)$. Substituting $\rho = \rho_B + \rho_S$, $p = p_B + p_S$ and $\mathbf{u} = \mathbf{u}_B + \mathbf{u}_S$, such that $\rho_S \ll \rho_B$, $p_S \ll p_B$ and $|\mathbf{u}_S| \ll |\mathbf{u}_B|$ and subtracting equation (IV.26a) from equation (IV.26b) gives us equation (IV.27).

$$\frac{\partial^2 \rho_S}{\partial t^2} - c^2 \nabla^2 \rho_S = 2\rho_B \frac{\partial^2 (u_{B,i} u_{S,j})}{\partial x_i \partial x_j} + \frac{\partial^2 (\rho_S u_{B,i} u_{B,j})}{\partial x_i \partial x_j}$$
$$+ 2\left(\frac{\partial \rho_B}{\partial x_i}\right)\frac{\partial (u_{B,i} u_{S,j} + u_{B,j} u_{S,i})}{\partial x_j} + 2\left(\frac{\partial^2 \rho_B}{\partial x_i \partial x_j}\right)u_{B,i} u_{S,j} + \nabla^2 (p_S - c^2 \rho_S) \tag{IV.27}$$

If we account for temperature fluctuations in the background flow T_B (such that $\langle T_B \rangle = 0$), we obtain equation (IV.28).

$$\frac{\partial^2 \rho_S}{\partial t^2} - c^2 \nabla^2 \rho_S = 2\rho_B \frac{\partial^2 (u_{B,i} u_{S,j})}{\partial x_i \partial x_j} + \frac{\partial^2 (\rho_S u_{B,i} u_{B,j})}{\partial x_i \partial x_j}$$

$$+ 2\left(\frac{\partial \rho_B}{\partial x_i}\right) \frac{\partial (u_{B,i} u_{S,j} + u_{B,j} u_{S,i})}{\partial x_j} + 2\left(\frac{\partial^2 \rho_B}{\partial x_i \partial x_j}\right) u_{B,i} u_{S,j} + c^2 \nabla \cdot \left(\left(\frac{T_B}{T}\right) \nabla \rho_S\right)$$

$$\text{(IV.28)}$$

IV.C The governing equation for the geometrical acoustic limit

In the case of wavelength being very small compared to the length scales associated with velocity and temperature fluctuations and that the background flow is incompressible, equation (IV.27) becomes,

$$\frac{\partial^2 \rho_S}{\partial t^2} - c^2 \nabla^2 \rho_S \approx 2\rho_B \mathbf{u_B} \cdot \nabla(\nabla \cdot \mathbf{u}_S) + \mathbf{u_B} \cdot \left(\mathbf{u_B} \cdot \nabla(\nabla \rho_S)\right) \qquad \text{(IV.29)}$$

Note that we have kept terms of $O(\mathcal{M}a)$ and $O(\mathcal{M}a^2)$. We can rewrite the last term on right hand side as,

$$\mathbf{u_B} \cdot \left(\mathbf{u_B} \cdot \nabla(\nabla \rho_S)\right) = (\mathbf{u}_B \cdot \nabla)(\mathbf{u}_B \cdot \nabla)\rho_S - \left((\mathbf{u}_B \cdot \nabla)\mathbf{u}_B\right) \cdot \nabla \rho_S$$

Thus equation (IV.29) becomes,

$$\frac{\partial^2 \rho_S}{\partial t^2} - c^2 \nabla^2 \rho_S \approx 2\rho_B \mathbf{u_B} \cdot \nabla(\nabla \cdot \mathbf{u}_S) + (\mathbf{u}_B \cdot \nabla)(\mathbf{u}_B \cdot \nabla)\rho_S - \left((\mathbf{u}_B \cdot \nabla)\mathbf{u}_B\right) \cdot \nabla \rho_S$$

Substituting in the above equation,

$$\nabla \cdot \mathbf{u}_S = -\frac{1}{\rho_B}\left[\frac{\partial \rho_S}{\partial t} + \mathbf{u}_B \cdot \nabla \rho_S\right]$$

$$(\mathbf{u}_B \cdot \nabla)\mathbf{u}_B = -\left[\frac{\partial \mathbf{u}_B}{\partial t} + \frac{1}{\rho_B}\nabla p_B\right]$$

We obtain,

$$\frac{\partial^2 \rho_S}{\partial t^2} - c^2 \nabla^2 \rho_S = -2\mathbf{u_B} \cdot \nabla \left(\frac{\partial \rho_S}{\partial t} + \mathbf{u}_B \cdot \nabla \rho_S \right) + (\mathbf{u}_B \cdot \nabla)(\mathbf{u}_B \cdot \nabla)\rho_S + \left(\frac{\partial \mathbf{u}_B}{\partial t} \right) \cdot \nabla \rho_S$$

$$+ \underbrace{\left(\frac{1}{\rho_B} \nabla p_B \right) \cdot \nabla \rho_S}_{O\left(\frac{\lambda}{l_0} \right)}$$

The last term is of $O\left(\frac{\lambda}{l_0} \right)$ since,

$$\frac{1}{\rho_B} \nabla p_B \cdot \nabla \rho_S \Big/ c^2 \nabla^2 \rho_S \sim \frac{\tilde{c}^2}{\rho_B} \nabla \rho_B \cdot \nabla \rho_S \Big/ c^2 \nabla^2 \rho_S \sim \frac{c^2 \left[1 + \frac{T_B}{T} \right]}{\rho_B} \nabla \rho_B \cdot \nabla \rho_S \Big/ c^2 \nabla^2 \rho_S$$

$$\sim O\left(\frac{\lambda}{l_0} \left[1 + \frac{T_B}{T} \right] \right)$$

Neglecting this term and rearranging the rest, we obtain equation (IV.5).

IV.D The governing equations for log-amplitude and phase fluctuations

We begin with equation (IV.6) and proceed by substituting the Rytov representation, $p_S(x,t) = e^{\Psi(x,t)}$, which gives,

$$\frac{1}{c^2} \left[\frac{\partial^2 \Psi}{\partial t^2} + \left(\frac{\partial \Psi}{\partial t} \right)^2 \right] - \nabla^2 \Psi - (\nabla \Psi)^2 = -\frac{2}{c^2} \left[\left(\frac{\partial \Psi}{\partial t} \right)(\mathbf{u}_B \cdot \nabla \Psi) + \mathbf{u}_B \cdot \nabla \left(\frac{\partial \Psi}{\partial t} \right) \right]$$

$$+ \left(\frac{T_B}{T} \right) \left[\nabla^2 \Psi + (\nabla \Psi)^2 \right] \qquad (IV.30)$$

The terms on the right hand side of the above equation are of $O(\mathcal{M}a)$. Using perturbative expansion of the form,

$$\Psi = \Psi_0 + (\mathcal{M}a)\Psi_1 + (\mathcal{M}a^2)\Psi_2 + \cdots$$

and substituting in equation (IV.30), we obtain successive equations in orders of $\mathcal{M}a$ which are,

O(1):

$$\frac{1}{c^2}\left[\frac{\partial^2 \Psi_0}{\partial t^2} + \left(\frac{\partial \Psi_0}{\partial t}\right)^2\right] - \nabla^2\Psi_0 - (\nabla\Psi_0)^2 = 0$$

where $\Psi_0 = \chi_0 + \iota\Phi_0$ such that $\chi_0 = \log(A_0)$ and $\Phi_0 = k_I\hat{m}\cdot\mathbf{x} - ft$. The unit vector along $\mathbf{k_I}$ is denoted by $\hat{m}$. On assuming that χ_0, k_I and f of the incident wave as constants, it is straightforward to check that the above equation is satisfied.

O($\mathcal{M}a$):

$$\frac{1}{c^2}\left[\frac{\partial^2\Psi_1}{\partial t^2} + 2\left(\frac{\partial\Psi_0}{\partial t}\right)\left(\frac{\partial\Psi_1}{\partial t}\right)\right] - \nabla^2\Psi_1 - 2(\nabla\Psi_0\cdot\nabla\Psi_1) = -\frac{2}{c^2}\left[\left(\frac{\partial\Psi_0}{\partial t}\right)(\mathbf{u}_B\cdot\nabla\Psi_0) + \mathbf{u}_B\cdot\nabla\left(\frac{\partial\Psi_0}{\partial t}\right)\right]$$

$$+\left(\frac{T_B}{T}\right)\left[\nabla^2\Psi_0 + (\nabla\Psi_0)^2\right]$$

On substituting Ψ_0, we obtain,

$$\frac{1}{c^2}\frac{\partial^2\Psi_1}{\partial t^2} - \nabla^2\Psi_1 = 2\iota\left(\frac{k_I}{c}\right)\left(\frac{\partial\Psi_1}{\partial t}\right) + 2\iota k_I(\hat{m}\cdot\nabla\Psi_1) - 2\left(\frac{k_I^2}{c}\right)(\hat{m}\cdot\mathbf{u}_B) - k_I^2\left(\frac{T_B}{T}\right)$$

On substituting $\Psi_1 = \chi_1 + \iota\Phi_1$ and equating the real and imaginary parts,

$$\underbrace{\frac{1}{c^2}\frac{\partial^2\chi_1}{\partial t^2}}_{O\left(\mathcal{M}a^2\left(\frac{\lambda}{l}\right)^2\right)} - \underbrace{\nabla^2\chi_1}_{O\left(\left(\frac{\lambda}{l}\right)^2\right)} = -2\left(\frac{k_I}{c}\right)\left(\frac{\partial\Phi_1}{\partial t}\right) \underbrace{}_{O(\mathcal{M}a)} - \underbrace{2k_I(\hat{m}\cdot\nabla\Phi_1)}_{O(1)} - \underbrace{2\left(\frac{k_I^2}{c}\right)(\hat{m}\cdot\mathbf{u}_B)}_{O(1)} - \underbrace{k_I^2\left(\frac{T_B}{T}\right)}_{O(\mathcal{M}a)}$$

$$\underbrace{\frac{1}{c^2}\frac{\partial^2\Phi_1}{\partial t^2}}_{O(\mathcal{M}a^2)} - \underbrace{\nabla^2\Phi_1}_{O(1)} = \underbrace{2\left(\frac{k_I}{c}\right)\left(\frac{\partial\chi_1}{\partial t}\right)}_{O(\mathcal{M}a)} + \underbrace{2k_I(\hat{m}\cdot\nabla\chi_1)}_{O(1)}$$

The order of magnitudes of the terms in the above equations imply that $\Phi_1 \sim O\left(\frac{1}{\mathcal{M}a}\left(\frac{\lambda}{l}\right)\right)$ and $\chi_1 \sim O\left(\frac{1}{\mathcal{M}a}\left(\frac{\lambda}{l}\right)^2\right)$. Equating the terms of $O(1)$, we obtain the equations,

$$(\hat{m} \cdot \nabla \Phi_1) = k_I \underbrace{\left[-\left(\frac{\hat{m} \cdot \mathbf{u}_B}{c}\right)\right]}_{n'(\mathbf{x},t)}$$

$$k_I(\hat{m} \cdot \nabla \chi_1) = -\frac{1}{2}\nabla^2 \Phi_1 \tag{IV.32a}$$

The term in brackets on the right hand side of equation (IV.32a) can be identified as the fluctuations in the refractive index of the medium. If the temperature fluctuations are externally induced in the flow and are of $O(\mathcal{M}a)$, the fluctuations in refractive index become,

$$n'(\mathbf{x},t) = \left[-\left(\frac{\hat{m} \cdot \mathbf{u}_B}{c}\right) - \frac{1}{2}\left(\frac{T_B}{T}\right)\right]$$

This expression was also obtained in [138, 139, 140]. If we assume for simplicity that the incident wave propagates along x-axis and that the total length of propagation is denoted by L (figure IV.4),

$$\frac{\partial \Phi_1}{\partial x} = -k_I\left(\frac{u_{B,x}}{c}\right)$$

$$k_I\frac{\partial \chi_1}{\partial x} = -\frac{1}{2}\nabla^2 \Phi_1$$

On integrating the above equations, we get,

$$\Phi_1(L,y,z,t) = k_I \int_0^L dx\ n'(x,y,z,t)$$

$$\chi_1(L,y,z,t) = -\frac{1}{2k_I}\left[\int_0^L dx\ \left(\frac{\partial^2 \Phi_1}{\partial y^2} + \frac{\partial^2 \Phi_1}{\partial z^2}\right)\right] - \frac{1}{2k_I}\underbrace{\left[\left(\frac{\partial \Phi_1}{\partial x}\right)_{(L,y,z,t)} - \left(\frac{\partial \Phi_1}{\partial x}\right)_{(0,y,z,t)}\right]}_{\frac{n'(L,y,z,t)-n'(0,y,z,t)}{2}}$$

If at $x = 0$ and $x = L$, we assume that the flow is bounded with a fixed temperature and no-slip boundary condition, the last term on the right hand side of the second equation would be zero. This gives us the equations (IV.8) and (IV.9).

Chapter V

General conclusion and perspectives

In this thesis, we study three different fluctuating quantities in turbulent flows; spontaneously generated temperature fluctuations, the spatio-temporal quantity of coherence for velocity fluctuations and parameter fluctuations of an acoustic wave incident on a turbulent flow.

In the first part of the thesis, we study the temperature fluctuations generated by viscous dissipation in a turbulent flow. We have devised an experiment with the von Kármán swirling flow where the boundaries are maintained at a fixed temperature. This ensures that the mean temperature of the flow is maintained constant. We observe that the magnitude of temperature fluctuations (its root mean square or RMS value) and the energy spectra do not behave according to large scale scaling obtained from dimensional arguments. We develop a theoretical model accounting for the intermittent behaviour of the dissipation process. On comparing the energy spectra for temperature fluctuations predicted by our model and the ones obtained experimentally, we can determine the value of the *intermittency exponent*, μ, for the dissipation process. Doing so, we obtain $\mu \approx 0.4$ which falls in the range of values, $0.25 < \mu < 0.5$, reported by previous experiments studying dissipation. This gives a new method of obtaining the intermittency exponent of the process of turbulent dissipation from one point temporal measurement of temperature. Our theoretical analysis also suggests that the total energy in the temperature fluctuations (or its RMS value) comes from dissipative events. The experimentally observed logarithmic dependence (as opposed to

quadratic dependence) of the RMS value of temperature fluctuations on the Reynolds number would thus likely be a result of the intermittent behaviour of dissipation in turbulent flows. Another feature of temperature fluctuations observed in our experiments is the presence of large negative bursts in its time signals. We show that these bursts are correlated to the negative bursts observed in pressure fluctuations in a turbulent flow which have been shown to arise from vorticity filaments by other studies. We can obtain the structure of these peaks using the method of *coherent averaging* and show that it matches the structure as predicted for a weakly compressible adiabatic Burgers vortex. This suggests that though the turbulent flow is of low Mach number and essentially incompressible, the vorticity filaments are compressible structures as seen from their pressure and temperature profiles. One more observation is the low-frequency power law behaviour of the energy spectrum of temperature fluctuations. To understand the physical origin of this low-frequency behaviour, further analysis is required. In conclusion, temperature fluctuations are observed to be entirely a result of intermittent events (vorticity filaments and dissipation).

The second part of this thesis focuses on the coherence of velocity fluctuations in turbulent flows. The spatio-temporal quantity of coherence measured from two point velocity signals in a turbulent flow depends on the spatial distance between the two points of measurement and frequency. We develop two experiments and use two different experimental techniques to validate the reproducibility of our results. From our experimental observations, coherence decays exponentially in space as well as frequency. Our theoretical model which is based on the effect of sweeping by the most energetic integral scales correctly predicts this behaviour. The sweeping effect though previously observed for one point energy spectrum of velocity fluctuations was not observed in two point statistics of velocity fluctuations in turbulent flows.

This brings us to the third and final part of the thesis where we study the effect of scattering on the acoustic wave propagation in turbulent flows. We study the fluctuations in amplitude[1] and phase of an acoustic wave incident on the turbulent flow. The two contributors to the amplitude and phase fluctuations of an acoustic wave are the inhomogeneities in temperature and velocity fluctuations in the turbulent flow. If the turbulent flow does not have any bulk sources of heat or temperature gradients, the sole source of the temperature inhomogeneities would be viscous dissipation which would be inherent to all turbulent flows. From the results on the study of spontaneously generated temperature fluctuations, we understand that the amplitude and phase fluctuations would be a result of the inhomogeneities in velocity fluctuations whereas temperature inhomogeneities would play a negligible role. We analytically show that the energy spectrum of phase fluctuations can be determined from the behaviour of coherence of velocity fluctuations. Our analytical predictions are in agreement with the energy spectra of phase fluctuations obtained experimentally. This implies that the most energetic integral scales sweep the acoustic wave propagating through the turbulent flow resulting in phase fluctuations whose behaviour is determined by the quantity of coherence. The integral scales would also sweep the structures of vorticity filaments and is likely the reason for low-frequency behaviour in the energy spectrum of phase fluctuations observed in our experiments. When it comes to amplitude fluctuations, a simple analytical form cannot be obtained without knowledge about the spatio-temporal behaviour of the second

---

[1]We actually study the quantity of *log-amplitude* fluctuations which for brevity we call simply as amplitude fluctuations.

gradients of velocity[2]. Experimentally, we make two observations. First, the time signal of amplitude fluctuations displays large negative bursts akin to the ones observed in temperature and pressure fluctuations in a turbulent flow. Second, the energy spectra of amplitude fluctuations display exponential decay with frequency. The latter observation suggests us the one-point energy spectrum as well as the two-point cross energy spectrum of the second gradient of velocity fluctuations would also decay exponentially with frequency. We note that obtaining the quantity of second gradient of velocity locally is challenging experimentally but nonetheless the expected exponential behaviour needs to be validated with further experiments. Lastly, we present the first experimental evidence in measuring the change in speed of sound due to multiple scattering in a turbulent flow and show that it follows the expected [18] scaling with the Mach number.

V.1 Perspectives

Future studies concerning the spontaneous generation of temperature fluctuations could answer the question on the source of low frequency fluctuations observed in the energy spectrum as well as the logarithmic dependence of the RMS of temperature fluctuations. Another possibility would be to study the two point statistics of spontaneously generated temperature fluctuations, for example the structure functions. All these questions would shed more light on the process of viscous dissipation in turbulent flows.

The study of coherence and the analytical model developed therein suggests that our observations should also be valid for the advection of passive scalars in turbulent flows. Future experimental work can test this hypothesis. Similar to coherence which is a two point spatio-temporal quantity, what is the effect of sweeping on other statistical quantities? The effect of sweeping deserves further understanding as it breaks the universality hypothesis of Kolmogorov's *K41* theory with the dynamics of inertial scales being affected by the integral scales.

Finally, the fluctuations in amplitude of an acoustic wave travelling through a turbulent flow displays sharp negative peaks which are reminiscent of the negative peaks observed in pressure and temperature fluctuations in a turbulent flow. We have shown that for the pressure and temperature fluctuations, the peaks are a result of the vorticity filaments. What is the source of the negative peaks in amplitude fluctuations of an acoustic wave? Is it possible that it is an observation of the vorticity filaments?

We hope that future experimental, analytical and numerical studies will be able to answer some, if not all, of these questions.

---

[2]By second gradients we mean the quantity $\frac{\partial^2 u_i}{\partial x_j^2}$ for any index $i, j \in 1, 2, 3$. Here u_i denotes the ith component of the velocity fluctuations.

Appendix A

Calibration of hot-wire probes

Throughout all the experiments, we use two 1D hot-wire probes (*Dantec 55P16*). We describe the procedure for their calibration.

A.1 King's law

The hot-wire probe consists of a sensing filament which is a tungsten wire of 5 µm diameter and 1.25 mm long, exposed to the fluid flow. The basic working principle is that as a current is passed through the wire the wire gets electrically heated owing to Joule dissipation. The wire loses heat to the cold surrounding fluid by forced convection as it is exposed to the flow. The heat transferred by the wire to the fluid via convection which is characterized by the Nusselt number would be a function of the other dimensionless numbers associated with the heat transfer problem. Combining empirical relations from experimental observations and theoretical approaches, one obtains[1] [141, 142, 143, 144],

$$\frac{V^2}{R(R - R_\infty)} = A + B\sqrt{u}$$

which is called the King's law. where A and B depend on the physical properties of the fluid and the characteristics of the wire at the ambient temperature denoted by T_∞. In the above relation, V, R and R_∞ are the voltage across the filament of the hot-wire probe, the resistance of the filament during measurement and the resistance of the filament at ambient temperature respectively. The velocity component of the flow perpendicular to the length of the filament is denoted by u.

When the hot-wire probes are operated in CTA (Constant Temperature Anemometry), the resistance (and thus the temperature) of the wire is kept constant with the aid of Wheatstone bridge. The filament of the hot-wire probe forms one arm of the Wheatstone bridge. This gives us a simple relation between the voltage across the filament of the hot-wire probe and the velocity of the surrounding fluid perpendicular to the length of the filament,

---

[1]This is true for small *overheat ratio*. The overheat ratio is defined as the ratio $\left(\frac{T - T_\infty}{T_\infty}\right)$. The temperature of the flow and the ambient temperature are denoted by T and T_∞ respectively.

$$V^2 = A + B\sqrt{u}$$

The Dantec system employs *overheat adjustment* and *temperature correction* as a part of hardware setup, which minimizes the effect of variation in ambient temperature on output voltage. Care was taken that, hardware setup was performed prior to calibration and every experiment. Thus henceforth, temperature effects would be neglected.

A.2 Setup

For calibration, we generate a flow with a high mean velocity compared to the amplitude of fluctuating part or in other words, with a very low value of the ratio $(u'/\langle u \rangle)$. Here u' denotes the RMS of the velocity fluctuations and $\langle u \rangle$ is the mean of the velocity. Thus under the condition that $(u'/\langle u \rangle) << 1$, on averaging the King's law, we obtain:

$$\langle V \rangle^2 = A + B\sqrt{\langle u \rangle} \tag{A.1}$$

where we have also assumed that $(V'/\langle V \rangle) << 1$ and V', $\bar{V}$ are the RMS and mean of the voltage respectively. The assumption on the voltage fluctuations being smaller than their mean is guaranteed since we calibrate using a flow with $u' \ll \langle u \rangle$. The purpose of calibration is to find the values of the constants 'A' and 'B' for both the hot-wire probes.

For generating a flow with minimum possible value of $u'/\langle u \rangle$, we use a small table-top wind tunnel which involves an *ebmpapst* 24 V DC centrifugal blower. At the exit of the blower, we attach a square mesh and a tunnel of roughly square cross-section. The mesh reduces $u'/\langle u \rangle$ of the flow along the axis of the tunnel. We also connect a 0-10 V DC variable control input, thus allowing us to vary the air-flow in the wind tunnel necessary to obtain calibration.

To calibrate a hot-wire probe, we need a flow with known velocity. For this purpose, we use *testo 425* which is a pre-calibrated 1D hot-wire probe which gives direct measurement of velocity. The testo 425 probe can also directly measure the mean velocity over a time of our choice. Thus, for every location of measurement by the hot-wire, we use testo 425 probe at exactly the same location using a translation stage to obtain the mean velocity at that location (which is $\langle u \rangle$ in eqn.(A.1)). This, in conjunction with the mean voltage measured by the hot-wire (which is $\langle E \rangle$ in eqn.(A.1)), gives us the constants A and B. We also use temperature probe in our calibration for using overheat adjustment and temperature correction of the hardware.

The setup is shown in fig.A.1. The point 'O' is the center of the cross-section. The velocities are measured at 2 cm from the opening of the wind tunnel exactly in front of the point 'O'.
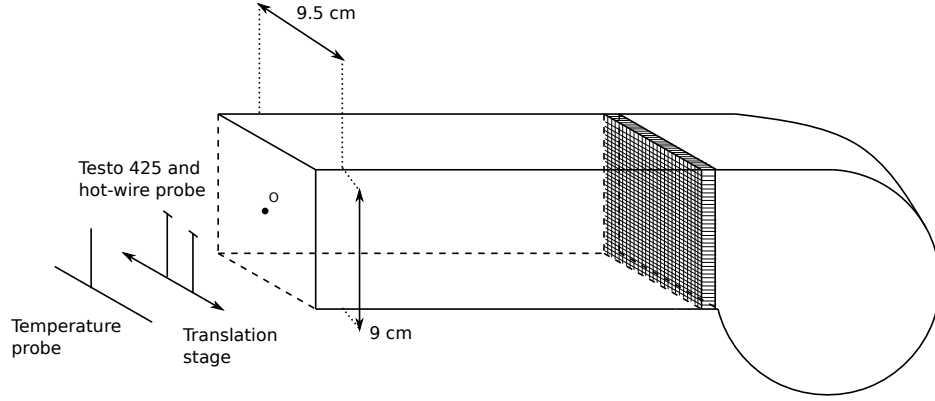
Fig. A.1   *Sketch of the calibration setup.*

A.3 Results

We measure the mean flow velocity using the testo for a duration of 2 min. This duration is enough to obtain a stationary value of the mean velocity. Fig.A.2 shows the calibration curves ($\langle V \rangle$ versus $\langle u \rangle$) for both the probes (whose voltages are denoted by V_1 and V_2). By fitting it to the functional form eqn.(A.1), we obtain,

$$V_1^2 = 1.744 + 0.7388\sqrt{u}$$
$$V_2^2 = 1.957 + 0.8031\sqrt{u}$$

Fig. A.2   *The mean voltage across the filament of hot-wire probes versus the mean velocity perpendicular to the filament. Probe 1 (red squares) and Probe 2 (blue circles). Black dashed and dotted dashed lines denote the fit using eqn.(A.1).*

Bibliography

[1] D. Seuss; *Oh, the places you'll go!* (Random House, New York) (1990); ISBN 9780679805274. 2
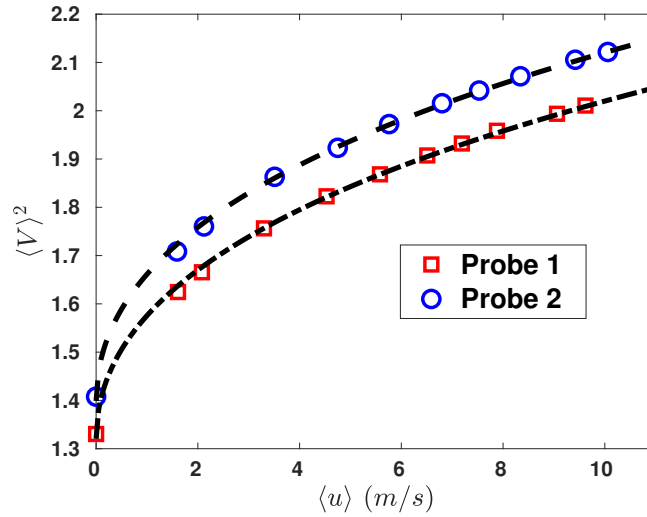
[2] M. Elia; *Journal d'Edward, hamster nihiliste, 1990-1990* (Flammarion, Paris) (2013); ISBN 2081290235. 1, 7, 77, 135, 185

[3] U. Frisch; *Turbulence: the legacy of AN Kolmogorov* (Cambridge university press) (1995). 1, 9, 24, 77, 78

[4] O. Reynolds; «XXIX. An experimental investigation of the circumstances which determine whether the motion of water shall be direct or sinuous, and of the law of resistance in parallel channels»; Philosophical Transactions of the Royal society of London p. 935–982 (1883). 1

[5] L. F. Richardson; «Atmospheric diffusion shown on a distance-neighbour graph»; Proceedings of the Royal Society of London. Series A, Containing Papers of a Mathematical and Physical Character **110**, p. 709–737 (1926). 1, 3

[6] S. B. Pope; *Turbulent flows* (Cambridge University Press, Cambridge New York) (2000); ISBN 9780521598866. 2, 78

[7] A. Kolmogorov; «The local structure of turbulence in incompressible viscous fluid for very large Reynolds numbers»; Cr Acad. Sci. URSS **30**, p. 301–305 (1941). 2

[8] A. Kolmogorov; «Dissipation of energy in locally isotropic turbulence»; dans «CR Dokl Acad Sci USSR», , tome 32p. 16–18 (1941). 2, 77

[9] A. Monin; *Statistical fluid mechanics, volume II: mechanics of turbulence.* 2, 10, 11, 63, 78, 79

[10] K. R. Sreenivasan; «On the universality of the Kolmogorov constant»; Physics of Fluids **7**, p. 2778–2784 (1995). 2

[11] A. Dinkelacker, M. Hessel, G. Meier & G. Schewe; «Investigation of pressure fluctuations beneath a turbulent boundary layer by means of an optical method»; The Physics of Fluids **20**, p. S216–S224 (1977). 4

[12] G. Schewe; «On the structure and resolution of wall-pressure fluctuations associated with turbulent boundary-layer flow»; Journal of Fluid Mechanics **134**, p. 311–328 (1983). 4

[13] P. Abry, S. Fauve, P. Flandrin & C. Laroche; «Analysis of pressure fluctuations in swirling turbulent flows»; Journal de Physique II **4**, p. 725–733 (1994). 4, 35, 45, 51, 66

[14] O. Cadot, S. Douady & Y. Couder; «Characterization of the low-pressure filaments in a three-dimensional turbulent shear flow»; Physics of Fluids **7**, p. 630–646 (1995). 4, 29, 45

[15] Z. Warhaft; «Passive scalars in turbulent flows»; Annual Review of Fluid Mechanics **32**, p. 203–240 (2000). 4, 8

[16] P. C. di Leoni, P. J. Cobelli & P. D. Mininni; «The spatio-temporal spectrum of turbulent flows»; The European Physical Journal E **38**, p. 1–10 (2015). 4, 78

[17] H. Tennekes; «Eulerian and Lagrangian time microscales in isotropic turbulence»; Journal of Fluid Mechanics **67**, p. 561–567 (1975). 4, 79, 81, 83, 93, 119, 160

[18] F. Lund; «Sound—vortex interaction in infinite media»; dans «Sound-Flow Interactions», p. 112–159 (Springer) (2002). 5, 137, 151, 152, 172, 175, 178, 187

[19] M. Beychok; *Fundamentals of Stack Gas Dispersion*; vol. 1 (Beychok) (1979). `https://books.google.fr/books?id=MEOEPQAACAAJ`. 7

[20] G. T. Csanady; *Turbulent diffusion in the environment*; tome 3 (2012). 7

[21] H. Moffatt; *Magnetic Field Generation in Electrically Conducting Fluids*; Cambridge Monographs on Mechanics (Cambridge University Press) (1978); ISBN 9780521216401. `https://books.google.fr/books?id=cAo4AAAAIAAJ`. 7

[22] E. Bodenschatz, W. Pesch & G. Ahlers; «Recent developments in Rayleigh-Bénard convection»; Annual review of fluid mechanics **32**, p. 709–778 (2000). 7

[23] K. R. Sreenivasan; «Turbulent mixing: A perspective»; Proceedings of the National Academy of Sciences p. 201800463 (2018). 8, 26

[24] B. I. Shraiman & E. D. Siggia; «Scalar turbulence»; Nature **405**, p. 639–646 (2000). 8

[25] G. Falkovich, K. Gawędzki & M. Vergassola; «Particles and fields in fluid turbulence»; Reviews of modern Physics **73**, p. 913 (2001). 8

[26] European Space Agency (ESA); «Nitrogen dioxide pollution mapped»; `https://www.esa.int/Applications/Observing_the_Earth/Copernicus/Sentinel-5P/Nitrogen_dioxide_pollution_mapped` (2018). 8

[27] NOAA ESRL Physical Sciences Division (PSD); «PSD Real-time Satellite Products»; `https://www.esrl.noaa.gov/psd/psd2/coastal/satres/data/html/mcsst.html` (2020). 8

[28] GSFC, NASA; `https://science.gsfc.nasa.gov/695/rsrch_areas.html` (2012). 8

[29] D. DE MARINIS, S. CHIBBARO, M. MELDI & P. SAGAUT; «Temperature dynamics in decaying isotropic turbulence with Joule heat production»; Journal of Fluid Mechanics **724**, p. 425–449 (2013). 9

[30] W. J. BOS; «The temperature spectrum generated by frictional heating in isotropic turbulence»; Journal of Fluid Mechanics **746**, p. 85–98 (2014). 9

[31] W. J. BOS, R. CHAHINE & A. V. PUSHKAREV; «On the scaling of temperature fluctuations induced by frictional heating»; Physics of Fluids **27**, p. 095 105 (2015). 9, 64

[32] A. PUSHKAREV, G. BALARAC & W. J. BOS; «Reynolds and Prandtl number scaling of viscous heating in isotropic turbulence»; Physical Review Fluids **2**, p. 084 606 (2017). 9

[33] W. J. BOS & R. ZAMANSKY; «Power fluctuations in turbulence»; Physical review letters **122**, p. 124 504 (2019). 9

[34] M. BRACHET; «Direct simulation of three-dimensional turbulence in the Taylor–Green vortex»; Fluid dynamics research **8**, p. 1 (1991). 9, 63

[35] B. J. BAYLY, C. LEVERMORE & T. PASSOT; «Density variations in weakly compressible flows»; Physics of Fluids A: Fluid Dynamics **4**, p. 945–954 (1992). 10, 17

[36] H. MOFFATT; «Six lectures on general fluid dynamics and two on hydromagnetic dynamo theory.»; (1977). 10

[37] L. LANDAU & E. LIFSHITZ; «Fluid Mechanics Pergamon»; New York **61** (1959). 10, 11, 17, 18

[38] A. MONIN; *Statistical fluid mechanics, volume I: mechanics of turbulence.* 10, 18

[39] Z. WARHAFT & J. LUMLEY; «An experimental study of the decay of temperature fluctuations in grid-generated turbulence»; Journal of Fluid Mechanics **88**, p. 659–684 (1978). 24

[40] T. ZHOU, R. ANTONIA, L. DANAILA & F. ANSELMET; «Transport equations for the mean energy and temperature dissipation rates in grid turbulence»; Experiments in Fluids **28**, p. 143–151 (2000). 24

[41] F. MOISY, H. WILLAIME, J. ANDERSEN & P. TABELING; «Passive scalar intermittency in low temperature helium flows»; Physical review letters **86**, p. 4827 (2001). 24

[42] S. CORRSIN; «Heat transfer in isotropic turbulence»; Journal of Applied Physics **23**, p. 113–118 (1952). 25

[43] H. K. WISKIND; «A uniform gradient turbulent transport experiment»; Journal of Geophysical Research **67**, p. 3033–3048 (1962). 25

[44] K. VENKATARAMANI & R. CHEVRAY; «Statistical features of heat transfer in grid-generated turbulence: constant-gradient case»; Journal of Fluid Mechanics **86**, p. 513–543 (1978). 25

[45] A. Sirivat & Z. Warhaft; «The effect of a passive cross-stream temperature gradient on the evolution of temperature variance and heat flux in grid turbulence»; Journal of Fluid Mechanics **128**, p. 323–346 (1983). 25, 27

[46] L. Mydlarski & Z. Warhaft; «Passive scalar statistics in high-Péclet-number grid turbulence»; Journal of Fluid Mechanics **358**, p. 135–175 (1998). 25, 27

[47] A. Yaglom; «On the local structure of a temperature field in a turbulent flow»; dans «Dokl. akad. nauk sssr», , tome 69p. 743–746 (1949). 26

[48] A. M. Obukhov; «Structure of temperature field in turbulent flow»; Rapport technique; AIR FORCE SYSTEMS COMMAND WRIGHT-PATTERSON AFB OH FOREIGN TECHNOLOGY DIVISION (1970). 26

[49] S. Corrsin; «On the spectrum of isotropic temperature fluctuations in an isotropic turbulence»; Journal of Applied Physics **22**, p. 469–473 (1951). 26

[50] G. K. Batchelor; «Small-scale variation of convected quantities like temperature in turbulent fluid Part 1. General discussion and the case of small conductivity»; Journal of Fluid Mechanics **5**, p. 113–133 (1959). 26

[51] T. Von Kármán; «Uber laminare und turbulente Reibung»; Z. Angew. Math. Mech. **1**, p. 233–252 (1921). 28

[52] G. K. Batchelor; «Note on a class of solutions of the Navier-Stokes equations representing steady rotationally-symmetric flow»; The quarterly journal of mechanics and applied mathematics **4**, p. 29–41 (1951). 28

[53] K. Stewartson; «On the flow between two rotating coaxial disks»; dans «Mathematical Proceedings of the Cambridge Philosophical Society», , tome 49p. 333–341 (Cambridge University Press) (1953). 28

[54] P. Zandbergen & D. Dijkstra; «Von Kármán swirling flows»; Annual review of fluid mechanics **19**, p. 465–491 (1987). 28

[55] S. Douady, Y. Couder & M. Brachet; «Direct observation of the intermittency of intense vorticity filaments in turbulence»; Physical review letters **67**, p. 983 (1991). 29, 45, 53

[56] R. Monchaux, M. Berhanu, M. Bourgoin, M. Moulin, P. Odier, J.-F. Pinton, R. Volk, S. Fauve, N. Mordant, F. Pétrélis *et al.*; «Generation of a magnetic field by dynamo action in a turbulent flow of liquid sodium»; Physical review letters **98**, p. 044 502 (2007). 29

[57] M. Berhanu, R. Monchaux, S. Fauve, N. Mordant, F. Pétrélis, A. Chiffaudel, F. Daviaud, B. Dubrulle, L. Marié, F. Ravelet *et al.*; «Magnetic field reversals in an experimental turbulent dynamo»; EPL (Europhysics Letters) **77**, p. 59 001 (2007). 29

[58] S. Fauve, C. Laroche & B. Castaing; «Pressure fluctuations in swirling turbulent flows»; Journal de physique II **3**, p. 271–278 (1993). 29, 45

[59] B. Mercier, E. Jondeau, T. Castelain, Y. Ozawa, C. Bailly & G. Comte-Bellot; «High frequency temperature fluctuation measurements by Rayleigh scattering and constant-voltage cold-wire techniques»; Experiments in Fluids **60**, p. 110 (2019). 30

[60] B. Dernoncourt, J.-F. Pinton & S. Fauve; «Experimental study of vorticity filaments in a turbulent swirling flow»; Physica D: Nonlinear Phenomena **117**, p. 181–190 (1998). 45, 135

[61] T. Ishihara, Y. Kaneda, M. Yokokawa, K. Itakura & A. Uno; «Spectra of energy dissipation, enstrophy and pressure by high-resolution direct numerical simulations of turbulence in a periodic box»; Journal of the Physical Society of Japan **72**, p. 983–986 (2003). 45

[62] J. Jimenez & A. A. Wray; «On the characteristics of vortex filaments in isotropic turbulence»; Journal of Fluid Mechanics **373**, p. 255–285 (1998). 47, 53

[63] R. Labbé Morales; *Ecoulements tourbillonnaires de von karman*; Thèse de doctorat; Lyon, École normale supérieure (sciences) (1996). 50, 74, 135

[64] E. D. Siggia; «Numerical study of small-scale intermittency in three-dimensional turbulence»; Journal of Fluid Mechanics **107**, p. 375–406 (1981). 53

[65] J. Jiménez, A. A. Wray, P. G. Saffman & R. S. Rogallo; «The structure of intense vorticity in isotropic turbulence»; Journal of Fluid Mechanics **255**, p. 65–90 (1993). 53

[66] N. A. K. Doan, N. Swaminathan, P. Davidson & M. Tanahashi; «Scale locality of the energy cascade using real space quantities»; Physical Review Fluids **3**, p. 084 601 (2018). 53

[67] Y. Aboelkassem & G. H. Vatistas; «New model for compressible vortices»; (2007). 55

[68] I. Cohen, P. Kundu & H. Hu; *Fluid Mechanics* (Elsevier Science) (2004); ISBN 9780080470238. 55, 138

[69] J. M. Burgers; «A mathematical model illustrating the theory of turbulence»; dans «Advances in applied mechanics», , tome 1p. 171–199 (Elsevier) (1948). 57

[70] R. D. Sullivan; «A two-cell vortex solution of the Navier-Stokes equations»; Journal of the Aerospace Sciences **26**, p. 767–768 (1959). 57

[71] W. Rankine; «A Manual on Applied Mechanics. Richard Griffin and Company, Glasgow, Scotland»; (1858). 57

[72] W. Kaufmann; «Über die Ausbreitung kreiszylindrischer Wirbel in zähen (viskosen) Flüssigkeiten»; Ingenieur-Archiv **31**, p. 1–9 (1962). 57

[73] M. P. Scully *et al.*; «Helicopter rotor wake geometry and airloads and development of laser Doppler velocimeter for use in helicopter rotor wakes»; (1972). 57

[74] C. Oseen; «Uber die Wirbelbewegung in einer reibenden Flussigkeit»; Ark. Mat. Astro. Fys. **7** (1912). 57

[75] H. Lamb; *Hydrodynamics* (Dover publications, New York) (1945); ISBN 9780486602561. 57

[76] L. M. Mack; «The compressible viscous heat-conducting vortex»; Journal of Fluid Mechanics **8**, p. 284–292 (1960). 57

[77] P. Bellamy-Knights; «Viscous compressible heat conducting spiralling flow»; The Quarterly Journal of Mechanics and Applied Mathematics **33**, p. 321–336 (1980). 57

[78] W. Merzkirch; «Theoretical and experimental investigation of an unsteady vortex flow.»; (1964). 57

[79] M. Mandella; *Experimental and Analytical Studies of Compressible Vortices* (Stanford University) (1987). 57

[80] T. Colonius, S. K. Lele & P. Moin; «The free compressible viscous vortex»; Journal of Fluid Mechanics **230**, p. 45–73 (1991). 57

[81] N. Rott; «On the viscous core of a line vortex»; Zeitschrift für angewandte Mathematik und Physik ZAMP **9**, p. 543–553 (1958). 58

[82] K. R. Sreenivasan & R. Antonia; «The phenomenology of small-scale turbulence»; Annual review of fluid mechanics **29**, p. 435–472. 63

[83] K. Sreenivasan & P. Kailasnath; «An update on the intermittency exponent in turbulence»; Physics of Fluids A: Fluid Dynamics **5**, p. 512–514 (1993). 63

[84] M. Tanaka & S. Kida; «Characterization of vortex tubes and sheets»; Physics of Fluids A: Fluid Dynamics **5**, p. 2079–2082 (1993). 63

[85] J. Herault, F. Pétrélis & S. Fauve; «$1/f^{\alpha}$ Low Frequency Fluctuations in Turbulent Flows»; Journal of Statistical Physics **161**, p. 1379–1389 (2015). 66

[86] G. I. Taylor; «The spectrum of turbulence»; Proceedings of the Royal Society of London. Series A-Mathematical and Physical Sciences **164**, p. 476–490 (1938). 78

[87] L. Canet, V. Rossetto, N. Wschebor & G. Balarac; «Spatiotemporal velocity-velocity correlation function in fully developed turbulence»; Physical Review E **95**, p. 023 107 (2017). 78

[88] A. Favre, J. Gaviglio & R. Dumas; «Measures de la corrélation dans le temps et l'espace et spectre de la turbulence en soufflerie. Colloq. Int. de Mécanique, Potiers»; Pub. Sci. et Tech. Ministere Air **251**, p. 293 (1951). 79

[89] G. Comte-Bellot & S. Corrsin; «Simple Eulerian time correlation of full-and narrow-band velocity signals in grid-generated,'isotropic'turbulence»; Journal of Fluid Mechanics **48**, p. 273–337 (1971). 79

[90] S. Chen & R. H. Kraichnan; «Sweeping decorrelation in isotropic turbulence»; Physics of Fluids A: Fluid Dynamics **1**, p. 2019–2024 (1989). 79, 81, 83

[91] M. NELKIN & M. TABOR; «Time correlations and random sweeping in isotropic turbulence»; Physics of Fluids A: Fluid Dynamics **2**, p. 81–83 (1990). 79

[92] T. SANADA & V. SHANMUGASUNDARAM; «Random sweeping effect in isotropic numerical turbulence»; Physics of Fluids A: Fluid Dynamics **4**, p. 1245–1250 (1992). 79

[93] A. G. DAVENPORT; «The spectrum of horizontal gustiness near the ground in high winds»; Quarterly Journal of the Royal Meteorological Society **87**, p. 194–211 (1961). 89, 133

[94] D. KRUG, W. J. BAARS, N. HUTCHINS & I. MARUSIC; «Vertical coherence of turbulence in the atmospheric surface layer: connecting the hypotheses of Townsend and Davenport»; Boundary-Layer Meteorology **172**, p. 199–214 (2019). 89

[95] W. J. BAARS, N. HUTCHINS & I. MARUSIC; «Self-similarity of wall-attached turbulence in boundary layers»; Journal of Fluid Mechanics **823** (2017). 89

[96] G. O. ROBERTS; «Dynamo action of fluid motions with two-dimensional periodicity»; Philosophical Transactions of the Royal Society of London. Series A, Mathematical and Physical Sciences **271**, p. 411–454 (1972). 91

[97] D. ARAGO & J. BIOT; «Refractive properties of binary mixtures»; Mem Acad Fr **15**, p. 7–11 (1806). 110

[98] A. LAGANÀ, R. RIVENC, J. LANGENBACHER, J. GRISWOLD & T. LEARNER; «Looking through plastics: Investigating options for the treatment of scratches, abrasions, and losses in cast unsaturated polyester works of art»; dans «ICOM-CC 17th Triennial Conference Preprints, Melbourne», p. 15–19 (2014). 112

[99] M. S. SONG, H. Y. CHOI, J. H. SEONG & E. S. KIM; «Matching-index-of-refraction of transparent 3D printing models for flow visualization»; Nuclear engineering and design **284**, p. 185–191 (2015). 112

[100] W. THIELICKE & E. STAMHUIS; «PIVlab–towards user-friendly, affordable and accurate digital particle image velocimetry in MATLAB»; Journal of open research software **2** (2014). 113

[101] M. J. LIGHTHILL; «On sound generated aerodynamically I. General theory»; Proceedings of the Royal Society of London. Series A. Mathematical and Physical Sciences **211**, p. 564–587 (1952). 135, 140

[102] M. J. LIGHTHILL; «On sound generated aerodynamically II. Turbulence as a source of sound»; Proceedings of the Royal Society of London. Series A. Mathematical and Physical Sciences **222**, p. 1–32 (1954). 135

[103] J. W. STRUTT & B. RAYLEIGH; *The theory of sound* (Dover) (1945). 135

[104] A. BEDARD; «Low-frequency atmospheric acoustic energy associated with vortices produced by thunderstorms»; Monthly Weather Review **133**, p. 241–263 (2005). 135

[105] B. R. ELBING, C. E. PETRIN & M. S. VAN DEN BROEKE; «Measurement and characterization of infrasound from a tornado producing storm»; The Journal of the Acoustical Society of America **146**, p. 1528–1540 (2019). 135

[106] C. SCHRAM; *Aeroacoustics of subsonic jets : prediction of the sound produced by vortex pairing based on particle image velocimetry*; Thèse de doctorat; Department of Applied Physics (2003). 135

[107] G. LILLEY; «A study of the silent flight of the owl»; dans «4th AIAA/CEAS aeroacoustics conference», p. 2340 (1998). 135

[108] J. W. STRUTT & B. RAYLEIGH; *The theory of sound*; tome 2 (Macmillan) (1896). 135

[109] A. OBUKHOV; «Scattering of sound in turbulent flow»; dans «Dokl. Akad. Nauk SSSR», , tome 30p. 611–614 (1941). 135

[110] D. BLOKHINTZEV; «The propagation of sound in an inhomogeneous and moving medium I»; The Journal of the Acoustical Society of America **18**, p. 322–328 (1946). 135

[111] R. H. KRAICHNAN; «The scattering of sound in a turbulent medium»; The Journal of the Acoustical Society of America **25**, p. 1096–1104 (1953). 135

[112] P. GROMOV, A. EZERSKII & A. FABRIKANT; «Sound scattering by a vortex wake behind a cylinder»; SPhAc **28**, p. 452–455 (1982). 135

[113] F. LUND & C. ROJAS; «Ultrasound as a probe of turbulence»; Physica D: Nonlinear Phenomena **37**, p. 508–514 (1989). 135

[114] C. BAUDET, S. CILIBERTO & J. PINTON; «Spectral analysis of the von kármán flow using ultrasound scattering»; Physical review letters **67**, p. 193 (1991). 135

[115] R. BERTHET; *Interaction son-écoulement*; Thèse de doctorat; École normale supérieure (Lyon) (2001). 135

[116] G. BRILLANT, F. CHILLÁ & J.-F. PINTON; «Transmission of sound through a single vortex»; The European Physical Journal B-Condensed Matter and Complex Systems **37**, p. 229–239 (2004). 135

[117] S. SEIFER & V. STEINBERG; «Flow induced ultrasound scattering: Experimental studies»; Physics of Fluids **16**, p. 1587–1602 (2004). 135

[118] S. SEIFER & V. STEINBERG; «Spatial and temporal turbulent velocity and vorticity power spectra from sound scattering»; Physical Review E **71**, p. 045 601 (2005). 135

[119] J.-F. PINTON & G. BRILLANT; «Sound and vorticity interactions: transmission and scattering»; Theoretical and Computational Fluid Dynamics **18**, p. 413–433 (2005). 135

[120] B.-T. CHU & L. S. KOVÁSZNAY; «Non-linear interactions in a viscous heat-conducting compressible gas»; Journal of Fluid Mechanics **3**, p. 494–514 (1958). 135

[121] V. I. TATARSKI; *Wave propagation in a turbulent medium* (Courier Dover Publications) (2016). 136, 137, 144, 147, 153

[122] L. A. CHERNOV; *Wave propagation in a random medium* (Courier Dover Publications) (2017). 136

[123] J. PINTON, C. LAROCHE, S. FAUVE & C. BAUDET; «Ultrasound scattering by buoyancy driven flows»; Journal de Physique II **3**, p. 767–773 (1993). 136

[124] J. ELICER-CORTÉS & C. BAUDET; «Ultrasound scattering from a turbulent round thermal pure plume»; Experimental thermal and fluid science **18**, p. 271–281 (1998). 136

[125] J. ELICER-CORTÉS, J. FUENTES, A. VALENCIA & C. BAUDET; «Experimental study of transition to turbulence of a round thermal plume by ultrasound scattering»; Experimental thermal and fluid science **20**, p. 137–149 (2000). 136

[126] J. C. ELICER-CORTÉS, R. CONTRERAS, D. BOYER, M. PAVAGEAU & R. HERNÁNDEZ; «Temperature spectra from a turbulent thermal plume by ultrasound scattering»; Experimental thermal and fluid science **28**, p. 803–813 (2004). 136

[127] A. PETROSSIAN & J.-F. PINTON; «Sound scattering on a turbulent, weakly heated jet»; Journal de Physique II **7**, p. 801–812 (1997). 136

[128] WIKIPEDIA; «Tornadogenesis — Wikipedia, The Free Encyclopedia»; http://en.wikipedia.org/w/index.php?title=Tornadogenesis&oldid=973333818 (2020). 136

[129] A. HAWKINSON; «One night I noticed a star changing colors and moving perceptibly.»; (2018). https://astronomy.com/magazine/ask-astro/2018/07/the-twinkle-of-stars. 136

[130] V. F. SOFIEVA, F. DALAUDIER & J. VERNIN; «Using stellar scintillation for studies of turbulence in the Earth's atmosphere»; Philosophical Transactions of the Royal Society A: Mathematical, Physical and Engineering Sciences **371**, p. 20120 174 (2013). 137

[131] V. E. OSTASHEV & D. K. WILSON; *Acoustics in moving inhomogeneous media* (CRC Press) (2015). 137

[132] S. CROW; «Aerodynamic sound emission as a singular perturbation problem»; Studies in applied mathematics **49**, p. 21–46 (1970). 140

[133] H. S. RIBNER; «Aerodynamic sound from fluid dilitations; a theory of the sound from jets and other flows»; Rapport technique; University of Toronto (1962). 140

[134] A. POWELL; «Theory of vortex sound»; The journal of the acoustical society of America **36**, p. 177–195 (1964). 140

[135] W. MÖHRING; «On vortex sound at low Mach number»; Journal of Fluid Mechanics **85**, p. 685–691 (1978). 140

[136] S. RYTOV; «Diffraction of light by ultrasonic waves»; Izvestiya AS USSR p. 223 (1937). 145

[137] F. Lin & M. Fiddy; «The Born–Rytov controversy: I. Comparing analytical and approximate expressions for the one-dimensional deterministic case»; JOSA A **9**, p. 1102–1110 (1992).   145

[138] A. Monin; «Characteristics of the scattering of sound in a turbulent atmosphere»; Sov. Phys. Acoust **7**, p. 370–373 (1962).   183

[139] V. I. Tatarskii; «The effects of the turbulent atmosphere on wave propagation»; Jerusalem: Israel Program for Scientific Translations, 1971 (1971).   183

[140] S. Clifford; «Propagation and scattering in random media»; Remote Sensing of the Troposphere (ed. VE Derr). University of Colorado, Boulder (1972).   183

[141] G. Comte-Bellot; «Hot-wire anemometry»; Annual review of fluid mechanics **8**, p. 209–231 (1976).   189

[142] L. V. King; «XII. On the convection of heat from small cylinders in a stream of fluid: Determination of the convection constants of small platinum wires with applications to hot-wire anemometry»; Philosophical transactions of the royal society of London. series A, containing papers of a mathematical or physical character **214**, p. 373–432 (1914).   189

[143] L. V. King; «LVII. On the precision measurement of air velocity by means of the linear hot-wire anemometer»; The London, Edinburgh, and Dublin Philosophical Magazine and Journal of Science **29**, p. 556–577 (1915).   189

[144] L. V. King; «The linear hot-wire anemometer and its applications in technical physics»; Journal of the Franklin Institute **181**, p. 1–25 (1916).   189

RÉSUMÉ

Dans cette thèse, nous étudions les fluctuations de vitesse et de température dans un écoulement turbulent, et leurs implications sur la propagation d'ondes acoustiques en turbulence. La première partie est consacrée à l'étude de la génération spontanée de fluctuations de température par un écoulement turbulent. Nous démontrons que ces fluctuations de température proviennent de deux types de structures intermittentes, les filaments de vorticité et les structures dissipatives. Dans la seconde partie, nous étudions les fluctuations spatio-temporelles de la vitesse, en utilisant la fonction de cohérence. Nous démontrons que la fonction de cohérence résulte d'un balayage des fluctuations de vitesse dans la gamme inertielle par les fluctuations plus lentes de l'échelle intégrale. L'effet du balayage est particulièrement intéressant pour l'étude des écoulements turbulents, car il ne rentre pas dans le cadre de la théorie *K41* de Kolmogorov. Enfin, nous étudions la propagation d'ondes acoustiques à travers un écoulement turbulent, et en particulier les fluctuations de phase et d'amplitude. Nous montrons que les fluctuations de phase peuvent être déduites de la fonction de cohérence des fluctuations de vitesse. Ces fluctuations résultent ainsi d'un effet de balayage de l'onde acoustique par l'écoulement turbulent. Nous mesurons également la variation de la vitesse du son induite par un effet de diffusion multiple par l'écoulement turbulent.

MOTS CLÉS

Turbulence, Fluctuations, Temperature, Dissipation, Filaments de vorticité, Cohérence, Ondes acoustiques, Fluctuations des paramètres, Diffusion multiple, Vitesse du son.

ABSTRACT

In this thesis, we study the velocity and temperature fluctuations in a turbulent flow and their implications on the propagation of acoustic waves in turbulence. The first part is devoted to the study of the spontaneous generation of temperature fluctuations by a turbulent flow. We demonstrate that these temperature fluctuations originate from two types of intermittent structures, vorticity filaments and dissipative structures. In the second part, we study the spatio-temporal fluctuations of velocity, using the coherence function. We demonstrate that the coherence function results from the sweeping of the velocity fluctuations in the inertial range by the slower fluctuations of the integral scale. The sweeping effect is particularly interesting for the study of turbulent flows, because it does not come within the scope of Kolmogorov's *K41* theory. Finally, we study the propagation of acoustic waves through a turbulent flow and in particular phase and amplitude fluctuations. We show that phase fluctuations can be deduced from the coherence function of turbulent speed fluctuations. These fluctuations thus result from a sweeping effect of the acoustic wave by the turbulent flow. We also measure the variation in the speed of sound induced by a multiple scattering effect of the turbulent flow.

KEYWORDS

Turbulence, Fluctuations, Temperature, Dissipation, Vorticity filaments, Coherence, Sweeping, Acoustic waves, Parameter fluctuations, Multiple scattering, Speed of sound.